THE UNIVERSITY *of* EDINBURGH

Measurement of $\Delta\Gamma_s$ using the B_s^0 decays to the final states $J/\psi\eta'$ and $J/\psi f_0$

Stefano Petrucci

Doctor of Philosophy
The University of Edinburgh
April 21, 2022

Abstract

The main research field of the Large Hadron Collider beauty (LHCb) experiment at Large Hadron Collider (LHC) is the study of CP violation and rare decays of beauty and charm hadrons. Measurement of the B_s^0 mixing parameters $\Delta\Gamma_s$, Γ_s, Δm_s and ϕ_s provide a precise test of the Standard Model (SM). New particles, as predicted in models of physics beyond the SM may alter the measured values of B_s^0 mixing parameters compared to the SM. In this thesis, a measurement of $\Delta\Gamma_s$ is made by comparing the lifetimes in the $B_s^0 \to J/\psi\eta'$ and $B_s^0 \to J/\psi f_0$ decay modes.

This work uses the full data set recorded by the LHCb detector between 2011 and 2018. The value of $\Delta\Gamma_s$ is determined by measuring the yields of the two channels in bins of decay time, computing the ratio between the two channels in each bin and performing a χ^2 minimization. This technique, combined with the choice of two decay channels with similar topology, reduces the impact of the time acceptance introduced by the detector.

The measured value of $\Delta\Gamma_s$ is

$$\Delta\Gamma_s = (0.081 \pm 0.011 \pm 0.009)\ \text{ps}^{-1}$$

where the first uncertainty is statistical and the second is systematic.

At the end of 2018 the LHC started a major upgrade to deliver better performance. During this period, most of the LHCb sub-detectors were upgraded as well as the data acquisition system. After the upgrade, the new software infrastructure will need to be more robust and scalable to face the higher luminosity delivered by the LHC. With this new configuration, monitoring the status of the detector and the data collected will be crucial to assure the best performance of the detector. For this reason, a prototype for the High Level

Trigger (HLT) monitoring system was designed, implemented and tested. The goal of this system was to check the feasibility of having a monitoring system running on off-the-shelf software instead of developing everything from scratch.

Declaration

I declare that this thesis was composed by myself, that the work contained herein is my own except where explicitly stated otherwise in the text, and that this work has not been submitted for any other degree or professional qualification except as specified.

Parts of this work have been published in [1].

(*Stefano Petrucci, April 21, 2022*)

Acknowledgements

I would like to thank my supervisor Matthew Needham for his help and guidance during these four years and a half. He gave me all the tools and advice I needed to complete this work. He also introduced me to the HLT team who helped me with the HLT monitoring part of the thesis. I would also like to thank the entire PPE group at the University of Edinburgh for welcoming me into their big family. In particular, I want to express my gratitude to Franz and Victoria (and Matt) for trusting me as a PPE PhD student during the selection process.

I want to thank Anthony, Max and Ozlem for their valuable suggestions and help from the very beginning to the end of the analysis. A big thank you also goes to some people at CERN: Conor for introducing me to the HLT team, Rosen for helping me and guiding me when prototyping the HLT monitoring system, Roel for sharing his deep knowledge about the HLT monitoring system and Flavio and Hristo for their help with the LHCb Online infrastructure as well as the discussions and suggestions about my work. Finally, I want to thank the HFLAV group for giving me access to their software to produce some of the plots in this work.

I would have never started this PhD without the help of Flavio and Pilloni. Without you guys, I would have never had the chance to work at CERN and to get the PhD position in Edinburgh.

Completing this work during the pandemic was hard but I was very lucky to have a great support from a lot of people to whom I want to express all my deepest gratitude. Without you guys, everything would have been way harder if not even impossible. I want to thank Lauren for being at my side during the entire journey and for introducing me to Scotland and all its beautiful places. You gave me all the support I needed and you were so patient while following my thoughts about the analysis. Another person who supported me and my experimental side is Tommaso. Apart from our long discussions about how to normalize distributions, I will never forget the training at home during lockdown and our single-arm pull-ups challenges while listening to Infected Mushroom. The funny way we met for the very first time is memorable but I will keep that story for another occasion. I want to thank Louise for hosting me from the very beginning of this Scottish adventure and for the coffee chats we had at the end of this long journey in

Edinburgh. Your hospitality at the very beginning of the PhD helped me a lot to settle down in Edinburgh. Before moving to the overseas people, I would like to thank Mahdi for his infinite support and suggestions during the entire PhD period and for our coffee breaks. I am also very grateful to Dan and Marge for helping me during the last part of my work.

Among the old friends from overseas, there are three people that are always present whenever I need any kind of support or advice and those are Ale, Max and Vale (strictly in alphabetical order). You are my best friends and knowing you are always there for me, gives me the strength I need to push my limits every day. Another person always at my side is Caro. Even if we lived in different countries for many years, you were always there whenever I needed it. You are my "little" sister but your support is always giant.

A special thank goes to "il Capo". When I started working at CERN you gave me all your advice and experience and soon, the work relationship turned into a great friendship. Your suggestions both about work and everyday life are always very helpful. A person who played an important role in this period is Sofia. You gave me precious support from the very first day we met. You and Andrea are two of the most genuine and selfless people I have ever met. I really enjoy spending time with you, especially when skiing (and après-skiing). After such a long journey it is mandatory to thank the "Vasca degli Squali": Cannizz, Enrico, Flavio, Iolanda, Marco and Simona. We started university together (even high-school with some of you) and I am so happy we built such a nice group supporting and "sharking" each other all the time. Even if far apart, I know that we can count on each other. There are other groups of friends I want to thank for their support across the years. Firstly "W la Foca" with Vero and Cannizz: we know each other from high-school and, even if in different countries, our friendship never changed. I want to thank David for sharing his passion about motorsport with me. David, I promise, I will learn how to release the braking pedal sooner! I would also thank Glenda for being such a good friend with every kind of suggestion, including how to make pizza. I will never forget our Skype aperitifs (before lockdown) with focaccia. Working abroad brings some challenges but having a yearly ski trip with the RoMASKI crew made me feel less homesick. Finally, I would also like to thank Emiliano for his big support during the very last part of my PhD.

Lot of people helped me during my stay in Geneva. Among them, I would like to thank the "Charly's Angels" who, from 2015, became my Swiss family as well as "il Bellotta" and the Kenobisboch group. Nothing is perfect unless you can do some climbing or skiing. A special thank goes to my climbing friends in Geneva: Romane, Stephanie, Rebecka, Corentin and Leo with whom we share our passion for climbing and skiing.

Finally, a special mention goes to Adriana: even if you did not actively contribute to this particular work, you are the one who taught me how to use a screwdriver for the first time!

At the very end of this long list, symbolizing the roots and the solid foundations

I can rely on, I want to thank my family. This achievement is the result of the values you taught me and the profound bond that makes us so strong and that, despite the distance, keeps us together.

Voglio iniziare ringraziando il mio supervisor Matthew Needham per l'aiuto e le sue indicazioni. Da lui in questi quattro anni e mezzo ho avuto tutti gli strumenti necessari per completare il mio lavoro, inoltre mi ha inserito nel gruppo HLT con cui ho potuto creare il prototipo per la parte di "HLT monitoring" di questa tesi.

Vorrei anche ringraziare l'intero gruppo PPE dell'università di Edimburgo per avermi accolto e, in particolare, Franz, Victoria e ancora Matt per aver riposto la loro fiducia in me durante la fase di selezione.

Ringrazio Anthony, Max e Ozlem per i preziosi suggerimenti e l'aiuto dall'inizio alla fine dell'analisi.

Un grande ringraziamento va anche ad alcune persone al CERN, Conor per avermi presentato al gruppo dell'HLT, Rosen per avermi aiutato e guidato mentre progettavo il prototipo del sistema di monitoring dell'HLT, Roel per aver condiviso la sua profonda conoscenza del sistema di monitoring dell'HLT e Flavio e Hristo per il loro aiuto con l'infrastruttura dell'Online e per le discussioni e i suggerimenti sul mio lavoro. Vorrei infine ringraziare HFLAV per avermi dato accesso al loro software per creare alcuni grafici di questa tesi.

Non avrei mai iniziato questo dottorato se non fosse stato per l'aiuto di Flavio e Pilloni, senza di voi non avrei avuto l'opportunità di lavorare al CERN e di ottenere il dottorato a Edimburgo.

Ultimare questo lavoro durante la pandemia è stato davvero difficile ma sono stato fortunato ad avere un grande sostegno da parte di tante persone a cui voglio esprimere la mia estrema gratitudine. Senza di loro sarebbe stato tutto più complicato. Ringrazio Lauren per essere stata al mio fianco durante questo viaggio e per avermi fatto conoscere i luoghi fantastici della Scozia, mi hai supportato tantissimo e sei stata veramente tanto paziente mentre seguivi tutti i miei pensieri e ragionamenti sull'analisi. Vorrei ringraziare Tommaso per aver sostenuto me e il mio lato sperimentale. Oltre alle infinite discussioni su come normalizzare le distribuzioni, non potrò dimenticare gli allenamenti a casa durante il lockdown e le sfide di trazioni a un braccio mentre ascoltavamo gli Infected Mushroom. Non dimenticherò neanche come ci siamo conosciuti ma questa storia la racconteremo un'altra volta. Vorrei ringraziare Louise per avermi ospitato all'inizio all'inizio di questa avventura Scozzese e per le chiaccherate davanti a un caffè verso la fine di questo lungo viaggio a Edimburgo. La tua ospitalità appena arrivato mi ha aiutato moltissimo ad ambientarmi in questa nuova città.

Prima di ringraziare le persone "al di là del mare", voglio esprimere la mia profonda riconoscenza a Mahdi per l'aiuto e i suggerimenti durante l'intero dottorato e le nostre pause caffè. Sono anche grato a Marge e Dan per la loro vicinanza durante l'ultima parte del lavoro.

Tra gli amici storici sulla terraferma, ci sono tre persone sempre presenti e pronte a sostenermi e aiutarmi, Ale, Max e Vale (rigorosamente in ordine alfabetico). Con voi ho condiviso momento per momento tutte le difficoltà, le gioie e le

preoccupazioni vissute. Siete i miei migliori e più grandi amici, sentirvi vicini mi dà la forza e il coraggio di affrontare gli ostacoli che incontro. Un'altra persona che sta sempre al mio fianco è Caro. Anche se per diversi anni abbiamo vissuto in paesi differenti, tu ci sei sempre stata quando ne avevo bisogno. Sei sempre la mia sorella "piccola" ma il tuo supporto è grandissimo.

Un ringraziamento speciale va al Capo. Quando ho iniziato a lavorare al CERN hai condiviso con me tutta la tua esperienza e quello che è nato come un semplice rapporto di lavoro si è trasformato in una grande amicizia. I tuoi consigli e suggerimenti sia sul lavoro che nella vita quotidiana sono preziosissimi. Un ruolo importante durante questo periodo lo ha avuto Sofia. Mi hai dato un grande aiuto dal giorno che ci siamo conosciuti. Tu e Andrea siete tra le persone più genuine e altruiste che abbia mai incontrato. È sempre bellissimo passare del tempo con voi, specialmente quando sciamo o facciamo l'après-ski. Dopo questo viaggio lunghissimo un pensiero speciale va alla "Vasca degli Squali": Cannizz, Enrico, Flavio, Iolanda, Marco e Simona. Abbiamo iniziato l'università insieme (con alcuni di voi addirittura il liceo) e mi rende felice vedere quanto siamo ancora affiatati, nonostante le distanze ci si "squala" ancora e possiamo sempre contare l'uno sull'altro. Ci sono altri gruppi di amici che vorrei ricordare per il sostegno negli anni, "W la Foca" con Vero e Cannizz: ci conosciamo dal liceo e, anche se viviamo in Paesi diversi, la nostra amicizia non è cambiata. Grazie David per condividere con me la tua passione per il motorsport, ti prometto che imparerò ad alzare prima il piede dal freno! Vorrei anche ringraziare Glenda per essere la grandissima amica a cui chiedere i consigli più disparati, incluso come fare la pizza, non posso non ricordare i nostri aperitivi su Skype e la focaccia, il tutto nel lontano periodo pre lockdown. Vivere all'estero crea delle sfide ma poter fare la settimana bianca ogni anno con il gruppo RoMASKI mi ha aiutato a sentire meno la lontananza.

Ringrazio Emiliano per il suo enorme supporto e aiuto durante l'ultima parte del dottorato.

Molte persone mi sono state vicine mentre ero a Ginevra, grazie a tutto il gruppo "Charly's Angels" che, dal 2015, è diventata la mia famiglia Svizzera e il Bellotta con il gruppo Kenobisboch. Come dico sempre, niente è perfetto a meno che tu non possa arrampicare e sciare. Un ringraziamento speciale per i miei compagni di arrampicata a Ginevra: Romane, Stephanie, Rebecka, Corentin e Leo, con loro ho condiviso la passione per l'arrampicata e lo sci.

Infine, una menzione speciale va ad Adriana, anche se non hai dato un contributo attivo a questo dottorato, sei la persona che mi ha insegnato a usare il cacciavite per la prima volta.

Alla fine di questa lunga lista, a simboleggiare le radici e le solide fondamenta su cui posso fare affidamento, voglio ringraziare la mia famiglia. Questo risultato è il frutto dei valori e degli insegnamenti ricevuti, del rapporto profondo che ci unisce.

Contents

List of Figures

List of Tables

List of Acronyms

ALICE A Large Ion Collider Experiment

ARGUS A Russian-German-United States-Swedish collaboration

ATLAS A Toroidal LHC ApparatuS

BDTG Gradient Boosted Decision Tree

CDF Collider Detector at Fermilab

CERN Conseil Européen pour la Recherche Nucléaire

CKM Cabibbo-Kobayashi-Maskawa

CMS Compact Muon Solenoid

DAQ Data AcQuisition

DLS Decay Length Significance

DSCB Double-Sided Crystal Ball

DST Data Summary Tape

ECAL Electromagnetic CALorimeter

ECS Experiment Control System

EFF Event Filter Farm

EGEE Enabling Grid for E-sciencE

FOI Field Of Interest

FPGA Field-Programmable Gate Array

GEM Gas Electron Multiplier

HCAL Hadron CALorimeter

HFLAV Heavy Flavor AVeraging

HLT High Level Trigger

HPD Hybrid Photo Detector

IPC Inter-Process Communication

IT Inner Tracker

L0 Level-0

LEP Large Electron–Positron

LHC Large Hadron Collider

LHCb Large Hadron Collider beauty

Linac 2 Linear accelerator 2

LS1 Long Shutdown 1

LS2 Long Shutdown 2

MaPhoto-Multiplier Tube (PMT) Multi-anode PMT

MVA MultiVariate Analysis

MWPC Multi-Wire Proportional Chambers

OS Operative System

OSG OpenScience Grid

OT Outer Tracker

PID Particle IDentification

PMT Photo-Multiplier Tube

PS Proton Synchrotron

PS PreShower

PSB Proton Synchrotron Booster

QCD Quantum ChromoDynamics

RICH Ring Imaging CHerenkov

ROC Receiver Operating Characteristic

SLAC Stanford Linear Accelerator Center

SM Standard Model

SPD Scintillator Pad Detector

SPS Super Proton Synchrotron

ST Silicon Tracker

TCP Transmission Control Protocol

TIS Trigger Independent of Signal

TOS Trigger On Signal

TT Tracker Turicensis

UA1 Underground Area 1

UA2 Underground Area 2

VELO VErtex LOcator

WLCG Worldwide Large Hadron Collider (LHC) Computing Grid

WLS WaveLength-Shifting

Chapter 1

Introduction

A key question yet to be answered by modern cosmology is to understand the origin of the asymmetry between matter and anti-matter in our universe. During the Big Bang equal amounts of matter and anti-matter were created but now the universe is dominated by matter. One possibility to create this asymmetry is baryogenesis [2] which requires the Sakharov conditions [3] to be met: the non-conservation of baryon number, the violation of the CP-symmetry and interactions happening outside the thermal equilibrium.

The main research field of the Large Hadron Collider beauty (LHCb) detector at Conseil Européen pour la Recherche Nucléaire (CERN) is the study of CP violation and rare decays of beauty and charm hadrons. This thesis studies the lifetime of the B_s^0 meson performing a relative measurement, $\Delta\Gamma_s$, between the $B_s^0 \to J/\psi\eta'$ and $B_s^0 \to J/\psi f_0$ decays.

The LHCb detector started a scheduled upgrade in December 2018. During this period most of LHCb sub-detectors were changed as well as the data acquisition system. A part of the work presented in this thesis is related to the design and prototyping of a new monitoring system for the upgraded detector.

The thesis is split into six chapters covering all the aspects of the work done during the PhD. Chapter 2 presents the current $\Delta\Gamma_s$ results both from the theoretical and experimental perspective. In this chapter, the theoretical background is discussed along with the methodology used to measure $\Delta\Gamma_s$ from the chosen decays. Chapter 3 describes the LHCb detector at CERN with focus on the sub-detectors and the data acquisition chain. Chapter 4 covers the steps of

the offline analysis and the simulation production. An in depth description of particle identification and track classification at LHCb is given. The Monte Carlo production and the offline analysis tools are described as well. Chapter 5 describes a prototype of the High Level Trigger (HLT) monitoring system developed for future upgrade purposes. The work in this chapter was carried out by the author with the support of the HLT and online teams. The main goal of the prototype was to demonstrate the feasibility of using off the shelf software to run the LHCb HLT monitoring system. Some preparation work was done by benchmarking the Run 2 HLT infrastructure and studying the Run 2 HLT monitoring system. The results from this work were presented at CHEP 2019 and are published in [1]. Chapter 6 describes the signal selection and the background studies done for the $\Delta\Gamma_s$ analysis. The work in this chapter and the following ones was carried out in collaboration with a small group from the University of Edinburgh and LAPP (Annecy). In this chapter, a more detailed view of the data used as well as selection cuts and background studies is presented. The last part of the chapter describes the MultiVariate Analysis (MVA) which is used to extract the signal from the very noisy background. Chapter 7 contains the core of the $\Delta\Gamma_s$ analysis. It describes how $\Delta\Gamma_s$ is calculated showing the mass fit models used and the binning scheme adopted. It also shows the validation studies performed assuring the lowest bias possible. The last part of the chapter covers the time acceptance study and the systematic uncertainties. Since $\Delta\Gamma_s$ is determined from a relative measurement, it is important to fully understand all the components that might introduce an acceptance verifying that they cancel when measuring $\Delta\Gamma_s$.

Chapter 2

Theory

In this chapter, an overview of the Standard Model (SM) of Particle Physics and the theoretical tools used in the analysis are presented. Particular emphasis is given to the B_s^0 meson system, focusing on the mixing mechanism and CP violation. The last section of this chapter is dedicated to describing the decay channels used in the analysis.

2.1 Standard Model

The SM describes all known fundamental particles and their interactions via the electromagnetic, strong and weak forces. It was formulated and developed during the second half of the twentieth century through the efforts of both the theoretical and experimental communities. In 1964 Gell-Mann and Zweig independently proposed the quark model [4]. The idea that hadrons were made of quarks and antiquarks gained experimental support from the discovery of electron-nucleon scattering at large angles (Deep Inelastic Scattering) at Stanford Linear Accelerator Center (SLAC) [5]. This phenomenon was interpreted by Feynman and Bjorken as proof that neutrons and protons were not point-like particles [4]. From the late 1950s and the 1970s, the community of theoretical physicists defined the interactions in the SM as a $SU(3) \times SU(2) \times U(1)$ gauge symmetry where the $SU(3)$ symmetry represents the strong interactions and the $SU(2) \times U(1)$ the electroweak interactions. In addition to these gauge symmetries, the Higgs mechanism is responsible for giving mass to the gauge bosons and the fermions

via the mechanism of spontaneous symmetry breaking [6].

The SM is shown schematically in fig. 2.1. In detail, in purple are listed the three families of quarks, in green the three families of leptons, in red the mediator of the forces and in yellow the Higgs boson. The electroweak force is mediated by the $W^{\pm}$, Z^0 and γ and the strong force by the gluons.

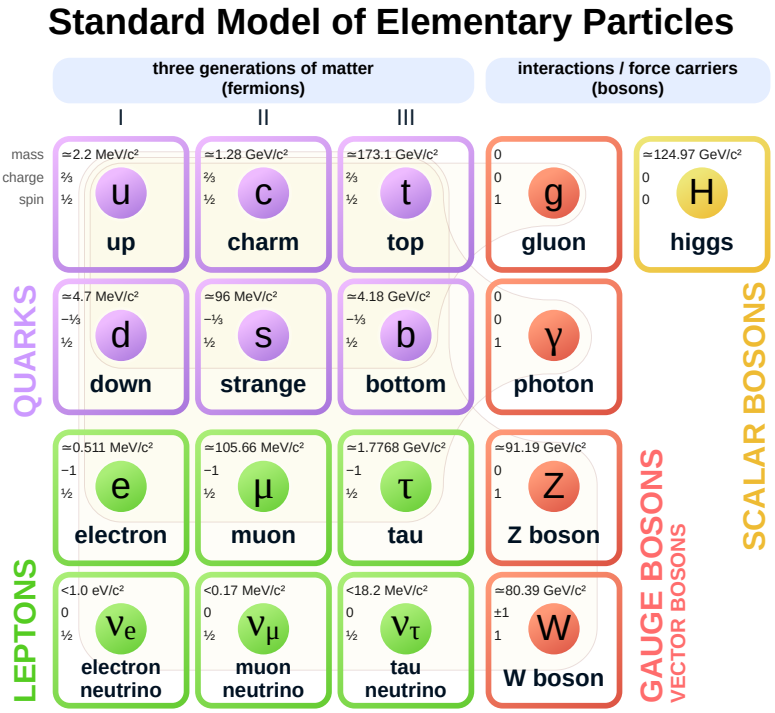

Figure 2.1 *Schematic representation of the SM. Fundamental particles are grouped by family: quarks (purple), leptons (green), gauge bosons (red) and scalar bosons (yellow). Quarks and leptons are divided into three families in increasing order of mass [7].*

The strong interaction is described by Quantum ChromoDynamics (QCD), which defines the interactions between quarks and gluons, and how they form composite particles such as protons and neutrons. The QCD charge is color and it can be red (R), green (G) and blue (B) with its anti-colors for antiparticles. One of the properties of QCD is *color confinement*: particles carrying color (e.g. gluons and quarks) cannot be isolated but they group together to form a colorless combination. For example, $q\overline{q}$ meson states have color ($R\overline{R}$, $G\overline{G}$, $B\overline{B}$) whilst baryons consisting of three quarks have color RGB (for qqq) and $\overline{RGB}$ (for $\overline{qqq}$)

The Electroweak interaction describes the behavior of two different forces: the electromagnetic and the weak. The electromagnetic force is propagated by the photon while the weak force is propagated by the charged $W^{\pm}$ bosons and the

neutral Z^0 boson. In the SM, flavor and lepton number are only changed by the charged current of the Weak interaction. Major contributions to unifying the electromagnetic and weak theories were made by Glashow, Salam and Weinberg [8, 9]. Experimentally, this picture was confirmed by the discovery of neutral currents by the Gargamelle neutrino experiment [10] and the direct observation of the W and Z bosons by the Underground Area 1 (UA1) and Underground Area 2 (UA2) collaborations [11, 12].

2.2 CP violation in the Standard Model

The C operator changes a particle into its own anti-particle while the P operator changes the handedness ($\overline{x} \rightarrow -\overline{x}$). Though the C and P symmetries are conserved by the strong and electromagnetic interactions, they are maximally violated by the weak interaction [13]. Experimentally, the combined operation CP is found not to be conserved by the weak interaction. This corresponds to a non-zero value of the phase in the Cabibbo-Kobayashi-Maskawa (CKM) matrix (section 2.3). There are three ways to generate CP violation:

- CP violation in the decay amplitude: this occurs when there is a difference in the decay rates of a particle to a final state and the corresponding decay for the anti-particle. This is the only source of CP violation possible in charged decays.
- CP violation in mixing: this occurs when the rate for meson - antimeson oscillation and for antimeson - meson oscillation are different.
- Due to interference between the mixing and decay amplitudes.

2.3 The CKM picture

In the SM the masses and mixing of quarks both arise from the Yukawa interaction with the Higgs field [14]

$$\mathcal{L}_Y = -Y^d_{ij}\overline{Q^I_{Li}}\phi d^I_{Rj} - Y^u_{ij}\overline{Q^I_{Li}}\epsilon\phi^* u^I_{Rj} + h.c., \tag{2.1}$$

where i, j denote the quark generation, $Y^{u,d}$ are 3×3 matrices, ϕ is the Higgs field, ϵ a 2×2 asymmetric tensor, *h.c.* implies the Hermitian conjugate, the Q_L^I are the left-handed quark doublets and u/d_R^I the right-handed up/down quark singlets. The interaction between the up and down quark families is then given by

$$-\frac{g}{\sqrt{2}}\left(\overline{u},\overline{c},\overline{t}\right)_L \gamma^\mu W_\mu^+ V_{\text{CKM}} \begin{pmatrix} d \\ s \\ b \end{pmatrix}_L + h.c., \tag{2.2}$$

and

$$V_{\text{CKM}} \equiv \begin{pmatrix} V_{ud} & V_{us} & V_{ub} \\ V_{cd} & V_{cs} & V_{cb} \\ V_{td} & V_{ts} & V_{tb} \end{pmatrix} \tag{2.3}$$

is a unitary matrix called the CKM matrix [15]. This matrix gives the probability of a transition from an up-type quark to a down-type quark: $P\left(q_i \to q_j\right) \propto |V_{ij}|^2$. Transitions closer to the diagonal are favored while transitions involving off-diagonal elements are suppressed. The strength of the interaction is more easily seen using the Wolfenstein parametrization [16],

$$V_{CKM} \approx \begin{pmatrix} 1 - \frac{1}{2}\lambda^2 & \lambda & A\lambda^3\left(\rho - i\eta\right) \\ -\lambda\left(1 + iA^2\lambda^4\eta\right) & 1 - \frac{1}{2}\lambda^2 & A\lambda^2 \\ A\lambda^3\left(1 - \rho - i\eta\right) & -A\lambda^2 & 1 \end{pmatrix} + \mathcal{O}\left(\lambda\right)^4, \tag{2.4}$$

where $\lambda = 0.2257^{+0.0009}_{-0.0010}$, $A = 0.814^{+0.021}_{-0.022}$, $\rho = 0.135^{+0.031}_{-0.016}$ and $\eta = 0.349^{+0.015}_{-0.017}$ [17].

The unitarity constraints of the CKM matrix can be written as

$$\sum_k |V_{ik}|^2 = 1, \tag{2.5}$$

and

$$\sum_k V_{ik} V_{jk}^* = 0. \tag{2.6}$$

It is possible to visualize the properties of eq. (2.6) in the complex plane. If, for

example, the first and third columns of the CKM matrix are considered, eq. (2.6) becomes $V_{ud}V_{ub}^* + V_{cd}V_{cb}^* + V_{td}V_{tb}^* = 0$ which is seen to be a triangle, the so called *unitarity triangle*, in the complex plane (fig. 2.2).

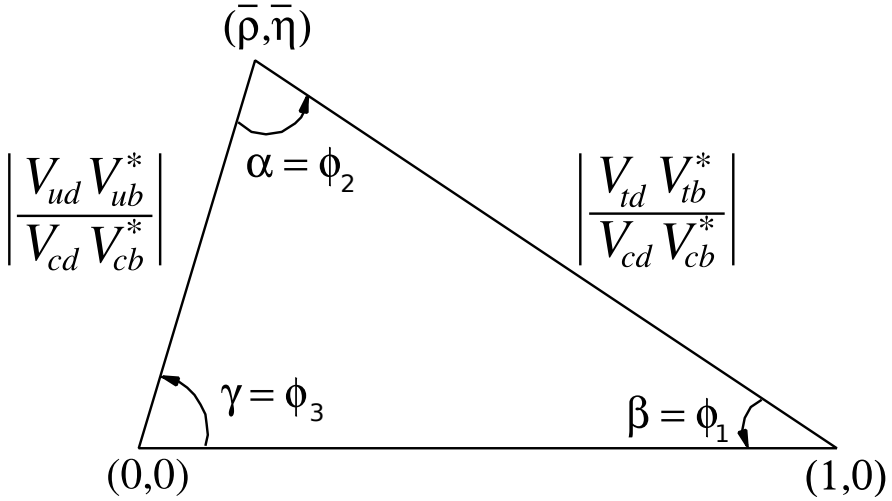

Figure 2.2 *Unitarity triangle for $V_{ud}V_{ub}^* + V_{cd}V_{cb}^* + V_{td}V_{tb}^* = 0$ represented in the complex plane [18].*

In the Wolfenstein parametrization the apex of the triangle is located at $(\overline{\rho}, \overline{\eta})$ [18]:

$$\overline{\rho} + i\overline{\eta} \equiv -\frac{V_{ud}V_{ub}^*}{V_{cd}V_{cb}^*} \equiv 1 + \frac{V_{td}V_{tb}^*}{V_{cd}V_{cb}^*}. \tag{2.7}$$

The angles of the triangle are defined as:

$$\alpha \equiv \arg\left(-\frac{V_{td}V_{tb}^*}{V_{ud}V_{ub}^*}\right) \tag{2.8}$$

$$\beta \equiv \arg\left(-\frac{V_{cd}V_{cb}^*}{V_{td}V_{tb}^*}\right) \tag{2.9}$$

$$\gamma \equiv \arg\left(-\frac{V_{ud}V_{ub}^*}{V_{cd}V_{cb}^*}\right). \tag{2.10}$$

Experimentally, the three angles are well measured as shown in fig. 2.3. Their values determined by the CKM fitter group, at the time of writing are $\alpha = \left(91.98^{+0.82}_{-1.40}\right)^\circ$, $\beta = \left(22.42^{+0.64}_{-0.37}\right)^\circ$ and $\gamma = \left(65.5^{+1.3}_{-1.2}\right)^\circ$ [19].

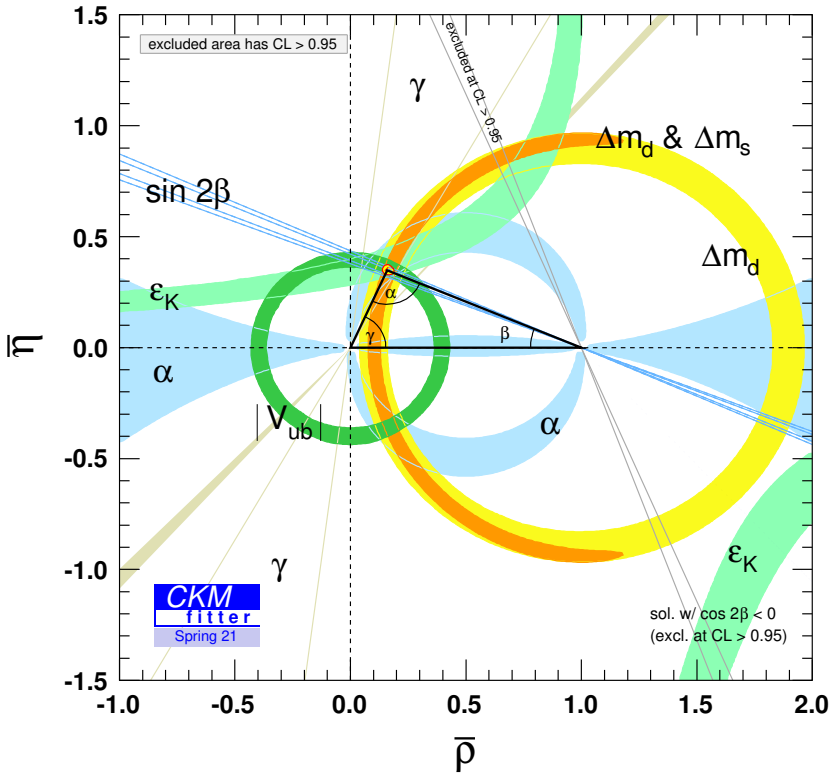

Figure 2.3 *Latest measurements of the CKM triangle [19].*

A triangle relevant for the studies of the B_s^0 meson is the one obtained from the second and third columns of the CKM matrix, fig. 2.4. The angle

$$\beta_s \equiv \arg\left(\frac{V_{ts}V_{tb}^*}{V_{cs}V_{cb}^*}\right). \tag{2.11}$$

is related to the phase difference between B_s^0 decays with and without mixing. In the SM, β_s is predicted to be small [20].

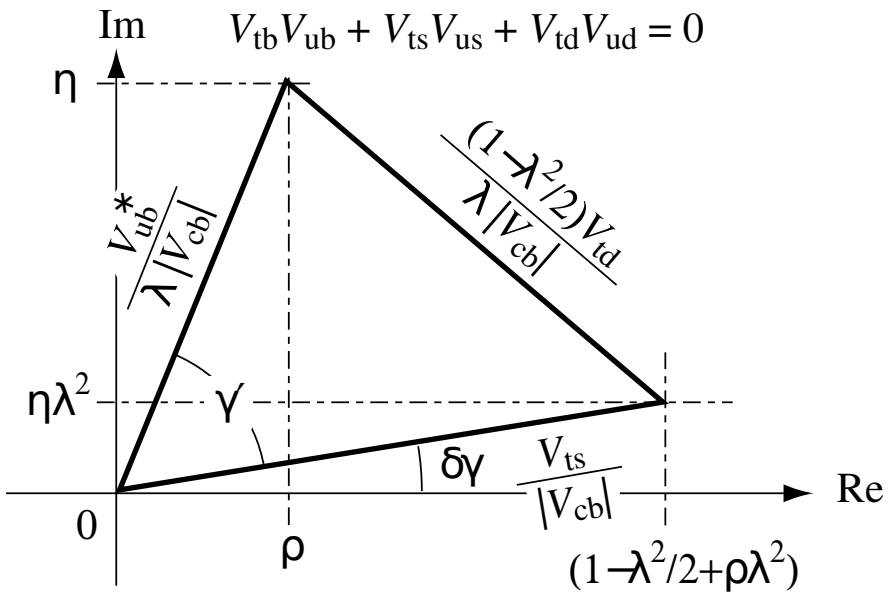

Figure 2.4 *Unitarity triangle for eq.* (2.11) *[21].*

2.3.1 Neutral meson oscillation

Neutral mesons have the ability to oscillate between their particle and their antiparticle as a consequence of adding the weak interaction term to the strong interaction Hamiltonian. In the SM there are four possible meson - anti-meson systems: neutral kaons, D, B^0 and B_s^0. The phenomenology of particle-antiparticle oscillation was first described by Gell-Mann and Pais [22] in 1954 for the $K^0 - \overline{K}^0$ system and experimentally confirmed at Brookhaven [23] in 1956. This thesis is focused on the b-meson therefore the formulae will be shown with a b quark coupled with either a d or a s quark labelled q. Mixing in the B^0 system was first observed by the A Russian-German-United States-Swedish collaboration (ARGUS) collaboration in 1987 [24]. In the B_s^0 system, mixing was first observed by the Collider Detector at Fermilab (CDF) [25] and subsequently confirmed by LHCb [26].

The formalism for meson oscillation is derived by solving the Schrödinger equation for the meson-antimeson system. Starting from the strong interaction Hamiltonian eq. (2.12), if the strong force was the only one interacting on the system, the neutral B_q system would have two $|B_q\rangle = |\bar{b}q\rangle$ and $|\overline{B_q}\rangle = |b\bar{q}\rangle$ states where $(q = d, s)$ with equal masses $m_q = m_{\bar{q}} \equiv m_0$,

$$\mathcal{H}_0 = \begin{pmatrix} m_0 & 0 \\ 0 & m_0 \end{pmatrix}. \tag{2.12}$$

Adding the weak Hamiltonian $\mathcal{H}_W$ to $\mathcal{H}_0$ introduces non-zero off-diagonal elements:

$$\mathcal{H} = \begin{pmatrix} m_0 + \delta E & W_{12} + \delta E_{12} \\ W_{12}^* + \delta E_{12}^* & m_0 + \delta E \end{pmatrix} - \frac{i}{2} \begin{pmatrix} \Gamma & \Gamma_{12} \\ \Gamma_{12}^* & \Gamma \end{pmatrix}. \tag{2.13}$$

The expression in eq. (2.13) can be written as

$$\mathcal{H} = \left(M - i\frac{\Gamma}{2} \right) \tag{2.14}$$

where M is the mass matrix and Γ is the decay matrix.

The off-diagonal elements are responsible for the $B_q^0 - \overline{B}_q^0$ mixing which is mediated by a box diagram (fig. 2.5). Due to these terms, neutral B_q^0 mesons propagate as a superposition of two mass eigenstates called the heavy (B^H) and the light (B^L) where

$$\begin{aligned} |B_q^L\rangle &= p\,|B_q^0\rangle + q\,|\overline{B}_q^0\rangle\,, \\ |B_q^H\rangle &= p\,|B_q^0\rangle - q\,|\overline{B}_q^0\rangle\,. \end{aligned} \tag{2.15}$$

The evolution of the $B_q - \overline{B}_q$ system follows the Schrödinger equation

$$i\frac{d}{dt} \begin{pmatrix} |B_q\,(t)\rangle \\ |\overline{B}_q\,(t)\rangle \end{pmatrix} = \mathcal{H} \begin{pmatrix} |B_q\,(t)\rangle \\ |\overline{B}_q\,(t)\rangle \end{pmatrix} \tag{2.16}$$

with $|p|^2 + |q|^2 = 1$. For the B_s^0, the ratio $|q/p|$ is measured to be 1.0003 ± 0.0014 [27]. Equation (2.13) can be simplified assuming $\Gamma_q^{12} \ll m_q^{12}$:

$$
\begin{aligned}
\Delta m_q &\equiv m_q^H - m_q^L = 2|m_q^{12}|, \\
\Delta\Gamma_q &\equiv \Gamma_q^L - \Gamma_q^H = 2|\Gamma_q^{12}|\cos\left(\phi_q^{12}\right), \\
m_q &\equiv \frac{1}{2}\left(m_q^L + m_q^H\right), \\
\Gamma_q &\equiv \frac{1}{2}\left(\Gamma_q^L + \Gamma_q^H\right), \\
\phi_q^{12} &\equiv \arg\left(-\frac{m_q^{12}}{\Gamma_q^{12}}\right),
\end{aligned}
\tag{2.17}
$$

where, in the B_s^0 system, $\phi_s^{12} = \beta_s/2$ is a CP violating phase that arises from the interference of decays with and without mixing.

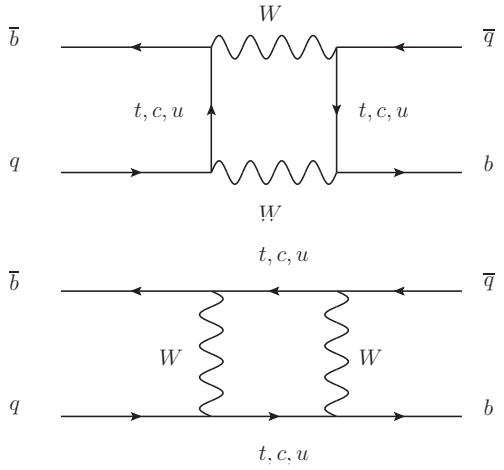

Figure 2.5 $B_q^0 - \overline{B}_q^0$ *oscillation diagrams.*

The SM predicts fast B_s^0 oscillations, $\Delta m_s^{\text{pred}} = 18.77 \pm 0.86$ ps^{-1} [28]. Experimentally, Δm_s has been measured precisely by LHCb using the decay $B_s^0 \to D_s^+\pi^-$ (fig. 2.6) and found to be 17.7656 ± 0.0057 ps^{-1} [29], in agreement with the SM expectation.

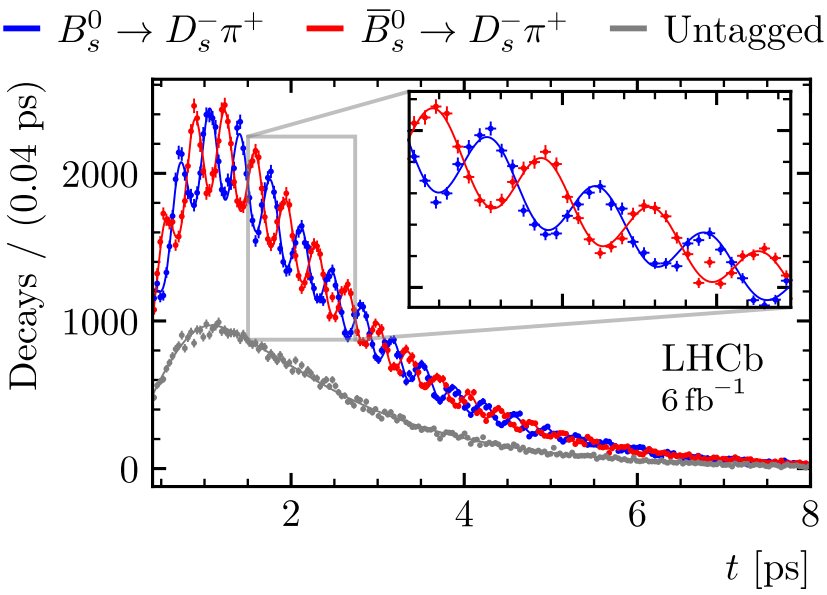

Figure 2.6 $B_s^0 - \overline{B}_s^0$ *oscillation measured by the LHCb collaboration [29].*

The decay rate of the light and heavy eigenstates of the B_s^0 meson into a given final state, f, can be written as:

$$\begin{aligned} \langle \Gamma \left(B_s^0 \left(t \right) \to f \right) \rangle &\equiv \Gamma \left(B_s^0 \left(t \right) \to f \right) + \Gamma \left(\overline{B}_s^0 \left(t \right) \to f \right) \\ &= R_H^f e^{-\Gamma_H^{(s)} t} + R_L^f e^{-\Gamma_L^{(s)} t}, \end{aligned} \tag{2.18}$$

where L and H are the light and heavy eigenstates corresponding to the CP-even and CP-odd eigenstates respectively. Equation (2.18) can be written as

$$\Gamma \left(B_s^0 \left(t \right) \to f \right) \propto e^{-\Gamma_s t} \left(\cosh \left(\frac{\Delta \Gamma_s t}{2} \right) + \mathcal{A}_{\Delta\Gamma}^f \sinh \left(\frac{\Delta \Gamma_s t}{2} \right) \right), \tag{2.19}$$

where

$$
\begin{aligned}
\Gamma_s &\equiv \frac{\Gamma_L^{(s)} + \Gamma_H^{(s)}}{2} = \frac{1}{\tau_{B_s^0}}, \\
\Delta\Gamma_s &\equiv \Gamma_L^{(s)} - \Gamma_H^{(s)}, \\
\mathcal{A}_{\Delta\Gamma}^f &\equiv \frac{R_H^f - R_L^f}{R_H^f + R_L^f}.
\end{aligned}
\tag{2.20}
$$

Assuming CP is conserved, for a CP even eigenstate, $\mathcal{A}_{\Delta\Gamma}^f = -1$ while for a CP odd eigenstate $\mathcal{A}_{\Delta\Gamma}^f = 1$.

The observable obtained by fitting eq. (2.18) with a single exponential is called the effective lifetime. In [30] it is shown that

$$
\begin{aligned}
\frac{\tau_f}{\tau_{B_s^0}} &= \frac{1}{1-y^2}\left(\frac{1 + 2\mathcal{A}_{\Delta\Gamma}^f y + y^2}{1 + \mathcal{A}_{\Delta\Gamma}^f y}\right) \\
&= 1 + \mathcal{A}_{\Delta\Gamma}^f y + \left[2 - \left(\mathcal{A}_{\Delta\Gamma}^f\right)^2\right] y^2 + \mathcal{O}\left(y^3\right)
\end{aligned}
\tag{2.21}
$$

where $2y = \Delta\Gamma_s/\Gamma_s$.

Recent SM predictions for $\Delta\Gamma_s$ are listed in table 2.1. The central values are in good agreement with each other but the renormalization scheme leads to a $\sim 10\%$ uncertainty. To improve the prediction for $\Delta\Gamma_s$, a full NNLO calculation is required.

Value [$\times 10^{-2}\text{ps}^{-1}$]	Renormalization scheme	Method	Reference
9.1 ± 1.3	$\overline{MS}$	QCD factorization	Lenz *et. al.* [28]
9.2 ± 1.4	$\overline{MS}$	Lattice	Davies *et. al.* [31]
8.8 ± 1.8	$\overline{MS}$	NLO + NNLO pQCD	Asatrian *et. al.* [32]
7.7 ± 2.2	Pole mass	NLO + NNLO pQCD	Asatrian *et. al.* [32]
$8.3^{+5.0}_{-1.2}$	Pole mass	NLO + NNLO pQCD	Gerlach *et. al.* [33]
$9.0^{+0.2}_{-0.3}$	$\overline{MS}$	NLO + NNLO pQCD	Gerlach *et. al.* [33]

Table 2.1 *Recent SM predictions for* $\Delta\Gamma_s$.

fig. 2.7 summarizes the latest experimental measurements of $\Delta\Gamma_s$ and Γ_s from the $B_s^0 \to J/\psi\phi$ mode via a tagged time-dependent angular analysis. The experimental measurements are not in the best of agreement, particularly for

Γ_s, though the $\Delta\Gamma_s$ measurements also show poor agreement. To resolve the tensions in the experimental data, new measurements are needed.

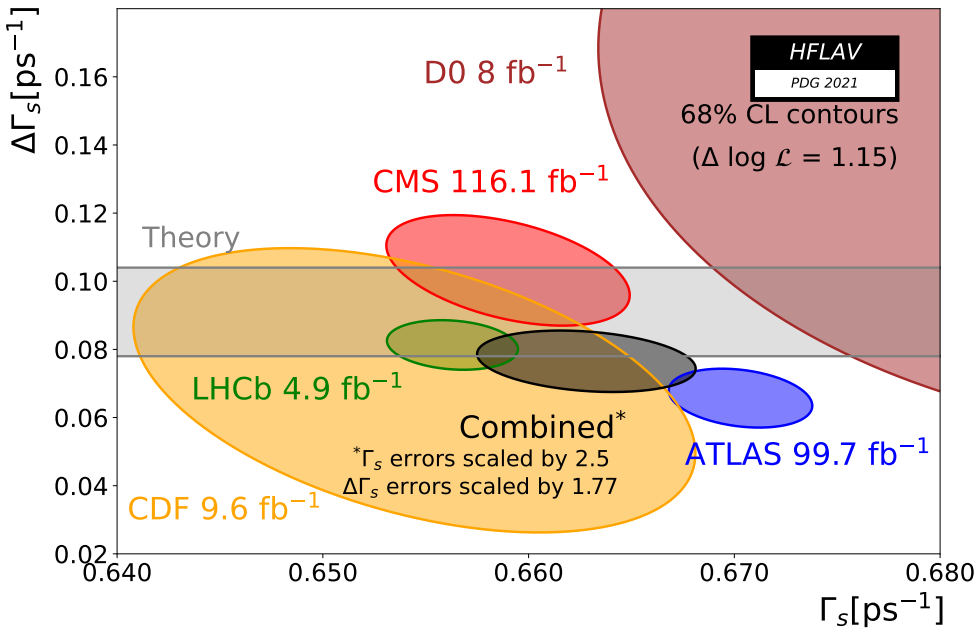

Figure 2.7 *Current status of Γ_s and $\Delta\Gamma_s$ measurement from Heavy Flavor AVeraging (HFLAV) [20]. The gray band shows the SM prediction while the blue, red and green circles represents the A Toroidal LHC ApparatuS (ATLAS), Compact Muon Solenoid (CMS) and LHCb measurements respectively. The black circle is the combination of all measurements. To account for the poor agreement of the values in the averaging, scale factor are applied by Heavy Flavor AVeraging (HFLAV).*

2.4 Method

In 2011 Fleischer and collaborators [30, 34] proposed to measure ϕ_s by combining lifetime measurements from CP-even and CP-odd modes. This approach has the advantage that neither an angular analysis nor flavor tagging are required. However, for this approach to be meaningful, ϕ_s must be large. Since now ϕ_s is measured to -0.050 ± 0.019 [20], in practice CP-even modes measure the light mass eigenstate lifetime (τ_L) while CP-odd modes measure the heavy mass eigenstate lifetime (τ_H) to high precision. Thus, measuring the difference in the lifetimes between a CP odd and a CP even mode allows to determine $\Delta\Gamma_s$.

The main goal of this work is to measure $\Delta\Gamma_s$ following a similar approach to that used by the A Toroidal LHC ApparatuS (ATLAS) collaboration [35] to place a

limit on the B^0 mixing parameter, $\Delta\Gamma_d$. If CP violation is negligible, eq. (2.19) can be written as

$$\Gamma\left(B_s^0(t) \to f\right) \propto e^{-\Gamma_s t}\left[\cosh\left(\frac{\Delta\Gamma_s t}{2}\right) - \sinh\left(\frac{\Delta\Gamma_s t}{2}\right)\right] \tag{2.22}$$

for the CP-even eigenstate and as

$$\Gamma\left(B_s^0(t) \to f\right) \propto e^{-\Gamma_s t}\left[\cosh\left(\frac{\Delta\Gamma_s t}{2}\right) + \sinh\left(\frac{\Delta\Gamma_s t}{2}\right)\right] \tag{2.23}$$

for the CP-odd eigenstate.

In a time interval $[t_1, t_2]$, the yields for the light and heavy eigenstates can be obtained by integrating eq. (2.22) and eq. (2.23). Giving

$$N_L = \left[\frac{e^{t(\frac{-\Delta\Gamma_s}{2} - \Gamma_s)}}{\Gamma_s + \frac{\Delta\Gamma_s}{2}}\right]_{t_1}^{t_2} \tag{2.24}$$

and

$$N_H = \left[\frac{e^{t(\frac{\Delta\Gamma_s}{2} - \Gamma_s)}}{\Gamma_s - \frac{\Delta\Gamma_s}{2}}\right]_{t_1}^{t_2}. \tag{2.25}$$

Writing $2y = \Delta\Gamma_s/\Gamma_s$ and taking the ratio of eq. (2.24) and eq. (2.25) gives

$$\frac{N_L}{N_H} = \frac{\left[e^{-\Gamma_s t(1+y)}\right]_{t_1}^{t_2}}{\left[e^{-\Gamma_s t(1-y)}\right]_{t_1}^{t_2}} \cdot \frac{1-y}{1+y}. \tag{2.26}$$

Thus, $\Delta\Gamma_s$ can be extracted from eq. (2.26), by comparing the yields of the light and heavy states in time bins. The fit is performed in the time range $0.5 - 10$ ps using eight time bins. A detailed description of the binning scheme optimization is shown in section 7.1.1.

A similar approach can be used if the time acceptance is uniform within a lifetime bin. In that case an additional factor taking into account the relative efficiencies between the light and heavy states has to be included in eq. (2.26)

$$\frac{N_L}{N_H} = A_r \frac{\left[e^{-\Gamma_s t(1+y)}\right]_{t_1}^{t_2}}{\left[e^{-\Gamma_s t(1-y)}\right]_{t_1}^{t_2}} \cdot \frac{1-y}{1+y} \tag{2.27}$$

where $A_r = \epsilon_H/\epsilon_L$.

Simulation studies show that such an approach is unbiased if A_r is evaluated at either the bin barycenter or the position described in [36] using an exponential with the mean lifetime $\frac{1}{\Gamma_s}$ (see section 7.3.1).

In this analysis, the chosen CP even channel is $B_s^0 \to J/\psi\eta'$ with $\eta' \to \rho^0\gamma$ and the chosen CP odd channel is $B_s^0 \to J/\psi f_0$. Both decays are expected to be dominated by the tree-level process shown in fig. 2.8. Experimentally, since the two channels are topologically very similar the time acceptance will largely cancel in the relative lifetime measurement.

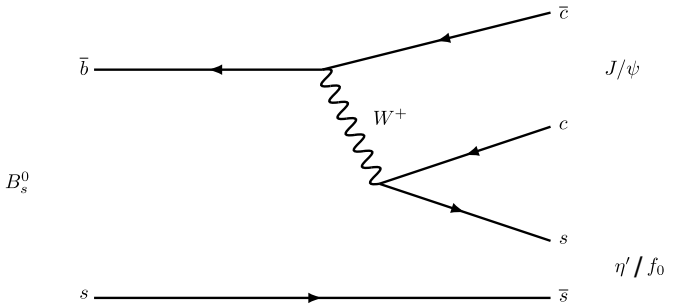

Figure 2.8 *$B_s^0 \to J\psi\eta'$ and $B_s^0 \to J/\psi f_0\,(980)$ Feynman diagrams.*

2.4.1 Impact of Hadronic phase shifts

In [34, 35, 37] the impact of the strong phase shifts on the determination of τ_L and τ_H from the $B_s^0 \to J/\psi\eta'$ and $B_s^0 \to J/\psi f_0$ decay modes is studied in-depth. Allowing for strong phase shifts and considering the case of a CP eigenstate, eq. (2.20) becomes

$$\mathcal{A}_{\Delta\Gamma}^f = \pm\sqrt{1-C_f^2}\cos\left(\phi_s + \Delta\phi_f\right), \tag{2.28}$$

where $\Delta\phi_f$ is a hadronic phase shift, C_f is the direct CP asymmetry and the sign is negative for a CP even state and positive for a CP odd state. In [34, 37] ranges for these hadronic parameters are estimated, $\left|C_{J/\psi f_0}\right| \lesssim 0.05$, $\left|C_{J/\psi\eta'}\right| \lesssim 0.05$, $-3^\circ < \Delta\phi_{f(J/\psi\eta')} < 0^\circ$ and $-2.9^\circ < \Delta\phi_{f(J/\psi f_0)} < 2.8^\circ$. In order to check the

impact on $\Delta\Gamma_s$, a simplified simulation was performed. In this simulation, ϕ_s was sampled from a Gaussian distribution generated around the PDG value of ϕ_s: -0.050 ± 0.019 [20]. The hadronic values are sampled uniformly using the ranges given above. The values of the effective lifetimes calculated using eq. (2.21), which assume CP conservation and that hadronic effects can be neglected. These are then used to determine $\Delta\Gamma_s$. The result of the simulation is shown in fig. 2.9. The bias on $\Delta\Gamma_s$ introduced by ignoring CP violation, the hadronic phase shift and the direct CP asymmetry is $\mathcal{O}\left(10^{-2}\right) \mathrm{ns}^{-1}$, which is a factor 10^3 smaller than the statistical uncertainty of this analysis.

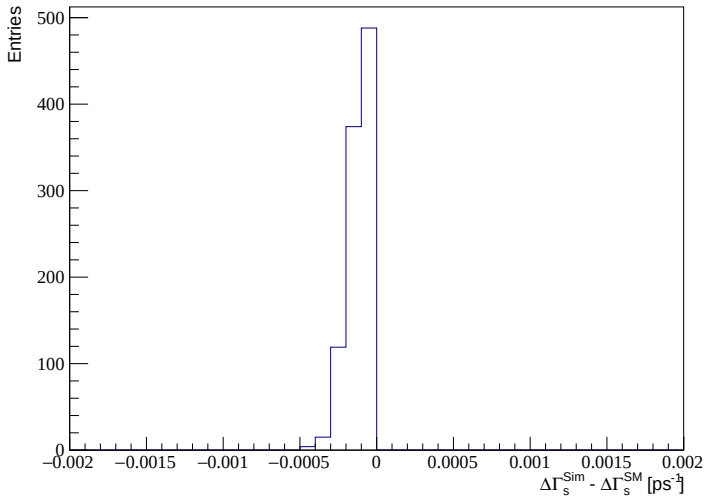

Figure 2.9 *Difference between the input value of $\Delta\Gamma_s$ in the toy simulation described in the text and the value calculated from the difference between the effective lifetimes τ_H and τ_L*

Chapter 3

The LHCb detector at CERN

The CERN was founded in 1952 with the mandate of establishing a physics research organization in Europe. At the end of June 1953 a convention establishing the new organization was signed by the twelve founding Member States [38]. The organization was ratified on the 29th September 1954 but the name CERN was kept unchanged. At that time research on physics was focused on studying the internal structure of the atom and for this reason the word "nuclear" was used in the naming. Nowadays, our understanding of the internal components of the atom is much deeper the main research field of CERN has moved to high energy particle physics. To perform such studies accelerators are built to collide particles.

3.1 The LHC at CERN

In fig. 3.1 the CERN accelerator complex is shown. The work in this thesis is focused on data collected by the LHCb experiment [39] at the Large Hadron Collider (LHC) [40]. Located in the 27 km long tunnel previously used for the Large Electron–Positron (LEP) collider [41], the LHC is the largest collider in the world and has a design energy of 7 TeV per beam ($\sqrt{s}$ = 14 TeV). It was built between 1998 and 2008 and is located hundred meters under the ground at the border between France and Switzerland. Protons are obtained from stripping electrons from gaseous hydrogen and accelerated by a series of machines. The first step in the injector chain is the Linear accelerator 2 (Linac 2). Linac 2 increases

the proton energy to 50 MeV. It is followed by the Proton Synchrotron Booster (PSB), an accumulator ring, that groups protons into bunches and increases the energy to 1.4 GeV. This is a crucial step since the final structure of the beam is generated here. At this point, bunches of protons are sent into the Proton Synchrotron (PS) and the Super Proton Synchrotron (SPS) finally reaching the LHC injection energy of 450 GeV. Once the LHC is filled with the two beams, the machine accelerates them up to nominal energy, it squeezes the bunches and it makes them to collide at the four interaction points.

Each collision point hosts a detector: A Large Ion Collider Experiment (ALICE) [42], dedicated to heavy-ion physics, ATLAS [43] and Compact Muon Solenoid (CMS) [44], two general-purpose detectors studying a wide range of physics and LHCb [39], a single-arm spectrometer focused on flavor physics.

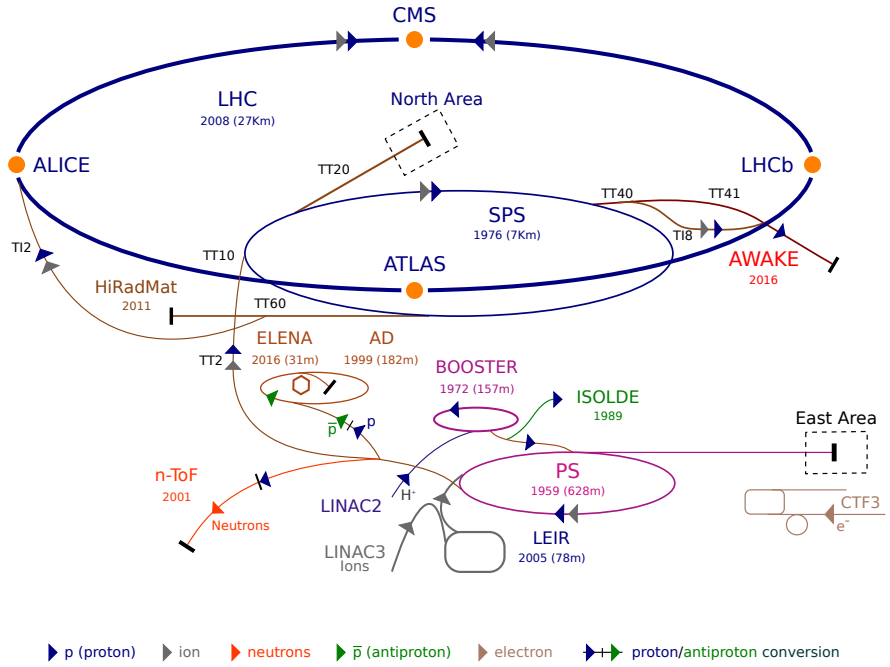

Figure 3.1 *Accelerator complex at CERN. The orange dots highlight the four collision points with their detectors in the LHC. In particular, the LHCb detector is on the right side of the LHC accelerator [45].*

Physics operation of the LHC began in 2010 when two proton beams collided for the very first time with an energy of 3.5 TeV per beam. The LHC life cycle is alternated between data taking and upgrades as shown in fig. 3.2. Run 1 refers to the data collected during 2011 and 2012; Long Shutdown 1 (LS1) is the period between 2013 and 2015 where the LHC was upgraded and its energy was increased to 6.5 TeV per beam; Run 2 is the last period of data taking from 2015

to 2018. At the end of 2018, Long Shutdown 2 (LS2) started and lasted until the beginning of 2022. The work on this thesis will always refer to the Run 1 and Run 2 configuration unless explicitly written.

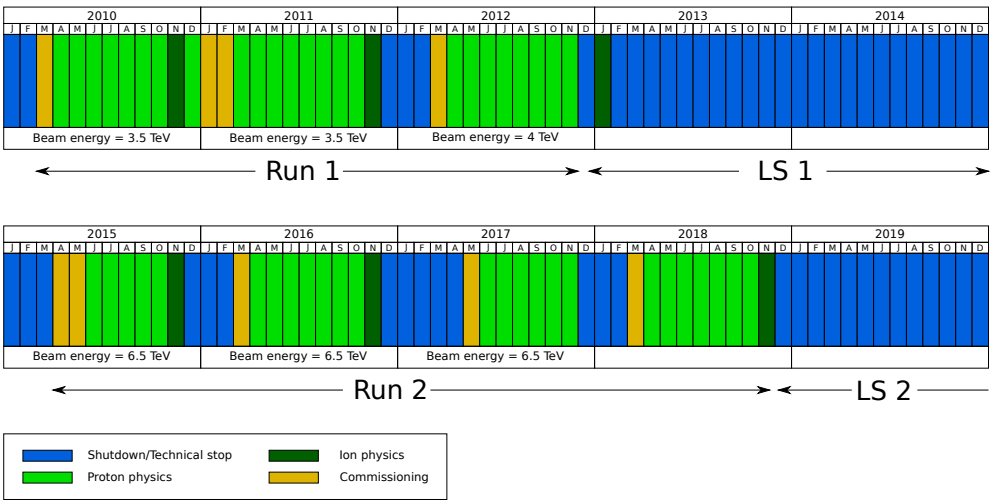

Figure 3.2 *LHC schedule for the Run 1 and Run 2 period. In light green the months when the machine was colliding protons.*

The properties of the beam delivered by the LHC are adapted to satisfy the requirements of each experiment. Since the LHCb physics program is focused on precision measurements, it is desirable to have ~ 1 visible interaction[1] per bunch crossing to easily allow association of a $b-$hadron to a primary vertex. For this reason the machine's optics is adapted to deliver an average pile-up $(\overline{\mu}) \sim 1.1$ [46]. The integrated luminosity recorded by the detector is shown in fig. 3.3: each line represents the luminosity delivered by the LHC every year. The average instantaneous luminosity is $2 - 4 \times 10^{32}$ cm^{-2}s^{-1} [47].

[1]A sizeable fraction of collisions are soft and do not produce any particles within the detector's acceptance. Visible interactions refer to proton-proton interactions that can be detected by the LHCb detector. This is defined as two or more tracks in the detector.

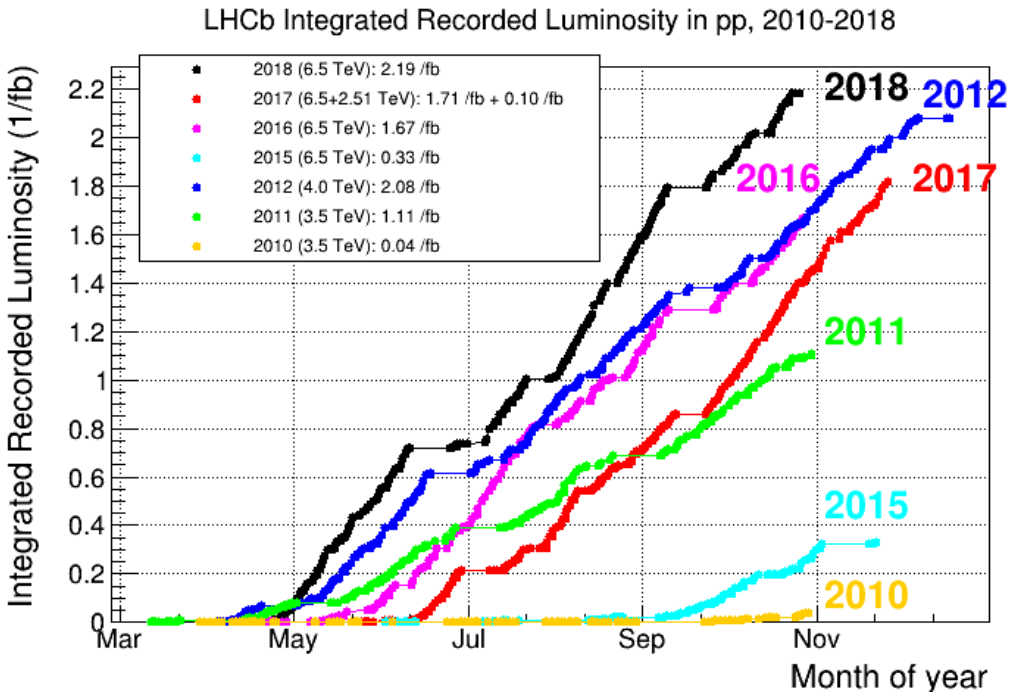

Figure 3.3 *Integrated luminosity recorded by the LHCb detector [48]. During Run 1 and Run 2. Each line represent a different year.*

3.2 The LHCb detector

The LHCb detector [39] is a single-arm forward spectrometer optimized to detect b- and c-hadrons. Its geometry is chosen by the fact that hadrons and anti-hadrons are preferentially produced in the same forward or backward cone as shown in fig. 3.4. A right-handed coordinate system is used with the z-axis aligned with the beam direction, positive z pointing towards the calorimeters and the positive y-axis vertically up as shown in fig. 3.5. The detector has an angular coverage between 10 to 300 mrad in the bending plane $x - z$ and between 10 to 250 mrad in the non-bending plane $y - z$. This corresponds to the pseudorapidity range $1.8 < \eta < 4.9$.

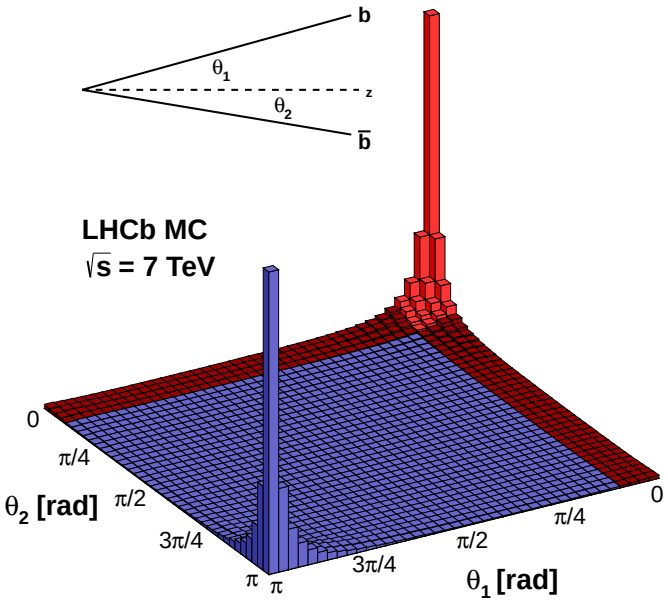

Figure 3.4 *Simulated $b\bar{b}$ pair production angle in respect to the beam. In red it is highlighted the LHCb acceptance [49].*

The detector is located at Point 8 inside the LHC tunnel. It consists of multiple sub-detectors, each performing a different task:

- Tracking system: to record the trajectory of charged particles
- Rich Imaging Cherenkov detectors: to perform particle identification
- Calorimeters (hadronic and electromagnetic): to measure the energy of hadrons and photons/electrons
- Muon system: tracking system located at the very end of the detector, optimized to detect muons.

A side view of the detector placed into the cavern in Point 8 with its dimensions and its sub-detectors is shown in fig. 3.5.

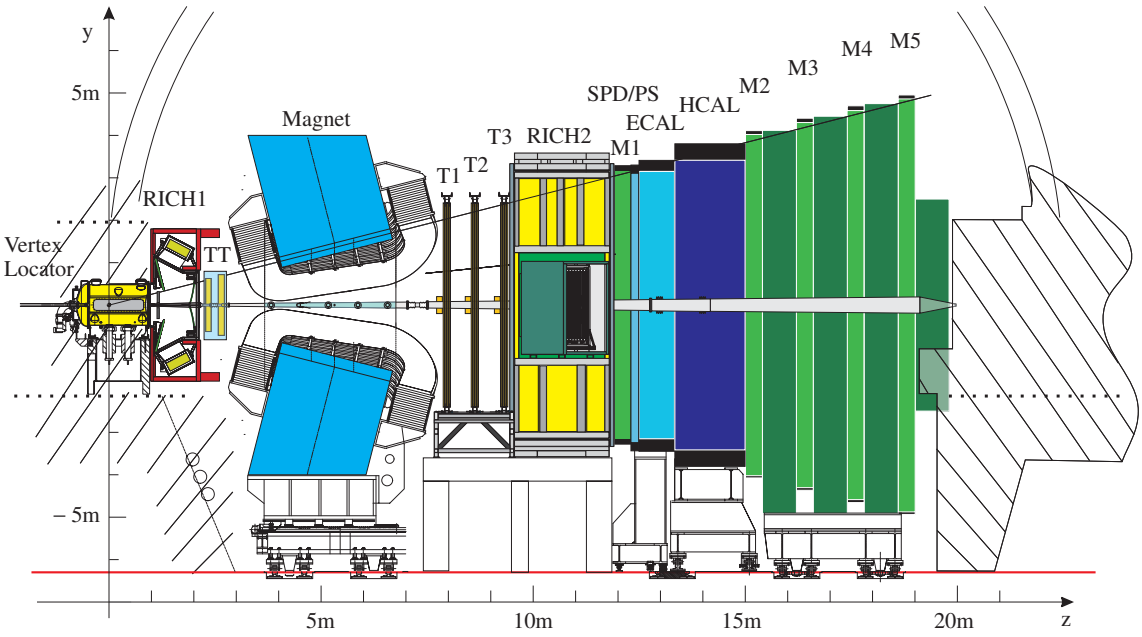

Figure 3.5 *The LHCb detector inside the cavern in Point 8. The names of each sub-detector and are written on top [39].*

3.2.1 Tracking systems

Determining the trajectory of charged particles is crucial to give precise information about vertices and, with the help of a magnet, particle momentum and charge. The tracking system consists of multiple tracking subsystems: the VErtex LOcator (VELO) [39], around the interaction point, the Tracker Turicensis (TT) [39], just before the magnet, and T1-T3 [39] stations, placed after the magnet. A more detailed description of each sub-detector is provided in the following subsection.

VELO

The main purpose of the VELO is to measure the trajectory of particles close to the interaction point. This allows to determine the location of primary and secondary vertices with high precision. Since the b-hadron flies a few centimeters before decaying, positioning the detector as close as possible to the interaction point is crucial. The VELO is made of 23 pairs of silicon strip modules providing radial (r) and angular (ϕ) coordinates of each hit (fig. 3.6). It is kept in a secondary vacuum, separated from the LHC primary vacuum and it is designed to be placed at 5 mm from the nominal beam axis. This distance is smaller

than the maximum aperture allowed during the beam injection phase. For this reason during injection and ramping of the LHC beam energies the VELO is retracted from the beamline and only inserted when stable beams are declared. The proximity to the interaction point allows the reconstruction of displaced vertices, a signature of b- and c-hadrons. The VELO detects particles within the range $1.6 < \eta < 4.9$. [50].

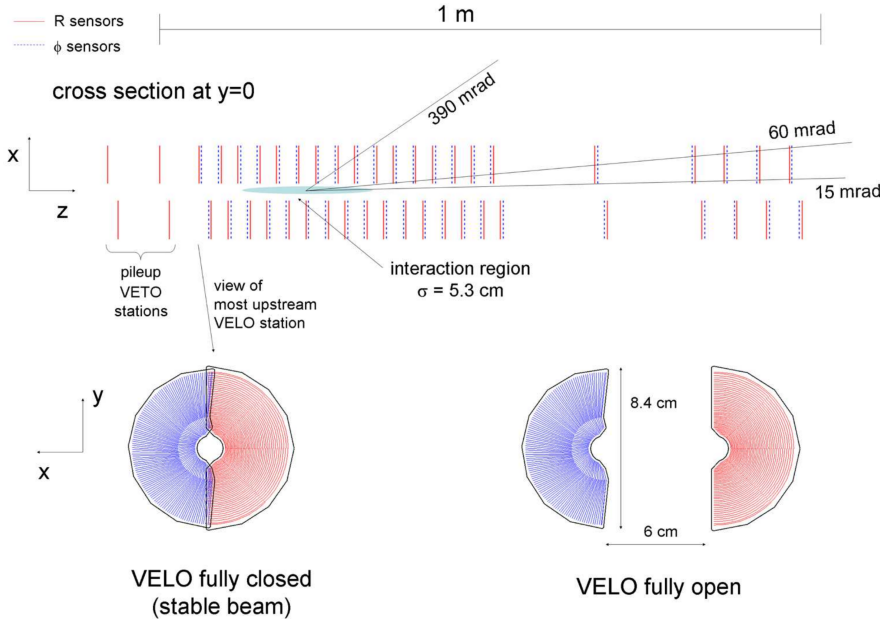

Figure 3.6 *VELO geometry. The top picture shows the position of the VELO modules. The two bottom pictures show the shape of a single pair of modules respectively in fully closed position (left) and in fully retracted position (right) [39].*

Magnet

In order to measure the momentum of charged particle, a warm dipole magnet [39] is placed five meters downstream of the interaction point. The magnet is made of two identical coils with a saddle shape and placed on top of each other as shown in fig. 3.7a. The total weight of the yoke is around 1500 tons while the two coils weight 54 tons. The magnetic field as a function of the z-coordinate is plotted in fig. 3.7b.

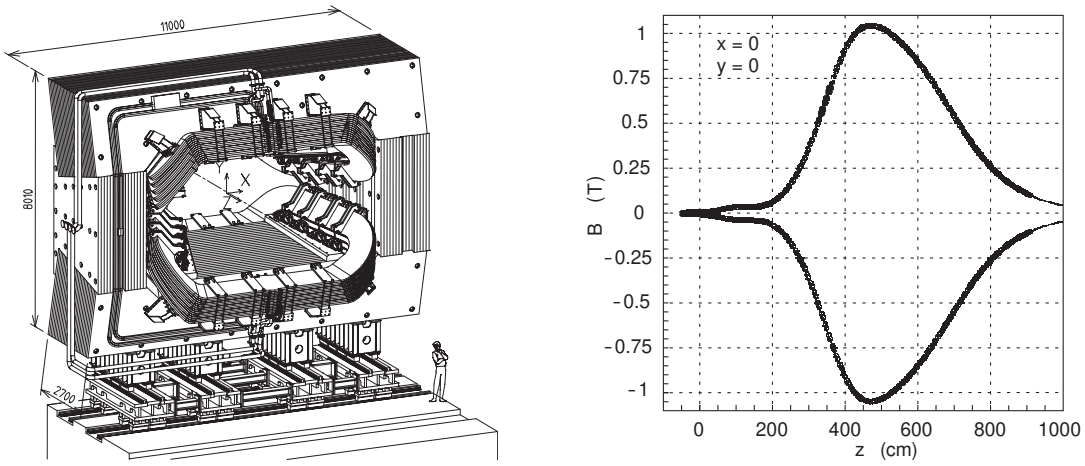

(a) **(b)**

Figure 3.7 *View of the LHCb magnet and its magnetic field. In fig. 3.7a the view on the x-y plane of the LHCb magnet and in fig. 3.7b the magnetic field as a function of the z position for both polarities [39].*

The integral of the magnetic field between $z = 0$ m and $z = 10$ m is 4 Tm. The measurement of the deflection of charged particles by the magnet allows to determine the momentum with a precision better than 1% for momenta up to 200 GeV/c [51].

Silicon Tracker

The Silicon Tracker (ST) project consists of two sub-detectors: the TT and Inner Tracker (IT) [39] that make use of silicon strip technology and are developed in common. The TT is a 150 cm wide and 13 cm high tracker located right before the LHCb magnet. The IT is placed inside the three tracking stations (T1-T3) and it covers an area 120 cm wide and 40 cm high. Both detectors (fig. 3.8) use silicon microstrip technology with a strip pitch of ~ 200 μm giving a resolution around 60 μm. Each station has four layers with a $(x-u-v-x)$ configuration of the strips where external strips are placed in vertical position and the central ones are respectively tilted by $-5°$ and $5°$ with respect to the vertical.

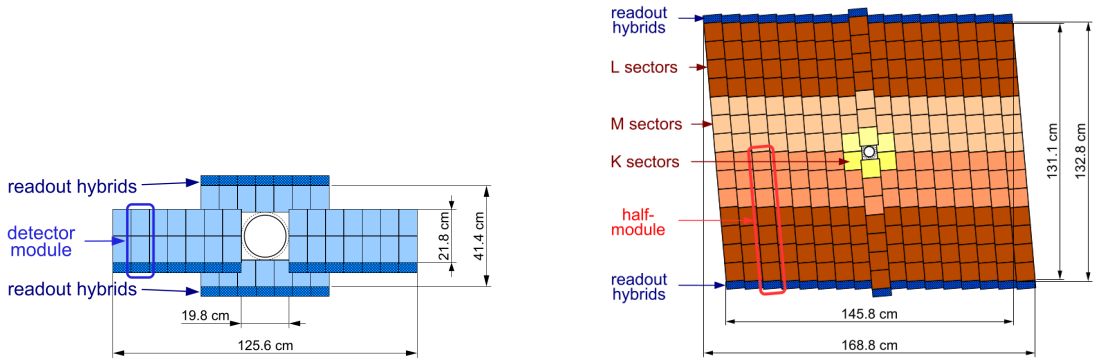

Figure 3.8 *The ST detectors: on the left the IT tracking station scheme; on the right the TT tracking station scheme [39]. Both pictures have a central hole corresponding to the beam pipe.*

Outer Tracker

The Outer Tracker (OT) is a drift chamber detector [39] used to track charged particles in the outer part of the T-stations. The detector is made of gas-tight straw-tube modules arranged in three stations. In order to have a drift time below 50 ns and a drift-coordinate resolution of 200 μm, a gas mixture of Argon (70%) and CO_2 (30%) is chosen. Each station has the same configuration used for the ST $(x-u-v-x)$ with x layers in vertical position and $u-v$ layers tilted by $\pm 5^\circ$ with respect to the vertical. The OT scheme is shown in fig. 3.9.

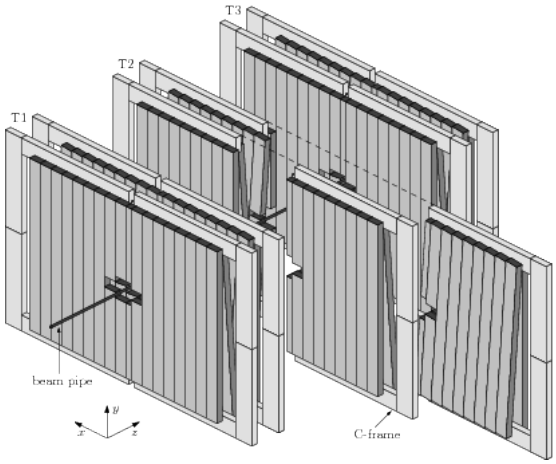

Figure 3.9 *The OT system surrounding the beam pipe and the IT downstream of the magnet [52].*

3.2.2 Particle identification

The Particle IDentification (PID) system is designed to identify different particles travelling inside the LHCb detector. The main sub-detector used for this purpose is the Ring Imaging CHerenkov (RICH) which is able to identify charged hadrons ($\pi, \mathrm{K}, \mathrm{p}$). The RICH system consists of two RICH detectors: RICH1, downstream of the VELO and RICH2, located after the magnet. The RICH1 detector covers the medium-low momentum region $(2 - 40)\,\mathrm{GeV}/c$ over the full LHCb acceptance $(25 - 300)$ mrad. RICH2 covers the high momentum range $(15 - 100)\,\mathrm{GeV}/c$ over a smaller angular range $(15 - 120)$ mrad [53].

Both RICH systems detect Cherenkov radiation emitted by charged particles travelling through the detector. When a charged particle travels inside a medium with a speed greater than the speed of light in the same medium, it emits the Cherenkov radiation [54] in a conical shape around its trajectory. The emission angle, θ, between the direction of the particle and the emitted radiation is

$$\cos(\theta) = \frac{1}{n\beta}, \tag{3.1}$$

where n is the refractive index of the medium and $\beta = v/c$.

A series of mirrors is used to deflect the Cherenkov light on Hybrid Photo Detectors (HPDs) located on the side of the detector, away from the detector's acceptance. The material used to generate Cherenkov radiation in Run 2 is fluorocarbon gas: C_4F_{10} for RICH1 and CF_4 for RICH2 [53]. During Run 1 RICH1 had both fluorocarbon gas and aerogel radiators. With the Run 2 configuration, the material within the experimental acceptance is 8% radiation length (X_0) for RICH1 and 15% X_0 for RICH2 [53]. In fig. 3.10 the layout of the RICH detectors is shown.

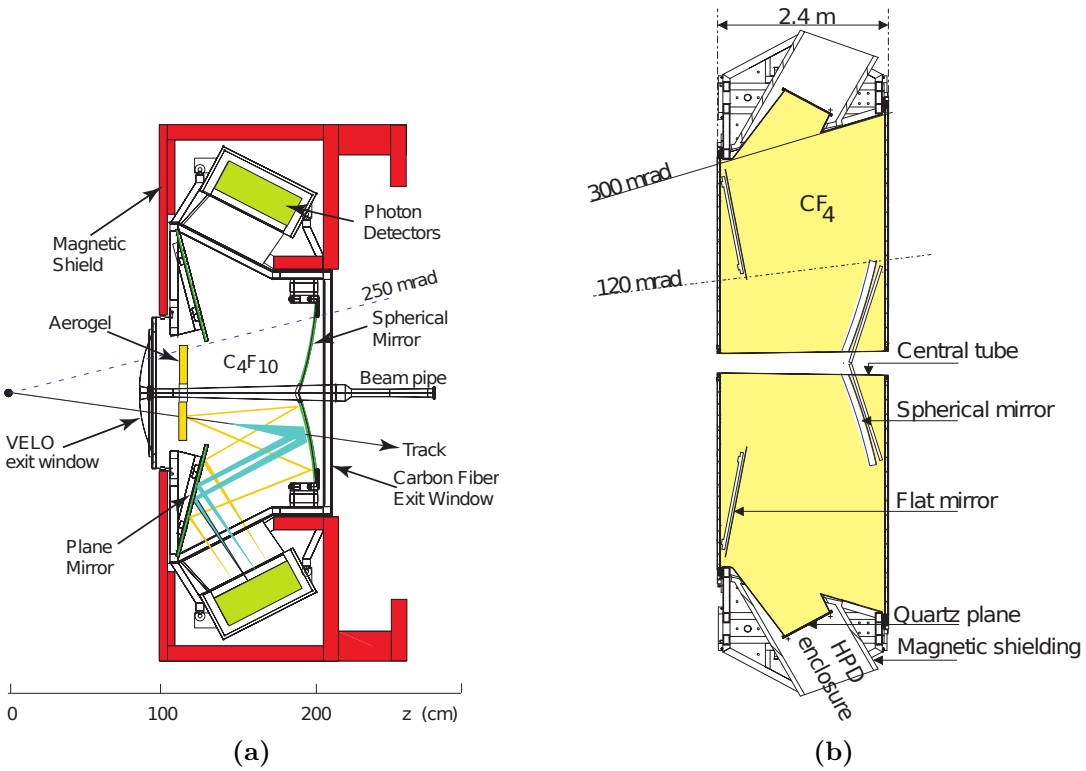

Figure 3.10 *Scheme of RICH1 (fig. 3.10a) and RICH2 (fig. 3.10b) [39].*

Combining the momentum computed by the tracking system with the Cherenkov angle allows to compute the mass of the particle. In fig. 3.11 is shown the reconstructed Cherenkov angle as a function of the momentum of the charged particles. The plot shows good separation between different type of particles up to 100 GeV/c.

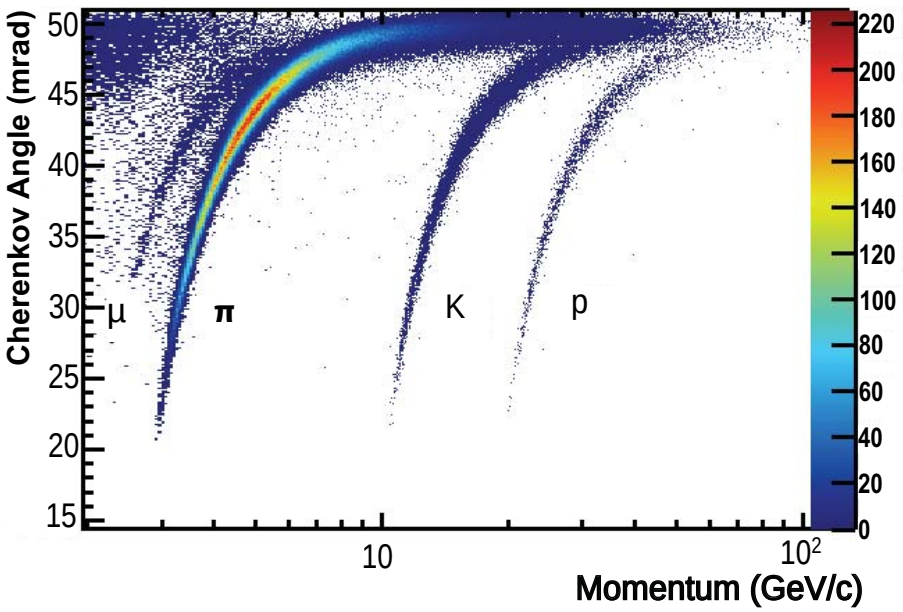

Figure 3.11 *Cherenkov angle computed by RICH1 detector as a function of the particle's momentum computed by the tracking system [53].*

3.2.3 Calorimeters

The calorimeters measure the energy of the hadronic and the electromagnetic component of the incident particles using materials that emit light after absorbing energy carried by particles. When interacting with a scintillator, particles lose a fraction of their energy which is absorbed by the detector's material and re-emitted in the form of light. In order to precisely measure the shower energy, the depth of a calorimeter needs to be sufficient to fully absorb the incoming particle and the products of its interaction with the detector. Calorimeters are usually classified into two main groups: hadronic calorimeters and electromagnetic calorimeters. Since the radiation length (X_0) is small compared to the hadronic interaction length (Λ_0), the electromagnetic calorimeter is placed before the hadronic one. Electrons and photons will interact in the Electromagnetic CALorimeter (ECAL) whilst hadrons tend to interact later in the Hadron CALorimeter (HCAL).

The LHCb calorimeter system [39] is made of four sub-systems: ECAL, HCAL, PreShower (PS), Scintillator Pad Detector (SPD). Since the hit density falls rapidly as the distance to the beampipe increases, the calorimeters have variable

lateral segmentation as shown in fig. 3.12. In particular, the ECAL is segmented into three zones while the HCAL is segmented into two sections due to the bigger size of hadronic showers.

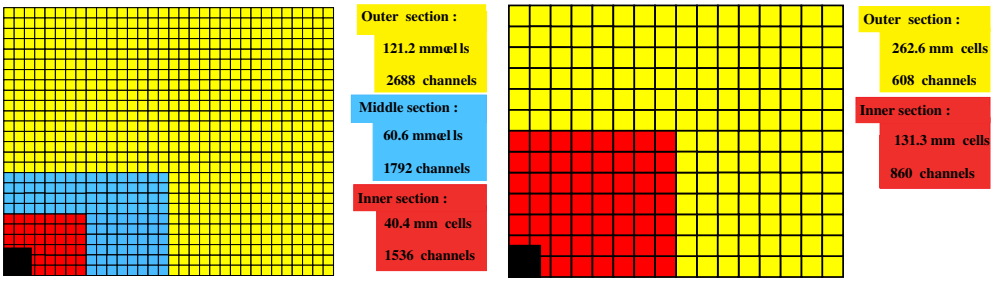

Figure 3.12 *Cross section of one quarter of the SPD, PS and ECAL on the left and of the HCAL on the right [39]. The cell dimensions on the right plot are given for the ECAL, the need to be reduced of* $\sim 1.5\%$ *for SPD and PS [55].*

Each component of the calorimeter system works in the same way: particles deposit energy in the scintillating material causing the emission of photons. These photons are then transmitted to the Multi-anode Photo-Multiplier Tube (PMT) (MaPMT) via a WaveLength-Shifting (WLS) fiber. To assure a good granularity, the LHCb calorimeters have a sandwich structure alternating stopping plates (e.g. iron, lead, etc.) with scintillating material fig. 3.13.

The ECAL is fundamental to the identification and selection of photons and electrons. The geometric center of the ECAL is at $z = 12.5$ m and it covers the acceptance of 25 mrad $< \theta_x <$ 300 mrad in x and 25 mrad $< \theta_y <$ 250 mrad. The ECAL is made of several modules, each perpendicular to the beam direction and it is built of alternating layers of 2 mm thick lead, 120 μm thick white reflecting Tyvek and 4 mm thick scintillating plastic. The total length of a module is 42 cm corresponding to 25 X_0.

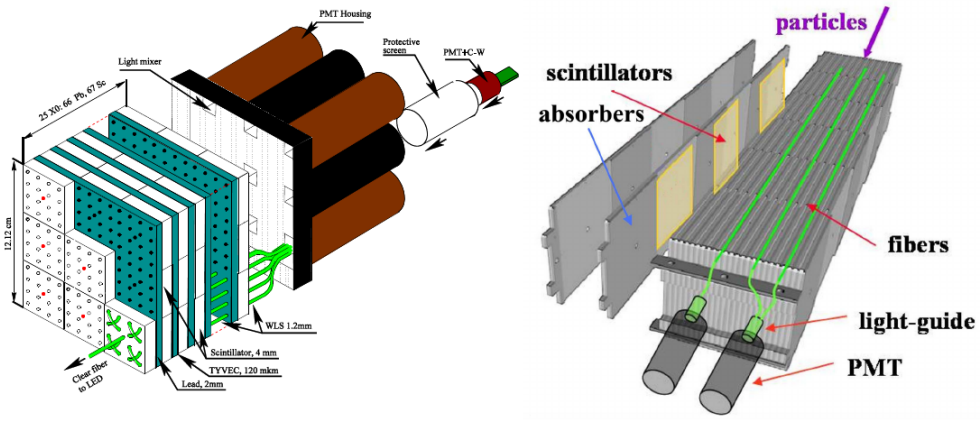

Figure 3.13 *ECAL structure (left) and HCAL structure (right) [39].*

The geometric center of the HCAL is at $z = 13$ m. It has a sampling design and it is divided into modules each with size $(4.04 \times 4.04)\,\mathrm{cm}^2$ parallel in respect to the beam direction. A module has a multi-layer structure alternating a 1 cm thick tile of iron with 3 mm thick scintillating material. The total depth of the HCAL correspond to 5.6 hadronic interaction lengths. The layout of the HCAL is shown in fig. 3.13 (right).

3.2.4 Muon system

A displaced $J/\psi \to \mu^+\mu^-$ decay gives a clear signature for a charmonia decay. Both decays used in this thesis strongly rely on muons: $B_s^0 \to J/\psi\,(\mu^+\mu^-)\,\eta'$ and $B_s^0 \to J/\psi\,(\mu^+\mu^-)\;\; f_0\,(980)$.

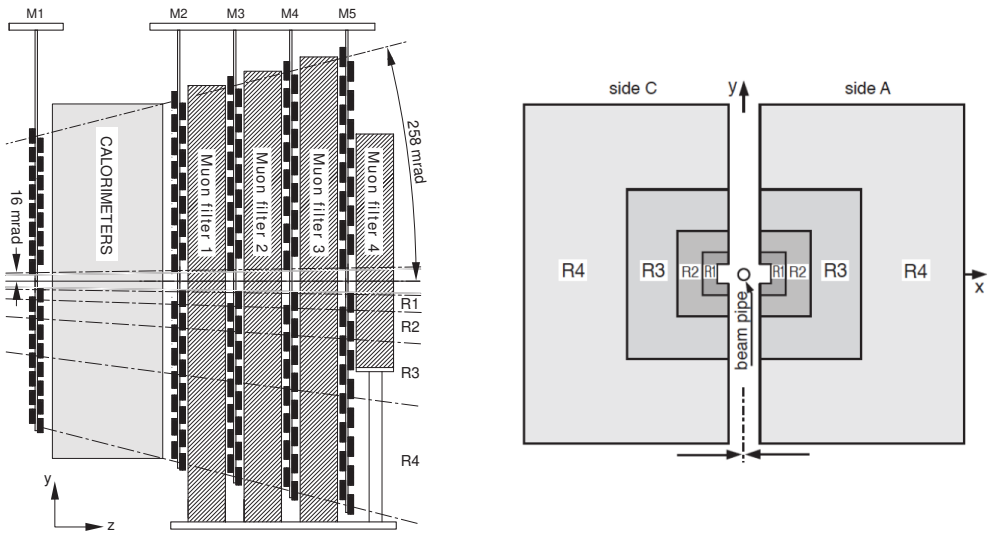

Figure 3.14 *LHCb muon system showing the transversal section (right side) and the longitudinal section (left side) [39].*

The muon system provides both fast signals for the Level-0 (L0) trigger and more precise information for muon identification both at HLT level and offline. It is composed of five stations as shown in the left figure in fig. 3.14. The last four stations are placed after the HCAL and they are interleaved with 80 cm thick iron plates. The first muon station (M1), is placed right before the calorimeters and is used to improve the p_T resolution for the L0 trigger. The absorbing power of the full system is around 20 interaction lengths (Λ_0) and the minimum momentum for a muon to cross all five stations is around 6 GeV/c [39].

The full muon system is made of 1368 Multi-Wire Proportional Chambers (MWPC) achieving a 5 ns resolution with a space of 2 mm between wires and a gap of 5 mm between tracking planes. The gas mixture used is $Ar/CO_2/CF_4$ with 40% Ar and a variable concentration of CO_2/CF_4 [39]. In order to verify the performance of the MWPC after irradiation, aging tests were made at the ENEA-Casaccia research center in Rome [56]. The test simulated the different radioactive dose absorbed in every part of the muon detector. Every region except the innermost part of the M1 station (R1) satisfied the requirements to host MWPC detectors. As the R1 region is more exposed to radiation, this part of the muon system uses triple-Gas Electron Multiplier (GEM) detectors which are able to absorb a higher radiation dose before having a decrease in performance [56]. The triple-GEM consists of a sandwich of three GEM foils placed between anode and cathode. This configuration allows the tracking of particles travelling inside the detector. In fig. 3.15 the layout of a triple-GEM detector is shown with

its dimensions and layer configuration.

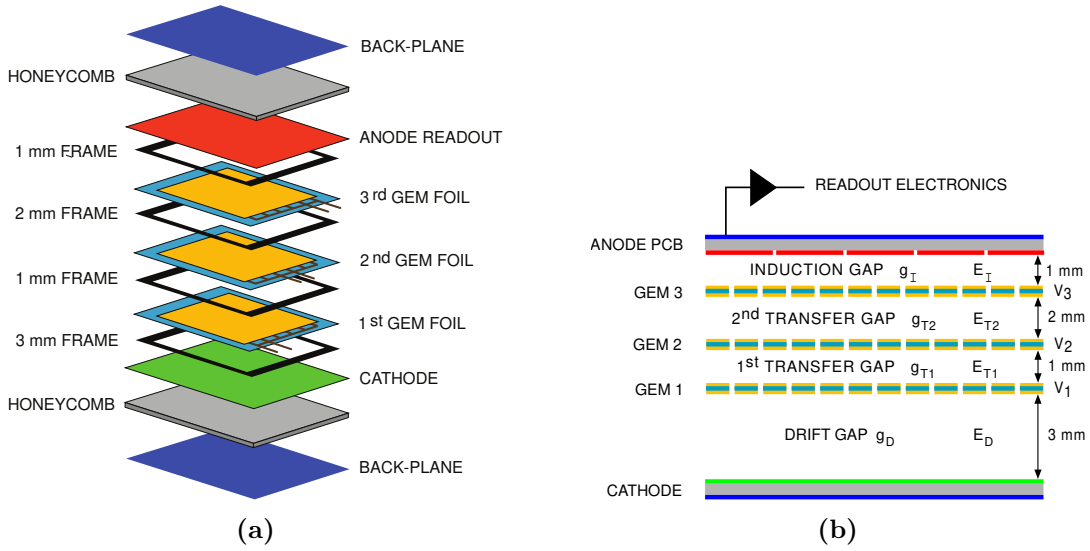

Figure 3.15 *Schematic of the triple-GEM (fig. 3.15b) and exploded view of the triple-GEM detector placed into the R1 region (fig. 3.15a) [39].*

3.2.5 The online system

The LHCb online system is responsible for transporting data from the front-end electronics to the permanent storage system [39]. This also includes the configuration and monitoring of all the operational and environmental parameters.

Each sub-detector has front-end electronics modules that records the signal from each bunch crossing. On receipt of a L0 trigger decision, data collected by the front-ends are transmitted via optical fibers to TELL1 [57] boards located off detector. In the TELL1 board the data are processed by four pre-processing Field-Programmable Gate Array (FPGA) modules and different operations such as data compression are performed, depending on the sub-detector. The data fragments outputted by these FPGA are then sent to a fifth FPGA which formats them into a raw IP-packet. This is sent to the Data AcQuisition (DAQ) system using an Ethernet board interfaced to the Experiment Control System (ECS). Clock and timing signals are transmitted using separate interfaces. The ECS is responsible to monitor the status of the entire LHCb detector including the DAQ system and the Event Filter Farm (EFF). A scheme of the online architecture is shown in fig. 3.16.

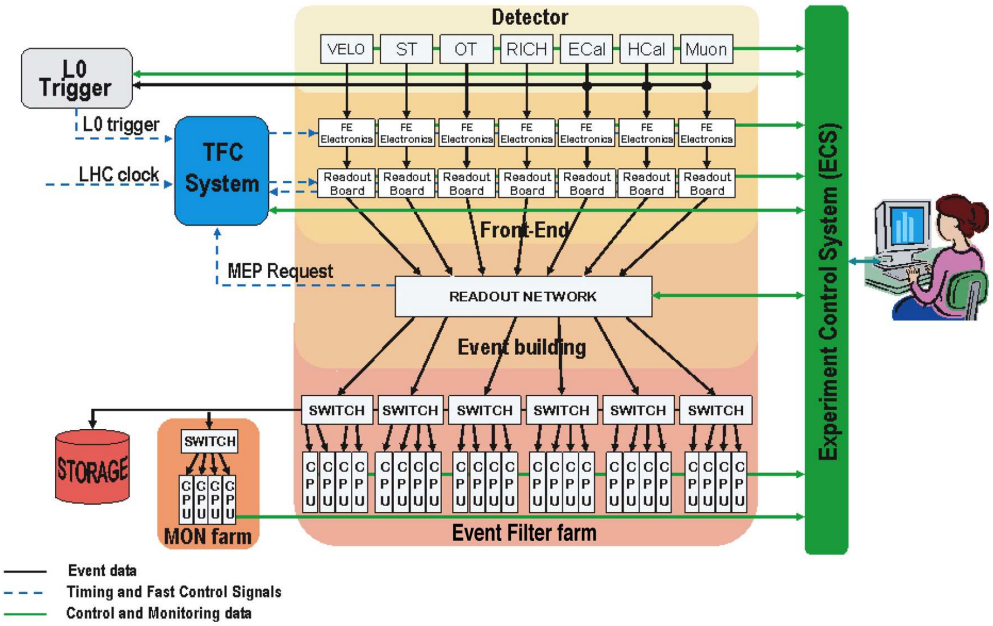

Figure 3.16 *LHCb online architecture. From top to bottom the sub-detectors' readout systems, the front-end electronics, the event building and the EFF [39].*

3.2.6 Trigger system

The detector and the full acquisition chain has to deal with the 40 MHz bunch crossing rate of the LHC. At an instantaneous luminosity of $\mathscr{L} = 2 \times 10^{32}\text{cm}^{-2}\text{s}^{-1}$, the rate of visible proton-proton interactions containing either b- or c-hadrons is around 100 kHz [39]. Therefore, an event selection system is needed to lower the data rate coming from the detector. This procedure has to be performed during data taking, because the storage system is not able to record every event on disk[2]. For this reason, a two-stage trigger system is used to select candidates for physics analysis. The first step of the trigger, the L0, is hardware based and uses custom electronics modules. The subsequent trigger stage, the HLT, is software based and uses commercial computers in the EFF.

Level-0

The main task of the L0 trigger is to reduce the event rate from 40 MHz to 1 MHz, the maximum rate the HLT can process. At this stage, only limited information is available: the hadron with the highest transverse energy, electron

[2]The throughput is $\mathcal{O}\,(1\ TB/s)$ for a bunch crossing rate of 40 MHz.

and photon clusters in the calorimeters and the two muons with the highest transverse momentum. As shown in fig. 3.17, the L0 trigger is subdivided into two components: the L0 calorimeter trigger and the L0 muon trigger. Information from those systems is combined by the L0 decision unit which collects all the information computed by the muon trigger system and the calorimeter system to evaluate the final decision.

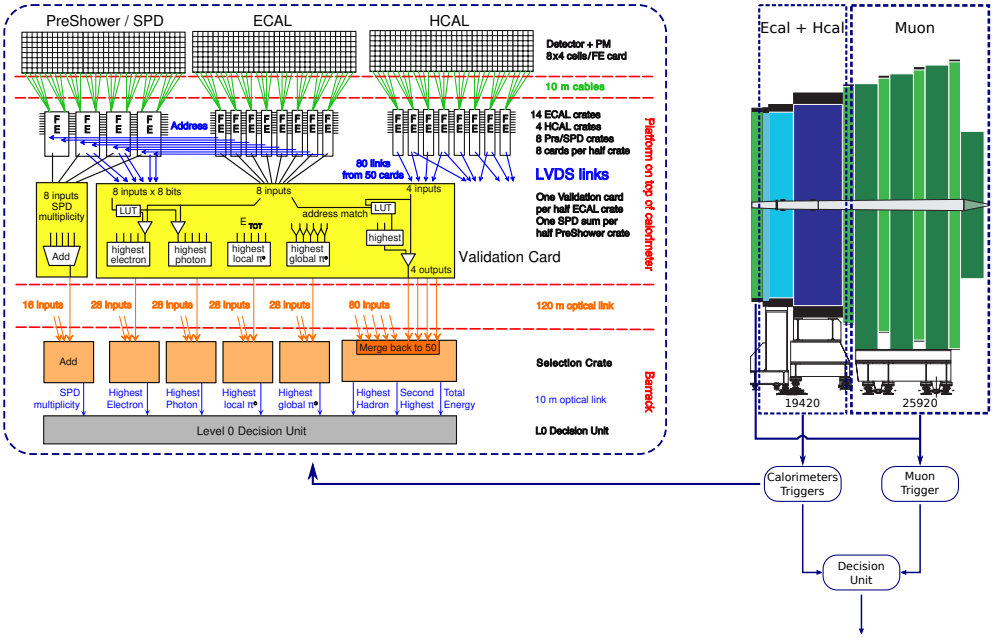

Figure 3.17 *The L0 scheme with a detailed view of the calorimeter trigger (left side): ECAL, HCAL and muon stations signals are sent to a decision unit which takes care of selecting candidate events [39].*

The calorimeter trigger system selects the electromagnetic and hadronic clusters with the highest transverse energy. Each cluster is associated to a particle using the information from the full calorimeter system (SPD, PS, ECAL and HCAL). The muon trigger system selects the two muons with the highest transverse momentum for each quadrant of the muon system by requiring at least three hits in the muon pads [58].

High Level Trigger

The Run 2 HLT is divided into two stages: HLT1 and HLT2. Both HLT systems are C++ applications running on the 2000 nodes of the EFF. All nodes run both HLT1 and HLT2 instances using different computing power. During the data taking, the HLT1 step runs with high priority writing its output on a disk buffer

while the HLT2 runs with low priority. At this stage, the trigger has full access to the entire detector and can perform a more complex analysis of the incoming data. During periods with no beam, e.g. after beam dump or during filling, almost all the computing power is dedicated to the HLT2 while HLT1 is automatically switched off. Starting from Run 2, real time alignment was included into the HLT as shown in fig. 3.18. During Run 1, the full HLT selection was run online, without using the intermediate buffer.

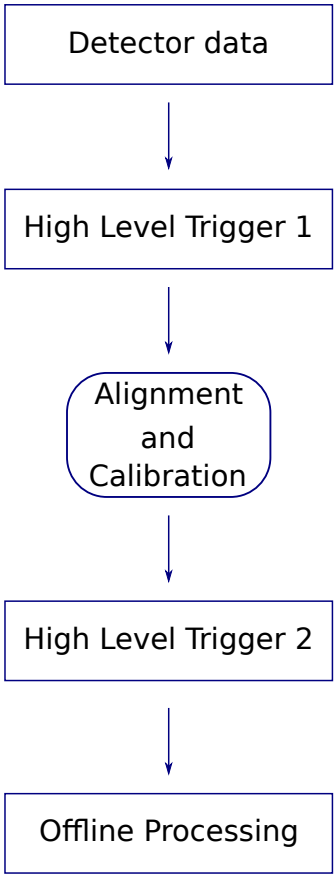

Figure 3.18 *Real time alignment information included between HLT1 and HLT2, starting from Run 2.*

The HLT1 step confirms the high-p_T L0 candidate with the addition of information from the tracking system, using only the regions around the candidate direction, when possible. This allows particles to be selected according to another property that characterize particles from b-hadron decays: their high impact parameter to the proton-proton interaction vertex. If a candidate is not confirmed, the event is rejected. The HLT1 output rate is 110 kHz [59]

At the rate HLT2 is executed, it is possible to run a complete event reconstruction outputting data at 12.5 kHz. Displaced vertices separated from the interaction

point, typical of a b-hadron decay, are searched for. Two types of selection are made: inclusive and exclusive. Inclusive selections aim to collect decays of resonances which are useful both for physics and calibration (D^*, J/ψ, etc.). Exclusive selections are specifically designed to provide the highest possible efficiency for fully-reconstructed b-hadron decays of interest, using all the available information, including the mass, vertex quality and displacement [60]. In this thesis, inclusive HLT1 and HLT2 trigger lines are used to select the J/ψ candidates from the signal coming from the muon stations:

- The `HLT1DiMuonHighMass` [61] line selects a pair of opposite sign muons that are consistent with a common vertex. The invariant mass of the pair is required to be above 2.7 GeV/c^2
- The `Hlt2DiMuonDetachedJPsiDecision` [61] line is designed to select J/ψ from b-hadron decays. It confirms the `HLT1DiMuonHighMass` decision and applies a small mass window around the J/ψ candidate, $\mid m_{\text{cand}} - m_{J/\psi} \mid < 120$ MeV/c^2. As seen in fig. 3.20, this window is wide enough to keep all $J/\psi \to \mu^+\mu^-$ decays. In addition, a cut is made on the distance between the primary and secondary vertices divided by the estimated uncertainty, the Decay Length Significance (DLS) at 3σ.

These lines are chosen as they are minimally time biasing.

An event can be selected by the trigger in several ways. First, the signal of interest may be responsible for the event being selected. This is referred to as Trigger On Signal (TOS). It is also possible some other feature will give a trigger. This is referred to as Trigger Independent of Signal (TIS). In this analysis, only HLT TOS triggers were used. Figure 3.19 shows the performance plots for the HLT triggers.

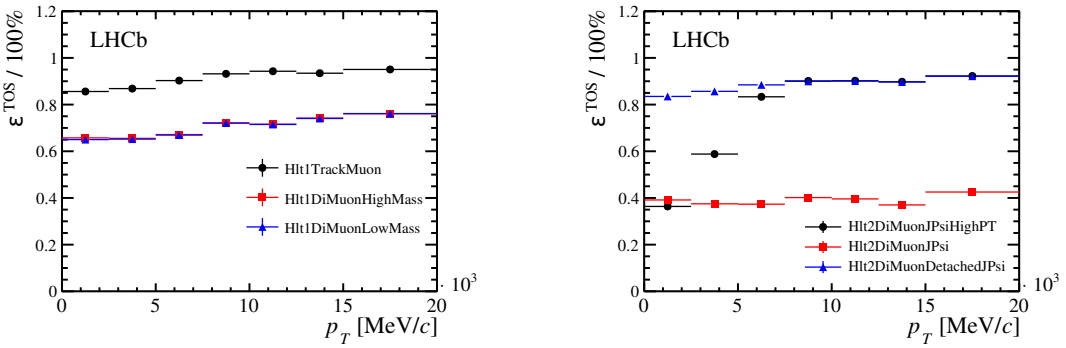

(a) **(b)**

Figure 3.19 *HLT1 (fig. 3.19a) and HLT2 (fig. 3.19b) performance as a function of $P_T\,(B)$ [51]*

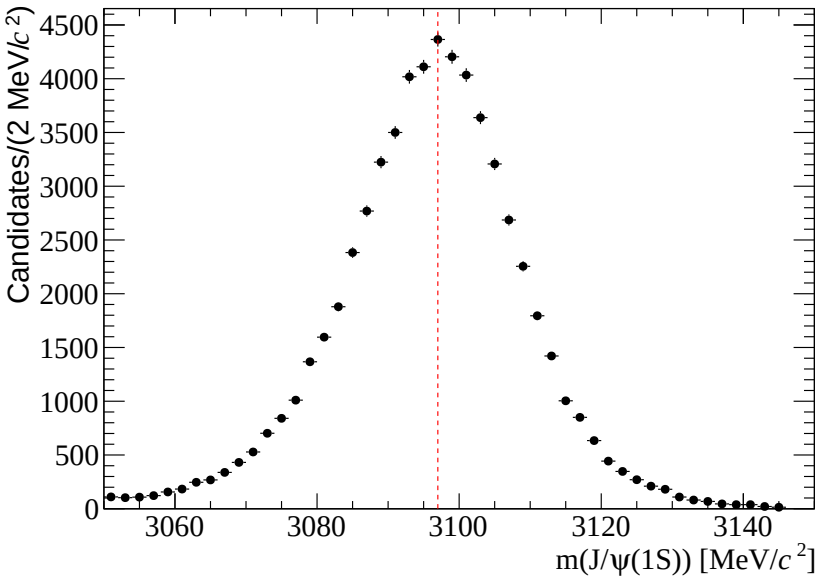

Figure 3.20 *J/ψ mass distribution from the 2016 Monte Carlo after the stripping selection. The vertical dashed line correspond to the J/ψ mass value from PDG.*

Chapter 4

Data processing and simulation

The raw data acquired by the detector need to be processed before being used for analyses. Figure 4.1 shows the data path from the detector to permanent storage. The output of the trigger is read by the Brunel [62] application which converts signals in the detector to higher level analysis objects such as tracks and clusters. Further data reduction is achieved by filtering ("stripping") interesting events with the DaVinci application [63]. After this stage data are ready to be processed by analysts. A similar path is followed in the simulation where proton-proton collisions and the detector's output are simulated and injected into the data processing chain.

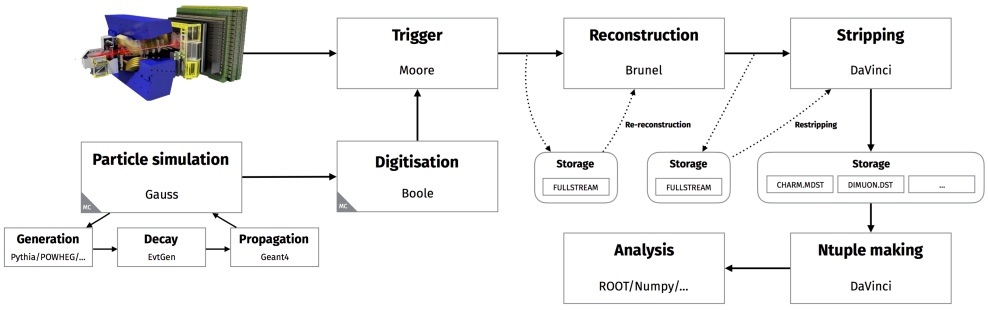

Figure 4.1 *LHCb data flow [64]. On the left side the LHCb detector and the Monte Carlo simulations generating raw data. On the right side the entire reconstruction chain.*

4.1 Event reconstruction

Extracting the properties of the particles travelling inside the LHCb detector using the available sub-detector information is referred to as reconstruction. During Run 1, a simplified track reconstruction which used a first alignment estimate was run in the trigger step. For Run 2, a new procedure referred to as Real Time Alignment and Calibration that allowed full reconstruction with full offline alignment at HLT2 level was introduced. This means that the output of the trigger in Run 2 is already offline quality. Particular attention is focused on track reconstruction and particle identification (hadron, muon, electron, photon and neutral pion reconstruction).

4.1.1 Track reconstruction

Using the tracking system described in section 3.2.1 it is possible to determine the trajectory of charged particles traversing the LHCb detector. Tracks are classified according to which detector have deposited hits as illustrated in fig. 4.2 [51]:

- **Long tracks** have hits recorded in both VELO and T stations; TT hits are added to the track if present. Since these tracks traverse the full length of the spectrometer, the momentum calculation is the most accurate.
- **Upstream tracks** have hits recorded in VELO and TT stations. Their momentum is usually below ~ 3 GeV/c, too low to reach the T stations.
- **Downstream tracks** have hits recorded in TT and T stations. These tracks are typically associated to long lived particles such as K_s or Λ decaying outside the VELO acceptance.
- **VELO tracks** pass only through the VELO. They are typically large-angle or backwards tracks.
- **T tracks** have hits recorded only in the T stations. They are usually generated by secondary interactions.

In this study only long tracks are used.

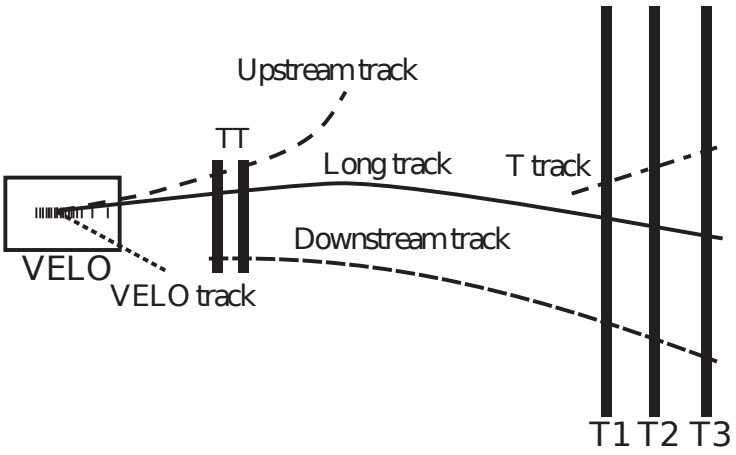

Figure 4.2 *Track classification showing the different tracks and the tracking devices [51].*

The reconstruction starts with standalone reconstruction in the VELO. Tracks are reconstructed in two stages. The first stage is a two dimensional reconstruction using the r hits alone. After this step, three dimensional tracks are reconstructed by adding the ϕ hits. In this step, due to CPU constraints, not all combinations are considered. This leads to an efficiency dependence on the distance of the track to the beamline and hence a decay time acceptance. This effect is largest for Run 1 [65] and reduced in Run 2 due to improvements to the reconstruction algorithm [46].

Long tracks are reconstructed from VELO seeds using an optical method to extrapolate and match information in the T-stations [66]. Hits in the TT station are used to confirm the track. The tracks found are then refitted with a Kalman filter [67]. This takes into account both the energy loss by the particles interacting with the matter and multiple scattering.

Due to the high density environment, mistakes are possible during the pattern recognition phase, e.g. matching of VELO and T-segments from different particles. To identify fake tracks or tracks not associated to any charged particle (ghost tracks), a neural network is trained using the information from the track fit and the track kinematics [68].

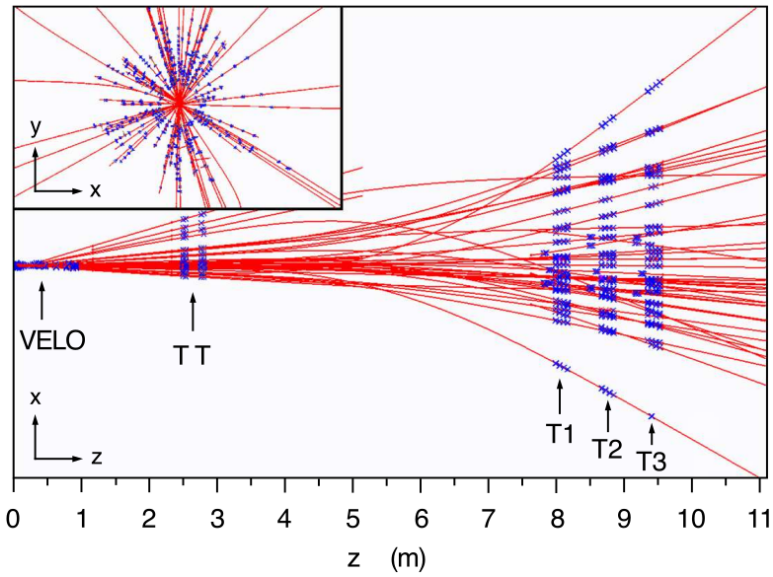

Figure 4.3 *Reconstructed tracks (red) starting from the hits recorded by the trackers (blue). The top left part of the picture shows a x-y section of the VELO [39].*

Figure 4.3 shows the reconstructed tracks in a typical event. The displayed event has 26 long tracks, 11 upstream tracks, 4 downstream tracks, 26 VELO tracks and 5 T tracks [39].

4.1.2 Particle identification

Charged particles are identified combining the information collected by the two RICH detectors, the two calorimeters and the muon system. Neutral particles (γ, π^0) are identified using the ECAL.

To have optimal particle identification, there are two main classes of tools to identify particles: `ProbNNpi` / `ProbNNk` / `ProbNNmu` for charged particles and `isNotE` / `isNotH` / `isPhoton` for neutral particles. These tools use multivariate techniques combining information from simulations with the output of the PID and tracking systems [69] to return the probability of the identity of a given particle. In particular, `isNotH` uses the information from the energy deposited in the PS detectors, the ratio of the energy in the HCAL in the trajectory of the cluster in the ECAL and the energy of the cluster in the ECAL to discriminate photons from non-electromagnetic deposits generated by hadrons. A full description of `isNotH` and the training variables used in its classifier can be found in [70].

Hadron identification

Charged hadron identification is performed with the RICH detectors as discussed in section 3.2.2. At this stage, information from the trackers are added and a log-likelihood approach is used to match the reconstructed tracks with the patterns recorded by the RICH detectors. Figure 3.11 shows how different particles are grouped by type after reconstructing the signals from RICH detectors. The likelihood is maximized by changing the particle hypothesis [39].

Muon identification

Only muons with momentum above 3 GeV/c reach the muon system. Muon identification is performed by looking at hits inside a Field Of Interest (FOI) created starting form track extrapolation for each tracking station. The boolean identification variable `isMuon` requires a muon candidate to have hits recorded in a minimum number of stations (two or four, depending on the momentum) within the corresponding FOI. In order to improve the selection purity, information from the tracking system is added as well as the average track-hit distance of the hits contained into the FOI.

Electron identification

Electron identification is performed by associating the energy released in the ECAL to the one computed from the corresponding track in the tracking system. In fig. 4.4 the ratio of the uncorrected energy of the cluster in the ECAL and the momentum of the corresponding track is shown for electrons and hadrons. Another handle to identify electrons is to detect the Bremsstrahlung photons radiated by the electron before the magnet. In fig. 4.5 is illustrated the topology for the case where the photon is emitted before or after the magnet: the first case would produce a cluster with energy E_1 while the second case does not create a separate cluster. The identification is the same in both cases: if the electron radiated a photon, the E_2 energy will be compared to the momentum, p, while the energy E_0 will be the sum of the energy of the two clusters ($E_0 = E_1 + E_2$).

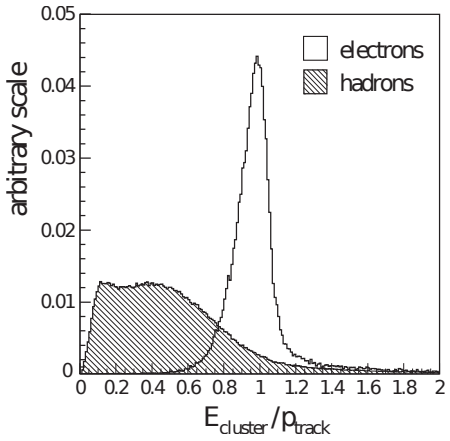

Figure 4.4 *Ratio between the uncorrected energy of the cluster in the ECAL and the associated track momentum for electrons (transparent histogram) and hadrons (solid histogram) [39].*

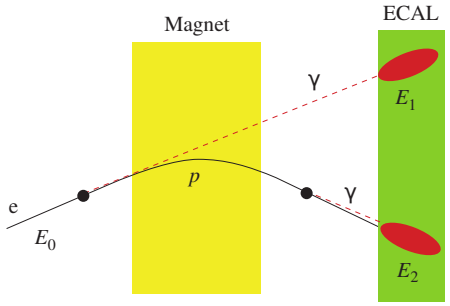

Figure 4.5 *Scheme of the Bremsstrahlung effect with an electron (on the left) radiating one photon before the magnet (yellow) and another one right before the ECAL (green) [39].*

Photon identification

Photons are identified by a cluster in the calorimeter without any corresponding track in the tracking system. A high χ^2 on track to ECAL cluster extrapolation is a signature for a photon candidate. The χ^2 distribution for electrons shows a clear peak for small values of χ^2 while a typical cut for photons is $\chi^2_\gamma > 4$ as shown in fig. 4.6 [39]. Photons are classified into three classes corresponding to three different variables: `PhotonID` (single photons), `MergedID` (merged π^0) and `PhotonFromMergedID` (split-photons). Those variables are computed by comparing the χ^2 of the photon, the energy in the PS and the energy of the seed with reference histograms and assigning a confidence level [71].

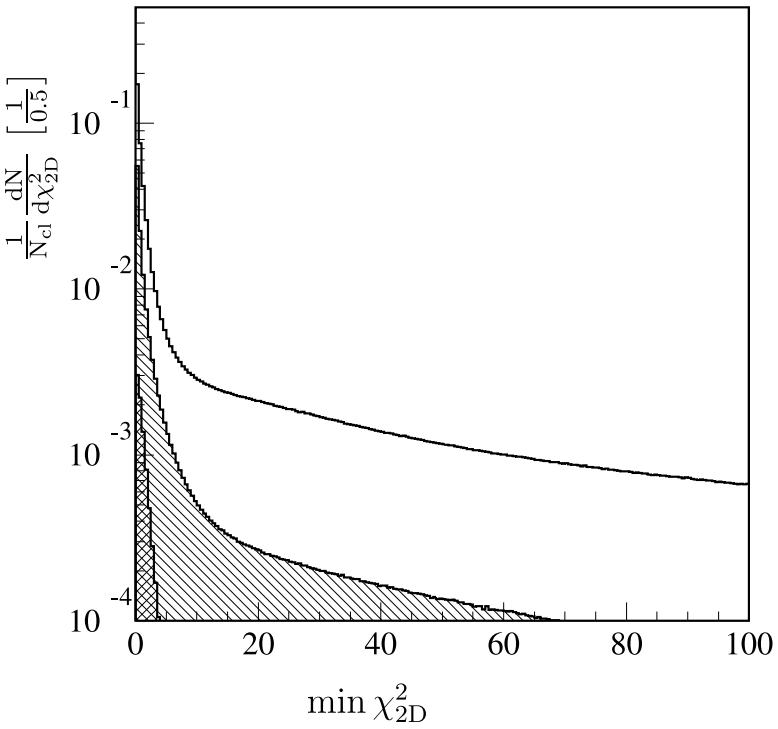

Figure 4.6 *χ^2 distribution for reconstructed clusters (empty histogram), tracks (dashed histogram) and MC electrons (crossed histogram) [72].*

π^0 reconstruction

Low energy π^0 are reconstructed from well separated photons while for pions with higher p_T, most of the photon pairs cannot be resolved as a two separated clusters within the ECAL granularity.

4.2 Monte Carlo simulation at LHCb

A detailed simulation is needed both to model the detector response and acceptance, and to understand background processes. The LHCb Monte Carlo software is split into Gauss and Boole [73] applications for simulation and digitization respectively. Gauss is split in multiple phases: event generation and tracking performed using Pythia [74], detector simulation using Geant4 [75] and radiative corrections using PHOTOS [76]. During the generation phase, proton-proton collisions are simulated reproducing the "real life" conditions happening in the LHC such as change of luminosity and the smearing of the interactions due to the longitudinal and transverse dimensions of the bunches [77]. Following the

generation phase, particles are tracked through the LHCb detector using Geant4. In fig. 4.7 the simulation of particles travelling inside RICH1 and RICH2 is shown.

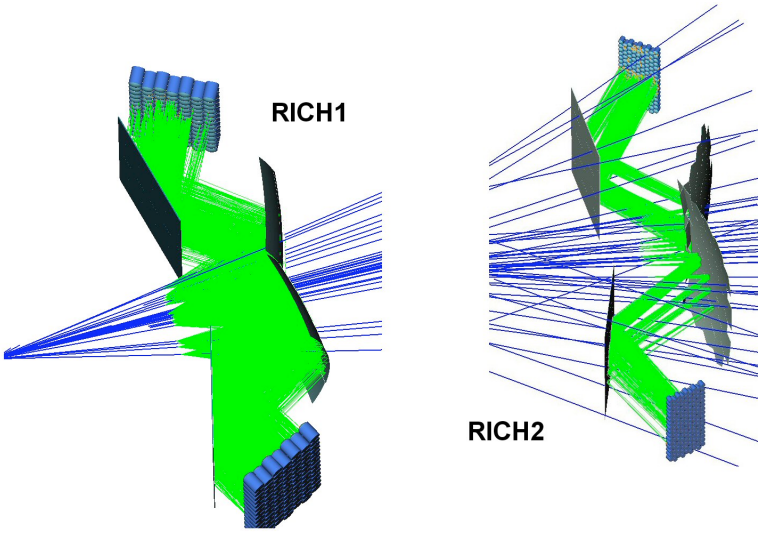

Figure 4.7 *RICH simulation [77] simulating the particles (blue lines) interacting with the detector and generating the Cherenkov photons (green).*

Only the information required to generate the detector output are saved. More detailed information such as Cherenkov photons (fig. 4.7) or the shower information in the calorimeter can be stored for special studies but are not included in the normal Monte Carlo production.

The Boole application simulates the detector and the readout electronics's response as well as the L0 output. It outputs data in the same format as that coming from the detector.

4.3 Event reconstruction with Brunel

Brunel [62] is the software application dedicated to the event reconstruction. It can process both collision data from the DAQ and simulation generated by Boole.

The reconstruction phase starts with clustering the hits in the trackers generating the input for the tracking pattern recognition software which perform a first estimate of the track trajectory without performing an accurate fit. After a preliminary track fit, a full Kalman filter [67] is performed as well as a *clone-killing* [78] step to remove duplicates where the hits from one particle are split between two tracks. The output of this phase is used as input to the calorimeter,

RICH and muon system reconstruction algorithms that provide PID information [77]. After the full reconstruction is performed, data are stored on tape using a custom file format, the Data Summary Tape (DST).

4.4 Offline analysis: stripping and DaVinci

The DST files generated by Brunel can be used for the analysis but they are not accessible to normal users due to computing restrictions [64]. An additional step of filtering called the stripping is performed before analysts access the data produced by the LHCb detector. The stripping procedure is carried out using DaVinci [63]. It outputs DST and μDST files in *streams* where events are grouped together by selection type. For example, the dimuon stream contains events with a muon pair.

The DaVinci application is used to read the DST and μDST and to generate the data set for analysis. DaVinci provides access to physical variables such as four vectors, vertices and PID information.

4.4.1 The Worldwide LHC Computing Grid

All the above steps need to be supported by a robust computing facility. When LHC started delivering data, the computational resources required were far beyond what was dedicated to the previous accelerators. Considering the technology available at that time, having a computing farm at CERN was impractical. For this reason a distributed solution adopting Grid technologies has been put in place. The Worldwide LHC Computing Grid (WLCG) was built on top of existing Grid infrastructures: OpenScience Grid (OSG) in USA and Enabling Grid for E-sciencE (EGEE) in Europe [79].

The WLCG has a three level hierarchical structure where each level performs different tasks:

- Tier 0: located at CERN. This is the place where data collected by the experiment are stored and distributed to the Tier 1 sites. Tier 0 is also responsible for the first reconstruction, the safe-keeping of raw data and data reprocessing during the LHC down-times.

- Tier 1: responsible to keep a fraction of raw and reconstructed data. There are 13 Tier 1 sites and they are also responsible of reprocessing, saving and distributing to Tier 2 large amount of data. Simulations are also produced.
- Tier 2: data analysis and simulation production and reconstruction. There are around 155 Tier 2 sites around the world.

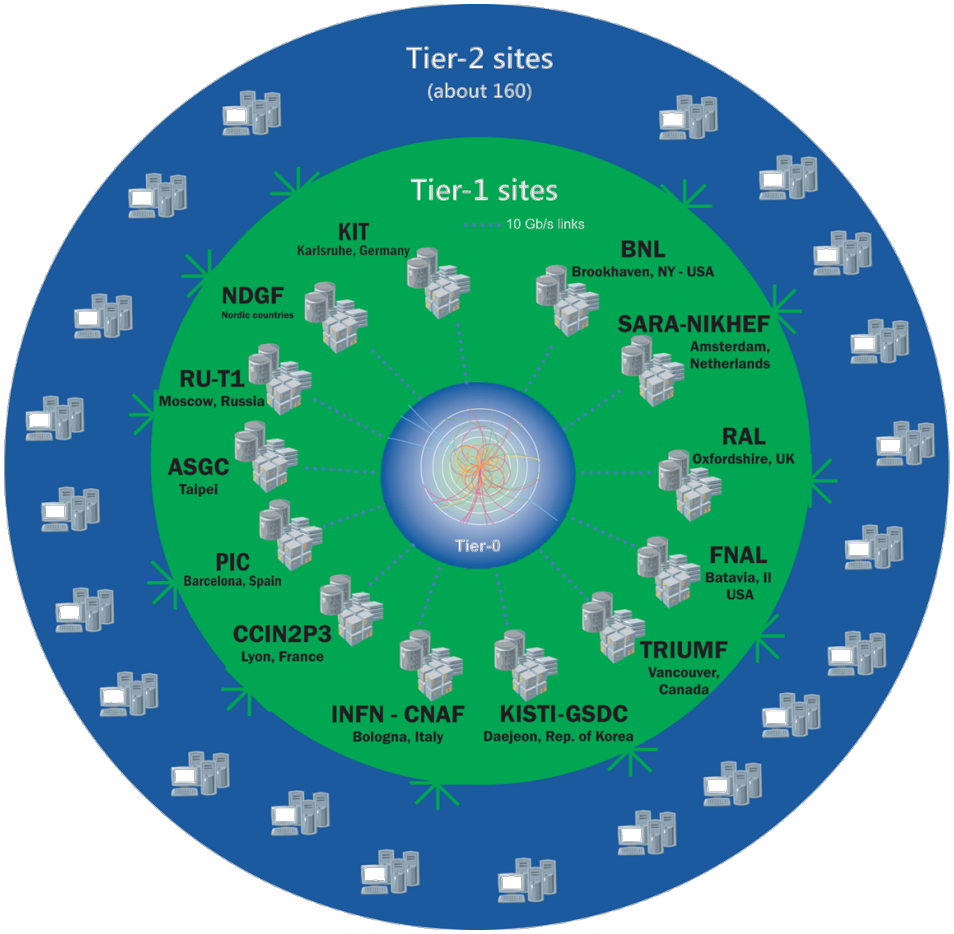

Figure 4.8 *WLCG Tier scheme [80]*

CERN and Tier 1 centers are responsible for processing the raw data with CERN storing the full data set and distributing a copy of it to the Tier 1 sites. The Tier 2 centers are mainly dedicated to Monte Carlo production using both CERN and Tier 1 sites as a repository for the simulated data [39]. The data set and Monte Carlo samples used in this thesis were reconstructed using the WLCG resources.

Chapter 5

HLT monitoring system

As described in section 3.2.6, the HLT is split in two stages, the first step runs HLT1, synchronous to the collisions delivered by the LHC writing its output to a local disk buffer. The second step, HLT2, asynchronously processes HLT1 output. Efficient monitoring of the data being processed by the HLT applications is critical to promptly diagnose detector or software problems. From Run 3, starting in spring 2022, the LHCb experiment will run in a trigger-less configuration where the detector will be read by the EFF at 30 MHz. The Run 3 HLT will have the same two-level configuration as in Run 2. With a fully software trigger, monitoring efficiently the data processed by the application is even more crucial due to the higher event rate.

This chapter presents the multi-level hierarchical structure of the Run 2 monitoring infrastructure as well as a prototype of a high-level transport layer based on commercial libraries emulating the HLT1 Run 3 workload.

5.1 The LHCb HLT monitoring infrastructure

Events rejected by the trigger are permanently lost. For this reason, detecting problems during the data taking is crucial. To achieve this, a small fraction of the HLT computing resources is assigned to generating monitoring histograms and counters. Since HLT applications are distributed on every server of the EFF, the monitoring information are scattered over the entire farm. This requires a system to collect, merge and publish them. Due to the different tasks and time

requirements of the HLT1 and HLT2, the Run 2 monitoring infrastructure has two separate implementations, one for each HLT stage.

5.1.1 HLT1

The HLT1 is the selection stage before the storage buffer. Therefore, it has to perform a fast decision to either accept an event and write it to disk or reject it. For this reason, the number of monitoring histograms and counters produced is limited. Monitoring information is generated on each HLT1 node by processing a fraction of the data acquired. The output of the HLT1 monitoring application is therefore scattered on the full EFF and it is in the form of "full histograms" containing all the metadata (axis, bin labels, titles, etc.). Those histograms and counters are then collected, merged and published using the DIM framework [81] as shown in fig. 5.2b. This is a well tested and widely used monitoring infrastructure system. It is made of three components: *Servers*, *Clients* and *Name Server*. Data are distributed as a service where the client has to register to the required service. The DIM infrastructure has a central server, the *Name Server*, where *Servers* register specifying the type of information to publish. *Clients* check with the *Name Server* if the required service is available and which address to look at. Once the *Name Server* delivers the information about the *Server*, *Client* and *Server* start a one-to-one communication, keeping the *Name Server* free, as shown in figs. 5.1 and 5.2a.

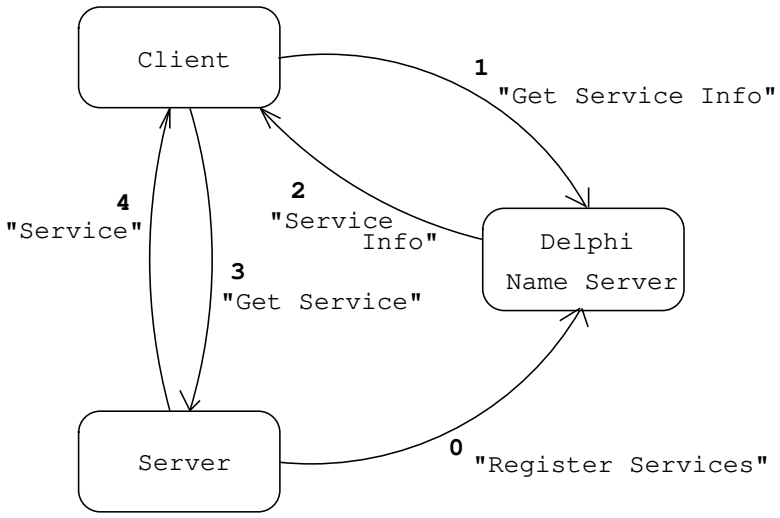

Figure 5.1 *DIM communication scheme [81]. Once a* server *comes online, it registers itself to the* name server *which makes it available to the* client*. The* client *can now request the service it requires, receiving the address of the* server *from the* name server*. After getting the coordinates of the* server*, the* client-server *communication can start, without involving the* name server*.*

If a client wants to access a missing or unavailable service, the *Name Server* takes care of it notifying the *Client* once the service is back online. In case the *Name Server* fails, due to the one-to-one nature of the transfer protocol, all the communications already started between *Client* and *Server* will not be interrupted. All the new requests for a service will need to be sent again once the *Name Server* comes back online.

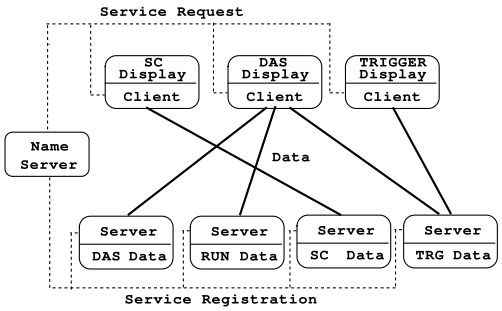

(a) *Scheme of how DIM distributes information from* Servers *to* Clients *[81].*

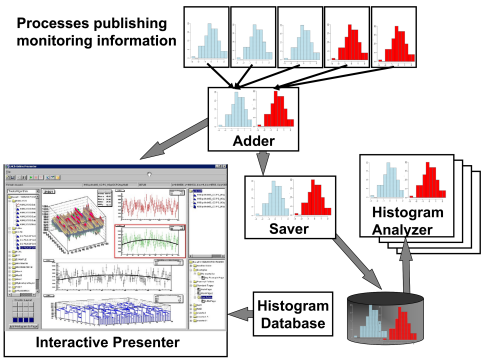

(b) *Scheme of histograms are collected, merged and published by DIM collecting [82].*

Figure 5.2 *Scheme of the DIM infrastructure implementation. Figure 5.2b shows how the histograms are processed and distributed while Figure 5.2a shows how* Servers *and* Clients *communicate with each other.*

5.1.2 HLT2

The HLT2 monitoring infrastructure is different to HLT1 since the number of histograms produced at this stage is much higher. It consists of around 50000 processes producing 4000 histograms each. This results in 200 million histograms that need to be aggregated for each of up to a hundred data taking intervals that are being processed simultaneously. Building the HLT2 monitoring infrastructure using DIM is not ideal due to the high bandwidth required by the protocol: moving full histograms with their metadata has a huge impact on the network. For this reason, a new infrastructure was built for the HLT2 monitoring. There are two main differences between the HLT1 and HLT2 monitoring infrastructures: the HLT2 monitoring system implements a hierarchical structure of the farm and it sends only the increments of the histograms. The structure of the farm is shown in fig. 5.3: the HLT2 nodes are grouped into *subfarms* each of which processes its part of the histograms sending the increments to a specific node in charge of merging all the histograms' fragments pushing them to the last layer of aggregation. Once all the histograms are merged, they are written to permanent storage.

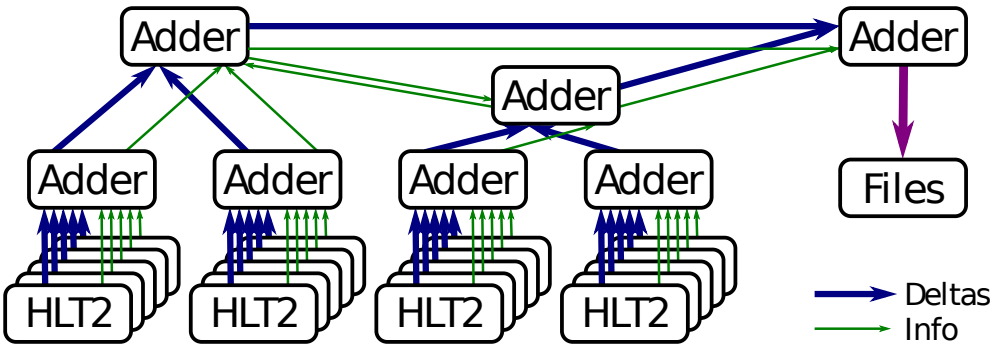

Figure 5.3 *Hierarchical scheme of the EFF: nodes are grouped in* subfarms *pushing the processed information to the next level of aggregation. The top layer of aggregation takes care of collecting all the fragments and to write the final histograms/counters to permanent storage [1]. The scheme shows the two different types of messages: deltas in blue (the increment in respect to the previous message) and info in green (metadata of the histograms/counters).*

Network bandwidth is minimized by sending histogram increments and only exchanging metadata when necessary, using a custom lightweight protocol based on `boost::serialize` [83]. The transport layer is implemented with ZeroMQ [84], which supports Inter-Process Communication (IPC) and Transmission Control Protocol (TCP) communication, queue handling, asynchronous request/response and multipart messages. Ports and interconnections in distributed systems such as the EFF are defined within ZeroMQ and then ZeroMQ takes care of determining the optimal routing and handling the queues using additional buffers. It adapts well to new hardware architecture supporting multithreaded applications using native Operative System (OS) threads. ZeroMQ also allows great flexibility offering a wide range of connection patterns as shown in Figure 5.4.

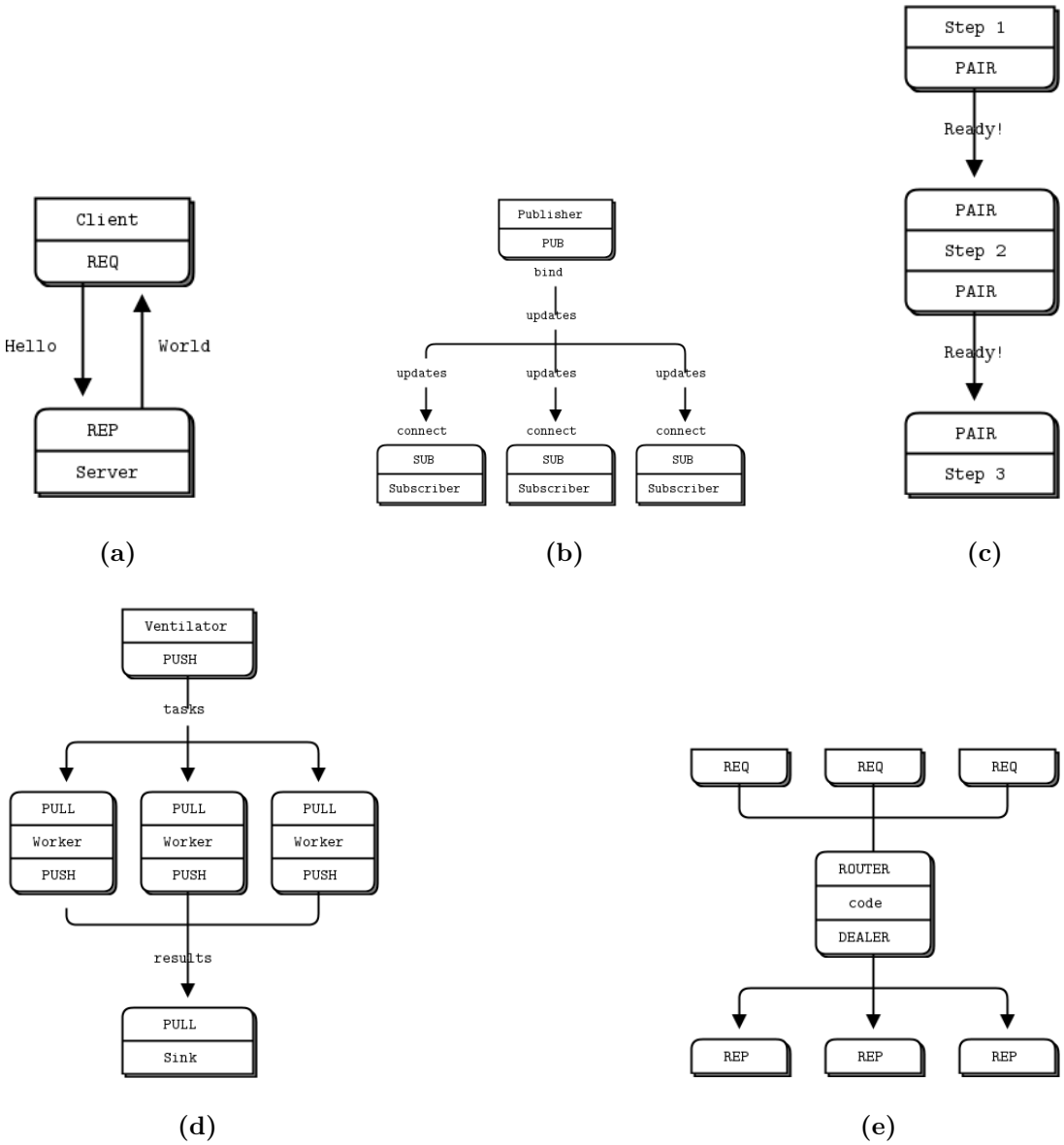

Figure 5.4 *ZeroMQ main connection patterns. Figure 5.4a shows a synchronous request between client and server. Figure 5.4b shows a publisher/subscriber scheme: the publisher sends information only to the services already subscribed to its service. Figure 5.4c exclusive pair: used in case of pairs of threads to coordinate them without interfering. Figure 5.4d shows a classic push-pull scheme: push will distribute the tasks to the clients while pull will queue the messages from all the connected clients. Figure 5.4e shows a non-blocking request-reply scheme where the router and the dealer take care of addressing the messages.*

In the HLT2 monitoring system, the *subfarm* nodes push the fragments and the info messages to the *subfarm adder* which, after collecting and merging all the

information, will push them to the *top level adder*. While ZeroMQ finds the best path to deliver the messages, the queue parameters require fine tuning in order to avoid dropping incoming messages due to a full queue. Finding the right parameters is not a trivial process and software simulating the farm workload was heavily used to optimize the queue parameters.

Performance measurements

Knowing the impact of the HLT2 monitoring system on the computing resource is important both to understand the impact of the monitoring system on the overall performance of the EFF and to provide a reference point for future developments. Though important, this type of measurement was not done before. In order to better measure the resources used by the HLT2 monitoring system, the test is performed running only the HLT2 monitoring applications on the EFF nodes. For 24 hours[1], network load and CPU/ram load from the *subfarm* adder were logged. Getting the load information from a *subfarm* adder gives a picture of the worse case scenario since it has to receive and merge all the fragments coming from all the nodes below it. Figure 5.5 shows the measurements highlighting that the node itself was running under low stress and the network was not under a high load. Demonstrating that the network load is low is a very important check since with the purely software trigger in Run 3 there will be a huge increase in network traffic.

[1]Due to some issue, RAM measurements were performed over 10 minutes only but it was still possible to reach the plateau.

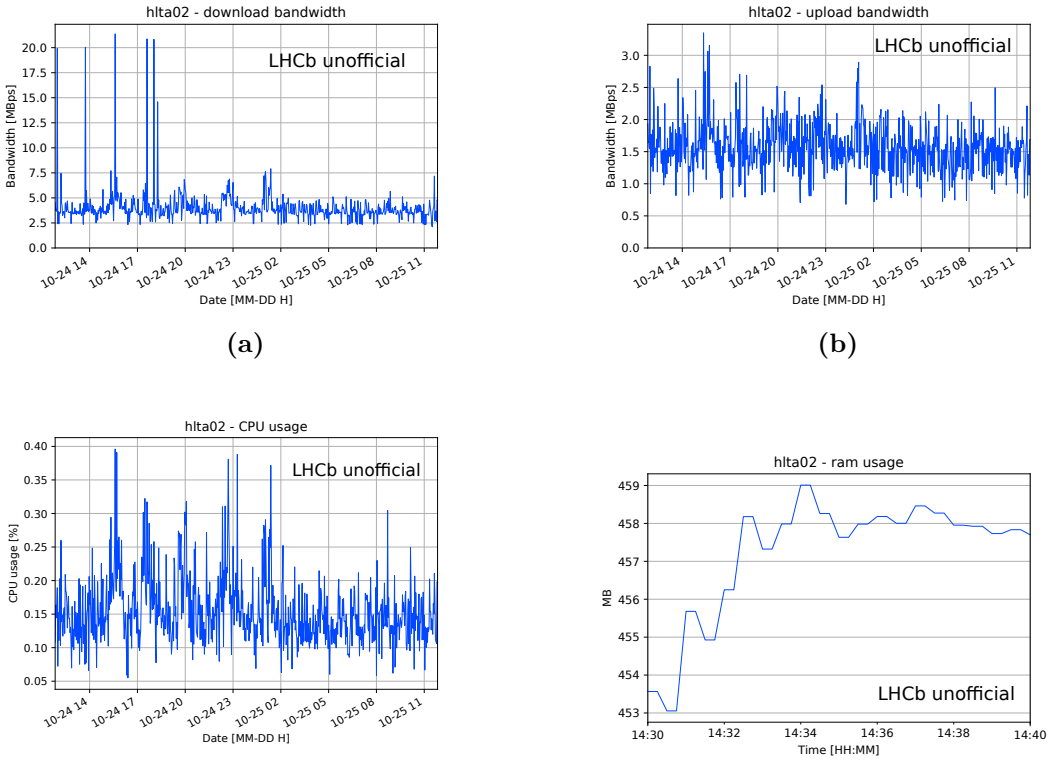

Figure 5.5 *Performance measurements for the HLT2* subfarm *adder. Figure 5.5a shows the download bandwidth, Figure 5.5b shows the upload bandwidth, Figure 5.5c shows the CPU usage and Figure 5.5d shows the RAM usage.*

5.2 Prototyping a monitoring system using Kafka

The need to prototype a new monitoring system starting from the HLT2 approach came after a deep analysis of the ZeroMQ system and its limits. In particular, it was decided to investigate using commercial streaming platforms taking care of the distribution of the data, including queue optimization. In this way, the only custom made part will be the messages. Among multiple streaming platforms, Apache Kafka was chosen [85] since it is already in use within the LHCb online team for logs and monitor [86]. Kafka is a distributed streaming platform that allows to publish and subscribe to streams of records. Kafka processes streams of records as they occur and stores records in a fault-tolerant way [85].

With Kafka, multiple clients are allowed to read from the same queue. This feature is very powerful since it allows to share the workload between different

machines. It also allows to quickly add additional instances, if needed.

5.2.1 Infrastructure and configuration

The prototype was hosted on the LHCb Online infrastructure Kubernetes' [87] pods and ConfluentKafka [88] was used to interact with it. This API allows very easy access to the queue for both pushing and reading the messages. Kafka has four core APIs, two of them are interesting for this project: producers, publishing messages into the queue and consumers, reading the messages from the queue. With a producer-consumer configuration, multiple producers were used to emulate the HLT nodes pushing the monitoring information inside the queue and a single consumer was used as a top level adder, collecting the monitoring information, merging them and publishing them. This configuration with multiple producers and a single consumer was chosen in order to test how many producers are needed in order to saturate a single consumer. For this reason the three level structure of the farm used for the Run 2 HLT2 monitoring system was not implemented.

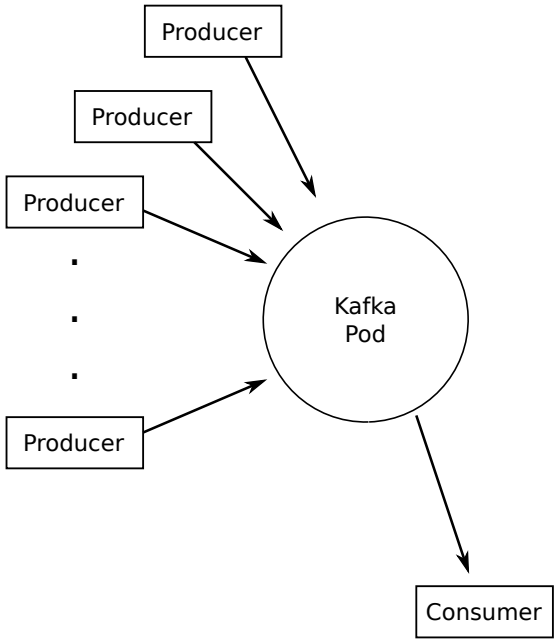

Figure 5.6 *Scheme of the prototype implementation: multiple producers send their messages to the Pod running Kafka, a single consumer reads from it [1].*

Message configuration

The target for this test is to have around 400 producers resembling the HLT1 case for Run3. Since the infrastructure was never tested before for this particular use, a reduced workload configuration was chosen, emulating a HLT1 task instead of HLT2. Each producer sends:

- 10 KB/s to emulate $\sim$ 1000 counters
- 100 KB/10s to emulate $\sim$ 100 1D histograms
- 10 MB/60s to emulate multiple 1D and 2D histograms

Due to the threshold Kafka puts on the message size, the 10 MB message was split into 50 parts which were sent sequentially, one after the other.

5.2.2 Send and receive

The main focus of the prototype is to test the streaming platform, not the messages, therefore synthetic messages are generated and sent. Future implementations will deliver real histograms and counters instead of random generated ones. Messages were generated by the senders, filled with a random payload and sent using Kafka. From the receiver side, every time a message is received, its content is decoded, the ID of the corresponding histogram is calculated and the hash of the payload is performed in order to simulate the histogram aggregation.

5.2.3 Tests

The prototype was first tested on a single machine running consumer, producer and the Kafka instance. After that, the entire test was moved to multiple machines connected to the same Kafka instance as shown in fig. 5.6.

The first test in this configuration was to check the integration with the instance provided by LHCb Online performing a stress test with multiple producers fig. 5.7 shows a twelve hours stress test with the first six hours running a $\sim$ 200 producers-single consumer configuration and the last six hours with a $\sim$ 400 producers-single consumer configuration.

The stress test demonstrates the system performs well under a heavy load. In particular, a single consumer was able to handle a HLT1-like load (203 producers configuration) without any problems. It also showed that it can handle an even higher stress condition without intermediate aggregation level, with a 406 producers configuration. This particular configuration, increases the stress on the network, with the output throughput hitting 220 MB/s. Future implementations of the prototype will run with multiple consumers sharing the workload and a top-level consumer reading the consumers' output and merging it. This configuration will benefit from Kafka as well. Another Kafka instance collecting the first level of aggregation together with a top level consumer will perform the same operations as the consumer used in this prototype.

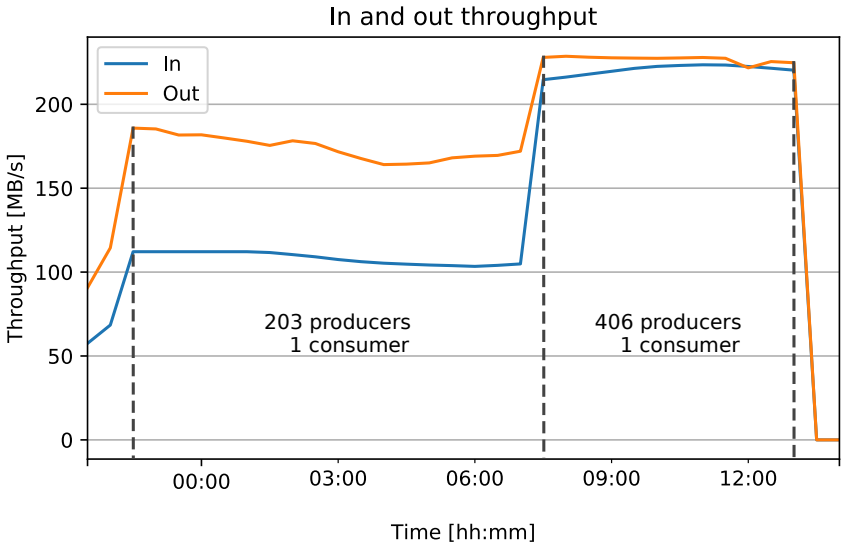

Figure 5.7 *Throughput measurement of the Kafka queue. In blue the incoming messages, in orange the outgoing messages. Two configurations were tested and the difference is clearly visible at ∼ 7:30 where the throughput increases by a factor two. During the first part of the test, the prototype was running with 203 producers and a single consumer. In the second part, the number of producers was increased to 406 keeping only a single consumer. The difference between input and output throughput is due to protocol overhead and it is under investigation [1].*

After verifying that the system could handle a high load for a prolonged amount of time, resilience to failures was tested. During data taking it is common to have failures in the computing infrastructure (both hardware and software). Having a queue system that quickly adapts to such issues it is a crucial part for a reliable monitoring system. Due to the multiple producers-single consumer configuration,

the test is performed switching off the consumer which is the single point of failure of the entire system. In this way, the queue will start filling-up with messages and, once back online, the consumer will need to catch-up with the not-processed messages in the queue. This test was performed assuming a failure in the Kafka instance is recovered within five minutes therefore the consumer was shut down for five minutes. There are two major points to verify: if the Kafka instance can handle non-consumed messages for five minutes and, once the consumer is back, if the consumer can catch up with the producers, increasing the output throughput.

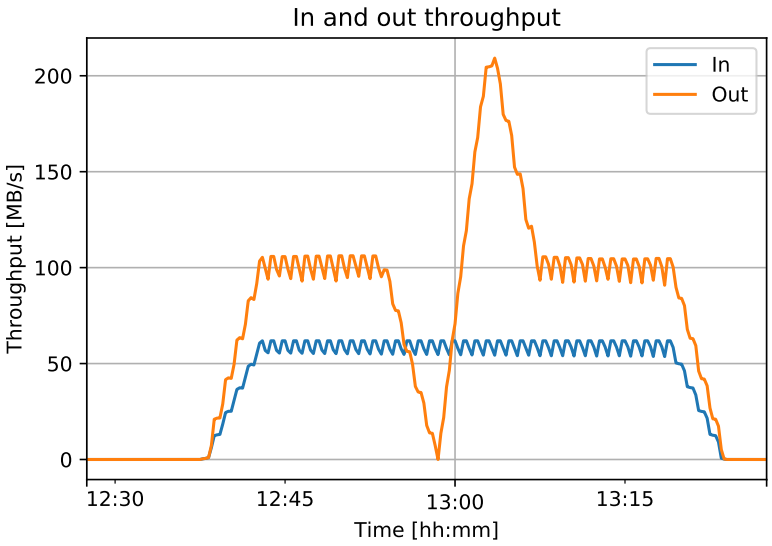

Figure 5.8 *Throughput measurement of the Kafka queue. In blue the incoming messages, in orange the outgoing messages. The producers input messages for the entire test while the consumer was stopped for 5 minutes between ∼ 12:50 and ∼ 13:00. Once the consumer is back, the throughput increases above the 100MB/s level in order to empty the queue and catch-up with the producers. Once the queue is emptied, the output throughput levels down to the initial value. This test was performed with 105 producers and a single consumer. The difference between the input and output throughput is due to protocol overhead and it is under investigation [1].*

In fig. 5.8 the failure of the consumer is simulated. The configuration used in this test is with 105 producers and a single consumer. The system was left running for a few minutes in order to achieve a steady state. After reaching a stable configuration with the input and output throughput stable at ∼ 60 MB/s and ∼ 100 MB/s respectively, the consumer was shut down for five minutes. Once the consumer was brought back online, it starts catching-up with the producers

by increasing the output throughput. This is clearly seen in fig. 5.8. Between 12:55 and 13:00 the consumer was switched off and the output throughput drops to zero. Then around 13:00 the consumer is brought back online and the output throughput increases up to 200 MB/s in order to empty the queue. Once the producer consumed all the unprocessed messages, the system goes back to a steady state as before the failure test.

In fig. 5.8 is possible to see two additional features: periodical spikes due to the 10 MB/60s messages and slow changes in the output throughput when the consumer is switched on and off due to averaged measurements.

Tests performed on the prototype showed that it is well integrated in the Kafka instance provided by the LHCb Online infrastructure and it can handle a HLT1-like workload with a single node reading all the monitoring information delivered by the HLT1 machines. It also showed effective recovery in response to a failure. This feature is fundamental because, in case of problems, it gives time either to restart the consumer or to create a new one. Future implementations will resemble the workload required by HLT2. In order to lower the input throughput on the consumer, a configuration with multi level aggregation will be implemented and tested.

Chapter 6

Signal selection and background study

This chapter describes how data collected by LHCb is processed to select events that include $B_s^0 \to J/\psi\eta'$ and $B_s^0 \to J/\psi f_0$ decays and to understand the background of these decays. The development of a supervised classifier to distinguish between the signal and the background is also discussed.

6.1 Data set and signal selection

In this analysis the full data set recorded by the LHCb detector between 2011 and 2018 is used. In table 6.1 the integrated luminosity and the beam energy for each year of running is shown.

Year	Integrated luminosity [fb^{-1}]	Energy [TeV]
2011	1.0	7
2012	2.0	8
2015	0.30	13
2016	1.6	13
2017	1.7	13
2018	2.1	13

Table 6.1 *Integrated luminosity and beam energy for Run 1 and Run 2 [89].*

Candidates considered for this analysis must pass a set of trigger lines that are chosen so as not to bias the lifetime. At the L0 trigger level, no explicit trigger requirement is applied. However, the majority of events ($\sim$ 83.6%) in Monte Carlo samples are TOS on the `L0Muon` or `DiMuon trigger`.

At the HLT level, both the $B_s^0 \to J/\psi\eta'$ and the $B_s^0 \to J/\psi f_0$ candidates are selected by inclusive triggers, designed to identify the $J/\psi \to \mu^+\mu^-$ decay. The list of triggers used is summarized in table 6.2 while a description of each trigger line can be found in section 3.2.6.

Trigger stage	Particle	Name
L0	B_s^0	`L0Global_Dec`
HLT1	J/ψ	`Hlt1DiMuonHighMassDecision_TOS`
HLT2	J/ψ	`Hlt2DiMuonDetachedJPsiDecision_TOS`

Table 6.2 *List of triggers used in this analysis.*

After passing the trigger selection, additional cuts are applied at the stripping level using the `FullDSTDiMuonJpsi2MuMuDetachedLine` line. This line reconstructs a J/ψ by selecting a pair of muons with high transverse momentum and with invariant mass within 100 MeV/c^2 of the nominal J/ψ mass. It also applies loose requirements on the quality of the vertex and the decay length significance. In table 6.3 the cuts applied at the stripping level are summarized. The only cut that biases the reconstructed lifetime distribution is the DLS cut.

Cut	Value
$p_T\,(\mu^\pm)$ [MeV/c]	500
Decay Length Significance [σ]	< -3 `OR` > 3
$\lvert m\,(\mu^+\mu^-) - m\,(J/\psi)\rvert$ [MeV/c^2]	< 100
PID (μ)	> 0.0
$\chi^2_{\rm vx}\,(\mu^+\mu^-)$	< 20

Table 6.3 *Cuts applied in the stripping selection.*

In the next sections, the cut based pre-selection, vetoes against specific backgrounds and MVA requirements are discussed. The same selection was applied to the Monte Carlo sample used to model the background and as signal sample for the multivariate analysis. In table 6.4 the Monte Carlo samples used in the analysis are listed. The samples are split across the years of running.

Decay	Events generated	Year
$B_s \to J/\psi\eta'$	13×10^6	Run 1 + Run 2
$B_s \to J/\psi\phi\,(\pi^+\pi^-\pi^0)$	2×10^6	2016
$B^0 \to J/\psi\pi^+\pi^-$	3×10^6	2016
$B_s \to J/\psi\pi^+\pi^-$	10×10^6	2016
$B^0 \to J/\psi K^+\pi^-$	1×10^6	2016
$B^0 \to J/\psi X$	10×10^6	2016
$B_s \to J/\psi\eta'\,(\eta\pi^+\pi^-)$	1×10^6	2016
$B_s \to J/\psi\phi\,(K^+K^-)$	2×10^6	2016
$B_s \to J/\psi X$	10×10^6	2016
$B^+ \to J/\psi K^+$	5×10^6	2016
$B^+ \to J/\psi X$	11×10^6	2016

Table 6.4 *Monte Carlo samples used in this analysis.*

6.1.1 Pre-selection

After the trigger and stripping selection, additional cuts are applied to remove combinatorial background and specific background from partially reconstructed b-decays. Both decay channels have common requirements to select a B_s^0 decay and good quality of tracks and vertices. Loose cuts on PID and ghost probability variables are applied to reject misidentified particles and ghost tracks. Only photons with $p_T\,(\gamma) > 500$ MeV/c are selected in order to reduce combinatorial background. A loose cut is also applied on the χ^2_{IP} of the B_s^0 candidate and the B_s^0 vertex χ^2 (computed requiring mass constraints on the J/ψ and η'). To select a B_s^0 decay, a mass window on the reconstructed candidate invariant mass is applied as well as checks on the quality of the reconstructed vertex. Finally, a lower cut on the B_s^0 decay time is made at 0.5 ps to reduce combinatorial background due to particles produced in the proton-proton interaction and to select a time range where the acceptance is flat (section 7.3.1). In fig. 6.1 mass distribution of the reconstructed $J/\psi\eta'$ decay after the pre-selection cuts is shown.

Cut	η'	$f_0\,(980)$
$\mu^{\pm}_{\text{ghost}}$	< 0.2	
$\mu^{\pm}_{\text{PROBNNmu}}$	> 0.2	
$\lvert m\,(\mu^+\mu^-) - m\,(J/\psi\,(1S))\rvert\,[\text{MeV}/c^2]$	< 50	
$\pi^{\pm}_{\text{ghost}}$	< 0.2	
$\pi^{\pm}_{\text{PROBNNpi}}$	> 0.2	
$\pi^{\pm}_{\text{PROBNNp}}$	< 0.7	
$\pi^{\pm}_{\text{PROBNNk}}$	< 0.7	
$\lvert m\,(\rho^0\gamma) - m\,(\eta')\rvert\,[\text{MeV}/c^2]$	< 50	
$p_T\,(\eta')\,[\text{MeV}/c]$	> 2000	
$p_T\,(\gamma)\,[\text{MeV}/c]$	> 500	
CL_γ	> 0.2	
$\tau_{B_s}\,[\text{ps}]$	> 0.5	
$\chi^2_{\text{ip}}\,(B_s)$	< 25	
$\chi^2_{\text{vx}}\,(B_s)$	< 4	
$m\,(B_s)\,[\text{MeV}/c^2]$	$\in (4900, 5700)$	
$m_{\text{DTF}}\,(J/\psi\;\eta')\,[\text{MeV}/c^2]$	$\in (5150, 5650)$	
$m\,(J/\psi\;\eta')\,[\text{MeV}/c^2]$	$\in (5000, 6500)$	
$\chi^2_{\text{DTF}}\,(J/\psi\;\eta')$	> 0	
$\chi^2_{\text{DTF}}\,(J/\psi\;\eta')$	< 4	
$m\,(\pi^+\;\pi^-)\,[\text{MeV}/c^2]$	$\in (600, 900)$	
$\text{ADOCACHI2CUT}\,(\rho^0 \to \pi^+\pi^-)$	< 30	
$\chi^2_{\text{vx}}\,(\rho^0)$	< 20	
$\lvert m\,(\pi^+\;\pi^-) - m\,(f_0\,(980))\rvert\,[\text{MeV}/c^2]$		< 90
$\text{ADOCACHI2CUT}\,(f_0\,(980) \to \pi^+\pi^-)$		< 30
$\chi^2_{\text{vx}}\,(f_0\,(980))$		< 20
$m\,(J/\psi\;f_0\,(980))\,[\text{MeV}/c^2]$		$\in (5000, 6500)$
$m_{\text{DTF}}\,(J/\psi\;f_0\,(980))\,[\text{MeV}/c^2]$		$\in (5150, 5650)$
$\chi^2_{\text{DTF}}\,(J/\psi\;f_0\,(980))$		> 0
$\chi^2_{\text{DTF}}\,(J/\psi\;f_0\,(980))$		< 5
$p_T\,(\pi^+) + p_T\,(\pi^-)\;\;[\text{MeV}/c]$		> 1000

Table 6.5 *Pre-selection cuts for signal and normalization modes. This selection was applied after the stripping one. The ADOCACHI2CUT function applies a χ^2 cut on the tracks of the daughter particles [90].*

Year	Events before pre-selection	Events passing the pre-selection
2011	158301	18072
2011	390721	42267
2015	280141	22949
2016	1666742	161026
2017	1329703	136599
2018	1447902	143007

Table 6.6 *Summary of the number of events passing the pre-selection for the $B_s^0 \to J/\psi\eta'$ channel.*

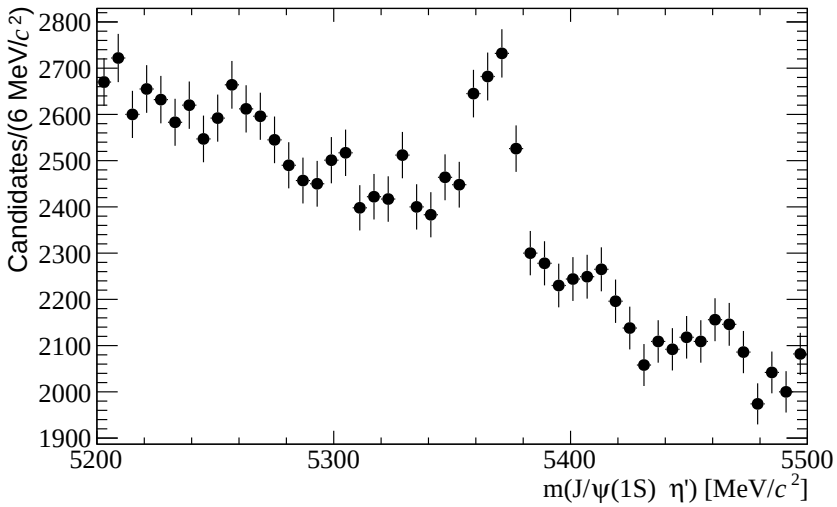

Figure 6.1 *Mass distribution for the 2016 $B_s^0 \to J/\psi\eta'$ after applying the pre-selection cuts.*

6.2 Backgrounds

Several sources of background are present in the data sample. *Combinatorial background* is generated by selecting particles that do not originate from the signal decay. This type of background is reduced by the cuts listed in table 6.5 and the subsequent multivariate analysis. It has a monotonic distribution in mass. The other sources of background are *peaking backgrounds*. These are generated when other b-decays are reconstructed as the signal decay mode due to particle misidentification. The characteristic of these background components is the presence of a peaking structure in the invariant mass distribution. In the following sections, possible sources of peaking background are presented together with the strategy to veto them.

6.2.1 $B_s^0 \to J/\psi\eta'$ peaking background study

Various sources of peaking background are considered as described below.

$B^0/B_s^0 \to J/\psi\pi^+\pi^-$

Fully reconstructed $B^0 \to J/\psi\pi^+\pi^-$ and $B_s^0 \to J/\psi\pi^+\pi^-$ decays will be mistaken for signal if, once combined with a random photon, they match the η' selection criteria (fig. 6.2). To remove background from this source, if $m\,(J/\psi\pi^+\pi^-) > 5249$ MeV/c^2 the candidate is rejected. This cut reduces this background by an order of magnitude whilst retaining more than 99% of the signal (table 6.7). As shown in fig. 6.3, the peaking structure in the $J/\psi\pi^+\pi^-$ invariant mass is removed by the veto.

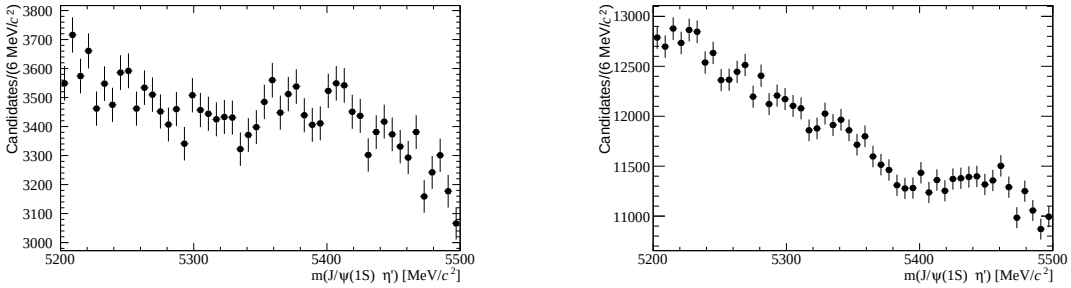

(a) **(b)**

Figure 6.2 *Reconstructed $J/\psi\eta'$ mass from 2016 Monte Carlo background samples: fig. 6.2a shows the $B^0 \to J/\psi\pi^+\pi^-$ Monte Carlo, fig. 6.2b shows the $B_s^0 \to J/\psi\pi^+\pi^-$ Monte Carlo. Only stripping and loose selection cuts applied.*

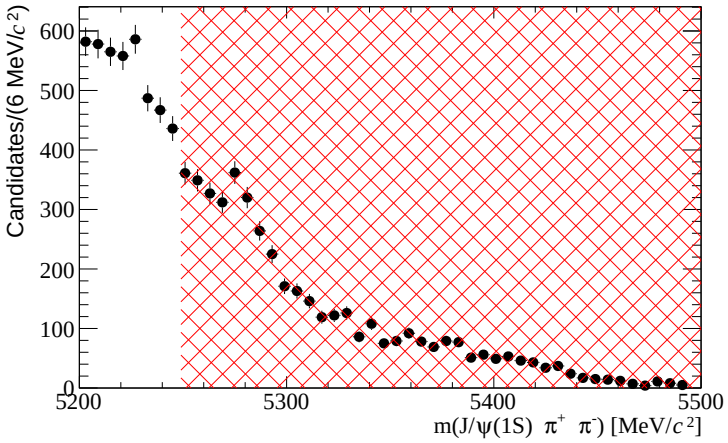

Figure 6.3 *Reconstructed $J/\psi\pi^+\pi^-$ mass from 2016 data sample. The red (hatched) area highlights the region removed by the veto.*

$B_s^0 \to J/\psi\,(\phi \to K^+K^-)$

This decay is selected when both kaons are wrongly reconstructed as pions and a random photon is added. This decay is greatly reduced by the PID cuts applied at the selection level (see table 6.5). Since no peaking structure is seen in the reconstructed $J/\psi K^+K^-$ mass (fig. 6.4), no veto is applied

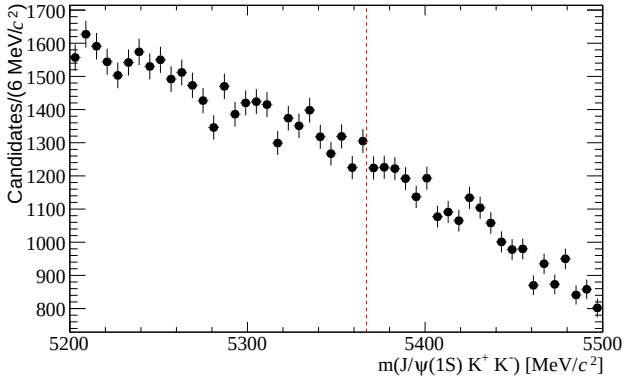

Figure 6.4 *Reconstructed $J/\psi K^+K^-$ mass in 2016 data sample. The B_s^0 mass is highlighted with the red dotted line: no evident peaking structure is present around the B_s^0 mass.*

$B^0 \to J/\psi\,(K^{*0} \to K^+\pi^-)$

This decay is selected if the kaon is misidentified as a pion and a random photon is added. Since only one of the two particles is misidentified, there are two possible

combinations. When building the veto for this decay, both combinations were taken into account. To veto this component, both the $K^+\pi^-$ and $J/\psi K^+\pi^-$ invariant masses and the PID information are considered. If $m\left(J/\psi K^+\pi^-\right)$ is within 35 MeV/c^2 of the nominal B^0 mass value and the $K^+\pi^-$ mass is within 50 MeV/c^2 of the K^{*0} mass, no candidate is selected. If $m\left(J/\psi K^+\pi^-\right)$ is within 30 MeV/c^2 of the PDG value of the B^0 mass, a tighter PID cut is applied, requiring `ProbNNk` for both pions to be smaller than 0.5 and `ProbNNpi` for both pions to be greater than 0.4. This veto combined with the selection in table 6.5 removes $\sim$ 87% of the background from this source while keeping 98% of the signal in the simulation. In fig. 6.5 the invariant mass of the $J/\psi K^+\pi^-$ system, after applying the veto, is shown. No evident peaking structure is present.

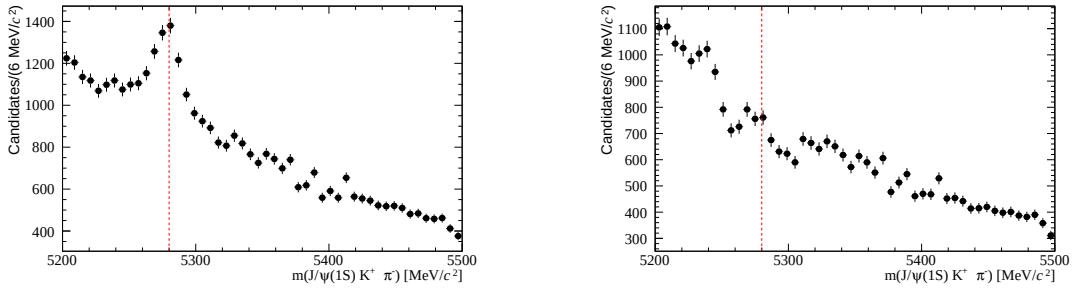

(a) **(b)**

Figure 6.5 *Reconstructed $J/\psi K^+\pi^-$ mass from 2016 data sample: before veto (left) and after veto (right). The red dashed line shows the B^0 mass value from the PDG.*

$B^+ \to J/\psi K^+$

This decay can be selected by misidentifying the kaon as a pion and adding a random pion and photon. This background is strongly suppressed by the veto described in section 6.2.1. Figure 6.6 shows the invariant mass of the $J/\psi K^+$ system after applying the vetoes. Around 95% of the $B^+ \to J/\psi K^+$ decay is removed.

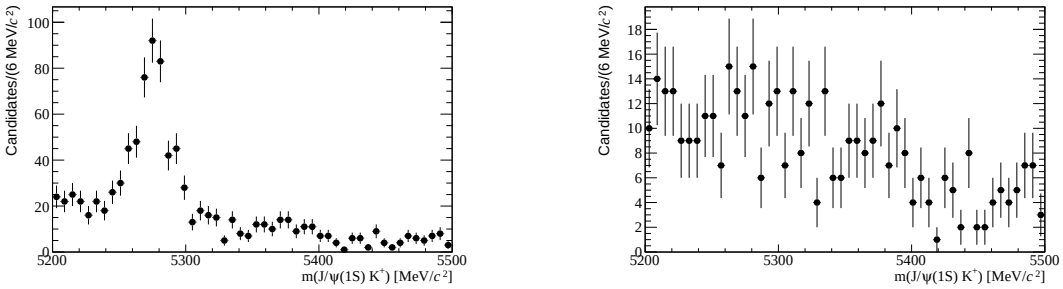

(a) **(b)**

Figure 6.6 *Reconstructed $J/\psi K^+$ mass from 2016 data sample: before veto (left) and after veto (right).*

$B_s^0 \to J/\psi\,(\phi \to \pi^+\pi^-\pi^0)$

This decay mode is selected when the two charged pions, combined with one of the photons coming from the neutral pion, passes the η' selection. The selection cuts in table 6.5 remove $\sim 86\%$ of the background component while keeping most of the signal. In particular, the most effective cuts are the mass window around the nominal value of the η' mass, the $p_T\,(\eta')$ cut and by the $p_T\,(\gamma)$ cut. To further reduce this background component, a similar approach to [91] is followed. The η' has helicity 0 since it is a pseudoscalar meson while the ρ^0 can have three helicity states $(\pm 1, 0)$. The photon has helicity ± 1 since it is a massless vector boson. Therefore, in the $\eta' \to \rho^0\gamma$ decay, the ρ^0 meson must have non-zero helicity. For this reason, the angular distribution of the pions coming from the decay $\eta' \to \rho^0\gamma$ is different to the distribution for this background. After comparing signal and background Monte Carlo distributions (fig. 6.7), a cut on $|\cos\left(\angle\left(\pi^+\pi^-\right)\right)| < 0.9$ was applied to reduce the background from this source. The $|\cos\left(\angle\left(\pi^+\pi^-\right)\right)|$ variable is also used as training variable in the MVA. This cut, removes an additional 12% of background from this source.

Component	Signal efficiency [%]	Veto efficiency [%]
$B^0 \to J/\psi\pi^+\pi^-$	99.4	92.2
$B_s^0 \to J/\psi\pi^+\pi^-$	99.4	90.6
$B^0 \to J/\psi K^+\pi^-$	98.0	87.2

Table 6.7 *Peaking background veto efficiencies. Signal efficiency is the amount of signal remaining after the selection cuts and the given peaking background veto. Background removal is the percentage of background removed by the veto and selection cuts, tested on the background Monte Carlo sample reconstructed as the $B_s^0 \to J/\psi\eta'$. In both cases, the selection cuts are the ones listed in table 6.5.*

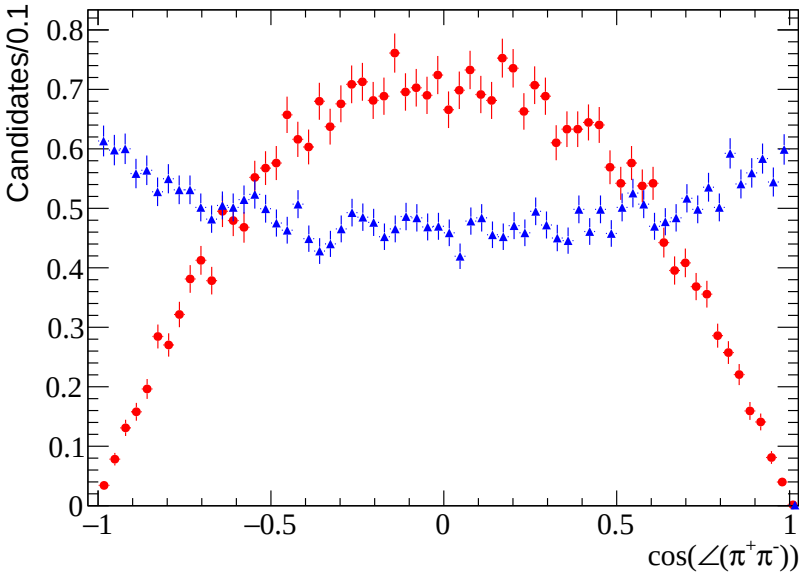

Figure 6.7 $\cos(\angle(\pi^+, \pi^-))$ *from 2016 Monte Carlo: the blue triangles are the background Monte Carlo* $\left(B_s^0 \to J/\psi\left(\phi \to \pi^+\pi^-\pi^0\right)\right)$ *while the red dots are the* η' *Monte Carlo sample.*

6.2.2 $B_s^0 \to J/\psi f_0$ background study

The peaking backgrounds considered in the $B_s^0 \to J/\psi f_0$ mode are discussed below.

$B^0 \to J/\psi K^+\pi^-$

This decay is selected when the kaon is reconstructed as a pion. It is suppressed by the PID requirements and a similar veto to that used for the η' mode in

section 6.2.1 is applied. This reduces background from this source by a further factor of two. A component to model the remaining background from this source is included in the fit (see section 7.2.1).

$B^+ \to J/\psi K^+$ **and** $B^+ \to J/\psi \pi^+$

The $B^+ \to J/\psi K^+$ decay is selected when a kaon is reconstructed as a pion and a random pion is added, satisfying the selection criteria for the f_0. These backgrounds are suppressed by rejecting any candidate where either of the two possible $J/\psi K^+$ or $J/\psi \pi^+$ mass combinations is within ± 30 MeV/c^2 of the nominal B^+ mass [92]. The K^+ is reconstructed from the pion with the highest `ProbNNk` while the π^+ is the pion with the lowest `ProbNNk`. The efficiency of this veto is tested on the inclusive Monte Carlo samples and found to remove $\sim 66\%$ of background events from these source. A component for these decay modes will be added into the mass fit model (see section 7.2.2).

$B_s^0 \to J/\psi\,(\eta' \to \pi^+\pi^-\gamma)$

This decay mode is selected if the photon is not reconstructed. No veto is applied but it is modeled and included as background component in the mass fit (see section 7.2.2).

6.2.3 Signal samples after vetoes

In fig. 6.8 the mass spectra for the η' and f_0 channels in the 2016 data set after applying the pre-selection cuts and peaking background vetoes are shown.

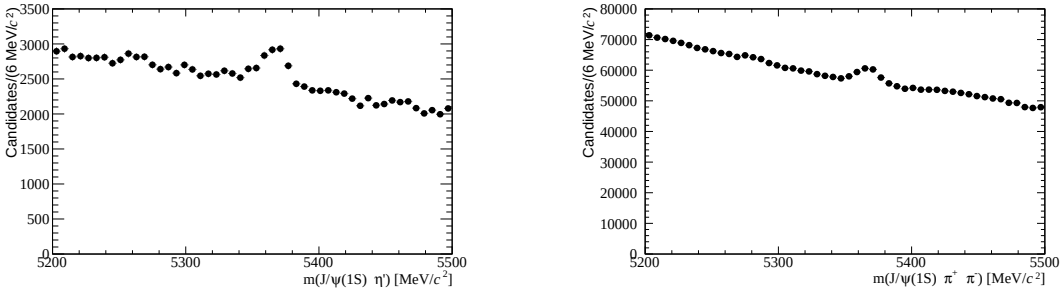

(a) *$J/\psi\eta'$ mass, η' channel* **(b)** *$J/\psi\pi^+\pi^-$ mass, f_0 channel*

Figure 6.8 *Mass spectrum from 2016 data for both channels after the pre-selection cuts. All the selection cuts and peaking background vetoes were applied.*

Though peaks are seen at the B_s^0 mass, the combinatorial background remains high. Therefore the last step of the selection is to reduce the combinatorial background with a MVA.

6.3 MVA

To further reduce the combinatorial background, a multivariate classifier is used for both modes. The TMVA [93] toolkit was chosen to perform the classification. Several possible classifiers were considered and the Gradient Boosted Decision Tree (BDTG) chosen as it gave good performance and excellent signal-background separation (fig. 6.10). Separate classifiers were trained for the two channels in order to profit from the information of the photon available in the η' channel. In both cases, signal Monte Carlo and the high mass side-band from data are used for training. To reduce possible biases introduced by the different detector configurations for each year, four MVAs are trained: Run 1, 2015 and 2016 combined, 2017 and 2018.

6.3.1 Training

Before training, several corrections were made to the simulation sample to better match the data in terms of the kinematics and multiplicity. These are described in appendix A and appendix B.

Training samples

A supervised classifier needs a training sample for each category. In this case, a sample for the signal and one for the background are needed. For this analysis, the truth-matched Monte Carlo simulation sample is used as the signal sample and the *high-mass side-band* $(m\,(J/\psi\eta')_{\eta'};\, m\,(J/\psi\pi^+\pi^-)_{f_0} \in (5500-5650)\ \mathrm{MeV}/c^2)$ is used as the background sample.

Training variables

In selecting variables to be included in the MVA, care was given to chose variables that do not bias the lifetime distribution and that agree between data and Monte Carlo. In table 6.8 and table 6.9 the training variables used for both channels are listed. Since the work is focused on a relative measurement, the similar training variables were used for both channels. Both MVA algorithms were trained on the transverse momentum of the particles, the quality of the primary vertex fit, the isolation of the B_s^0 (appendix D), number of clusters in the TT and pseudorapidity of the B_s^0. For the η' MVA, photon information is also included in the training: the transverse momentum and the confidence level of the photon. Comparisons between data and Monte Carlo for the variables which are input to the MVA can be found in appendix E.

Variable name	Description
$\eta\left(B_s^0\right)$	B_s^0 pseudorapidity
$\chi^2_{\mathrm{DTF}}\left(B_s^0\right)/\mathrm{nDOF}$	Quality of the B_s^0 DTF fit
$p_T\left(B_s^0\right)$	B_s^0 transverse momentum
$\min\left(p_T\left(\pi_1\right), p_T\left(\pi_2\right)\right)$	Minimum of the pions transverse momentum
$\max\left(\mathrm{ghost}_{\mu_1}, \mathrm{ghost}_{\mu_2}\right)$	Maximum of the muons ghost probability
$\min\left(p_T\left(\mu_1\right), p_T\left(\mu_2\right)\right)$	Minimum of the muons transverse momentum
0.5 (Bs_1.80_cc_deltaEta + Bs_1.80_nc_deltaEta)	Average of the B_s^0 - cone difference in eta
Bs_1.80_cc_mult	Number of objects in the cone
Bs_1.80_cc_asy_PZ	Z components of the momentum asymmetry
Bs_1.80_cc_vPT	Vector-summed PT of the objects inside the cone
Bs_1.80_nc_deltaPhi	Difference in phi between the B_s^0 and the cone
CL_γ	Confidence level of the photon
$p_T\left(\gamma\right)$	Transverse momentum of the photon
$\cos\left(\angle\left(\pi_1, \pi_2\right)\right)$	Cosine of the helicity of the pions
$p_T\left(\eta'\right)$	η' transverse momentum
Bs_IPCHI2_OWNPV	Quality of the B_s^0 fit
TT occupancy	TT occupancy
nPi0R	π^0 veto

Table 6.8 *Training variables for the $B_s^0 \to J/\psi\eta'$ MVA.*

Variable name	Description
$\eta\left(B_s^0\right)$	B_s^0 pseudorapidity
$\chi^2_{\mathrm{DTF}}\left(B_s^0\right)/\mathrm{nDOF}$	Quality of the B_s^0 DTF fit
$p_T\left(B_s^0\right)$	B_s^0 transverse momentum
$\min\left(p_T\left(\pi_1\right), p_T\left(\pi_2\right)\right)$	Minimum of the pions transverse momentum
$\max\left(\mathrm{ghost}_{\mu_1}, \mathrm{ghost}_{\mu_2}\right)$	Maximum of the muons ghost probability
$\min\left(p_T\left(\mu_1\right), p_T\left(\mu_2\right)\right)$	Minimum of the muons transverse momentum
0.5 (Bs_1.80_cc_deltaEta + Bs_1.80_nc_deltaEta)	Average of the B_s^0 - cone difference in eta
Bs_1.80_cc_mult	Number of objects in the cone
Bs_1.80_cc_asy_PZ	Z components of the momentum asymmetry
Bs_1.80_cc_vPT	Vector-summed PT of the objects inside the cone
Bs_1.80_nc_deltaPhi	Difference in phi between the B_s^0 and the cone
Bs_IPCHI2_OWNPV	Quality of the B_s^0 fit
TT occupancy	TT occupancy

Table 6.9 *Training variables for the $B_s^0 \to J/\psi f_0$ MVA.*

6.3.2 MVA training and performance

The TMVA [93] framework is used to build the multivariate classifier. It offers a large variety of algorithms for classification like decision trees and neural networks. Among these, in this case the BDTG shows good performance in

terms of correctly classifying signal and rejecting most of the background (figs. 6.9 and 6.10 and appendix E). Hence, it was chosen for use in this analysis.

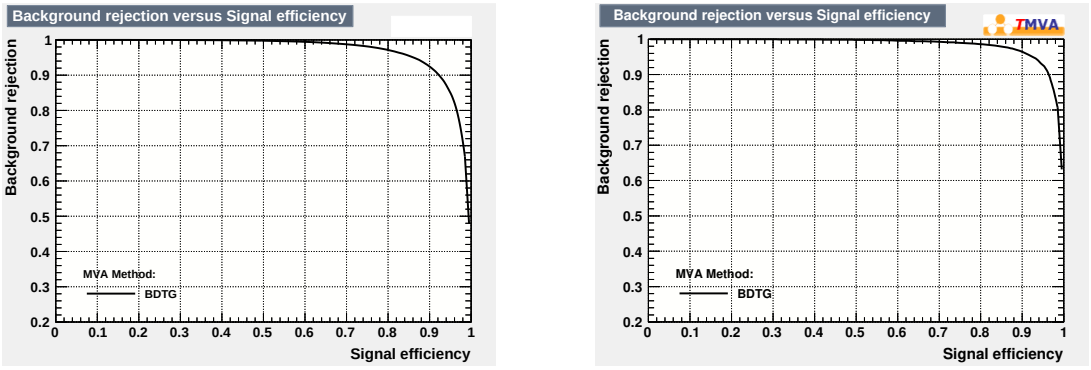

(a) $B_s^0 \to J/\psi f_0$ *channel* **(b)** $B_s^0 \to J/\psi\eta'$ *channel*

Figure 6.9 *2016 training, Receiver Operating Characteristic (ROC) curve for both channels. Both distributions show very high background rejection.*

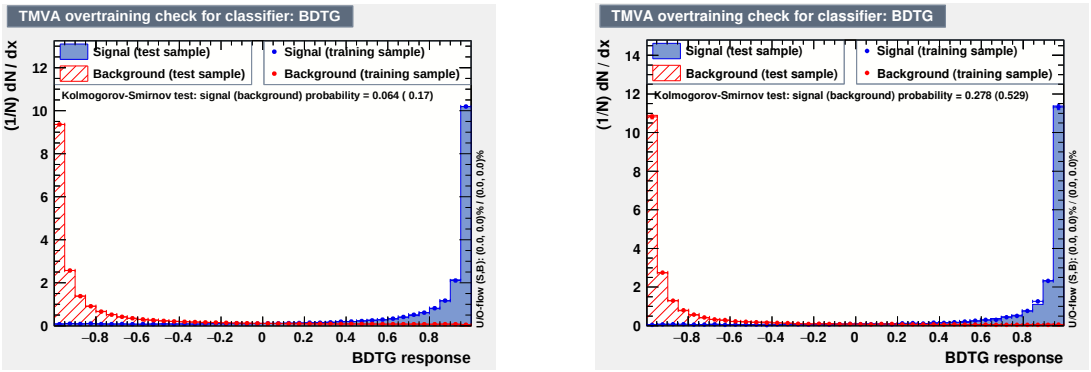

(a) $B_s^0 \to J/\psi f_0$ *channel* **(b)** $B_s^0 \to J/\psi\eta'$ *channel*

Figure 6.10 *2016 training, signal-background classification for both channels. In both cases, BDTG showed optimal separation between signal and background*

In appendix E the signal and background plots for the training variables are shown. The optimal BDTG cut for the $B_s^0 \to J/\psi\eta'$ mode is chosen by computing the yields in time bins for different BDTG cut values. These yields are input to toy studies that determine the cut which minimizes the error on $\Delta\Gamma_s$ (fig. 6.11).

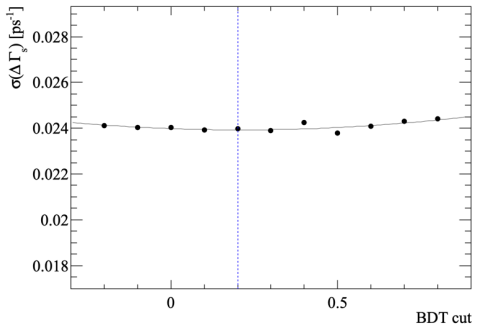

(a) *2011 - 2012 - $B_s^0 \to J/\psi\eta'$*

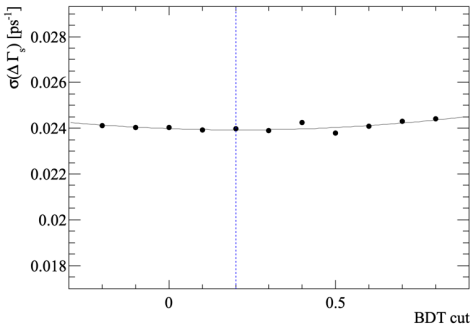

(b) *2015 + 2016 - $B_s^0 \to J/\psi\eta'$*

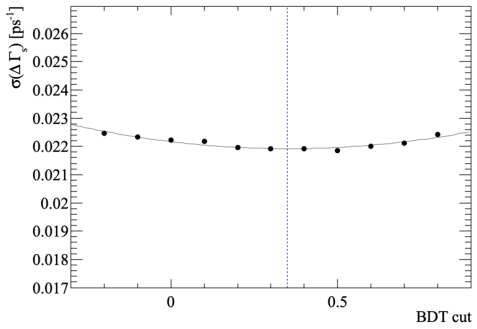

(c) *2017 - $B_s^0 \to J/\psi\eta'$*

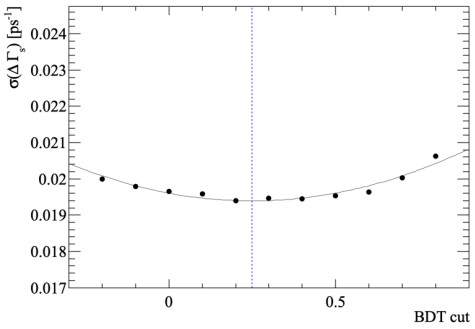

(d) *2018 - $B_s^0 \to J/\psi\eta'$*

Figure 6.11 *Fitted uncertainty as a function of the BDTG cut found in toy studies for the full η' data set. The black line is a quadratic fit, the dotted blue line is the chosen cut.*

The optimal BDTG cut for the $B_s^0 \to J/\psi f_0$ channel is chosen by fitting the Monte Carlo decay time distribution with an exponential, plotting the obtained slope of the exponential as a function of the BDTG cut and looking for a plateau as shown in fig. 6.12.

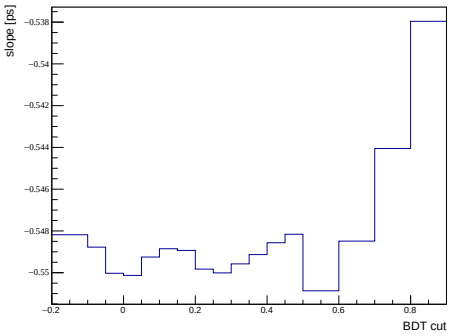

(a) *2011 - 2012 -* $B_s^0 \to J/\psi f_0$

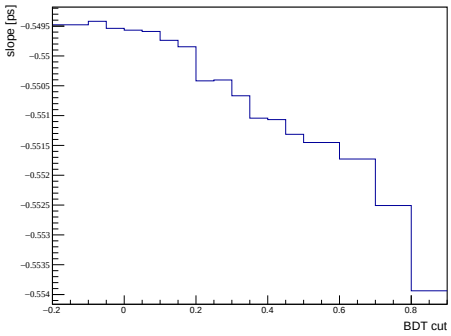

(b) *2015 + 2016 -* $B_s^0 \to J/\psi f_0$

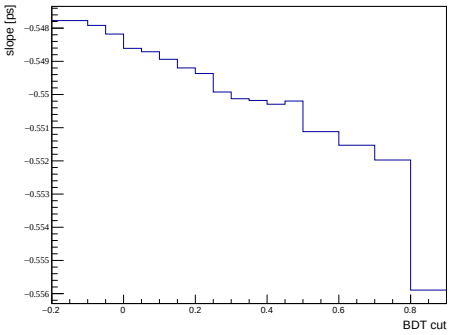

(c) *2017 -* $B_s^0 \to J/\psi f_0$

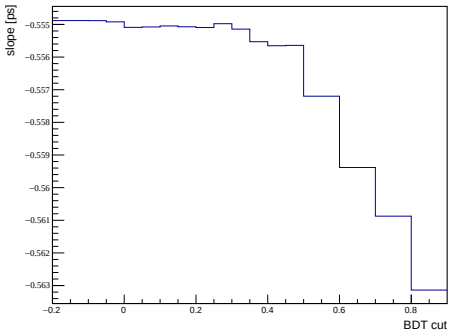

(d) *2018 -* $B_s^0 \to J/\psi f_0$

Figure 6.12 *Exponential slope from* $B_s^0 \to J/\psi f_0$ *Monte Carlo as a function of BDTG cut.*

The BDTG cuts applied to both channels are summarized in table 6.10.

Year	Channel	BDTG value
2011 + 2012	η'	0.20
	f_0	0.20
2015 + 2016	η'	0.40
	f_0	0.25
2017	η'	0.35
	f_0	0.25
2018	η'	0.25
	f_0	0.25

Table 6.10 *BDTG cuts for the four data sets. The BDTG output is required to be larger than the values listed in the table.*

Chapter 7

Measurement of $\Delta\Gamma_s$

In this chapter the tools used to measure $\Delta\Gamma_s$ will be described. The measurement is performed using eq. (2.26) where the yields for each mode are extracted from a simultaneous mass fit to the data in bins of lifetime. A χ^2 minimization of eq. (2.26) is used to extract $\Delta\Gamma_s$.

7.1 Fit validation

The fit procedure is tested and validated using toy studies. Toys were generated using the theoretical lifetime distribution for the CP-even and CP-odd components and applying a Gaussian smearing with $\sigma = 0.04$ ps to simulate the detector resolution. First, toys are generated with only the signal component and are fitted by minimizing eq. (2.26). Figure 7.1 are shown the pull and bias distributions obtained by generating 5000 toys with $N_{\eta'} = 9600$, $N_{f_0} = 60000$, $\Gamma_s = 0.6628$ ps^{-1} and $\Delta\Gamma_s = 0.077$ ps^{-1}. The number of events generated in the toys is roughly the same as the number of events in the data. Two distributions were taken into account: bias and pull. The bias is defined as the difference between the measured value and the theoretical one while the pull for a Gaussian distribution with mean μ and width σ is defined as $g \equiv (x - \mu)/\sigma$. The fitted pull, 0.97 ± 0.01, is consistent with unity, indicating the uncertainties are correctly estimated. The fitted bias, (0.05 ± 0.12) ns^{-1}, is consistent with zero.

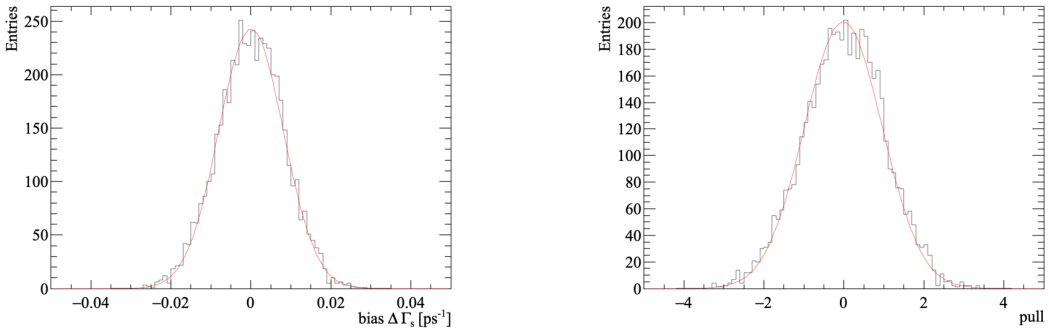

(a) **(b)**

Figure 7.1 *Toy studies: bias distribution (left) and pull distribution (right). 5000 toys were generated using* $N_{\eta'} = 9600$, $N_{f_0} = 60000$, $\Gamma_s = 0.6628\ \text{ps}^{-1}$ *and* $\Delta\Gamma_s = 0.077\ \text{ps}^{-1}$.

The bias and the uncertainty on $\Delta\Gamma_s$ as a function of the input $\Delta\Gamma_s$ are also studied (fig. 7.2). No dependence is seen.

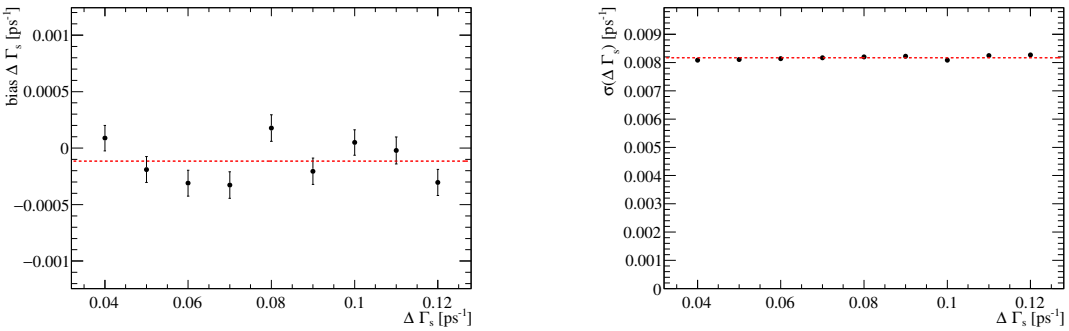

(a) **(b)**

Figure 7.2 *Toy studies: bias as a function of* $\Delta\Gamma_s$ *(left) and* $\sigma(\Delta\Gamma_s)$ *as a function of* $\Delta\Gamma_s$ *(right). 5000 toys were generated using* $N_{\eta'} = 9600$, $N_{f_0} = 60000$, $\Gamma_s = 0.6628\ \text{ps}^{-1}$ *and* $\Delta\Gamma_s = 0.077\ \text{ps}^{-1}$. *The red lines are a constant fit to guide the eye.*

The effect of fitting eq. (2.26) using a different value of Γ_s to the value used in generation was also studied. In fig. 7.3 the bias coming from using a different value when fitting $\Delta\Gamma_s$ to the generated value is shown. There is a linear correlation between the bias and the Γ_s shift. However the bias on the $\Delta\Gamma_s$ measurement is small compared to the expected precision as the fit has limited sensitivity to Γ_s. If $\Gamma_s^{\text{fit}} - \Gamma_s^{\text{input}}$ is considered to be within the current Γ_s uncertainty (the two blue lines) in fig. 7.3, the bias on $\Delta\Gamma_s$ is 1% of the expected statistical uncertainty on

$\Delta\Gamma_s$. This is considered as a systematic uncertainty.

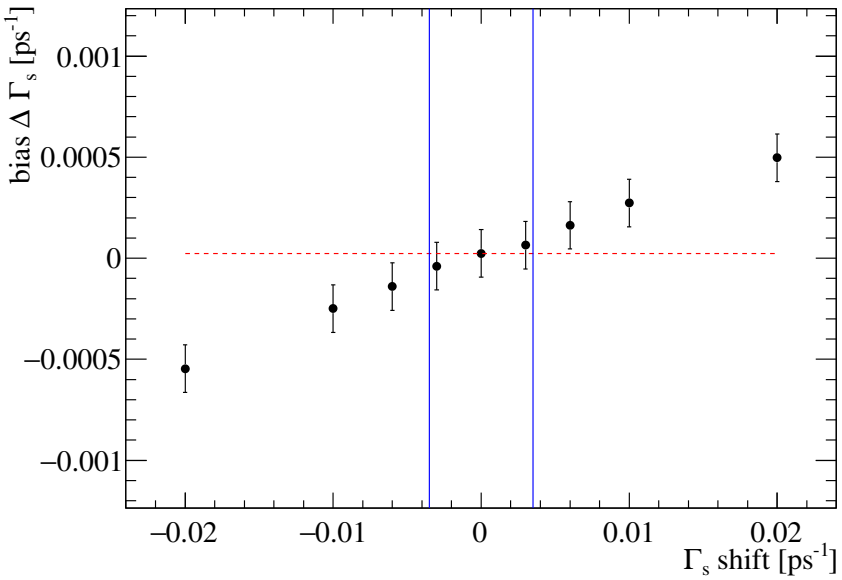

Figure 7.3 *Bias as a function of the difference between the input value of $\Delta\Gamma_s$ in the generation and fit of the toys. The toy parameters are the same as the ones used before. The red line is there to help identifying the value corresponding to $\Gamma_s^{\text{fit}} - \Gamma_s^{\text{input}} = 0$. The blue lines are the present uncertainty on Γ_s quoted from Heavy Flavor AVeraging (HFLAV) [20].*

7.1.1 Binning scheme

As described in section 2.4, the $\Delta\Gamma_s$ measurement is performed splitting the data set into lifetime bins. The optimal number of bins is studied with toy simulations. Both the bias and uncertainty on $\Delta\Gamma_s$ are studied and the two distributions in fig. 7.4 show having a small number of bins reduces the sensitivity to $\Delta\Gamma_s$. Based on these plots, it seems reasonable to use eight bins. Adding more bins would not improve the precision on $\Delta\Gamma_s$ but would make the simultaneous fit more complicated.

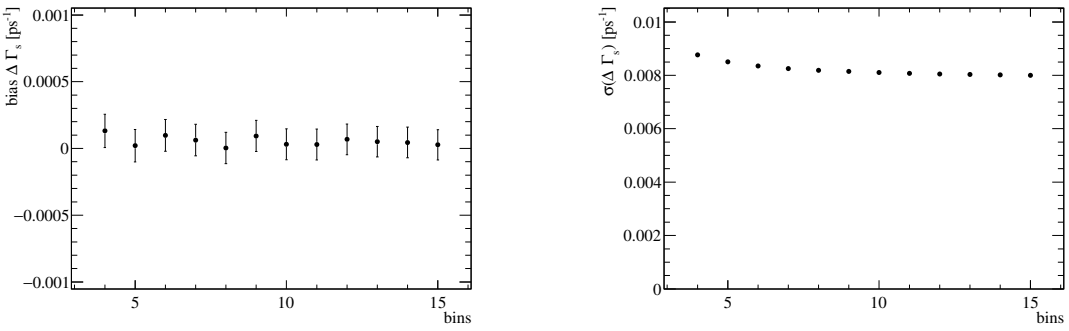

(a) **(b)**

Figure 7.4 *Toy studies to find the optimal number of bins. The left plot shows the bias on $\Delta\Gamma_s$ as a function of the number of bins and the right plot shows the error on $\Delta\Gamma_s$ as a function of the number of bins.*

The binning scheme was chosen to have a roughly equal yields in each bin as shown in appendix G. The resulting scheme is summarized in table 7.1.

Bin number	Bin edges [ps]
1	0.5 - 0.7
2	0.7 - 0.9
3	0.9 - 1.2
4	1.2 - 1.5
5	1.5 - 2.0
6	2.0 - 2.5
7	2.5 - 3.5
8	3.5 - 10.0

Table 7.1 *Binning scheme used in the analysis.*

7.2 Mass fit

The two modes have different background components to take into account as presented in section 6.2 therefore two fit models are built.

7.2.1 $B_s^0 \to J/\psi\eta'$ fit model

The fit model for the $J/\psi\eta'$ mass distribution consists of the four components given in table 7.2.

Component	PDF
$B_s^0 \to J/\psi\eta'$	Double sided crystal ball
$B^0 \to J/\psi\eta'$	Double sided crystal ball
$B_s^0 \to J/\psi\,(\phi \to \pi^+\pi^-\pi^0)$	Bifurcated Gaussian
Combinatorial background	Exponential

Table 7.2 *$B_s^0 \to J/\psi\eta'$ mass fit components.*

The $B_s^0 \to J/\psi\eta'$ component is found to be well modeled in the simulation by a Double-Sided Crystal Ball (DSCB) function. This is a function with a Gaussian core and power law tails as described in appendix F.1. A fit of this function to the simulation is shown in fig. 7.5 and the results are listed in table 7.3.

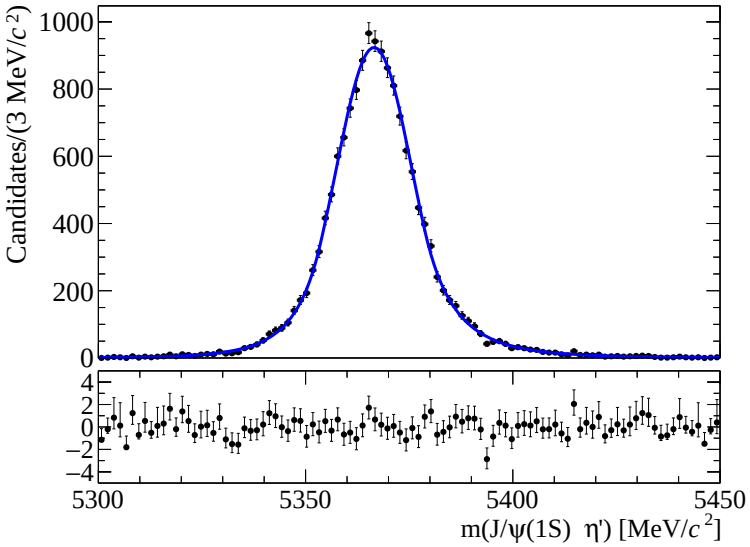

Figure 7.5 *Fit of the $J/\psi\eta'$ mass distribution to the 2016 simulation sample. Pulls are shown below the plot.*

Parameter	Value
μ	5366.56 ± 0.09 MeV/c^2
α_L	-1.52 ± 0.05
α_R	1.33 ± 0.04
n_L	5.3 ± 0.5
n_R	4.9 ± 0.4
σ	9.1 ± 0.1 MeV/c^2

Table 7.3 *$B_s^0 \to J/\psi\eta'$ fit parameters from the 2016 simulation.*

When fitting the data, the tail parameters are fixed to the simulation result while the mean and sigma are left floating.

To model the $B^0 \to J/\psi\eta'$ component a DSCB shape is also used (appendix F.1). The tail parameters are fixed to the B_s^0 fit. Typically, the mass resolution scales with the square root of the energy release (Q-value). Consequently, the sigma for the B^0 component is Gaussian constrained to be $\alpha_m \cdot \sigma_{B_s^0}$ where $\alpha_m = 0.97 \pm 0.03$. The uncertainty is chosen to allow for possible linear scaling. The position of the peak is Gaussian constrained by the known $B_s^0 - B^0$ mass splitting, $m_{B_s^0} - m_{B^0} = 87.22 \pm 0.16$ MeV/c^2, calculated using the values in [92]. The yield for this mode is left free since the fraction of B^0 to B_s^0 decays varies as a function of decay time.

The background model for the $B_s^0 \to J/\psi\phi\,(3\pi)$ component (see section 6.2.1) is modeled using the exclusive simulation sample. The fit model includes an exponential for the combinatorial background and a Bifurcated Gaussian (appendix F.2) for the $B_s^0 \to J/\psi\phi$ component (fig. 7.6). When including this background component into the $J/\psi\eta'$ mass fit, only the bifurcated Gaussian component is considered as the exponential shape is absorbed in the combinatorial background component. The yields for this mode are computed relative to the signal mode as $N^{B_s^0 \to J/\psi\phi} = f^\phi \cdot N^{B_s^0 \to J/\psi\eta'}$ where $f^\phi = (4.6 \pm 0.9) \times 10^{-2}$ is the relative selection efficiency computed using the simulation multiplied to the branching fraction of the decays. In the fit to the data the shape of this component is fixed to the simulation and f^ϕ to the value above.

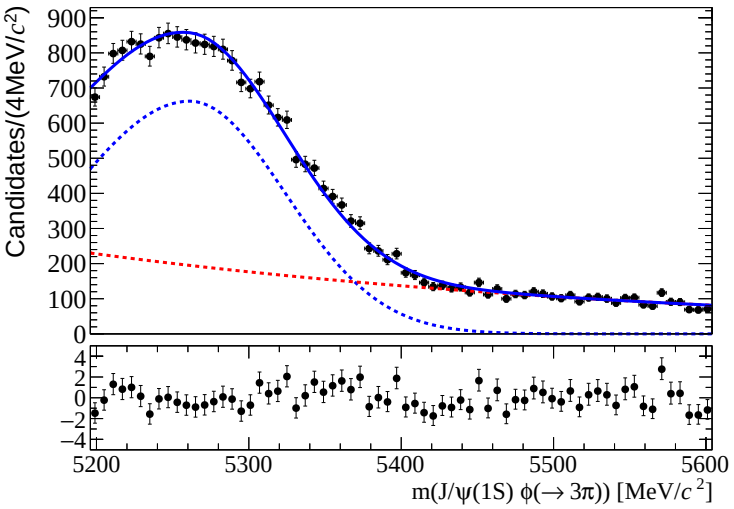

Figure 7.6 *$B_s^0 \to J/\psi\left(\phi \to \pi^+\pi^-\pi^0\right)$ fit model for the f_0 channel. Red dashed lines correspond to the combinatorial background component, the blue dashed line is the $B_s^0 \to J/\psi\phi$ component and the blue solid line is the full fit. Pulls are shown below the plot.*

Parameter	Value MeV/c^2
μ	5274.4 ± 4.2
σ_L	63.7 ± 8.2
σ_R	62.1 ± 3.4

Table 7.4 *$B_s^0 \to J/\psi\phi\left(\pi^+\pi^-\pi^0\right)$ fit results for the f_0 channel.*

As an example, in fig. 7.7 a fit of this model to 2016 $B_s^0 \to J/\psi\eta'$ data set is shown. The quality of the fit judged from the pulls is good. The χ^2/ndof for this model is 0.97.

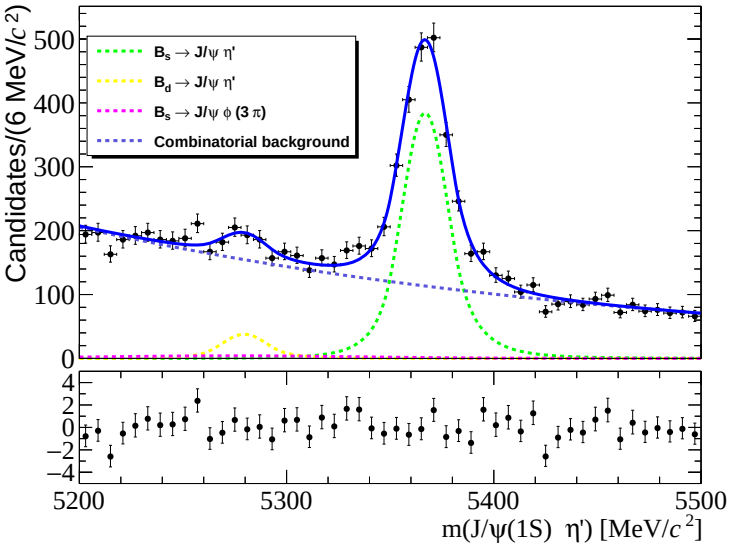

Figure 7.7 *Fit to the 2015-2016 $B_s^0 \to J/\psi\eta'$ data set of the model described in the text. The pulls are shown below the plot.*

7.2.2 $B_s^0 \to J/\psi f_0$ fit model

The fit model for the $B_s^0 \to J/\psi f_0$ decay mode has the six components listed in table 7.5.

Component	PDF
$B_s^0 \to J/\psi f_0$	DSCB
$B^0 \to J/\psi f_0$	DSCB
$B^0 \to J/\psi K^+\pi^-$	Modeled with RapidSim [94]
$B^+ \to J/\psi K^+ + B^+ \to J/\psi \pi^+$	Crystal ball + Gaussian
$B_s^0 \to J/\psi\,(\eta' \to \rho^0\gamma)$	Modeled with RapidSim
Combinatorial background	Exponential

Table 7.5 *$J/\psi f_0$ mass fit components.*

The B_s^0 peak is modeled with a DSCB function in the simulation (fig. 7.8). The results of the fit are summarized in table 7.6. When fitting the data, the tail parameters are fixed to the values obtained with the simulation while the mean and sigma are left free.

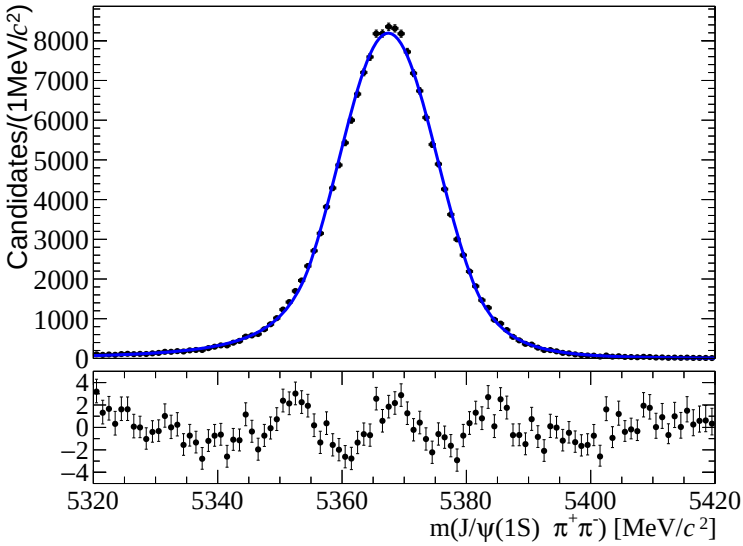

Figure 7.8 *Fit of the $B_s^0 \to J/\psi\pi^+\pi^-$ to the 2016 simulation.*

Parameter	Value
μ	5367.0 ± 0.031 MeV/c^2
α_L	-1.517 ± 0.027
α_R	1.718 ± 0.035
n_L	3.29 ± 0.21
n_R	6.6 ± 0.66
σ	7.99 ± 0.037 MeV/c^2

Table 7.6 *B_s^0 peak fit parameters - f_0 channel.*

The B^0 peak is modelled with a DSCB function. The tail parameters are fixed using the values from the $B_s^0 \to J/\psi f_0$ simulation sample while the sigma is Gaussian constrained to the B_s^0 value and the mean is Gaussian constrained to the known $B_s^0 - B^0$ mass splitting value.

The shape of the $B^0 \to J/\psi K^+\pi^-$ component with a $K \to \pi$ swap is modeled using the RapidSim [94] fast simulation package [94]. The histogram of the $J/\psi\pi^+\pi^-$ mass distribution from RapidSim is convolved with a Gaussian with a 10 MeV/c^2 width to simulate the detector resolution. This gives the shape shown in fig. 7.9. The yields for this mode are computed relative to the signal mode as $N^{B^0 \to J/\psi K^+\pi^-} = f \cdot N^{B_s^0 \to J/\psi f_0}$, where $f = (6.5 \pm 0.6) \times 10^{-2}$ is the relative selection efficiency computed using the simulation multiplied by the decay branching fraction and the f_s/f_d factor and it is set to be constant.

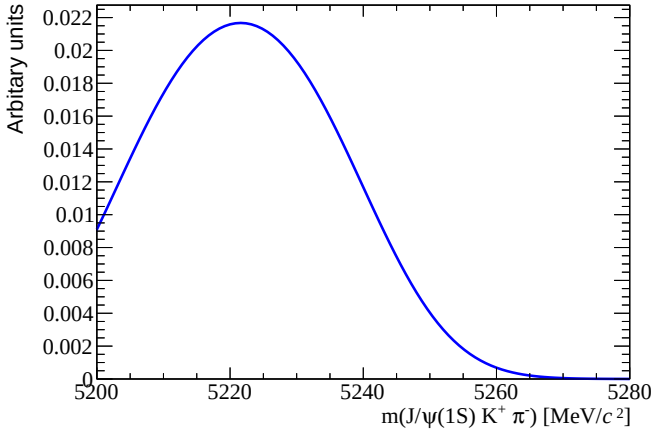

Figure 7.9 *$B^0 \to J/\psi K^+\pi^-$ fit model for the $B_s^0 \to J/\psi f_0$ decay mode.*

The $B^+ \to J/\psi K^+$ and $B^+ \to J/\psi\pi^+$ components are modeled using the inclusive B^+ Monte Carlo sample by the combination of a Crystal Ball function and a Gaussian. In fig. 7.10 the fit model for the $B^+ \to J/\psi K^+$ and $B^+ \to J/\psi\pi^+$ components are shown. Table 7.7 shows the fit output. These components are included in the final fit fixing the fit parameters to the values in table 7.7 and keeping the yields free.

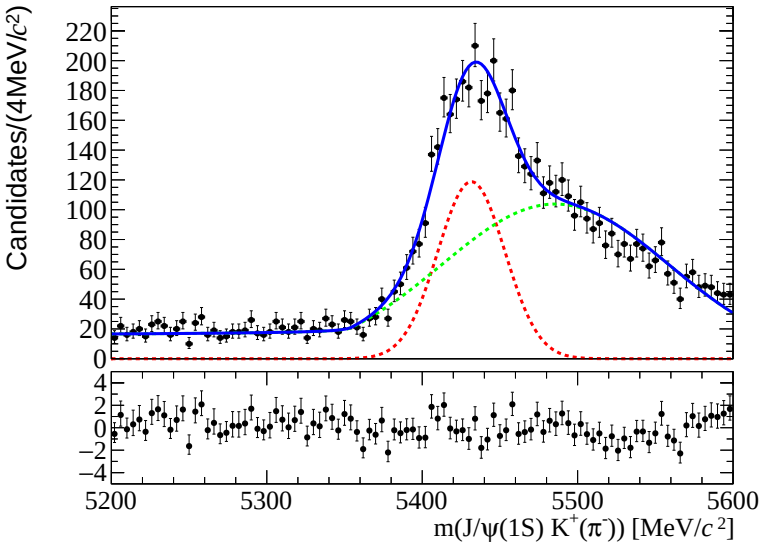

Figure 7.10 *$B^+ \to J/\psi K^+$ and $B^+ \to J/\psi\pi^+$ background fit model for the $B_s^0 \to J/\psi f_0$ decay mode.*

Parameter	Value
μ_{CB}	5504 ± 3.0 MeV/c^2
σ_{CB}	68 ± 1.3
n_{CB}	0.052 ± 0.001
α_{CB}	1.79 ± 0.040
μ_{Gauss}	5438 ± 1.2 MeV/c^2
σ_{Gauss}	28 ± 2.0 MeV/c^2
yields ratio	0.61 ± 0.02

Table 7.7 *$B^+ \to J/\psi K^+$ and $B^+ \to J/\psi \pi^+$ fit results from 2016 Monte Carlo.*

Due to the limited size of the full Monte Carlo sample, the $B_s^0 \to J/\psi\eta'$ background component is also modeled with the RapidSim [94]. The true $J/\psi\pi^+\pi^-$ mass shape obtained with RapidSim is convolved with the detector resolution. The resulting PDF is shown in fig. 7.11. The yields for this mode are computed relative to the signal mode as $N^{B_s^0 \to J/\psi\eta'} = f \cdot N^{B_s^0 \to J/\psi f_0}$, where $f = (6.5 \pm 1.0) \times 10^{-2}$ is the relative selection efficiency computed using the simulation multiplied by the decay branching fraction and it is set to be constant.

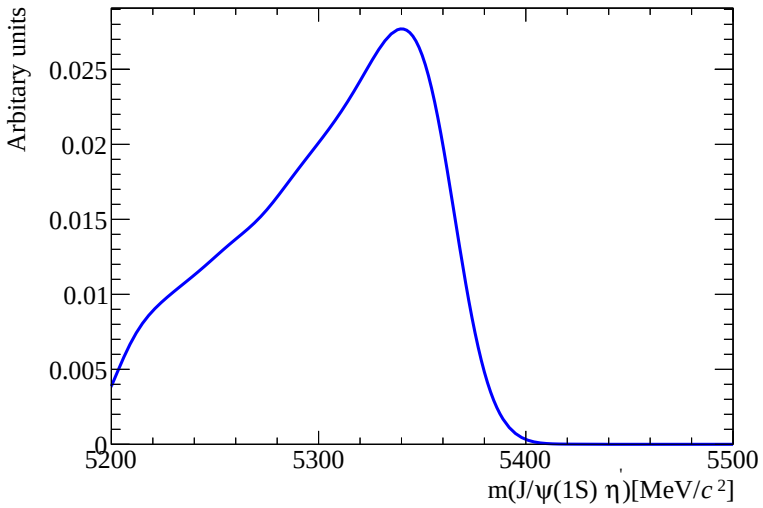

Figure 7.11 *$B_s^0 \to J/\psi\left(\eta' \to \rho^0\gamma\right)$ background model for the $B_s^0 \to J/\psi f_0$ decay mode. The shape is obtained from simulated events with RapidSim.*

The full mass fit for the 2015 and 2016 $J/\psi\pi^+\pi^-$ channel including all background components listed above is shown in fig. 7.12.

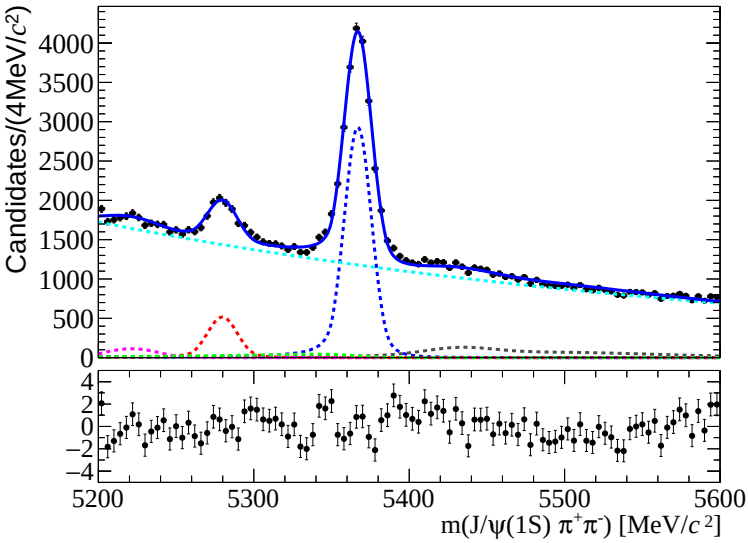

Figure 7.12 *$J/\psi\pi^+\pi^-$ invariant mass fit for the 2015 and 2016 f_0 data set. The purple dashed line is the $B^0 \to J/\psi K^*$ component, the red dashed line is the $B^0 \to J/\psi\pi^+\pi^-$ component, the green dashed line is the $B_s^0 \to J/\psi\eta'$ component, the gray dashed line is the $B^+ \to J/\psi\,(K^+/\pi^+)$ component, the light blue line is the combinatorial background and the dashed blue line is the signal component.*

7.2.3 Simultaneous fit

After testing the fit model on the full data set, the data set is split into the eight time bins (table 7.1) and a simultaneous fit is performed across the bins (fig. 7.13). The parameters of the fit are summarized in table 7.8 and table 7.9. The shape and yield of the combinatorial background is allowed to vary between bins. The shape of the B^0 component is shared between bins whilst the B^0 yield is a separate parameter for each bin since it depends on the B^0 lifetime. The fits for each time bin are shown in appendix G

Parameter	Shared	Status
$\mu_{B_s^0}$	Yes	Free
$\sigma_{B_s^0}$	Yes	Free
$\Delta m\,(B_s^0, B^0)$	Yes	Constrained
α_m	Yes	Constrained
$\mu_{\phi\to 3\pi}$		Fixed
$\sigma_{L,\phi\to 3\pi}$		Fixed
$\sigma_{R,\phi\to 3\pi}$		Fixed
B_s^0 yield	No	Free
B^0 yield	No	Free
Combinatorial background yield	No	Free
$B_s^0\,(3\pi)$ yield		Free
$n_{R,B_{(s)}^0}$		Fixed
$n_{L,B_{(s)}^0}$		Fixed
$\alpha_{R,B_{(s)}^0}$		Fixed
$\alpha_{L,B_{(s)}^0}$		Fixed
τ background	No	Free

Table 7.8 *$B_s^0 \to J/\psi\eta'$ simultaneous fit parameters: the central column shows the parameters shared across all bins and the right column shows the parameters left floating. $\mu_{\phi\to 3\pi}$, $\sigma_{L,\phi\to 3\pi}$ and $\sigma_{R,\phi\to 3\pi}$ refer to the Bifurcated Gaussian model used for the $B_s^0 \to J/\psi\phi\,(3\pi)$ decay and $n_{R,B_{(s)}^0}$, $n_{L,B_{(s)}^0}$, $\alpha_{R,B_{(s)}^0}$ and $\alpha_{L,B_{(s)}^0}$ are the Crystal Ball function parameter for the signal model. α_m is the σ scaling factor for the $B^0 \to J/\psi\eta'$ fit model.*

Parameter	Shared	Status
$\mu_{B_s^0}$	Yes	Free
$\sigma_{B_s^0}$	Yes	Free
$\Delta m\,(B_s^0, B^0)$	Yes	Constrained
α_m	Yes	Constrained
B_s^0 yield	No	Free
B^0 yield	No	Free
Combinatorial background yield	No	Free
$n_{R,B_{(s)}^0}$		Fixed
$n_{L,B_{(s)}^0}$		Fixed
$\alpha_{R,B_{(s)}^0}$		Fixed
$\alpha_{L,B_{(s)}^0}$		Fixed
τ background	No	Free
$\mu_{B^+\to J/\psi K^+}$		Fixed
$\sigma_{B^+\to J/\psi K^+}$		Fixed
$\mu_{B^+\to J/\psi \pi^+}$		Fixed
$\sigma_{B^+\to J/\psi \pi^+}$		Fixed
$B^+ \to J/\psi K^+,\ B^+ J/\psi \pi^+$ tail		Fixed
$B^+ \to J/\psi K^+,\ B^+ J/\psi \pi^+$ yield	No	Free
$\mu_{B^0\to J/\psi K^+\pi^-}$		Fixed
$\sigma_{B^0\to J/\psi K^+\pi^-}$		Fixed
$B^0 \to J/\psi K^+\pi^-$ yield		Fixed
$B_s^0 \to J/\psi \eta'$ yield		Fixed

Table 7.9 *$B_s^0 \to J\psi f_0$ simultaneous fit parameters: the central column shows the parameters shared across all bins and the right column shows the parameters left floating. $n_{R,B_{(s)}^0}$, $n_{L,B_{(s)}^0}$, $\alpha_{R,B_{(s)}^0}$ and $\alpha_{L,B_{(s)}^0}$ are the Crystal Ball function parameter for the signal model. α_m is the σ scaling factor for the $B^0 \to J/\psi\eta'$ fit model.*

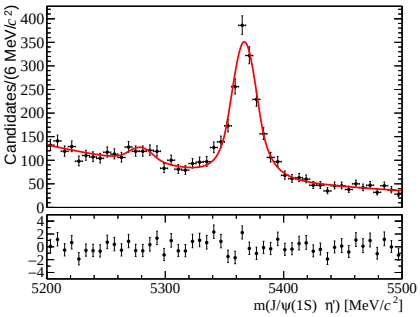

(a) *2011 - 2012* η'

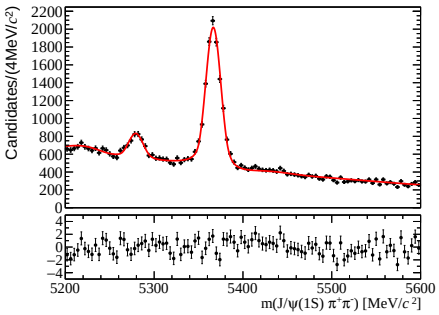

(b) *2011 - 2012* f_0

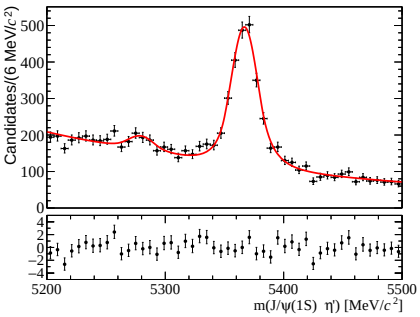

(c) *2015 - 2016* η'

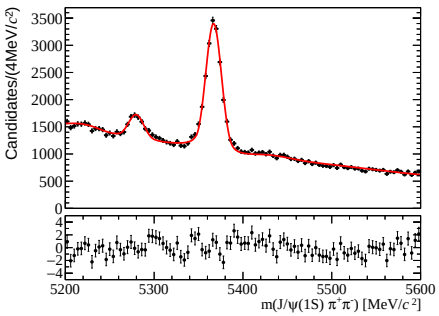

(d) *2015 - 2016* f_0

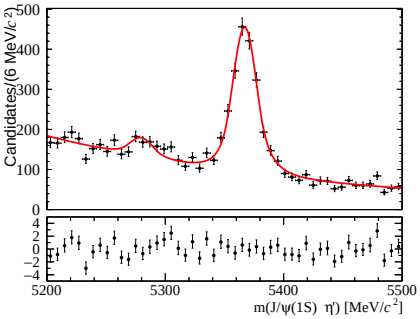

(e) *2017* η'

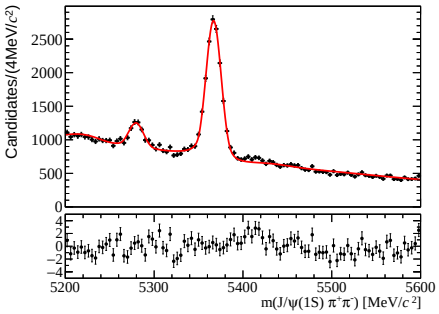

(f) *2017* f_0

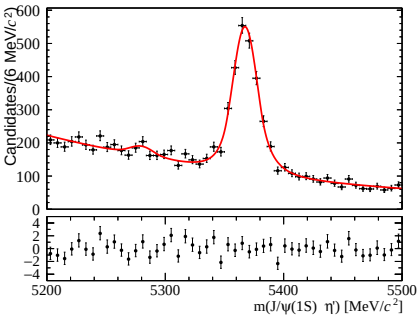

(g) *2018* η'

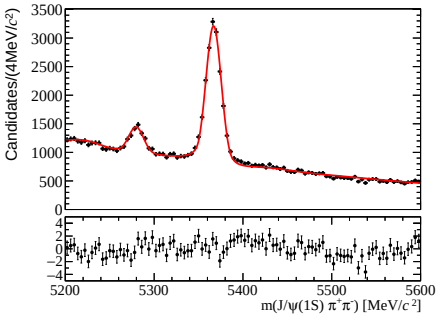

(h) *2018* f_0

Figure 7.13 *Simultaneous fit in lifetime bins for both channels. Right column shows the* η' *data set, left column the 2016* f_0 *data set. The red line shows the fit result.*

7.3 Time acceptance

Since a relative measurement between the two channels is made, the time acceptance largely cancels in the ratio. The validity of this assumption is probed below and the residual acceptance correction quantified for the example of the 2015–2016 data set. The results for the other years are given in appendix J. The time acceptance $\mathcal{A}(t)$ is defined as the ratio between the reconstructed lifetime distribution in the simulation to the input distribution. For both channels the Monte Carlo samples are generated with a lifetime of 1.543 ps.

There are four main contribution to the time acceptance: the candidate DLS, the χ^2_{IP} cut, the VELO tracking efficiency and the MVA. The overall acceptance, $\mathcal{A}_{tot}$, is the product of these effects.

The DLS cut in trigger and stripping at 3 removes events at low decay time. In fig. 7.14 the acceptance generated by the DLS cut is shown. The red line highlights the decay time cut applied in the analysis and the horizontal blue line is a fit to a constant to show the plateau region. It is clear that the choice of lower time cut at 0.5 ps minimizes the impact of the DLS cut on the analysis.

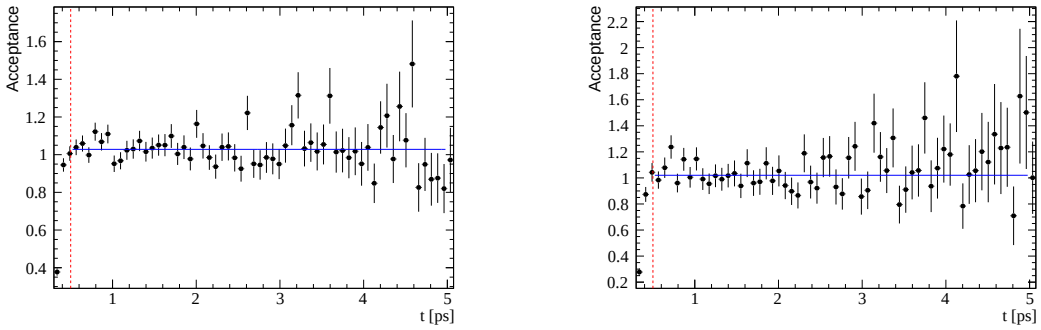

(a) **(b)**

Figure 7.14 *2016 DLS acceptance for both channels. Figure 7.14a is the η' channel and fig. 7.14b is the f_0 channel. The red line shows the decay time cut at 0.5 ps and the blue line is a fit with a constant helping identifying the plateau region.*

The cut on the candidate χ^2_{IP} removes candidates at large decay time. Figure 7.15 shows the acceptance due to the χ^2_{IP}. The efficiency distribution is well described by the form

$$\mathcal{A}^{\chi^2_{\text{IP}}}(t) \equiv (1 - \gamma t)\,. \tag{7.1}$$

The results of fitting this distribution are listed in table 7.10. This component is the largest source of acceptance for this analysis.

Channel	γ [ps^{-1}]
η'	$(-2.4 \pm 3.4) \times 10^{-4}$
f_0	$(13.1 \pm 6.5) \times 10^{-4}$

Table 7.10 χ^2_{IP} *acceptance fit results from 2015-2016 Monte Carlo.*

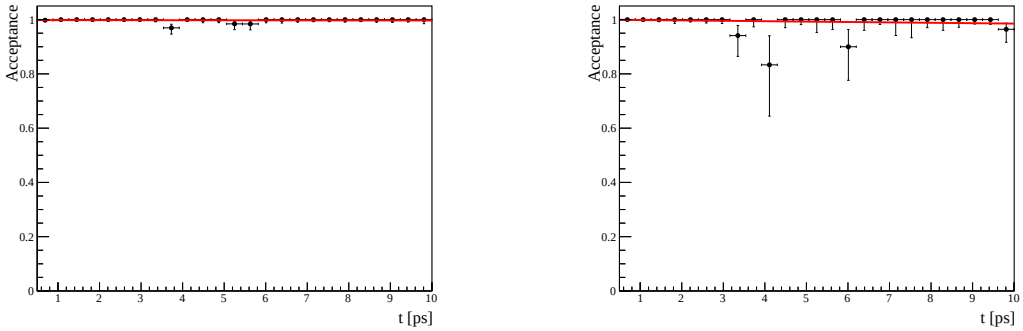

(a) η' **(b)** f_0

Figure 7.15 χ^2_{IP} *acceptance. Figure 7.15a shows the acceptance for the* $B^0_s \to J/\psi\eta'$ *channel, fig. 7.15b shows the* $B^0_s \to J/\psi f_0$ *channel.*

Due to the VELO track reconstruction algorithm (section 4.1.1), the efficiency for track reconstruction in the VELO depends on the distance of closest approach of the track to the beamline. This causes a decay time acceptance that is modeled as

$$\mathcal{A}^{\text{VELO}}(t) \equiv \left(1 - \beta t^2\right) \tag{7.2}$$

Figure 7.16 shows the fit of this form to 2016 simulation. The fit results are listed in table 7.11.

Channel	β [ps^{-2}]
η'	$(8.2 \pm 1.9) \times 10^{-4}$
f_0	$(5.9 \pm 0.5) \times 10^{-4}$

Table 7.11 *Results of fits of eq.* (7.2) *to the simulation.*

The results of acceptance between the channels agree within one sigma implying this effect largely cancels in the ratio.

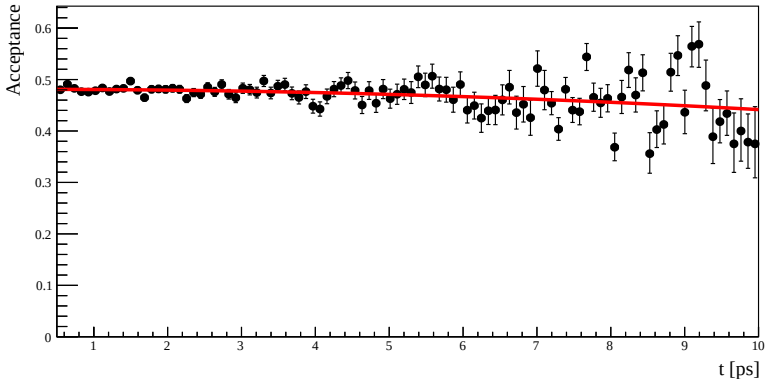

(a)

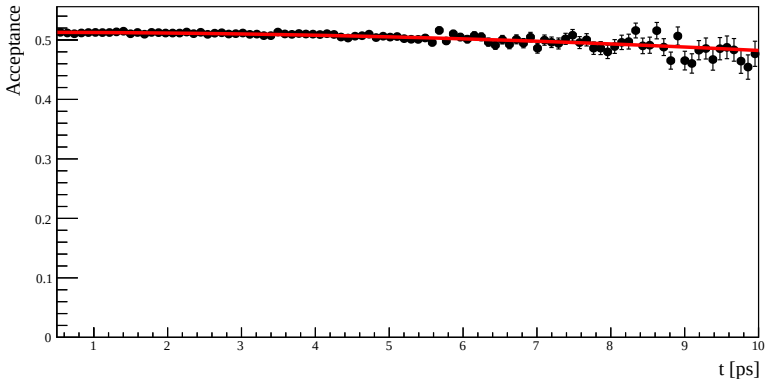

(b)

Figure 7.16 *2016 VELO β factor for both channels: fig. 7.16a is the $B_s^0 \to J/\psi\eta'$ channel, fig. 7.16b is the $B_s^0 \to J/\psi f_0$ channel.*

Since this analysis relies on MVA for signal-background classification, the effect of the MVA cut on the reconstructed lifetime distribution is checked. From the choice of variables in the MVA this requirement should be lifetime unbiased. In fig. 7.17 it can be seen that the efficiency of the MVA is indeed flat as a function of time.

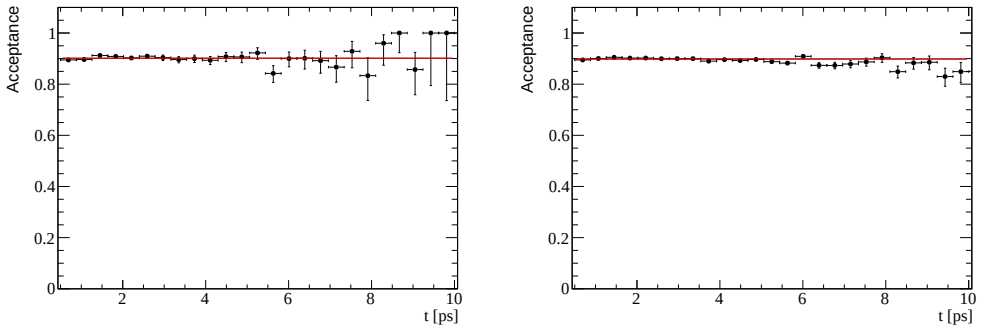

(a) **(b)**

Figure 7.17 *2016 MVA acceptance for both channels: fig. 7.17a η' channel, fig. 7.17b f_0 channel.*

7.3.1 Time acceptance fit

After checking the individual sources of time acceptance, a combined acceptance is calculated for each channel. Since the 2015 and 2016 data set, as well as Run 1, will be treated as a single one, the time acceptance is studied merging the 2015 and 2016, and the 2011 and 2012 Monte Carlo samples. The time acceptance distribution is computed using the re-weighted simulation, fitting the Monte Carlo sample for each mode with:

$$\mathcal{A}_{\text{fit}}(t) = (1 - bt)\, e^{-t/\tau_{\text{MC}}} \tag{7.3}$$

where the function $(1 - bt)$ corrects for the acceptance. Figures 7.18 and 7.19 show the fit of eq. (7.3) to the simulation samples while the results of the fit are listed in table 7.12. The quality of the fit judged by from the residuals is good. The larger size of the correction in the Run 1 data reflects the larger acceptance correction from the VELO tracking.

Year	Channel	b [ps^{-1}]	$b_{\eta'} - b_{f_0}$ [ps^{-1}]
2011 + 2012	η'	$(1.23 \pm 0.33) \times 10^{-2}$	$(3.8 \pm 5.5) \times 10^{-3}$
	f_0	$(8.5 \pm 4.4) \times 10^{-3}$	
2015 + 2016	η'	$(0.023 \pm 4.1) \times 10^{-3}$	$(-0.75 \pm 4.5) \times 10^{-3}$
	f_0	$(0.78 \pm 1.9) \times 10^{-3}$	
2017	η'	$(2.2 \pm 2.7) \times 10^{-3}$	$(-1.35 \pm 3.57) \times 10^{-3}$
	f_0	$(3.5 \pm 2.4) \times 10^{-3}$	
2018	η'	$(0.54 \pm 2.7) \times 10^{-3}$	$(-0.76 \pm 3.6) \times 10^{-3}$
	f_0	$(1.3 \pm 2.3) \times 10^{-3}$	

Table 7.12 *Acceptance slope values for both channels.*

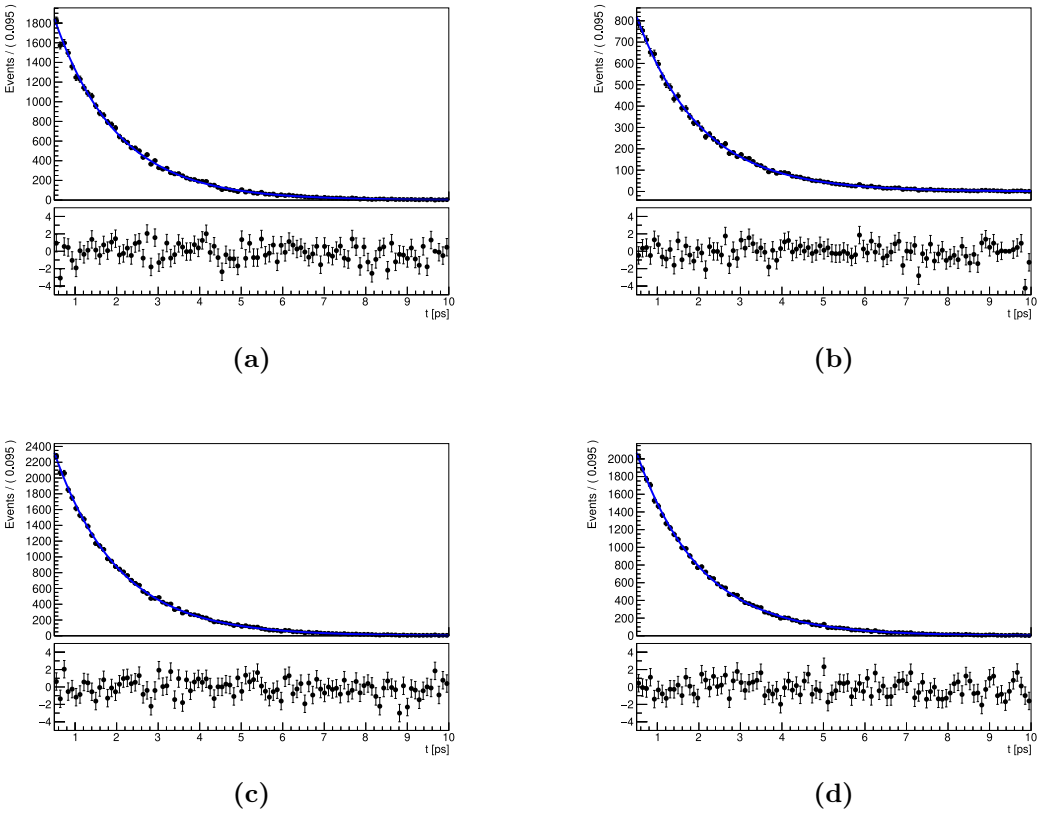

(a) **(b)**

(c) **(d)**

Figure 7.18 *Time acceptance fits for the $B_s^0 \to J/\psi\eta'$ channel from Monte Carlo sample. Figure 7.18a is the 2012 fit, fig. 7.18b is the 2016 fit, fig. 7.18c is the 2017 fit and fig. 7.18d is the 2018 fit.*

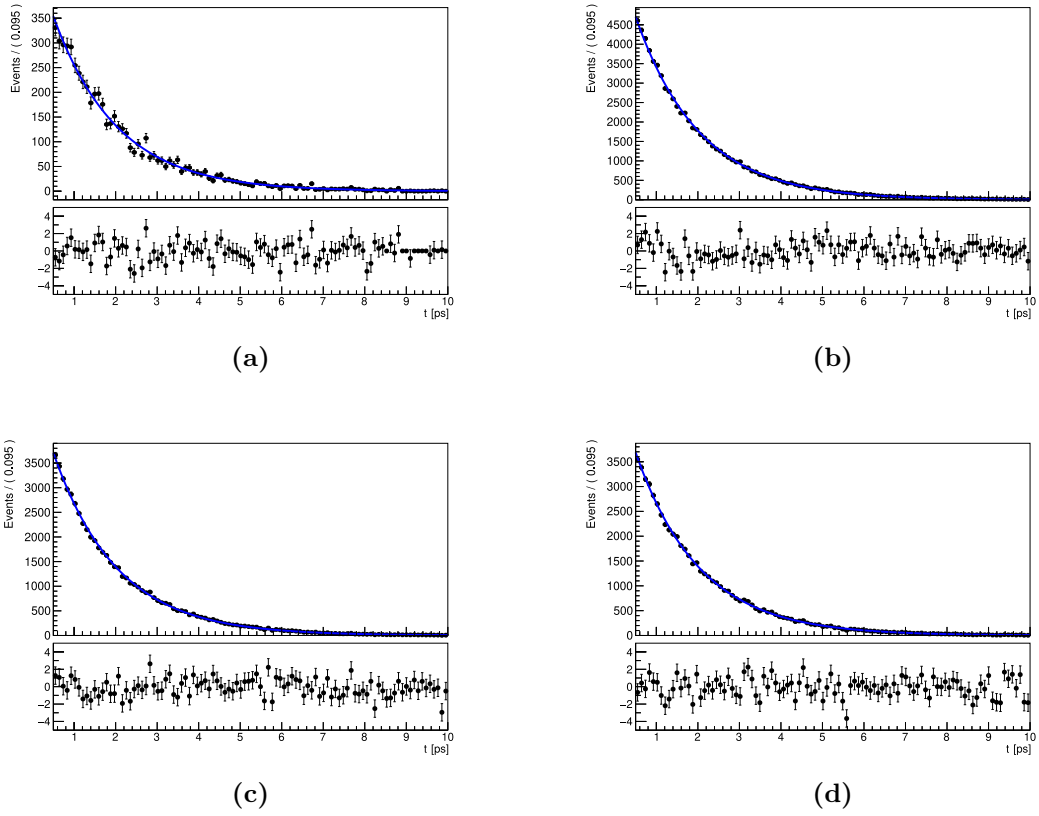

Figure 7.19 *Time acceptance fits for the $B_s^0 \to J/\psi f_0$ channel from Monte Carlo sample. Figure 7.19a is the 2012 fit, fig. 7.19b is the 2016 fit, fig. 7.19c is the 2017 fit and fig. 7.19d is the 2018 fit.*

The ratio between $B_s^0 \to J/\psi\eta'$ and $B_s^0 \to J/\psi f_0$ yields is corrected for the time acceptance by evaluating the ratio of the acceptance functions $(\mathcal{A}_{\text{fit}}^{\eta'}(t)\,/\mathcal{A}_{\text{fit}}^{f_0}(t))$ at the bin barycenter. The choice of the bin barycenter is motivated from toy studies similar to those described in section 7.1 and by the discussion in [36]. The results of the toy studies are listed in tables 7.14, 7.15, 7.16 and 7.17. The analytical formula of the acceptance correction is shown in eq. (7.4).

$$\frac{\mathcal{A}_{\text{fit}}^{\eta'}(t)}{\mathcal{A}_{\text{fit}}^{f_0}(t)} = \frac{1 - b_{\eta'} t}{1 - b_{f_0} t} \approx 1 - (b_{\eta'} - b_{f_0})\, t. \tag{7.4}$$

7.4 $\Delta\Gamma_s$ fit

The value of $\Delta\Gamma_s$ is determined by a χ^2 minimization of eq. (2.26) where the yields for each channel are taken from the simultaneous fits described in section 7.2.3.

In table 7.13 the values of $\Delta\Gamma_s$ separated by data set and corrected for the time acceptance are listed while fig. 7.20 compares the fit result (red line) to the experimental data (dots). The fit quality for each data set, judged from the probability of χ^2, is good. Figure 7.21 shows the values for the four years together with a weighted average. The results for the four years are consistent.

Year	$\Delta\Gamma_s$ [ps^{-1}]	Normalization	Prob χ^2	$\Delta\Gamma_s$ [ps^{-1}] no TA
2011 + 2012	0.043 ± 0.026	0.161 ± 0.006	0.75	0.047 ± 0.026
2015 + 2016	0.079 ± 0.022	0.154 ± 0.005	0.71	0.078 ± 0.022
2017	0.112 ± 0.023	0.153 ± 0.005	0.43	0.111 ± 0.023
2018	0.082 ± 0.020	0.161 ± 0.005	0.75	0.081 ± 0.020

Table 7.13 $\Delta\Gamma_s$ *measurement split by year. Where TA is the time acceptance.*

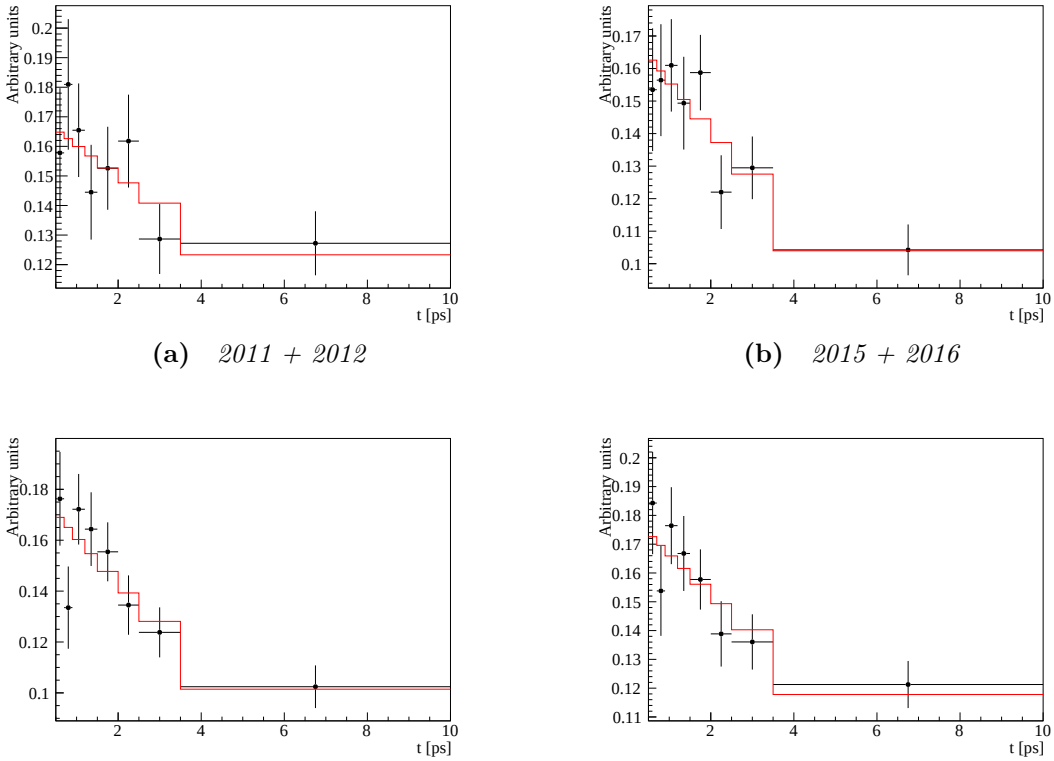

(a) *2011 + 2012* **(b)** *2015 + 2016*

(c) *2017* **(d)** *2018*

Figure 7.20 $\Delta\Gamma_s$ *fit results. The red line shows the fitted value while the points show the data.*

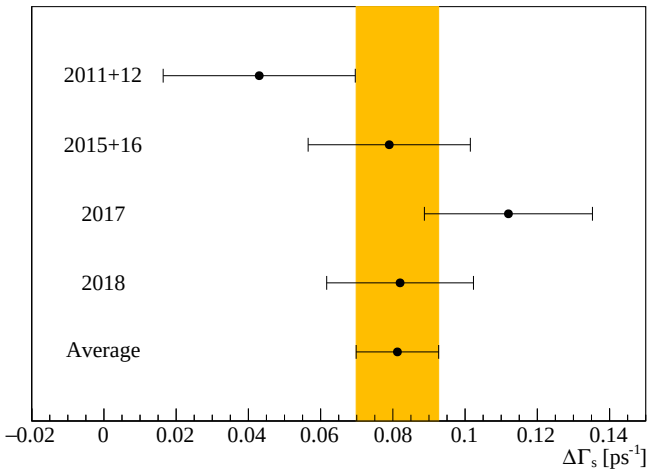

Figure 7.21 $\Delta\Gamma_s$ *measurements. From the top, each measure represent a period of data taking. The bottom measure is the weighted average across the Run 1 and Run 2 data set. The orange band is the* 1 σ *error band. The probability of* χ^2 *of the four measurements is 0.28.*

The weighted average across the full Run 1 and Run 2 data set is

$$\Delta\Gamma_s = (0.081 \pm 0.011)\ \text{ps}^{-1}$$

where the uncertainty is statistical.

7.5 Systematic uncertainties

Most systematic uncertainties cancel in the ratio. The statistical uncertainty due to the acceptance correction is obtained by computing $\Delta\Gamma_s$ changing the acceptance correction values to $\pm 1\sigma$. The two values of $\Delta\Gamma$ are then averaged and compared with the measured $\Delta\Gamma_s$. This uncertainty is included in the statistical error. The remaining sources of systematic uncertainty considered are shown in table 7.18. The normalization channel is $B_s^0 \to J/\psi\pi^+\pi^-$ with a cut within ± 90 MeV/c^2 of the nominal f_0 mass. Since this mass window is relatively broad other resonances decaying to the $J/\psi\pi^+\pi^-$ final state may be present. As discussed in section 2.4, this decay is dominated by CP-odd decays. In [95] the CP-even component in this decay is limited to be less than 0.6% at 95% confidence level. Toy studies where the $J/\psi\pi^+\pi^-$ final state is generated including a 0.6% CP-even component which is then neglected in the fit show

a bias < 0.1 ns^{-1} which is considered as systematic uncertainty. As shown in section 7.1, the $\Delta\Gamma_s$ fit is relatively insensitive to the value of Γ_s used. Varying the value of Γ_s by 0.0035 ps^{-1}, the current uncertainty on the world average, gives an uncertainty of 0.1 ns^{-1}. The method used assumes ϕ_s to be zero but the current Heavy Flavor AVeraging (HFLAV) average is $\phi_s = -0.05 \pm 0.019$ rad. Toy studies using the central value of the HFLAV average and neglecting CP violation give a bias of 0.1 ns^{-1} which is considered systematic uncertainty. The $z-$scale of the VELO is known to a precision of 2×10^{-4} [29]. Assuming a pure exponential distribution, this will cancel when performing the ratio between the two channels. This assumption was confirmed by toy studies. By default, the acceptance is calculated at the barycenter of the bin. Since the bins are relatively large, other possibilities are considered. There are different ways to evaluate the time acceptance, in this work the three strategies described in [36] are considered: the bin center, the bin barycenter and x_{lw}.

Tables 7.14, 7.15, 7.16 and 7.17 show the results of toy studies run with three methods to evaluate the time acceptance for each year.

Condition	Bias [$\times 10^{-4}$ps^{-1}]
No correction	37.1 ± 0.8
Bin center	16.2 ± 0.8
Bin barycenter	-1.6 ± 0.8
x_{lw}	-7.8 ± 0.8

Table 7.14 *Toy studies calculating the bias on $\Delta\Gamma_s$ for the acceptance function evaluated in different bin positions. The values are computed using 2011-2012 Monte Carlo and the corresponding values of b shown in table 7.12.*

Condition	Bias [$\times 10^{-4}$ps^{-1}]
No correction	-7.0 ± 0.8
Bin center	3.7 ± 0.8
Bin barycenter	0.5 ± 0.8
x_{lw}	2.0 ± 0.8

Table 7.15 *Toy studies calculating the bias on $\Delta\Gamma_s$ for the acceptance function evaluated in different bin positions. The values are computed using 2015-2016 Monte Carlo and the corresponding values of b shown in table 7.12.*

Condition	Bias $[\times 10^{-4}\text{ps}^{-1}]$
No correction	-14.8 ± 0.8
Bin center	3.1 ± 0.8
Bin barycenter	-1.8 ± 0.8
x_{lw}	0.3 ± 0.8

Table 7.16 *Toy studies calculating the bias on $\Delta\Gamma_s$ for the acceptance function evaluated in different bin positions. The values are computed using 2017 Monte Carlo and the corresponding values of b shown in table 7.12.*

Condition	Bias $[\times 10^{-4}\text{ps}^{-1}]$
No correction	-10.0 ± 0.8
Bin center	-0.5 ± 0.8
Bin barycenter	-3.0 ± 0.8
x_{lw}	-2.0 ± 0.8

Table 7.17 *Toy studies calculating the bias on $\Delta\Gamma_s$ for the acceptance function evaluated in different bin positions. The values are computed using 2018 Monte Carlo and the corresponding values of b shown in table 7.12.*

Based on the results shown in tables 7.14, 7.15, 7.16 and 7.17, a systematic uncertainty of 0.3 ns^{-1} is assigned.

A linear dependence of the acceptance on the decay time is assumed. Fitting the simulation with the form $1 - bt^n$ gives $n = 1.01 \pm 0.47$, validating this assumption. To evaluate a systematic uncertainty, acceptance functions with $n = 0.5$ and $n = 1.5$ are considered. Two values of $\Delta\Gamma_s$ are computed using $n = 0.5$ and $n = 1.5$, averaged and, the final value, compared with the one calculated with the reference acceptance. This gives a systematic uncertainty of 0.5 ns^{-1}.

To evaluate the systematic uncertainty due to the choice of signal model, the double sided Crystal Ball function is replaced by the sum of a Gaussian plus a Crystal Ball for both signal and normalization modes. The value of $\Delta\Gamma_s$ shifts by 2 ns^{-1} which is considered as the systematic uncertainty due to the signal mass model. To assess the impact of the background model, three different tests are performed: replacing exponential function by a first order Chebyshev polynomial for both channels, leaving the fraction of the Crystal Ball and Gaussian in the $B^+ \to J/\psi\pi^+$ and $B^+ \to J/\psi K^+$ component floating in the $B_s^0 \to J/\psi f_0$ fit

model and varying the f_ϕ fraction within $\pm 1\sigma$ of its uncertainty (section 7.2.1) in the $B_s^0 \to J/\psi\eta'$ mass model. Among the three tests, keeping the fraction of $B^+ \to J/\psi\pi^+$ and $B^+ \to J/\psi K^+$ floating produced the biggest variation: 9.1 ns^{-1}. This value is taken as the systematic uncertainty due to the background mass model.

Table 7.18 summarizes the systematic uncertainties used in the analysis. The total systematic uncertainty assigned is 9.3 ns^{-1}.

Source	Value [ns^{-1}]
Fit bias	0.3
Time acceptance function	0.5
CP-even component	0.1
CP violation	0.1
Γ_s	0.1
Signal mass model	2.0
Background mass model	9.1
z-scale	–
Quadrature sum	9.3

Table 7.18 *Systematic uncertainties on the measurement of* $\Delta\Gamma_s$*. Uncertainties less than* 0.1 ns^{-1} *are given as "–".*

Chapter 8

Conclusions

In this thesis, the full LHCb Run 1 and Run 2 data set, corresponding to an integrated luminosity of 9.0 fb^{-1} of proton-proton collisions, was analyzed to measure $\Delta\Gamma_s$ using the $B_s^0 \to J/\psi\eta'$ and $B_s^0 \to J/\psi f_0$ decays.

Particular attention was dedicated at studying and modelling the time acceptance as well as at using time unbiased selection. The fitting method was validated with toy studies focused on understanding and minimizing the bias on $\Delta\Gamma_s$.

The final result is

$$\Delta\Gamma_s = (0.081 \pm 0.011 \pm 0.009)\ \text{ps}^{-1}$$

where the first uncertainty is statistical and the second is systematic. The measured value of $\Delta\Gamma_s$ is in good agreement with the HFLAV world average, $\Delta\Gamma_s = 0.082 \pm 0.005\ \text{ps}^{-1}$, and theoretical predictions which are in the range $7.7 - 9.2\ \text{ns}^{-1}$. In figs. 8.1 and 8.2 the HFLAV $\Delta\Gamma_s$ versus Γ_s plots with the measured $\Delta\Gamma_s$ shown as the purple band. The analysis presented here does not measure Γ_s as it has limited sensitivity to its value. However, the HFLAV plot shows a wide range for Γ_s. Hence, $\Delta\Gamma_s$ is represented as a tilted horizontal band where the inclination angle is obtained by fitting $\Delta\Gamma_s$ with the maximum and minimum values of Γ_s shown in the plot.

The result obtained by analyzing Run 1 and Run 2 is dominated by the statistical uncertainty. During Run 3 and Run 4 LHCb plans to collect an integrated

luminosity of $\sim$ 50 fb^{-1} allowing the statistical uncertainty to be reduced by a factor of two, matching the current world average precision.

The full software trigger for Run 3 makes real time monitoring critical. Performance measurements of the Run 2 HLT monitoring system were computed and are shown in chapter 5. Due to the new configuration of the HLT, a new prototype of the HLT monitoring system using commercial software was developed and tested as a part of the PhD program.

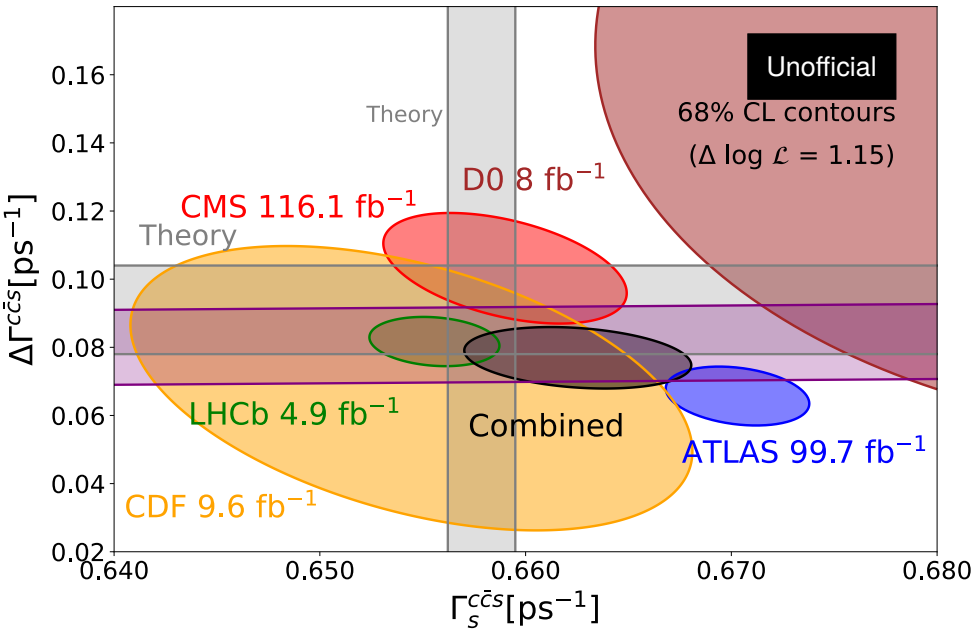

Figure 8.1 *$\Delta\Gamma_s$ versus Γ_s ($c\bar{c}s$) plot*[1] *updated with the measure presented in this work (horizontal purple band)*

[1]This is an unofficial plot generated using the software shared by HFLAV [20]

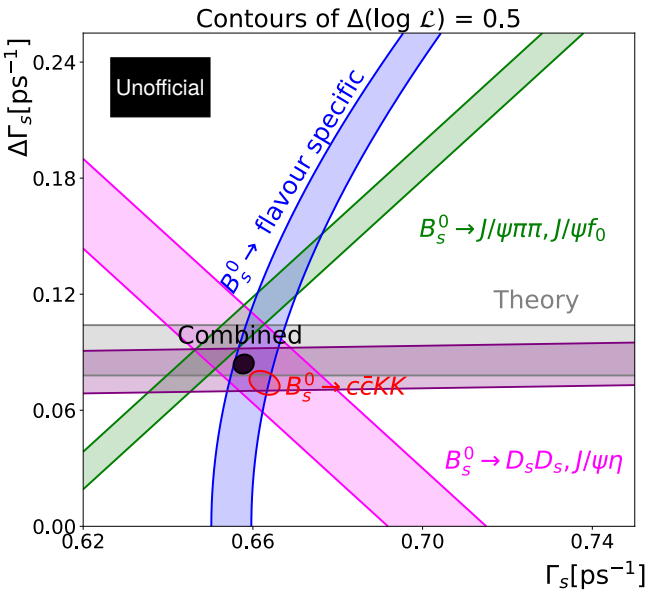

Figure 8.2 *$\Delta\Gamma_s$ versus Γ_s plot updated with the measure presented in this work (horizontal purple band)*

Appendix A

p_T re-weighting

In order to have a better agreement between data and Monte Carlo before the MVA training, the p_T spectra of the $B_s^0 \to J/\psi\eta'$ and $B_s^0 \to J/\psi f_0$ p_T decay samples are re-weighted. The f_0 channel was used to compute the weights since it is a larger and cleaner sample than the $B_s^0 \to J/\psi\eta'$ decay. The weights are computed by calculating the ratio between the s-weighted data and the Monte Carlo. The effect of the re-weighting procedure can be seen on s-weighted data and Monte Carlo distributions before re-weighting (fig. A.1a) and after (fig. A.1b) for the f_0 channel. Figure A.2 shows the B_s^0 p_T distributions for 2016 η' data and Monte Carlo.

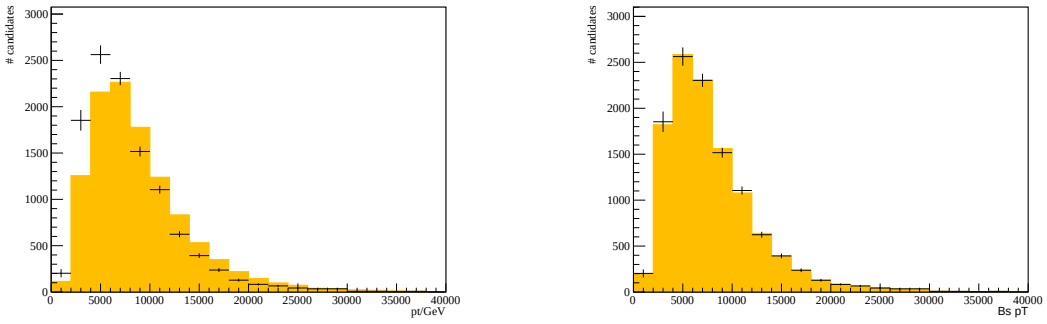

(a) **(b)**

Figure A.1 *$p_T\left(B_s^0\right)$ re-weighting for the f_0 channel. Figure A.1a shows 2016 data (dots) compared to out of the box 2016 simulation (histogram); fig. A.1b shows the same comparison with the re-weighted Monte Carlo.*

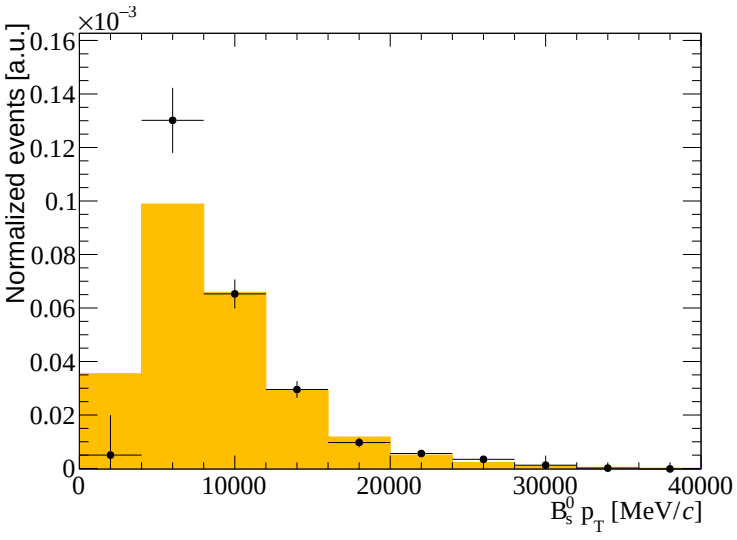

Figure A.2 *$p_T\left(B_s^0\right)$ re-weighting comparison for the 2016 η' channel. The dots represent the s-weighted data and the histogram the re-weighted Monte Carlo.*

Appendix B

TT occupancy shifting

The TT occupancy is larger in data than in the Monte Carlo as shown in fig. B.1. For this reason, the data and Monte Carlo samples were aligned by applying the shift values listed in table B.1.

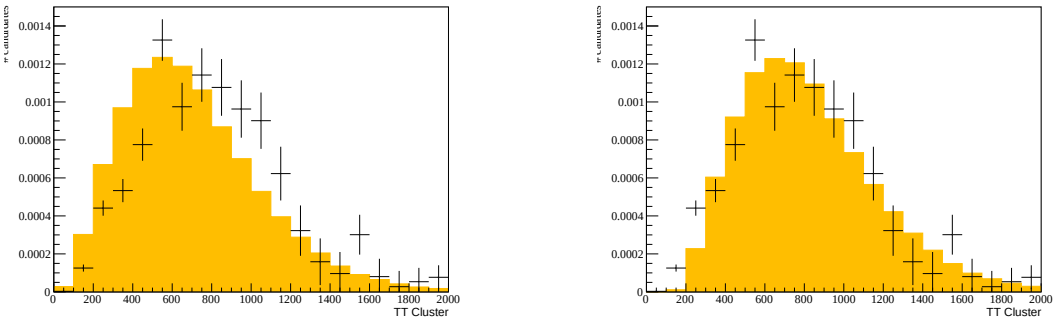

(a) **(b)**

Figure B.1 *TT occupancy distribution comparison between 2016 f_0 Monte Carlo (in yellow) and 2016 f_0 s-weighted data (black dots). Left plot shows the two distributions before the shift, right plot shows the distributions after the shift.*

Year	TT occupancy shift
2011 + 2012	+100
2015 + 2016	+120
2017	+120
2018	+120

Table B.1 *TT occupancy shift values*

Appendix C

χ^2_{IP} scaling

The calibration of the χ^2_{IP} is performed on the $B^0_s \to J/\psi f_0$ sample and applied to both samples of the analysis. To find the best calibration factor, a scan across multiple scaling factors was performed and a χ^2 test between the s-weighted data and the calibrated Monte Carlo sample is performed. The value minimizing the χ^2 is taken as the scaling factor. Figures C.1, C.2 and C.3 show the χ^2_{IP} distributions before and after the calibration was applied. In table C.1 the scaling factors for Run 1 and Run 2.

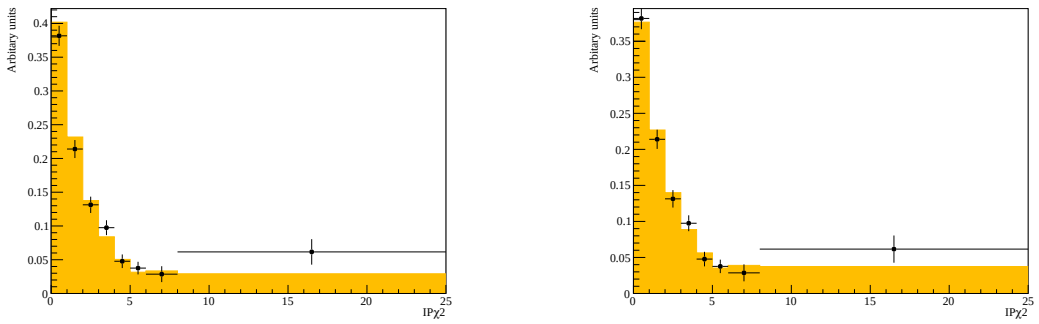

(a) **(b)**

Figure C.1 χ^2_{IP} *comparison for the 2016* f_0 *sample. Figure C.1a shows the Monte Carlo distribution (histogram) compared with s-weighted data (dots) before applying the scaling, fig. C.1b after.*

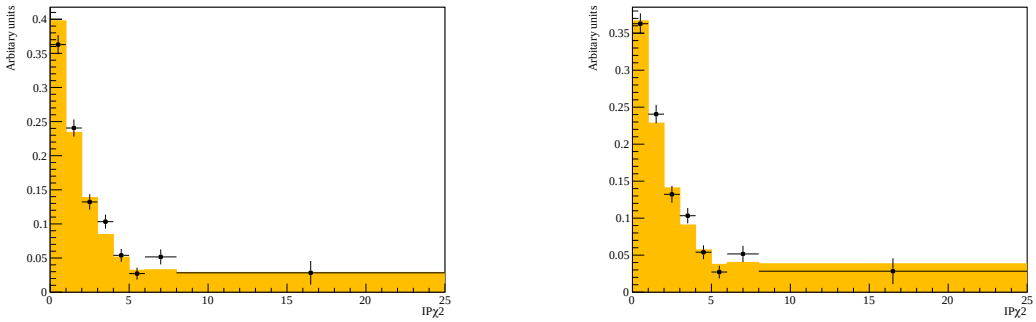

(a) **(b)**

Figure C.2 χ^2_{IP} *comparison for the 2017* f_0 *sample. Figure C.2a shows the Monte Carlo distribution (histogram) compared with s-weighted data (dots) before applying the scaling, fig. C.2b after.*

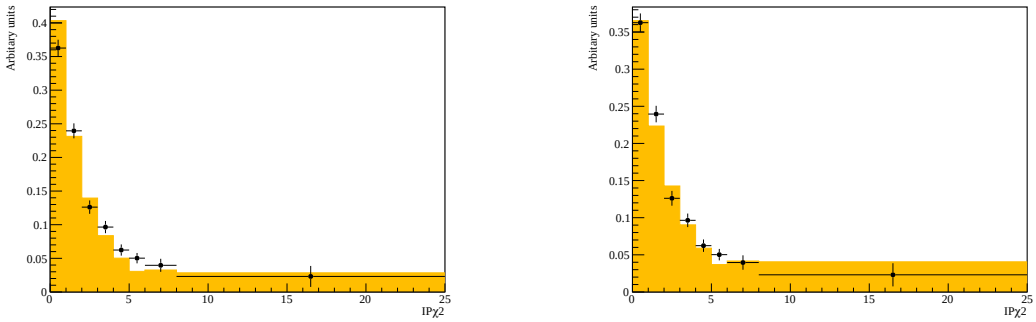

(a) **(b)**

Figure C.3 χ^2_{IP} *comparison for the 2018* f_0 *sample. Figure C.3a shows the Monte Carlo distribution (histogram) compared with s-weighted data (dots) before applying the scaling, fig. C.3b after.*

Year	Scaling factor
2011 + 2012	0.95
2015 + 2016	1.09
2017	1.11
2018	1.14

Table C.1 χ^2_{IP} *calibration factors*

Appendix D

Cone Isolation

In contrast to the particles of the underlying event, B mesons are produced with higher energy and tend to be more efficiently reconstructed at lower detector occupancy. These features can be exploited to discriminate signal against background, based on the kinematic and the number of particles contained inside a cone defined around the B flight direction. In the two-dimensional space of azimuth angle ϕ and pseudorapidity η, the cone angle can be represented by a circle with $\sqrt{\Delta\phi^2 + \Delta\eta^2}$ radius. In this analysis followed the same approach as [96], fixing the cone radius to be 1.8. This size was chosen to minimize the occurrence of events where only the signal final-state particles are contained inside the cone as they carry less information. Larger cones are avoided to retain a good signal to background separation in the asymmetry variables. This tool considers separately charged and neutral reconstructed objects, calculates the number of each species and (after removing signal objects) their average p, p_X, p_Y, p_Z, p_T and η values. Asymmetries are then calculated using these latter values and the signal ones. The transverse momentum asymmetry, for instance, is defined as

$$A_{p_T} = \frac{Bp_T}{Bp_T + \sum_i p_T^i}, \tag{D.1}$$

where B p_T is the transverse momentum of the signal candidate and the index i runs over the other particles in the cone. As shown in tables 6.8 and 6.9, five isolation cone variables are used to help signal-background classification in the MVA.

D.1 Data and Monte Carlo comparison

In this section, the comparison between data and Monte Carlo distributions of cone variables is shown. This is performed using 2016 data samples from which clean signal of abundant $B^+ \to J/\psi K^+$ decays are extracted. Given the small background contamination in the signal region, no statistical subtraction of it is performed and only events in a region around the signal peak are retained. Signal peaks in data and Monte Carlo are shown in fig. D.1. Global event variables such as number of SPD hits and number of reconstructed tracks, PVs, photons and neutral pions are compared in fig. D.2. Cone variables relevant to this analysis are shown in fig. D.3 and fig. D.4, for charged and neutral cones separately. The agreement in cone variables is good and is expected to improve after re-weighting the Monte Carlo events for global event variables discrepancies.

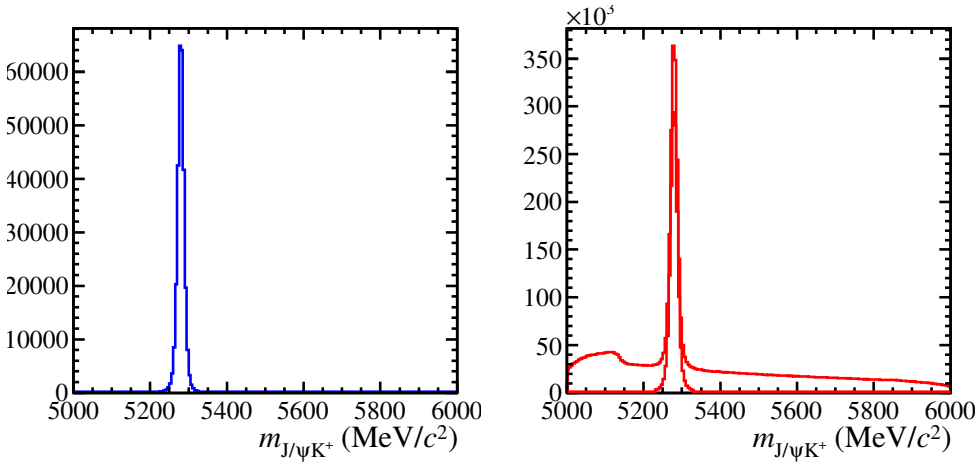

Figure D.1 *Invariant mass distribution of selected $B^+ \to J/\psi K^+$ candidates in 2016 MC (left) and data (right). The right plot shows distributions before and after offline selections which are also applied to the MC sample.*

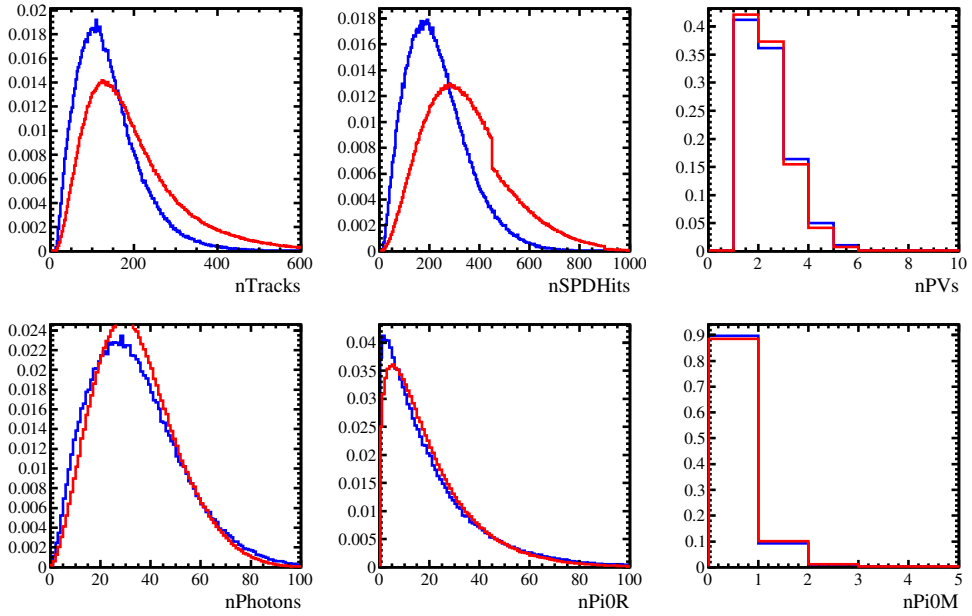

Figure D.2 *Global event variables for $B^+ \to J/\psi K^+$ candidates in data (red) and MC (blue).*

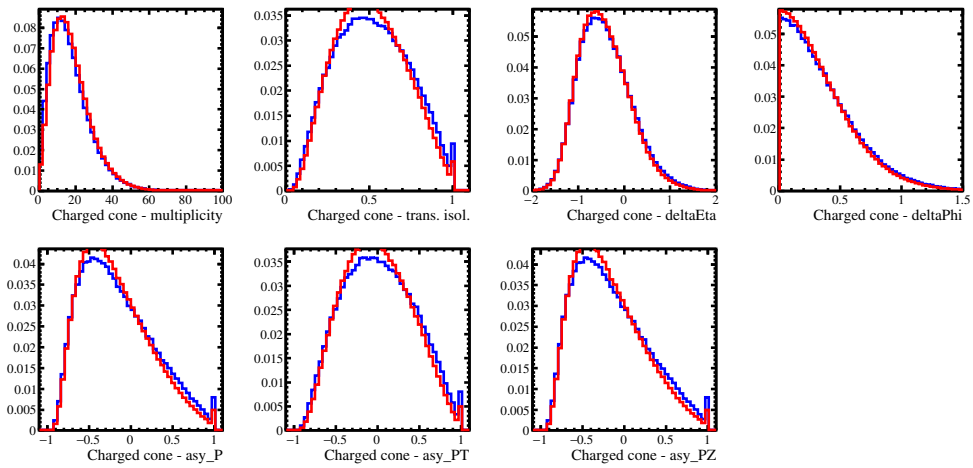

Figure D.3 *Charged cone variables for $B^+ \to J/\psi K^+$ candidates in data (red) and MC (blue).*

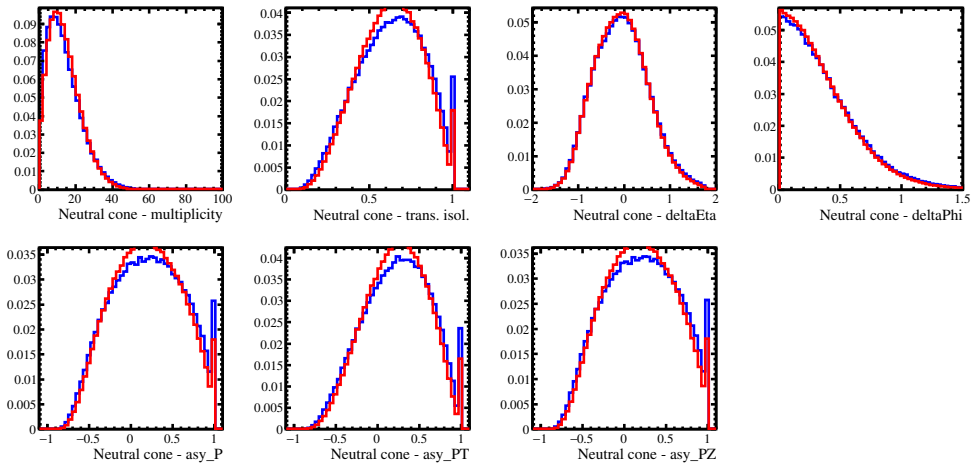

Figure D.4 *Neutral cone variables for $B^+ \to J/\psi K^+$ candidates in data (red) and MC (blue).*

Appendix E

MVA

E.1 Classifiers

Among the classifiers supported by TMVA, the BDT, BDTG and MLP were tested. In fig. E.1 the ROC curve of the three classifiers is shown. The integral of the three curves is close to one highlighting the good performance of three algorithms. Looking at the signal-background separation plots in fig. E.2, the BDT shows worse performance. Therefore, only the MLP and BDTG classifiers are considered further. Both classifiers show compatible performances in terms of the ROC curve. However, the BDTG is much faster to train. This characteristic is very helpful at the optimization stage where the classifier has to be trained multiple times in order to tune its parameters and the training variables. For this reason, the BDTG was chosen as default algorithm for both channels.

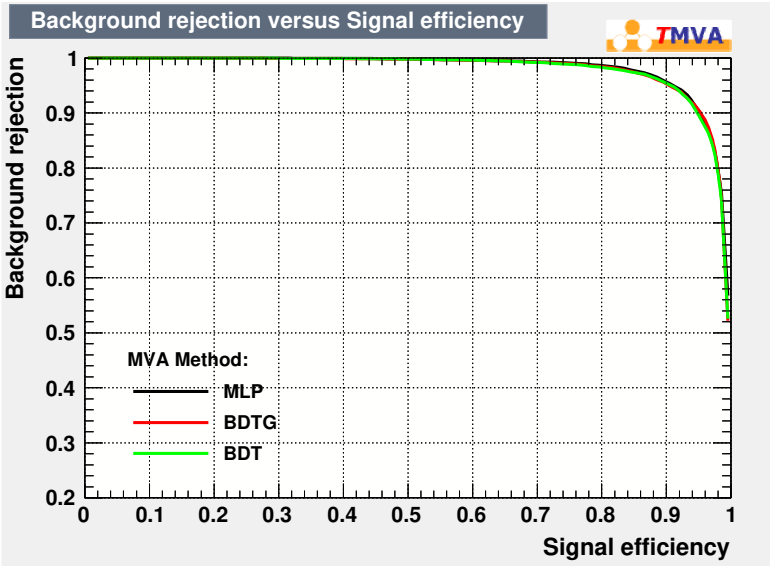

Figure E.1 *ROC curve for the three classifiers.*

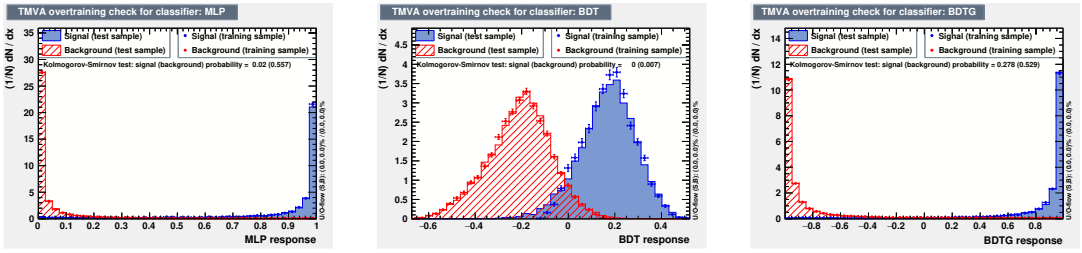

(a) **(b)** **(c)**

Figure E.2 *Signal-background separation between MLP (fig. E.2a), BDT (fig. E.2b) and BDTG (fig. E.2c).*

E.2 Input Variables

E.2.1 $B_s^0 \to J/\psi\eta'$

Table E.1 summarizes the MVA input variables and figs. E.3, E.4, E.5 and E.6 compare the variables between signal and background samples used for training. An additional check on the agreement between data and Monte Carlo training variables was performed using s-weighted data and it is shown in figs. E.7, E.8, E.9 and E.10. The output of the classifier for each MVA and the ROC curves are shown in figs. E.11, E.12, E.13 and E.14.

Variable name	Description
bs_rec_eta	B_s^0 pseudorapidity
bs_rec_chi2	Quality of the B_s^0 DTF fit
tmva_bs_pt	B_s^0 transverse momentum
tmva_min_pion_pt	Minimum of the pions transverse momentum
tmva_max_mu_ghost	Maximum of the muons ghost probability
tmva_min_mu_pt	Minimum of the muons transverse momentum
tmva_isolation_cone	Average of the B_s^0 - cone difference in eta
tmva_bs_cc_mult	Number of objects in the cone
tmva_bs_cc_asy_pz	Z components of the momentum asymmetry
tmva_bs_cc_vpt	Vector-summed PT of the objects inside the cone
tmva_bs_cc_delta_phi	Difference in phi between the B_s^0 and the cone
tmva_gamma_cl	Confidence level of the photon
tmva_gamma_pt	Transverse momentum of the photon
tmva_cos_hel_pion	Cosine of the helicity of the pions
tmva_etap_pt	η' transverse momentum
tmva_bs_ipchi2_ownpv	Quality of the B_s^0 fit
tmva_ntt_clusters	TT occupancy
tmva_pi0_r	π^0 veto

Table E.1 *Training variable names for the $B_s^0 \to J/\psi\eta'$ MVA.*

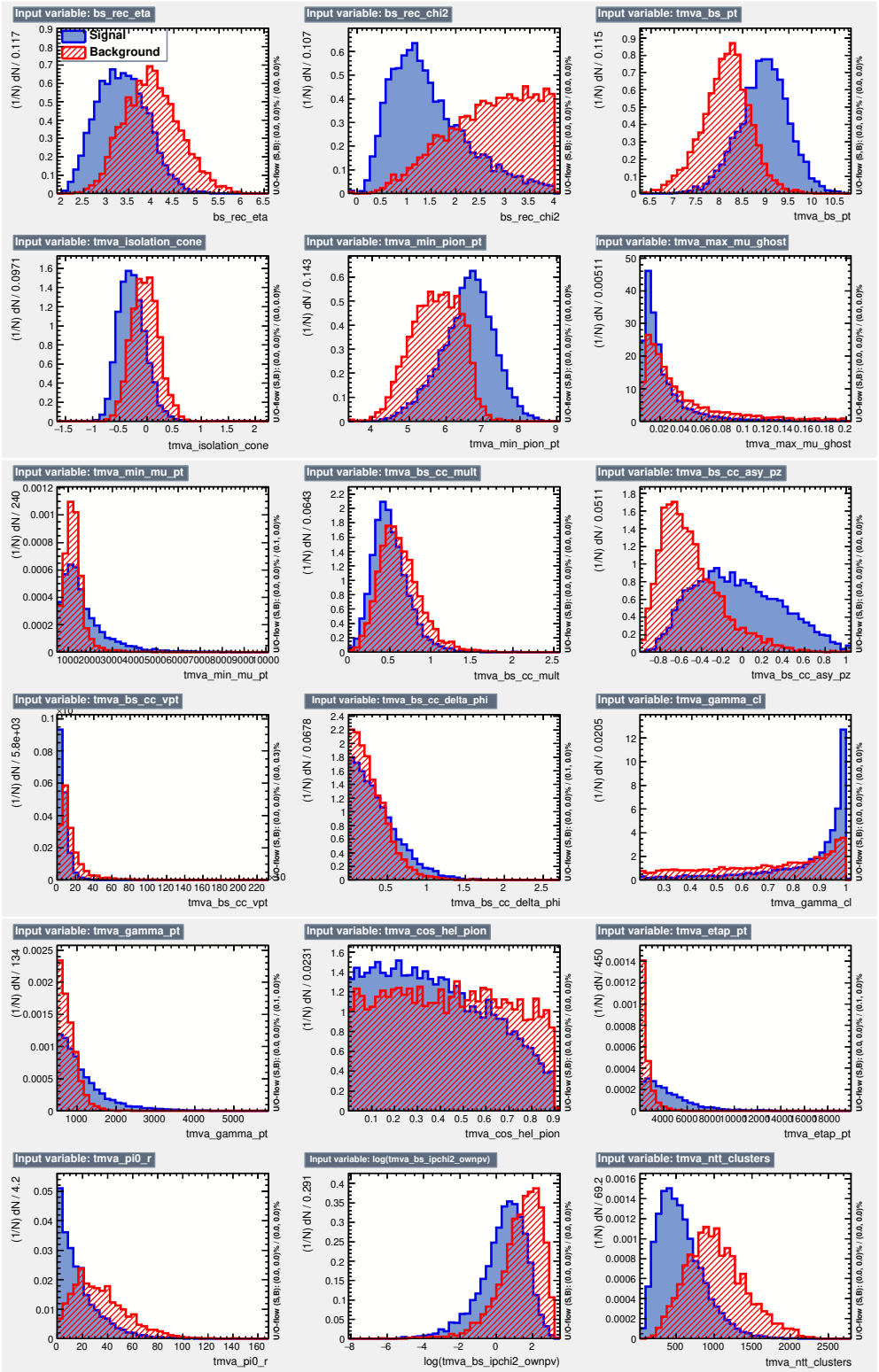

Figure E.3 *MVA input variables to the η' channel - 2012 data set.*

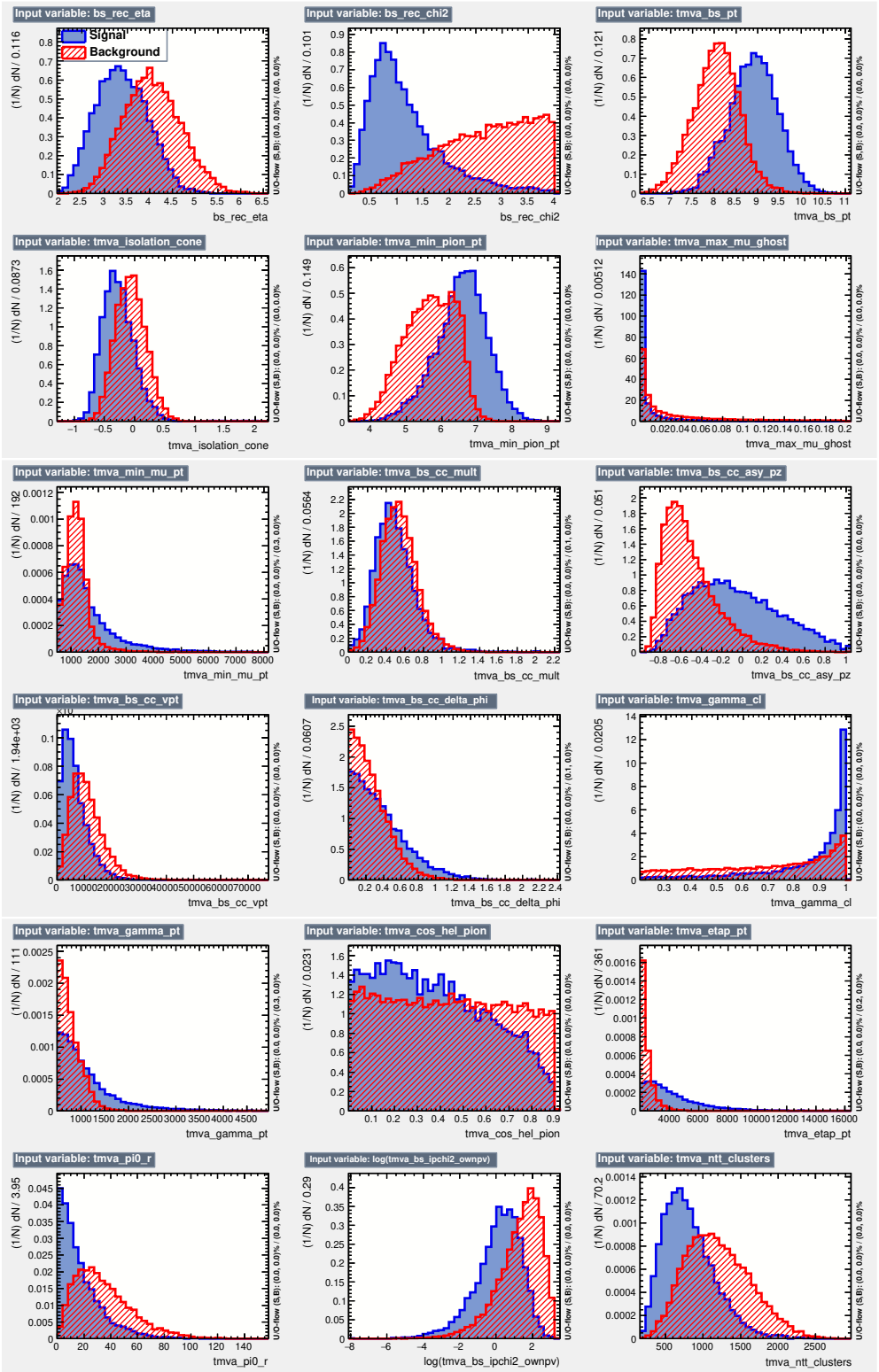

Figure E.4 *MVA input variables to the η' channel - 2016 data set.*

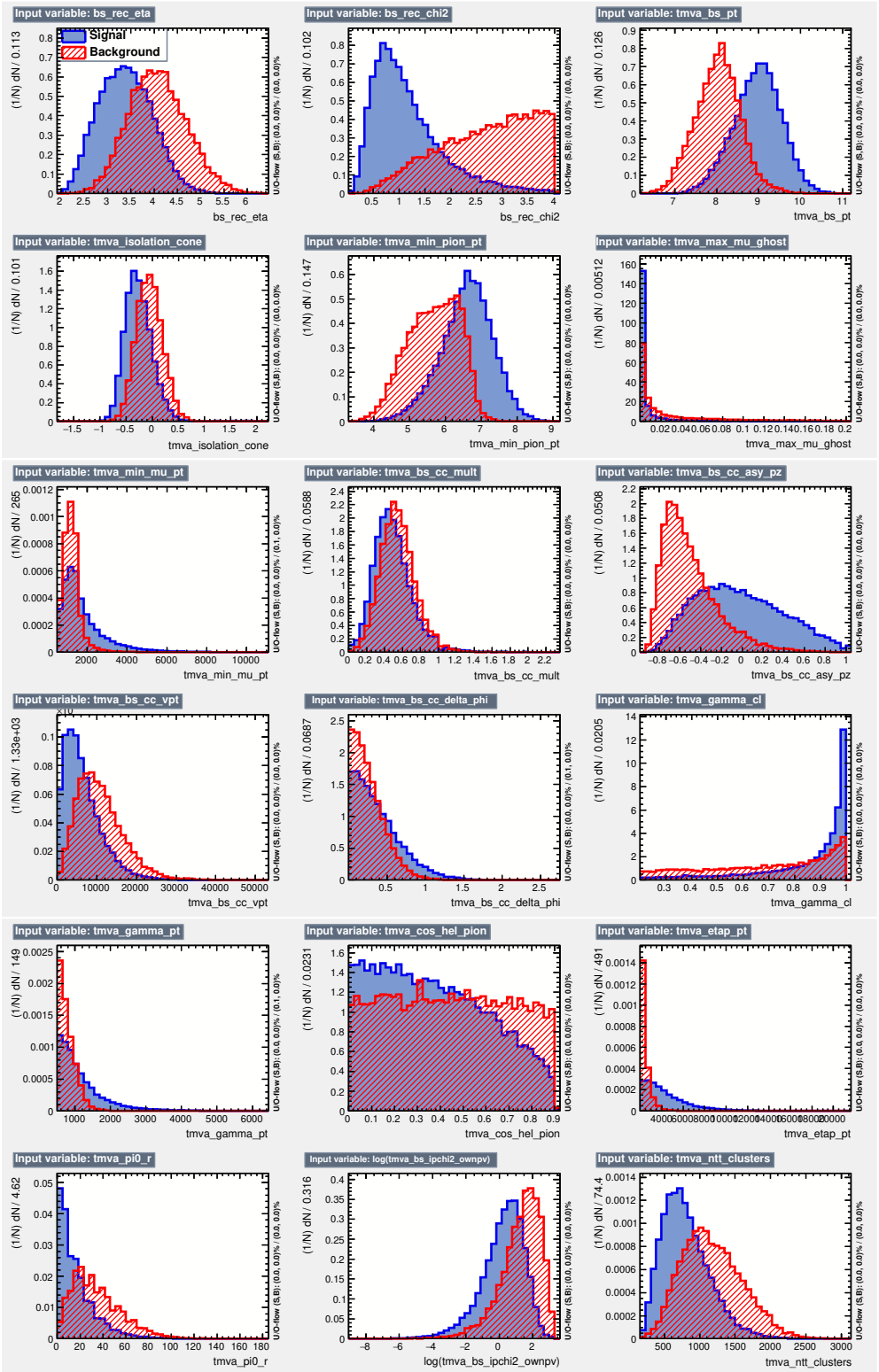

Figure E.5 *MVA input variables to the η' channel - 2017 data set.*

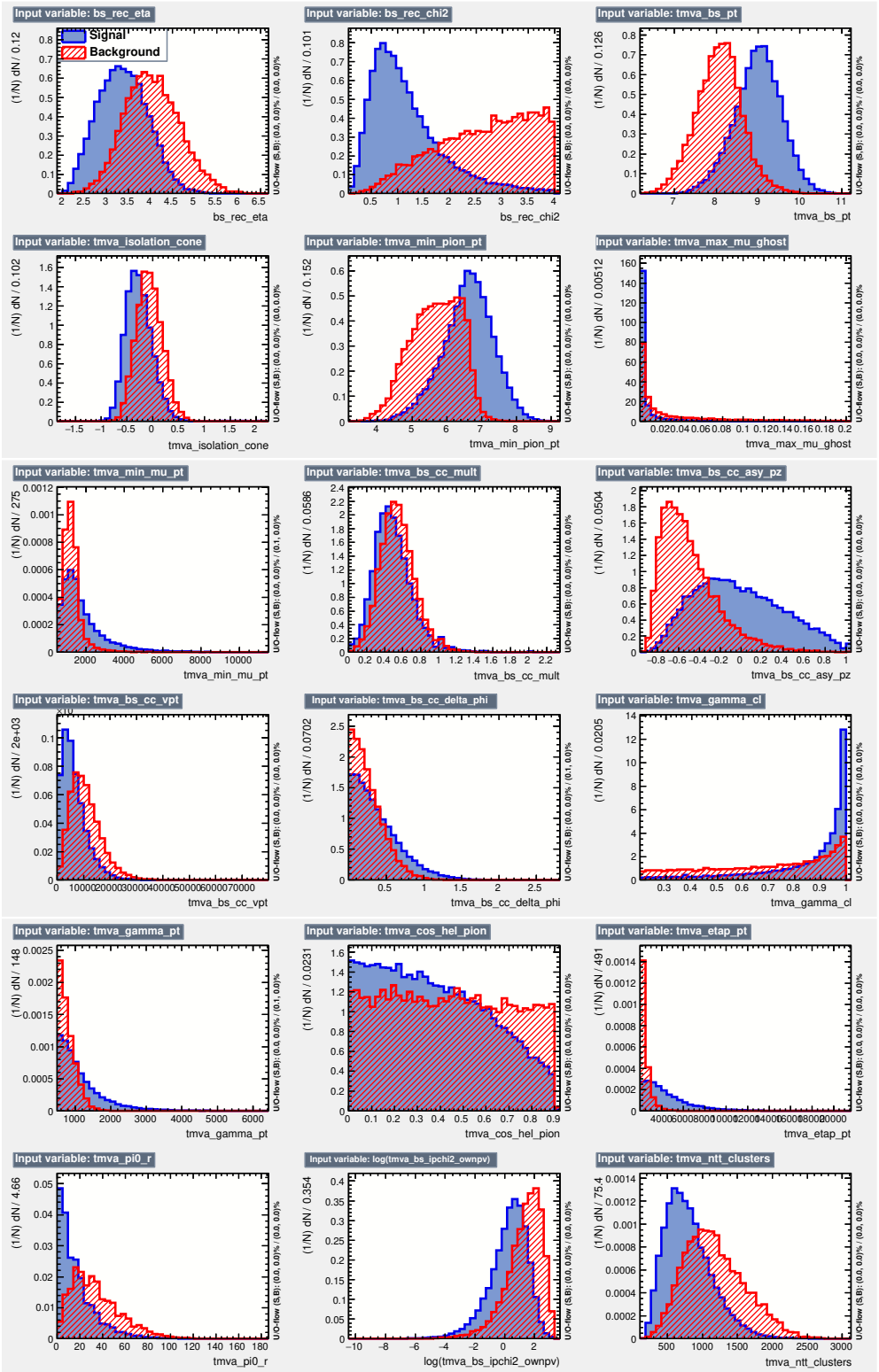

Figure E.6 *MVA input variables to the η' channel - 2018 data set.*

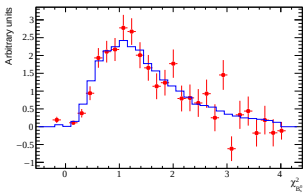

(a) $\chi^2\left(B_s^0\right)$

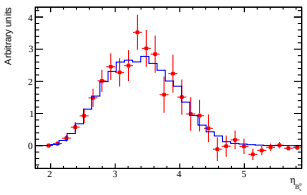

(b) $\eta\left(B_s^0\right)$

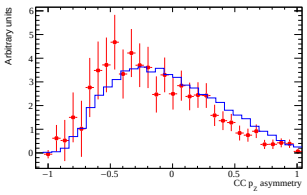

(c) B_s^0 *cc* p_Z *asymm.*

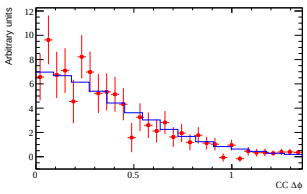

(d) B_s^0 *cc* $\Delta\phi$

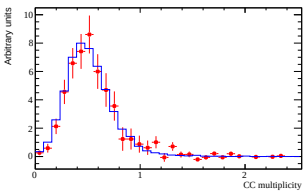

(e) *Mult* (B_s^0 *cc*)

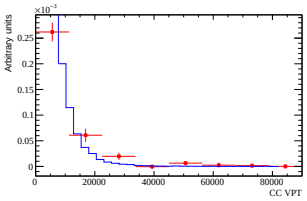

(f) B_s^0 *cc* $V\,p_T$

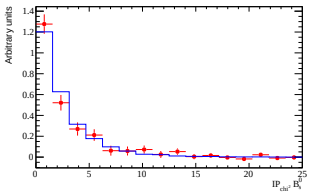

(g) $\chi^2_{\mathrm{IP}}\left(B_s^0\right)$

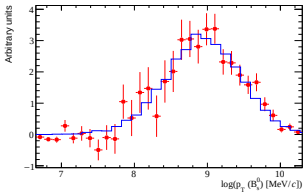

(h) $\log\left(p_T\left(B_s^0\right)\right)$

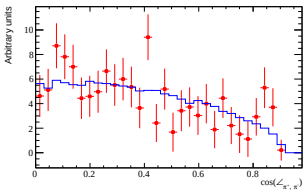

(i) $\cos\left(\angle\left(\pi_1,\pi_2\right)\right)$

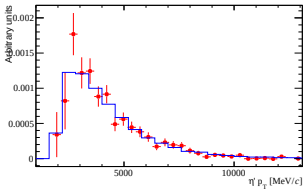

(j) $p_T\left(\eta'\right)$

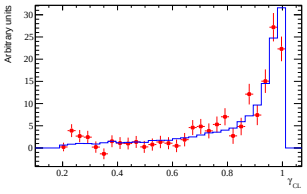

(k) γ_{CL}

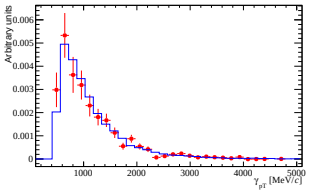

(l) $p_T\left(\gamma\right)$

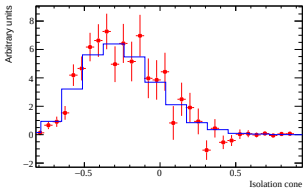

(m) *Isolation cone*

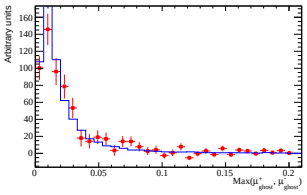

(n) $\min\left(\mu_1^{\mathrm{ghost}},\mu_2^{\mathrm{ghost}}\right)$

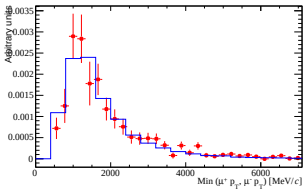

(o) $\min\left(p_T\left(\mu_1\right),p_T\left(\mu_2\right)\right)$

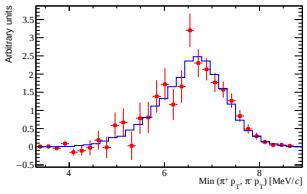

(p) $\min\left(p_T\left(\pi_1\right),p_T\left(\pi_2\right)\right)$

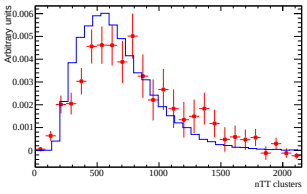

(q) *nTT clusters*

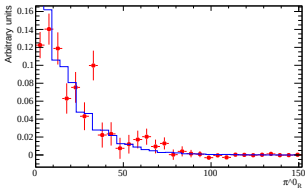

(r) $n\pi_r^0$

Figure E.7 *2012 s-weighted data (dots) and Monte Carlo (histogram) training variable comparison for the η' channel.*

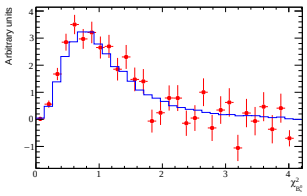

(a) $\chi^2\left(B_s^0\right)$

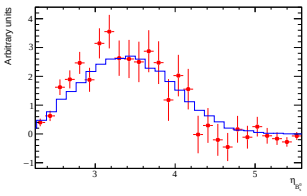

(b) $\eta\left(B_s^0\right)$

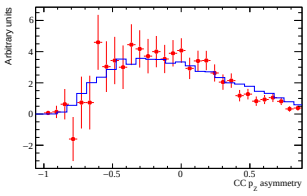

(c) B_s^0 *CC* p_Z *asymm.*

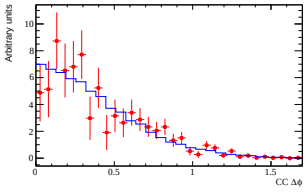

(d) B_s^0 *CC* $\Delta\phi$

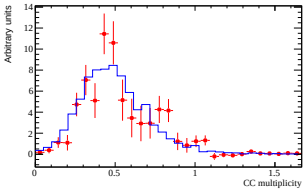

(e) *Mult* (B_s^0 *CC*)

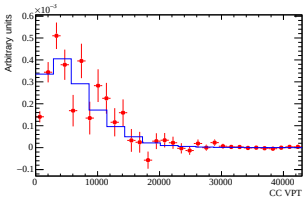

(f) B_s^0 *CC* $V\,p_T$

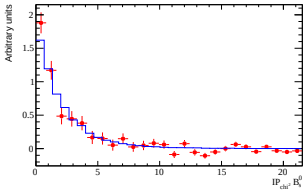

(g) $\chi^2_{\mathrm{IP}}\left(B_s^0\right)$

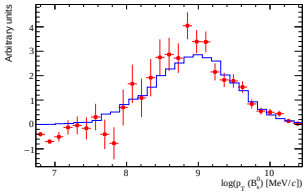

(h) $\log\left(p_T\left(B_s^0\right)\right)$

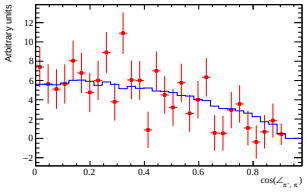

(i) $\cos\left(\angle\left(\pi_1,\pi_2\right)\right)$

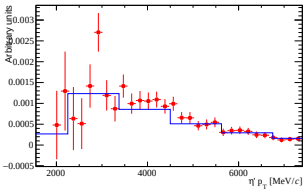

(j) $p_T\left(\eta'\right)$

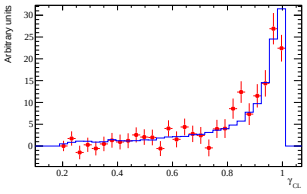

(k) γ_{CL}

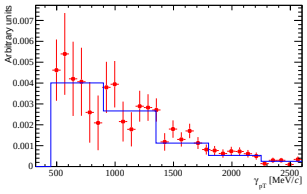

(l) $p_T\left(\gamma\right)$

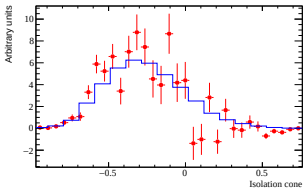

(m) *Isolation cone*

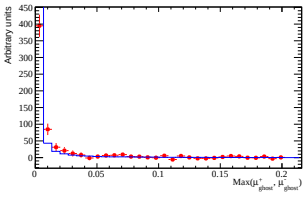

(n) $\min\left(\mu_1^{\mathrm{ghost}},\mu_2^{\mathrm{ghost}}\right)$

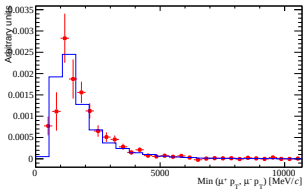

(o) $\min\left(p_T\left(\mu_1\right),p_T\left(\mu_2\right)\right)$

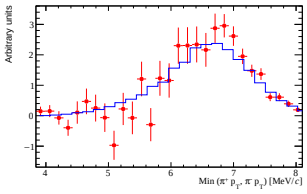

(p) $\min\left(p_T\left(\pi_1\right),p_T\left(\pi_2\right)\right)$

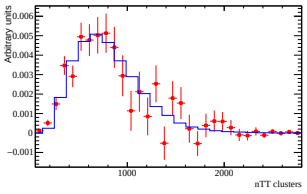

(q) *nTT clusters*

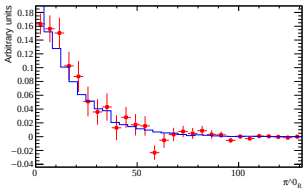

(r) $n\pi_r^0$

Figure E.8 *2016 s-weighted data (dots) and Monte Carlo (histogram) training variable comparison for the η' channel.*

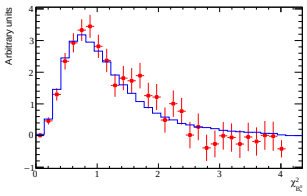

(a) $\chi^2\left(B_s^0\right)$

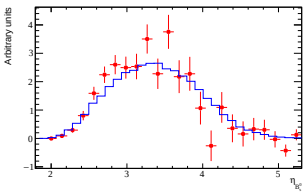

(b) $\eta\left(B_s^0\right)$

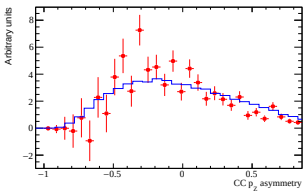

(c) B_s^0 *CC* p_Z *asymm.*

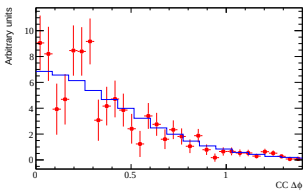

(d) B_s^0 *CC* $\Delta\phi$

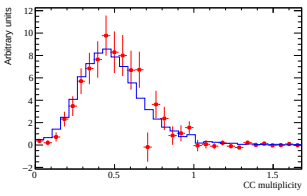

(e) *Mult* (B_s^0 *CC*)

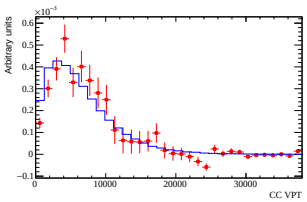

(f) B_s^0 *CC* V p_T

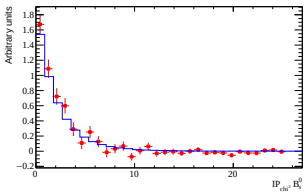

(g) $\chi^2_{\mathrm{IP}}\left(B_s^0\right)$

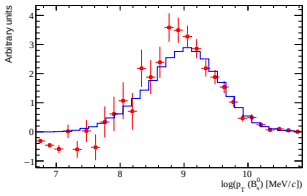

(h) $\log\left(p_T\left(B_s^0\right)\right)$

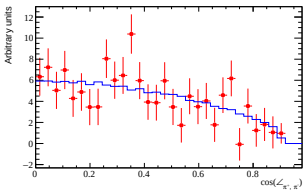

(i) $\cos\left(\angle\left(\pi_1,\pi_2\right)\right)$

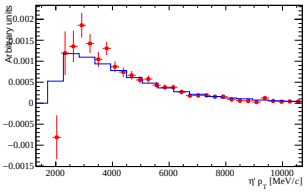

(j) $p_T\left(\eta'\right)$

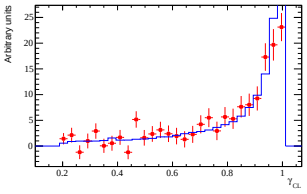

(k) γ_{CL}

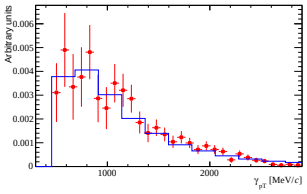

(l) $p_T\left(\gamma\right)$

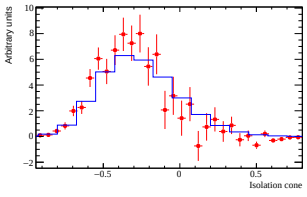

(m) *Isolation cone*

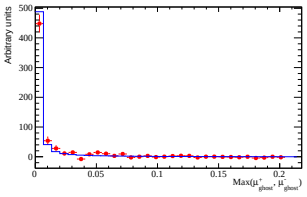

(n) $\min\left(\mu_1^{\mathrm{ghost}},\mu_2^{\mathrm{ghost}}\right)$

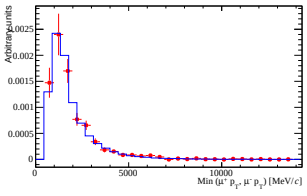

(o) $\min\left(p_T\left(\mu_1\right),p_T\left(\mu_2\right)\right)$

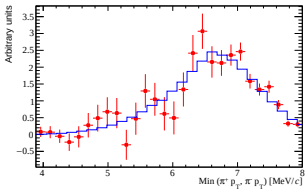

(p) $\min\left(p_T\left(\pi_1\right),p_T\left(\pi_2\right)\right)$

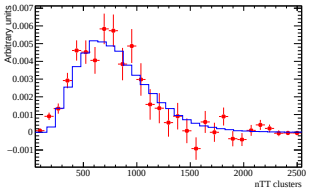

(q) *nTT clusters*

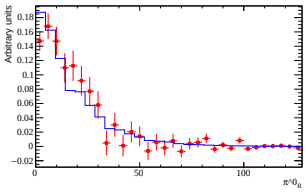

(r) $n\pi_r^0$

Figure E.9 *2017 s-weighted data (dots) and Monte Carlo (histogram) training variable comparison for the* η' *channel.*

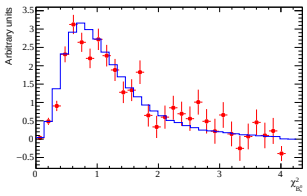

(a) $\chi^2\left(B_s^0\right)$

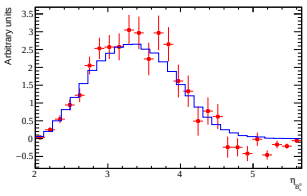

(b) $\eta\left(B_s^0\right)$

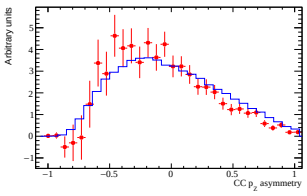

(c) B_s^0 *CC* p_Z *asymm.*

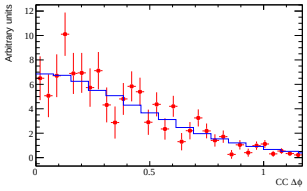

(d) B_s^0 *CC* $\Delta\phi$

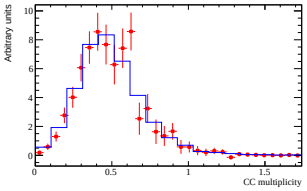

(e) *Mult* (B_s^0 *CC*)

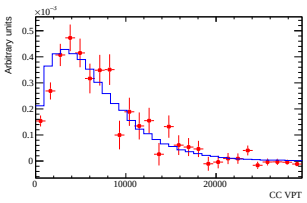

(f) B_s^0 *CC* $V\,p_T$

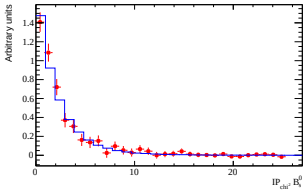

(g) $\chi^2_{\mathrm{IP}}\left(B_s^0\right)$

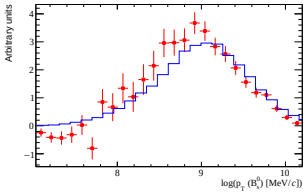

(h) $\log\left(p_T\left(B_s^0\right)\right)$

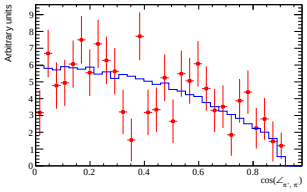

(i) $\cos\left(\angle\left(\pi_1,\pi_2\right)\right)$

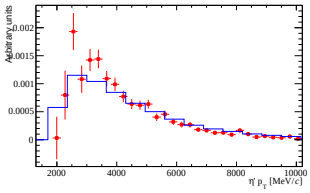

(j) $p_T\left(\eta'\right)$

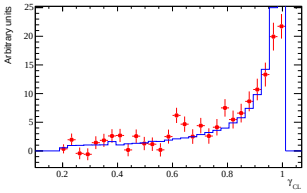

(k) γ_{CL}

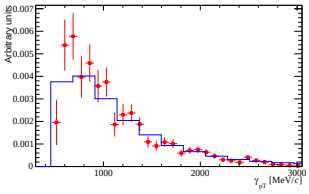

(l) $p_T\left(\gamma\right)$

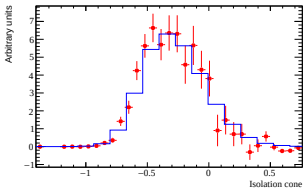

(m) *Isolation cone*

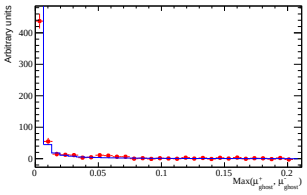

(n) $\min\left(\mu_1^{\mathrm{ghost}},\mu_2^{\mathrm{ghost}}\right)$

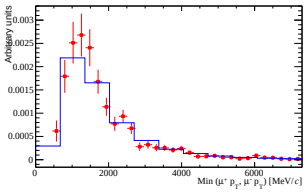

(o) $\min\left(p_T\left(\mu_1\right),p_T\left(\mu_2\right)\right)$

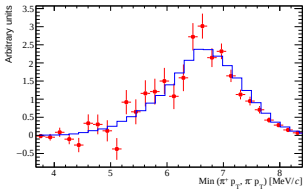

(p) $\min\left(p_T\left(\pi_1\right),p_T\left(\pi_2\right)\right)$

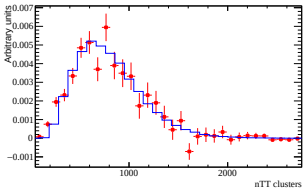

(q) *nTT clusters*

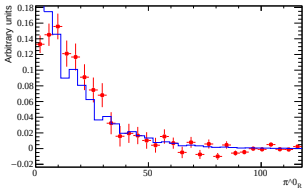

(r) $n\pi_r^0$

Figure E.10 *2018 s-weighted data (dots) and Monte Carlo (histogram) training variable comparison for the η' channel.*

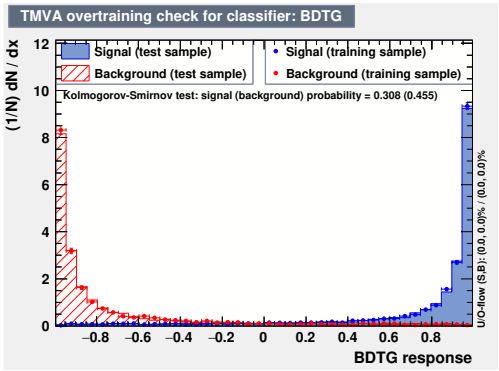

(a) *Signal-background separation*

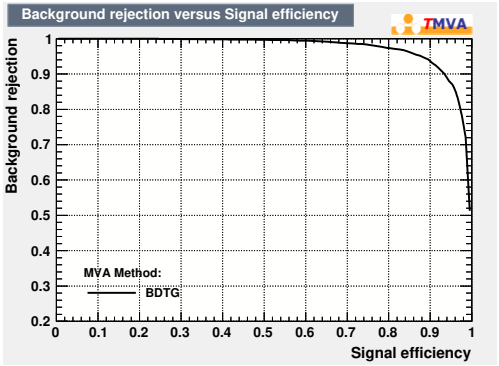

(b) *ROC curve*

Figure E.11 *Signal-background separation and ROC curve for the 2012 $B_s^0 \to J/\psi\eta'$ MVA.*

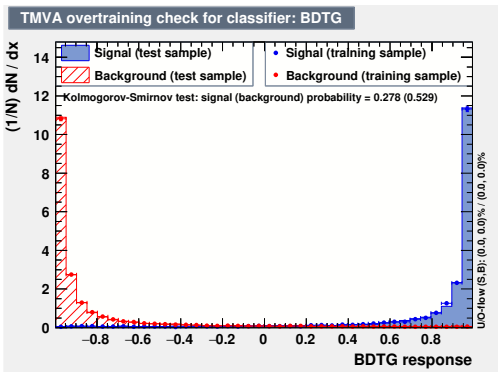

(a) *Signal-background separation*

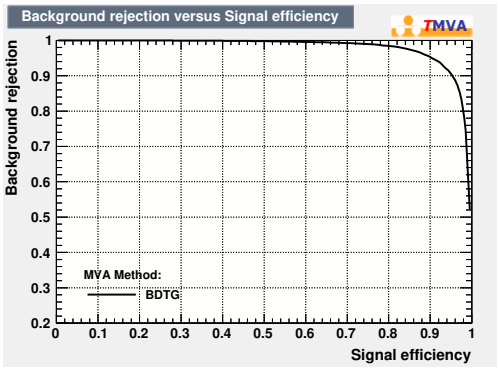

(b) *ROC curve*

Figure E.12 *Signal-background separation and ROC curve for the 2016 $B_s^0 \to J/\psi\eta'$ MVA.*

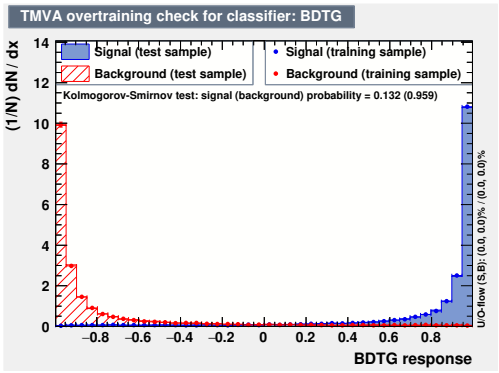

(a) *Signal-background separation*

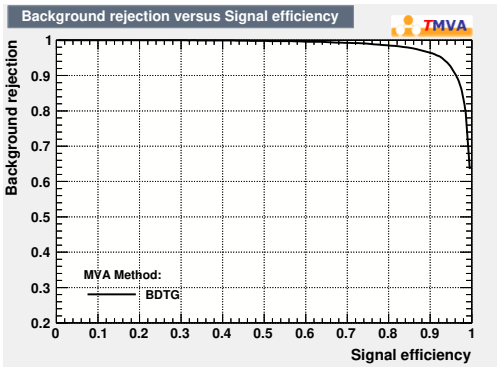

(b) *ROC curve*

Figure E.13 *Signal-background separation and ROC curve for the 2017 $B_s^0 \to J/\psi\eta'$ MVA.*

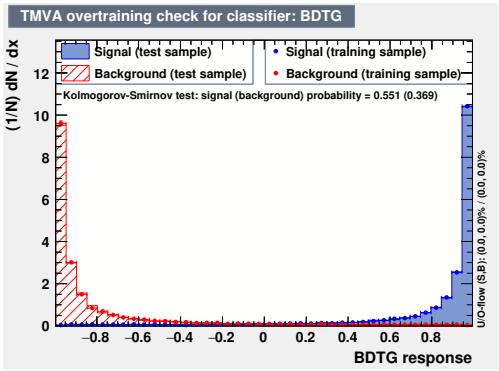

(a) *Signal-background separation*

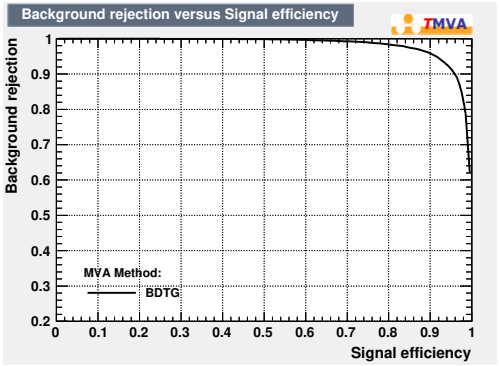

(b) *ROC curve*

Figure E.14 *Signal-background separation and ROC curve for the 2018 $B_s^0 \to J/\psi\eta'$ MVA.*

E.2.2 $B_s^0 \to J/\psi f_0$

Table E.2 summarizes the MVA input variables and figs. E.15, E.16, E.17 and E.18 compare the variables between signal and background samples used for training. An additional check on the agreement between data and Monte Carlo training variables was performed using s-weighted data and it is shown in figs. E.19, E.20, E.21 and E.22. The output of the classifier for each MVA and the ROC curves are shown in figs. E.23, E.24, E.25 and E.26.

Variable name	Description
Bs_eta	B_s^0 pseudorapidity
Bs_chi2ndof	Quality of the B_s^0 DTF fit
Bs_pt	B_s^0 transverse momentum
minpi_pt	Minimum of the pions transverse momentum
max_mu_ghost	Maximum of the muons ghost probability
minmu_pt	Minimum of the muons transverse momentum
cone	Average of the B_s^0 - cone difference in eta
Bs_1_80_mult	Number of objects in the cone
Bs_1_80_asy_PZ	Z components of the momentum asymmetry
Bs_1_80_vPT	Vector-summed PT of the objects inside the cone
Bs_1_80_dphi	Difference in phi between the B_s^0 and the cone
Bs_1_80_IT	Transverse isolation of the B_s^0 in the cone
Bs_IPCHI2_OWNPV	Quality of the B_s^0 fit
TT	TT occupancy

Table E.2 *Training variable names for the $B_s^0 \to J/\psi f_0$ MVA.*

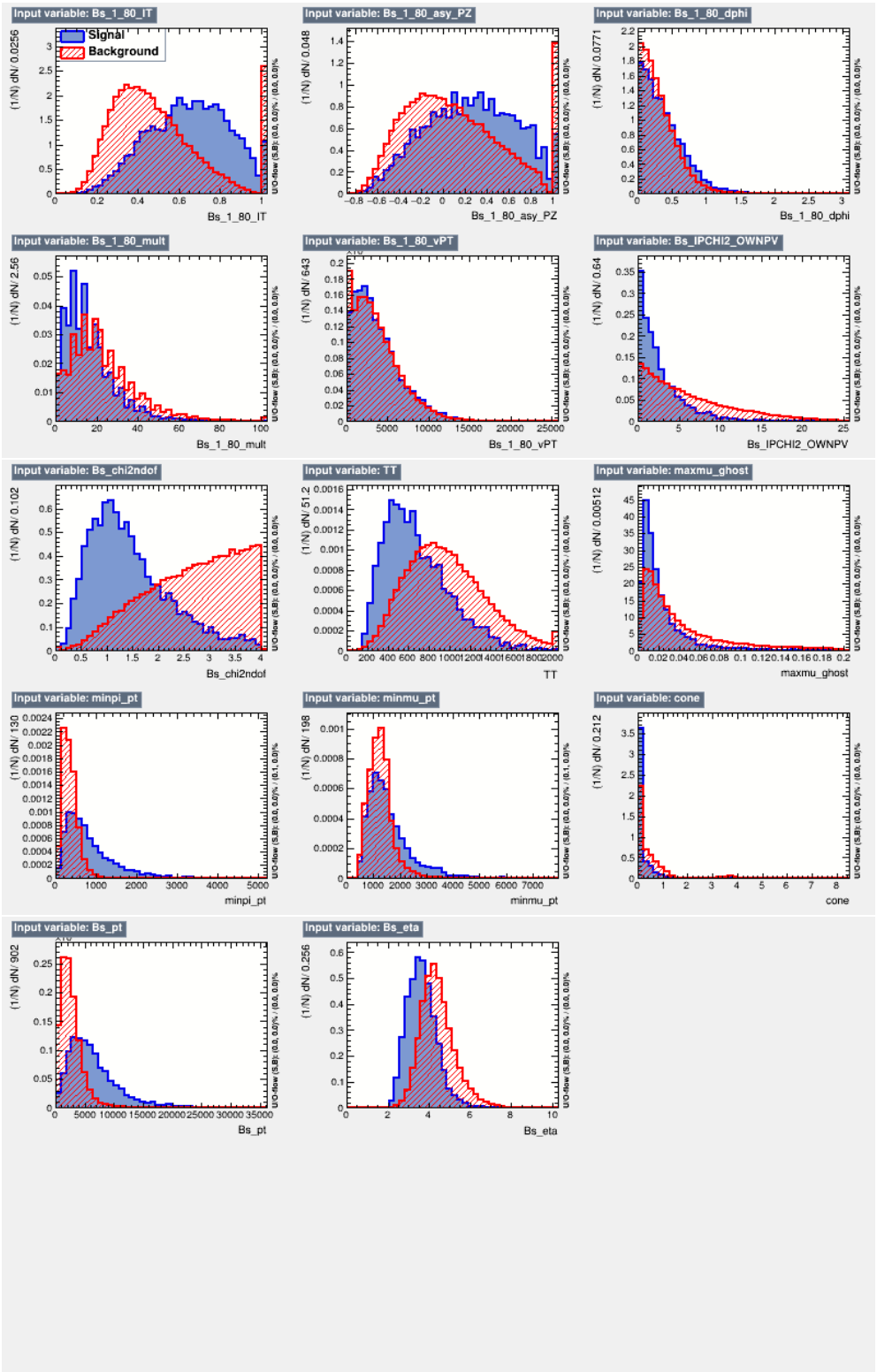

Figure E.15 *MVA input variables to the f_0 channel - 2012 data set.*

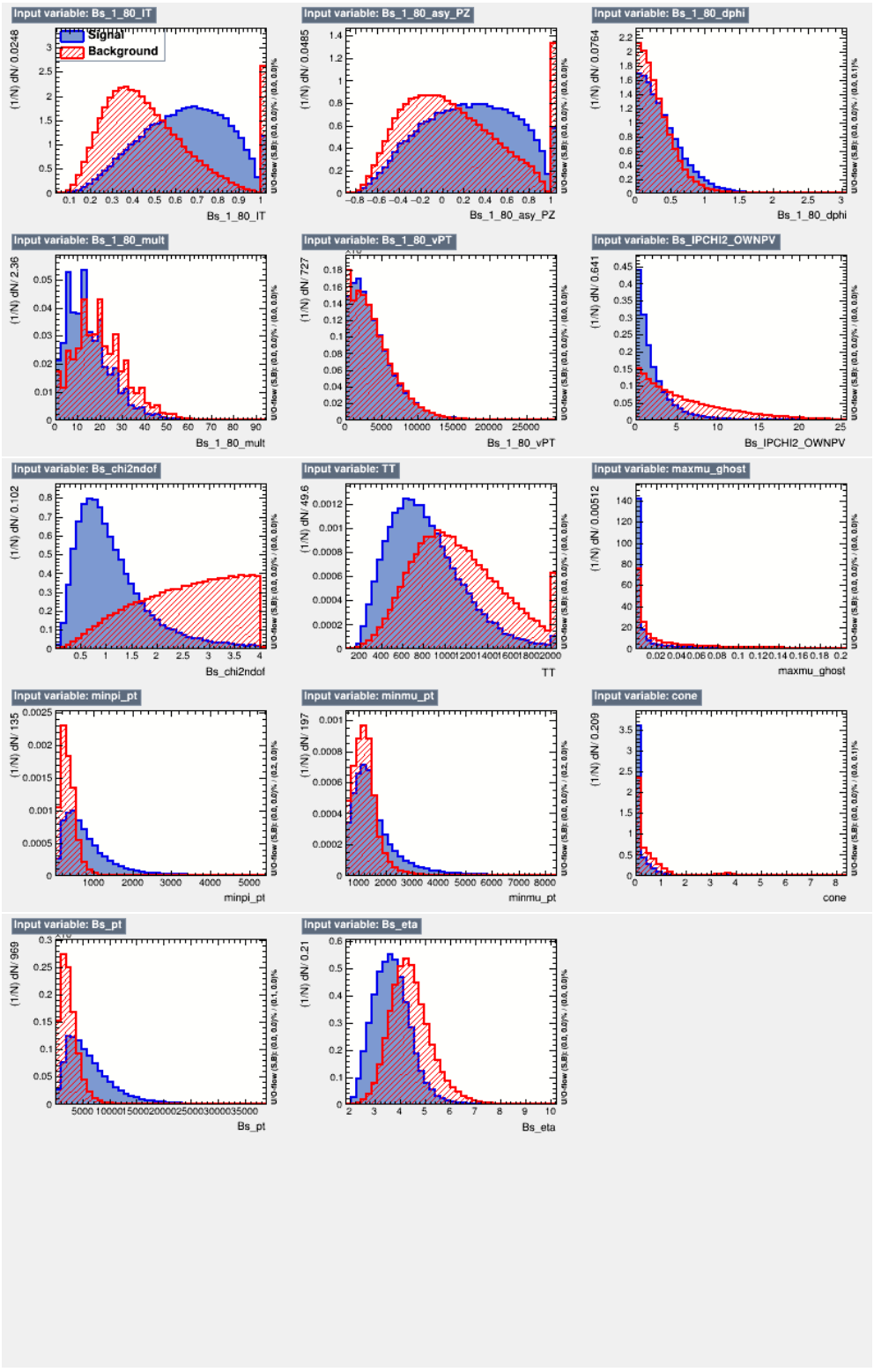

Figure E.16 *MVA input variables to the f_0 channel - 2016 data set.*

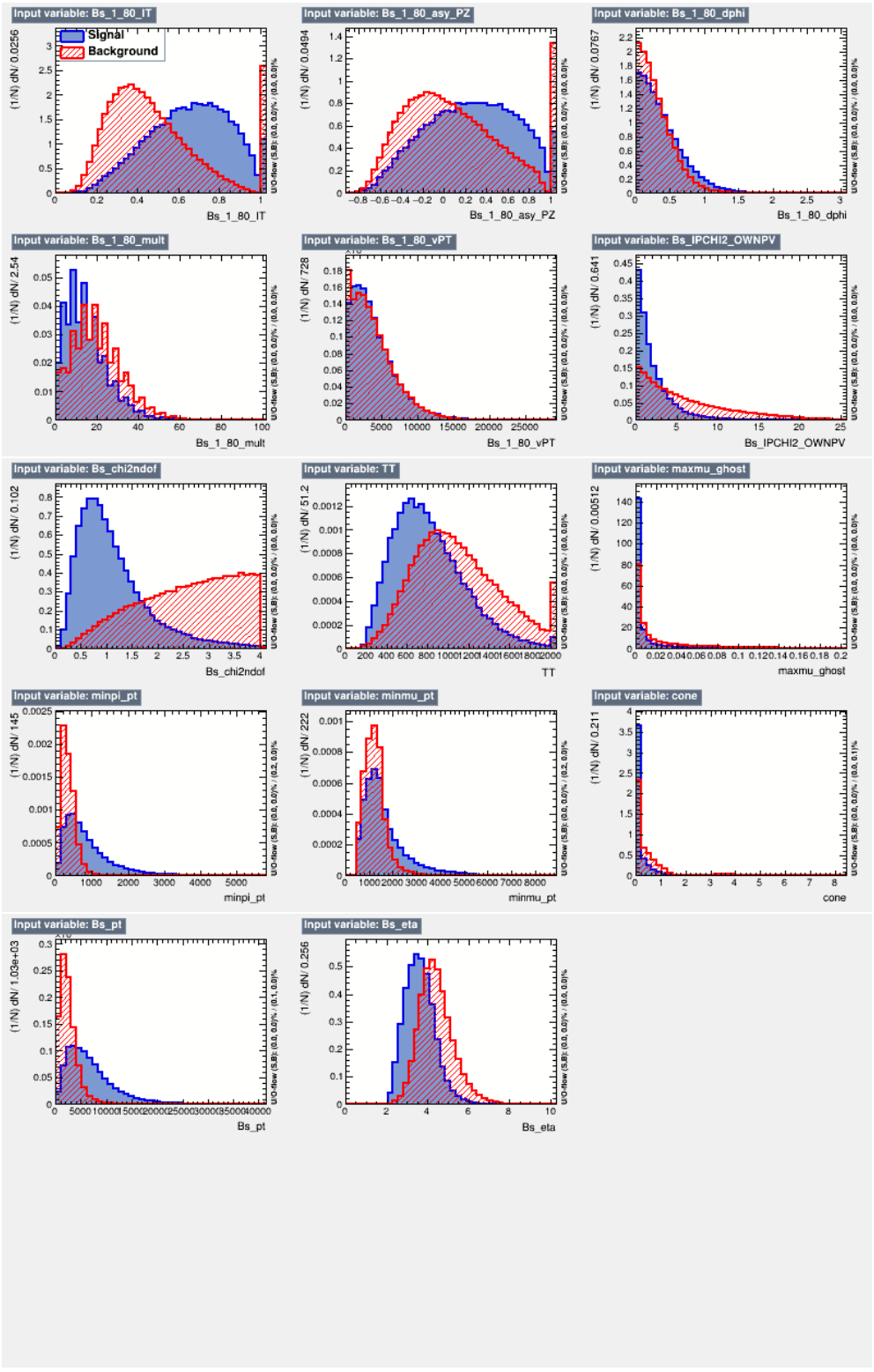

Figure E.17 *MVA input variables to the f_0 channel - 2012 data set.*

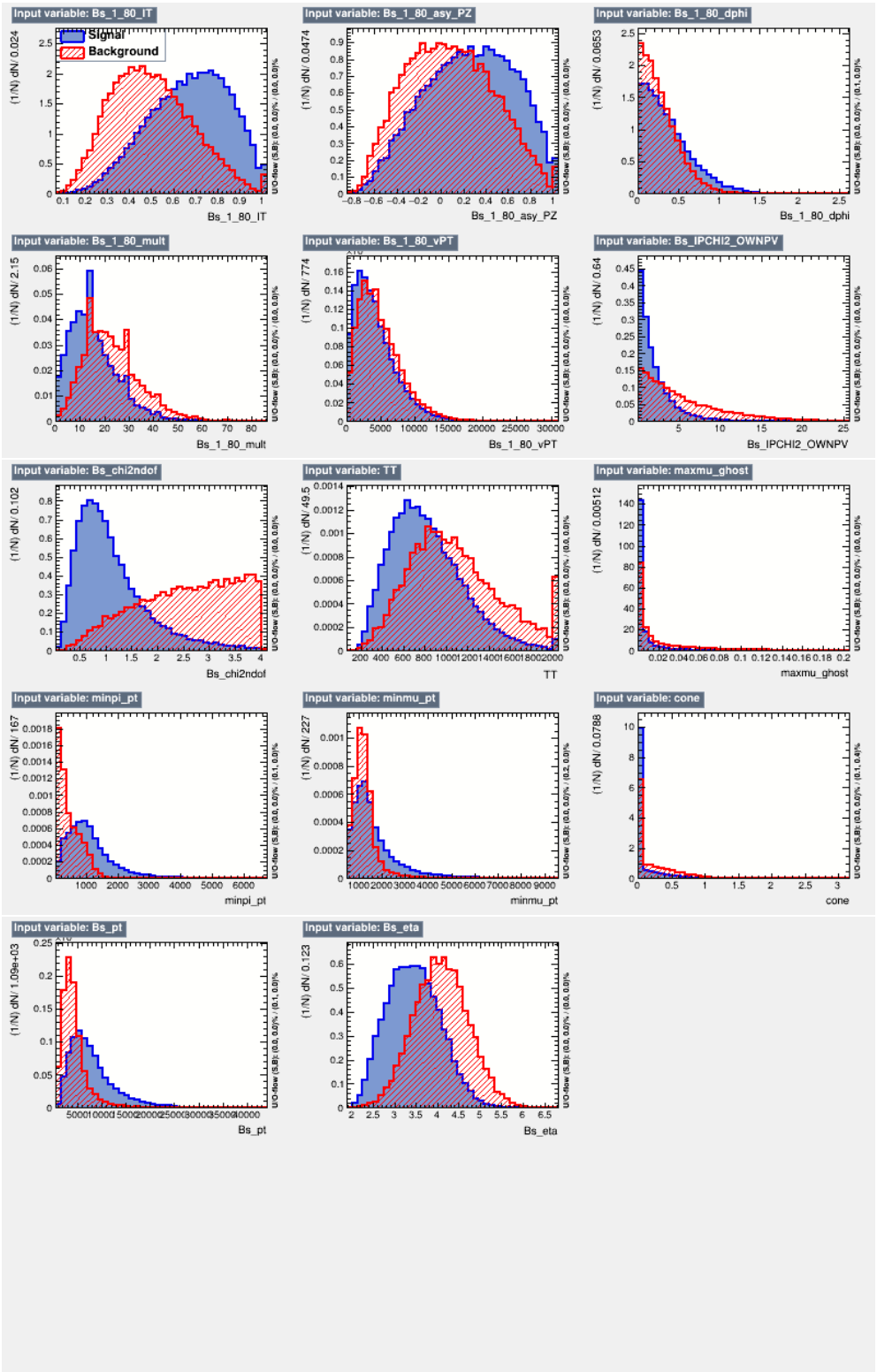

Figure E.18 *MVA input variables to the f_0 channel - 2018 data set.*

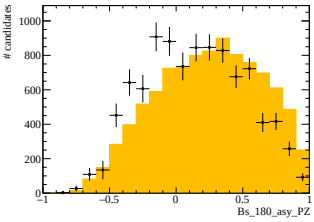

(a) B_s^0 *cc* p_Z *asymm.*

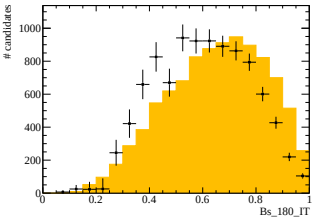

(b) B_s^0 *cc IT*

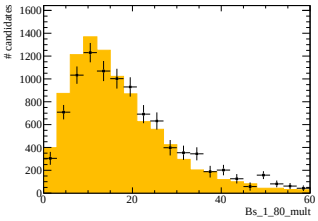

(c) *Mult* (B_s^0 *cc*)

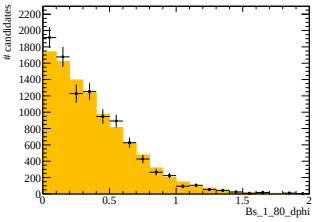

(d) B_s^0 *cc* $\Delta\phi$

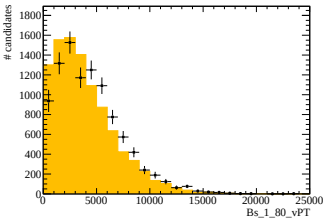

(e) B_s^0 *cc* $V\,p_T$

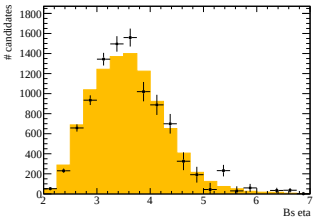

(f) $\eta\left(B_s^0\right)$

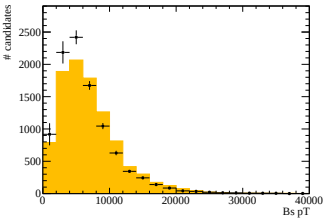

(g) $p_T\left(B_s^0\right)$

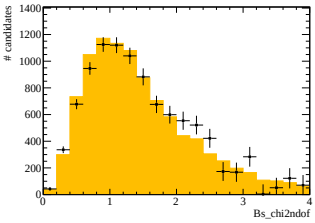

(h) $\chi^2\left(B_s^0\right)$

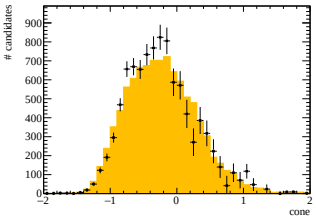

(i) *Isolation cone*

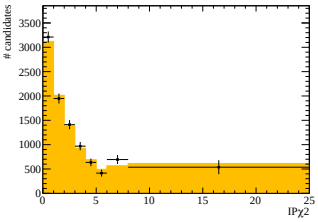

(j) $\chi^2_{\mathrm{IP}}\left(B_s^0\right)$

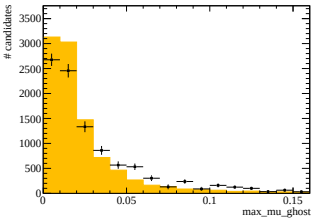

(k) $\min\left(\mu_1^{\mathrm{ghost}}, \mu_2^{\mathrm{ghost}}\right)$

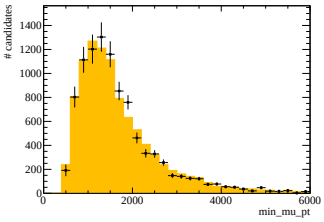

(l) $\min\left(p_T\left(\mu_1\right), p_T\left(\mu_2\right)\right)$

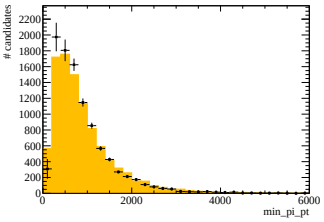

(m) $\min\left(p_T\left(\pi_1\right), p_T\left(\pi_2\right)\right)$

Figure E.19 *2012 s-weighted data (dots) and Monte Carlo (histogram) training variable comparison for the f_0 channel.*

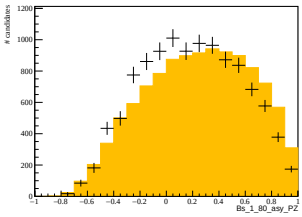

(a) B_s^0 cc p_Z *asymm.*

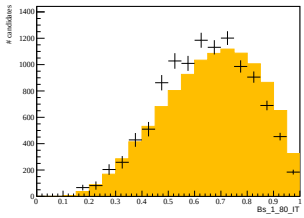

(b) B_s^0 cc *IT*

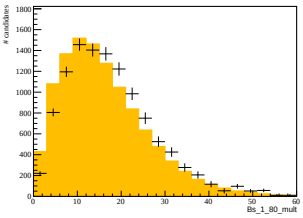

(c) *Mult* (B_s^0 cc)

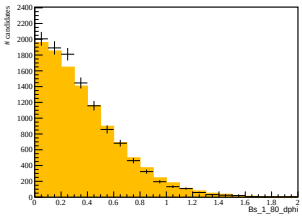

(d) B_s^0 cc $\Delta\phi$

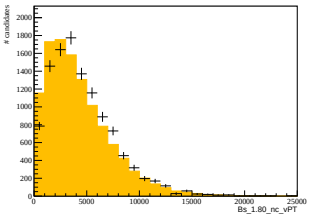

(e) B_s^0 cc $V\,p_T$

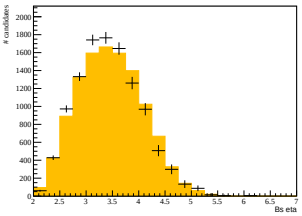

(f) $\eta\left(B_s^0\right)$

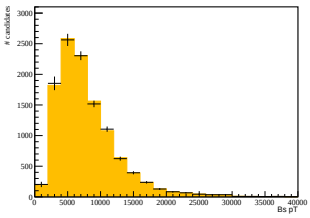

(g) $p_T\left(B_s^0\right)$

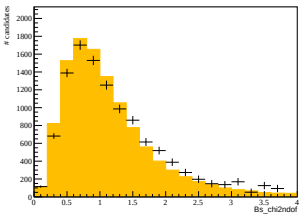

(h) $\chi^2\left(B_s^0\right)$

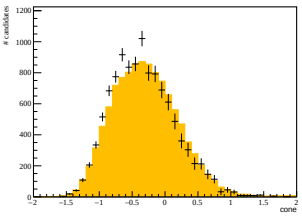

(i) *Isolation cone*

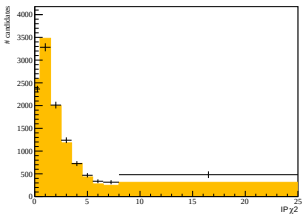

(j) $\chi^2_{\mathrm{IP}}\left(B_s^0\right)$

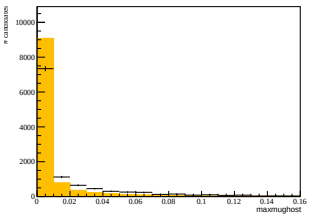

(k) $\min\left(\mu_1^{\mathrm{ghost}}, \mu_2^{\mathrm{ghost}}\right)$

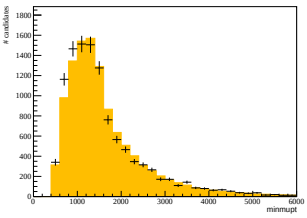

(l) $\min\left(p_T\left(\mu_1\right), p_T\left(\mu_2\right)\right)$

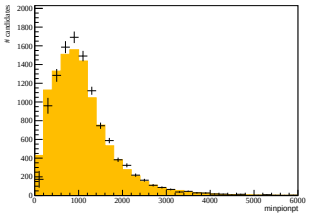

(m) $\min\left(p_T\left(\pi_1\right), p_T\left(\pi_2\right)\right)$

Figure E.20 *2016 s-weighted data (dots) and Monte Carlo (histogram) training variable comparison for the f_0 channel.*

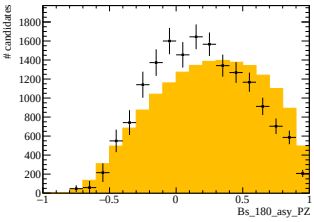

(a) B_s^0 *cc* p_Z *asymm.*

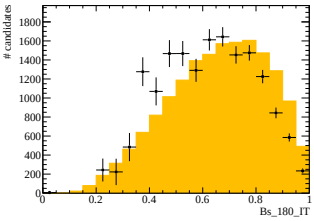

(b) B_s^0 *cc IT*

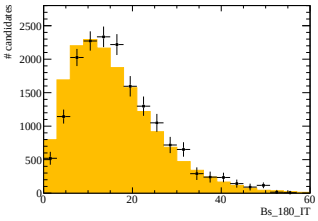

(c) *Mult* (B_s^0 *cc*)

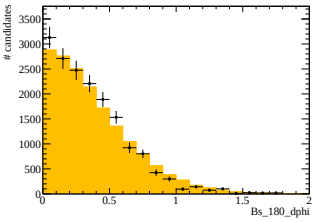

(d) B_s^0 *cc* $\Delta\phi$

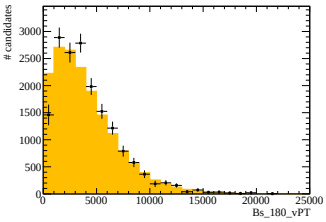

(e) B_s^0 *cc* $V\,p_T$

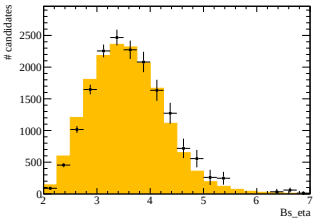

(f) $\eta\left(B_s^0\right)$

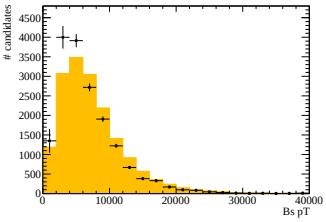

(g) $p_T\left(B_s^0\right)$

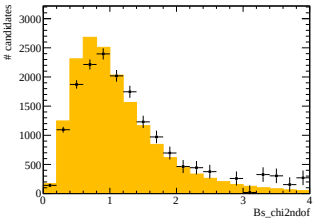

(h) $\chi^2\left(B_s^0\right)$

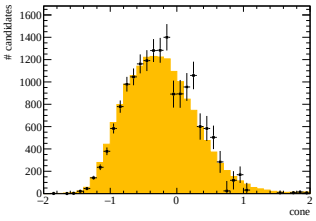

(i) *Isolation cone*

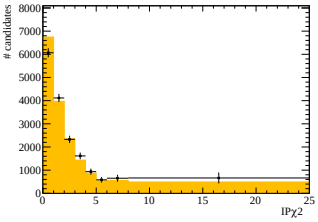

(j) $\chi^2_{\mathrm{IP}}\left(B_s^0\right)$

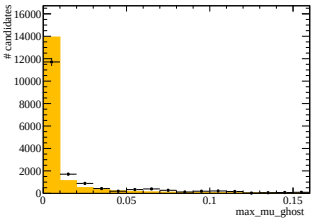

(k) $\min\left(\mu_1^{\mathrm{ghost}}, \mu_2^{\mathrm{ghost}}\right)$

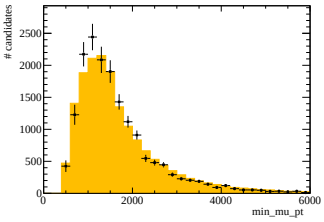

(l) $\min\left(p_T\left(\mu_1\right), p_T\left(\mu_2\right)\right)$

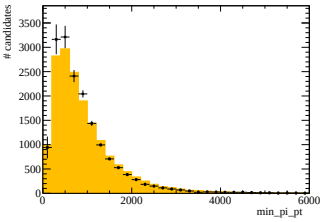

(m) $\min\left(p_T\left(\pi_1\right), p_T\left(\pi_2\right)\right)$

Figure E.21 *2017 s-weighted data (dots) and Monte Carlo (histogram) training variable comparison for the f_0 channel.*

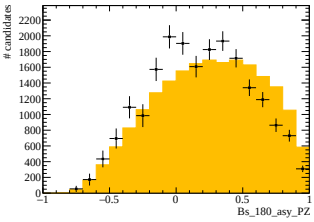

(a) B_s^0 *cc* p_Z *asymm.*

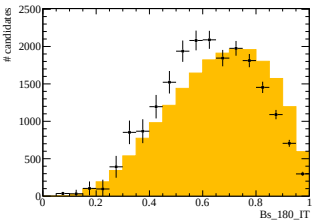

(b) B_s^0 *cc IT*

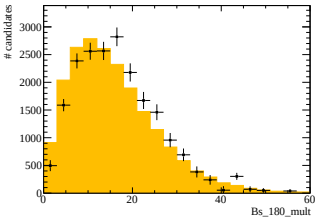

(c) *Mult* (B_s^0 *cc*)

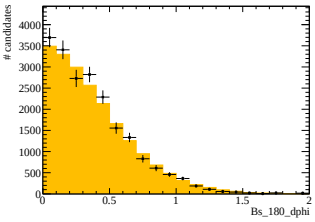

(d) B_s^0 *cc* $\Delta\phi$

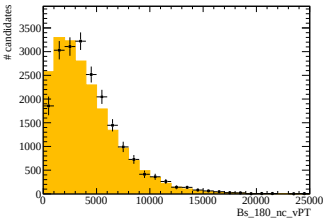

(e) B_s^0 *cc* $V\,p_T$

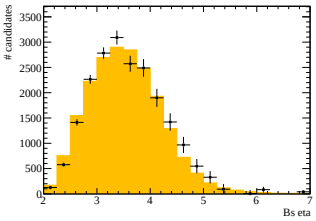

(f) $\eta\left(B_s^0\right)$

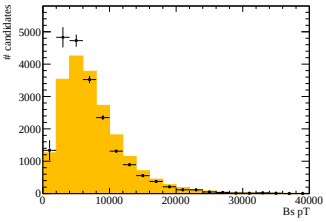

(g) $p_T\left(B_s^0\right)$

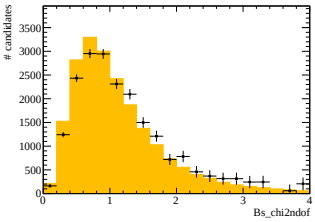

(h) $\chi^2\left(B_s^0\right)$

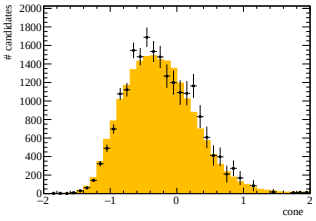

(i) *Isolation cone*

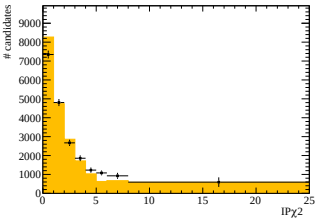

(j) $\chi^2_{\mathrm{IP}}\left(B_s^0\right)$

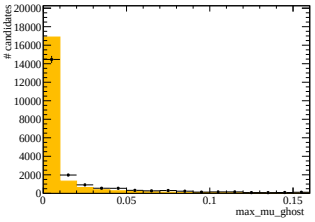

(k) $\min\left(\mu_1^{\mathrm{ghost}}, \mu_2^{\mathrm{ghost}}\right)$

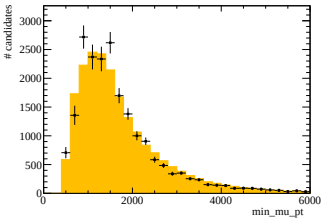

(l) $\min\left(p_T\left(\mu_1\right), p_T\left(\mu_2\right)\right)$

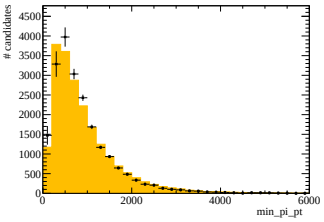

(m) $\min\left(p_T\left(\pi_1\right), p_T\left(\pi_2\right)\right)$

Figure E.22 *2018 s-weighted data (dots) and Monte Carlo (histogram) training variable comparison for the f_0 channel.*

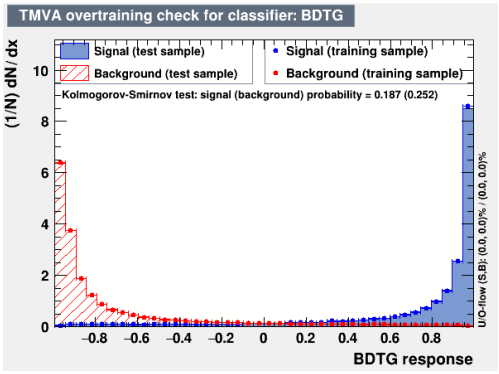

(a) *Signal-background separation*

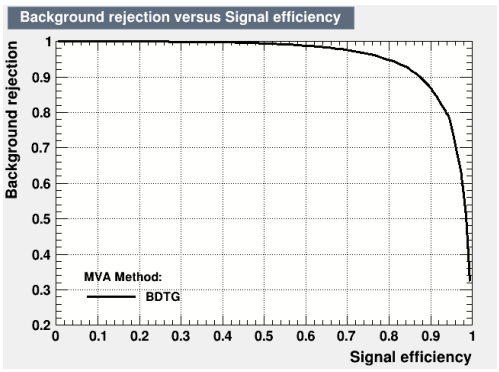

(b) *ROC curve*

Figure E.23 *Signal-background separation and ROC curve for the 2012 $B_s^0 \to J/\psi f_0$ MVA.*

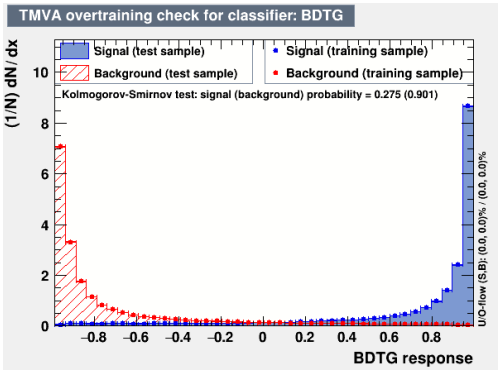

(a) *Signal-background separation*

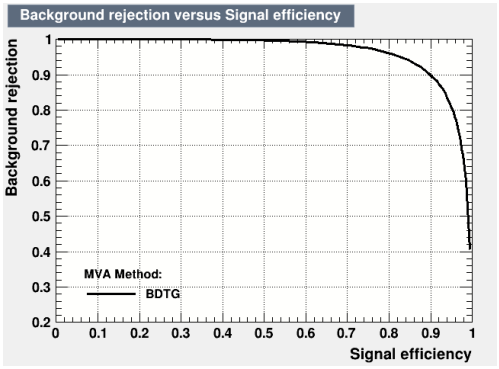

(b) *ROC curve*

Figure E.24 *Signal-background separation and ROC curve for the 2016 $B_s^0 \to J/\psi f_0$ MVA.*

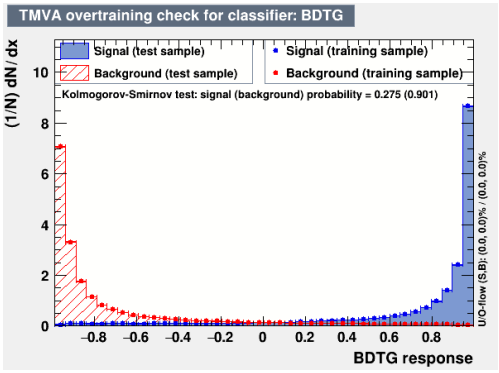

(a) *Signal-background separation*

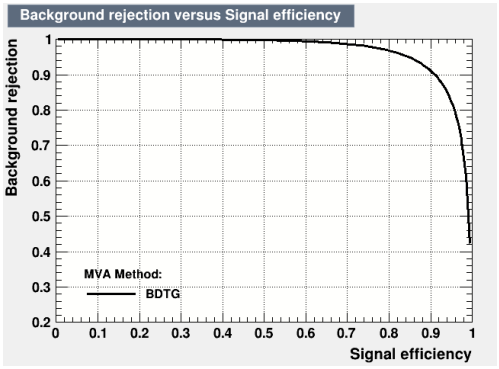

(b) *ROC curve*

Figure E.25 *Signal-background separation and ROC curve for the 2017 $B_s^0 \to J/\psi f_0$ MVA.*

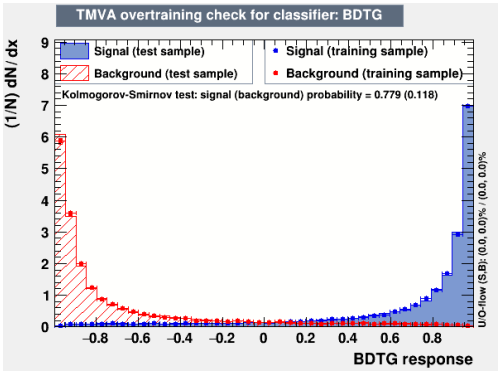

(a) *Signal-background separation*

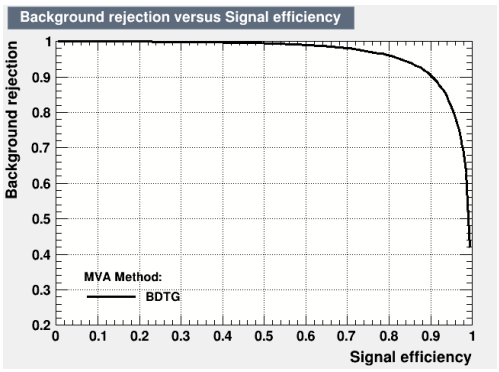

(b) *ROC curve*

Figure E.26 *Signal-background separation and ROC curve for the 2018 $B_s^0 \to J/\psi f_0$ MVA.*

Appendix F

PDFs used in the analysis

F.1 Double-Sided Crystal Ball

The DSCB function is a Gaussian distribution with power law tails. Its shape is controlled by 6 variables:

- μ: central value
- σ: width
- $\alpha_{L,R}$: defines the transition point from the Gaussian core to the power law trail on the left and right sides.
- $n_{L,R}$: exponential for the power law trail.

It has the functional form:

$$f(m) = \begin{cases} A_L \cdot (B_L - \frac{m-\mu}{\sigma})^{-n_L}, & \frac{m-\mu}{\sigma} < -\alpha_L \\ \exp(-\frac{1}{2} \cdot [\frac{m-\mu}{\sigma}]^2), & -\alpha_L < \frac{m-\mu}{\sigma} < \alpha_R \\ A_R \cdot (B_R + \frac{m-\mu}{\sigma})^{-n_R}, & otherwise \end{cases} , \tag{F.1}$$

where:

$$
\begin{aligned}
A_i &= (\frac{n_i}{|\alpha_i|})^{n_i} \cdot \exp(-\frac{|\alpha_i|^2}{2}), \\
B_i &= \frac{n_i}{|\alpha_i|} - |\alpha_i|.
\end{aligned}
\tag{F.2}
$$

F.2 Bifurcated Gaussian

The Bifurcated Gaussian function is a Gaussian with different sigmas left and right of the peak. It is defined as:

$$
f(x) = \begin{cases} A \exp\left(-\frac{(x-\mu)^2}{2\sigma_1^2}\right) & x < \mu \\ A \exp\left(-\frac{(x-\mu)^2}{2\sigma_2^2}\right) & \text{otherwise,} \end{cases}
\tag{F.3}
$$

where

$$
A = \sqrt{2/\pi}\,(\sigma_1 + \sigma_2)^{-1}\,. \tag{F.4}
$$

Appendix G

Binned fit

In the simultaneous fit, the σ of the B_s^0 is left free and it is shared across all decay time bins assuming this parameter does not have any decay time dependence. This hypothesis was checked on the 2016 $B_s^0 \to J/\psi\eta'$ simulation by checking the value of σ in bins of lifetime. The binning scheme adopted is the one chosen for the analysis (table 7.1).

Bin	σ [MeV/c^2]
1	9.06 ± 0.34
2	8.61 ± 0.56
3	8.31 ± 0.35
4	8.58 ± 0.53
5	9.44 ± 0.30
6	9.18 ± 0.33
7	9.21 ± 0.33
8	9.15 ± 0.38

Table G.1 *Values of σ in bins of decay time for the 2016 η' sample.*

As shown in table G.1 and in fig. G.1, the value of σ agrees across all decay time bins. The fit to a constant returned a $\chi^2/\text{ndof} = 1.14$ and the $\texttt{prob}\,(\chi^2) = 0.33$.

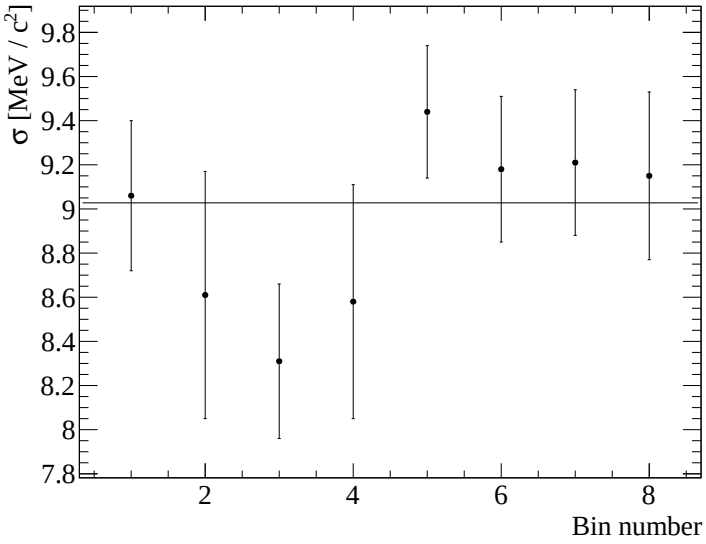

Figure G.1 *Values of σ in bins of decay time for the 2016 η' sample with a fit to a constant.*

G.1 $B_s^0 \to J/\psi\eta'$

In tables G.2, G.3, G.4 and G.5 the simultaneous fit results are listed while in figs. G.2, G.3, G.4 and G.5 the mass fit in each time bin for each year are shown.

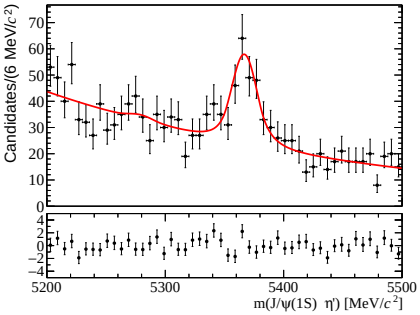

(a) $0.5\text{ ps} < t < 0.7\text{ ps}$

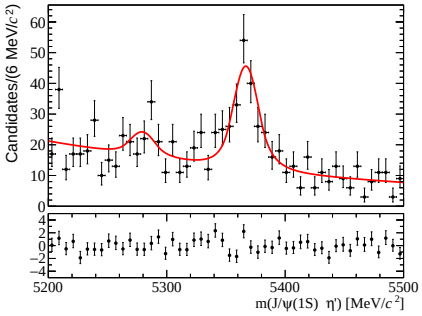

(b) $0.7\text{ ps} < t < 0.9\text{ ps}$

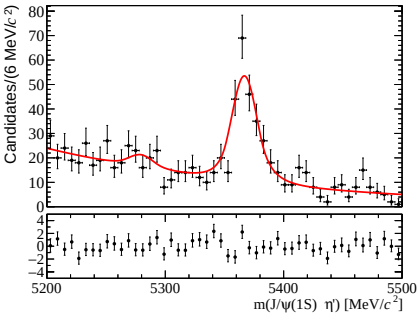

(c) $0.9\text{ ps} < t < 1.2\text{ ps}$

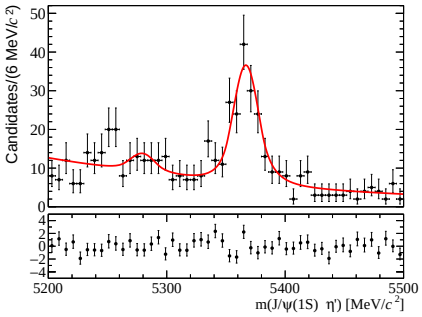

(d) $1.2\text{ ps} < t < 1.5\text{ ps}$

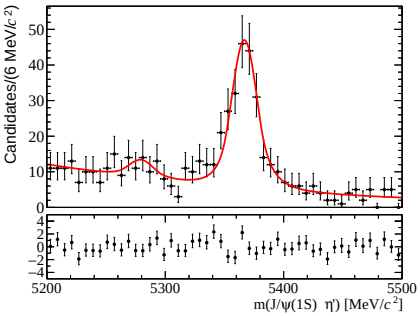

(e) $1.5\text{ ps} < t < 2.0\text{ ps}$

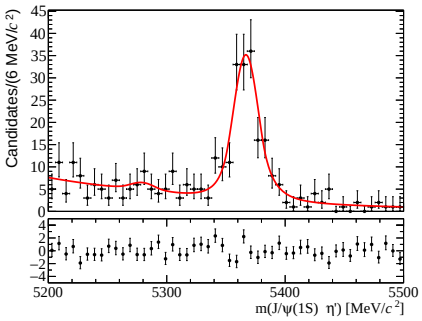

(f) $2.0\text{ ps} < t < 2.5\text{ ps}$

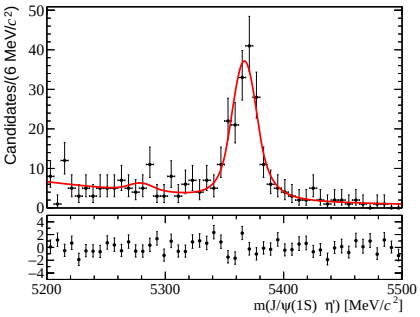

(g) $2.5\text{ ps} < t < 3.5\text{ ps}$

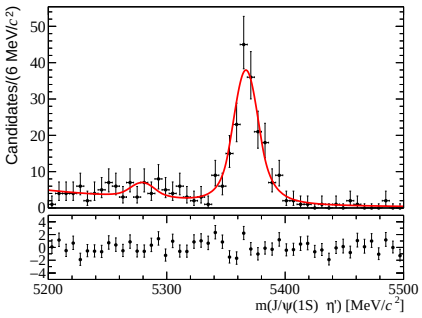

(h) $3.5\text{ ps} < t < 10.0\text{ ps}$

Figure G.2 *Fit to the eight time bins described in table 7.1 for the 2011-2012 η' data set. The fit to the model described in the text is shown in red. The pull distributions are shown below the plot.*

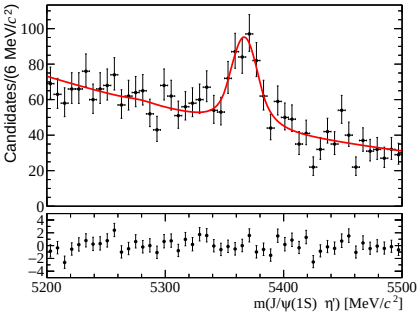

(a) $0.5\text{ ps} < t < 0.7\text{ ps}$

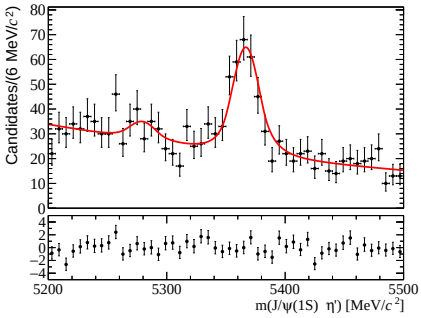

(b) $0.7\text{ ps} < t < 0.9\text{ ps}$

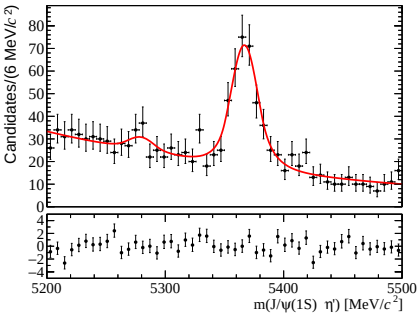

(c) $0.9\text{ ps} < t < 1.2\text{ ps}$

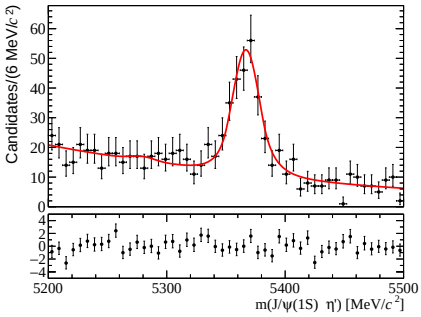

(d) $1.2\text{ ps} < t < 1.5\text{ ps}$

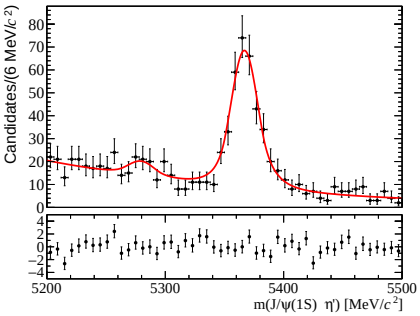

(e) $1.5\text{ ps} < t < 2.0\text{ ps}$

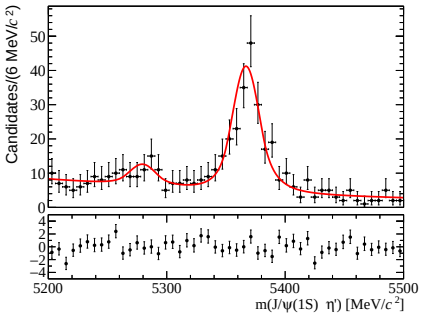

(f) $2.0\text{ ps} < t < 2.5\text{ ps}$

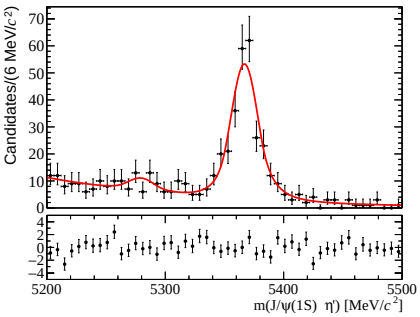

(g) $2.5\text{ ps} < t < 3.5\text{ ps}$

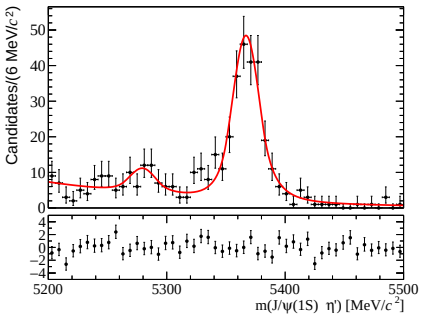

(h) $3.5\text{ ps} < t < 10.0\text{ ps}$

Figure G.3 *Fit to the eight time bins described in table 7.1 for the 2015-2016 η' data set. The fit to the model described in the text is shown in red. The pull distributions are shown below the plot.*

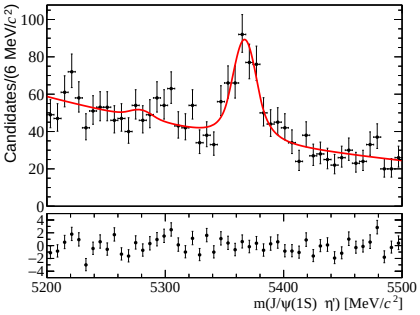

(a) $0.5\ \text{ps} < t < 0.7\ \text{ps}$

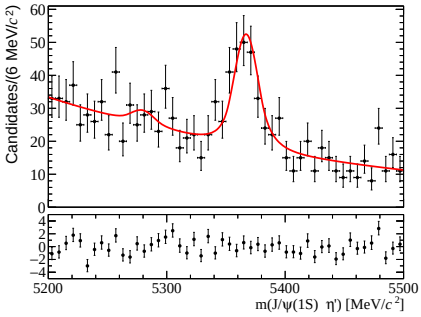

(b) $0.7\ \text{ps} < t < 0.9\ \text{ps}$

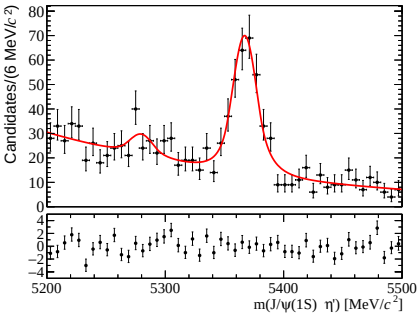

(c) $0.9\ \text{ps} < t < 1.2\ \text{ps}$

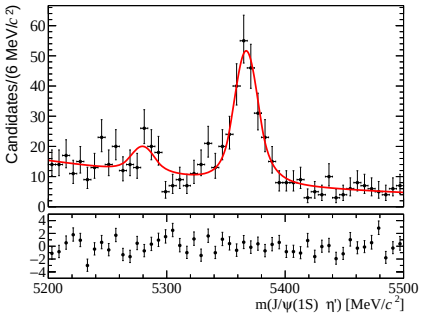

(d) $1.2\ \text{ps} < t < 1.5\ \text{ps}$

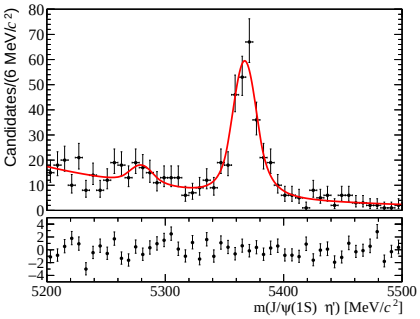

(e) $1.5\ \text{ps} < t < 2.0\ \text{ps}$

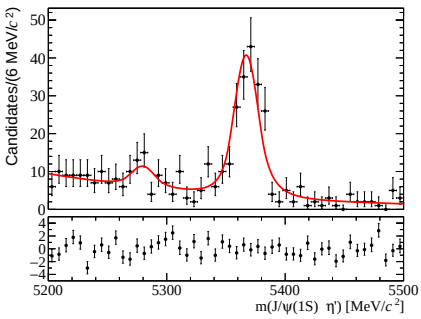

(f) $2.0\ \text{ps} < t < 2.5\ \text{ps}$

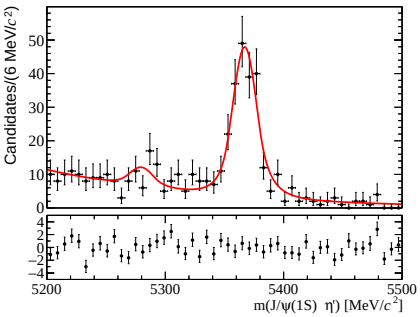

(g) $2.5\ \text{ps} < t < 3.5\ \text{ps}$

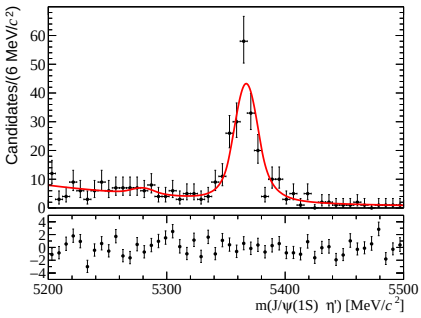

(h) $3.5\ \text{ps} < t < 10.0\ \text{ps}$

Figure G.4 *Fit to the eight time bins described in table 7.1 for the 2017 η' data set. The fit to the model described in the text is shown in red. The pull distributions are shown below the plot.*

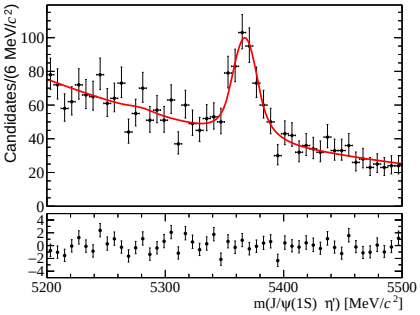

(a) $0.5\ \text{ps} < t < 0.7\ \text{ps}$

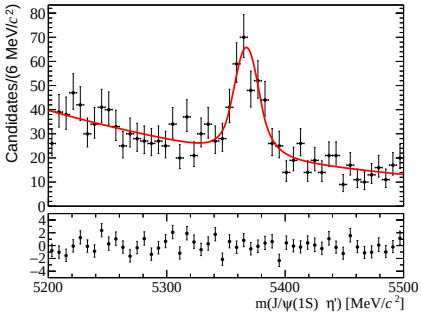

(b) $0.7\ \text{ps} < t < 0.9\ \text{ps}$

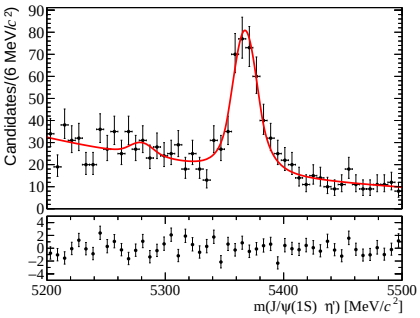

(c) $0.9\ \text{ps} < t < 1.2\ \text{ps}$

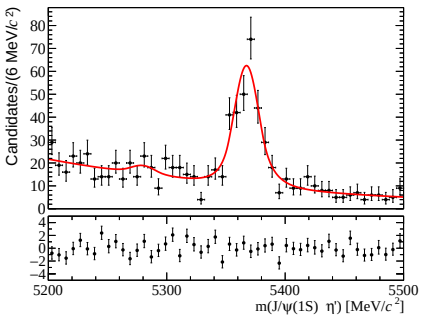

(d) $1.2\ \text{ps} < t < 1.5\ \text{ps}$

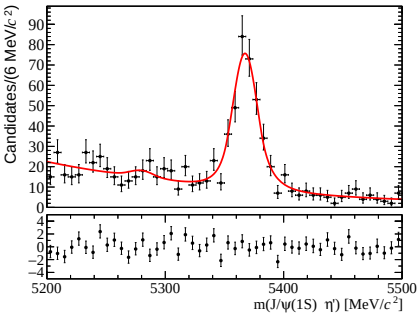

(e) $1.5\ \text{ps} < t < 2.0\ \text{ps}$

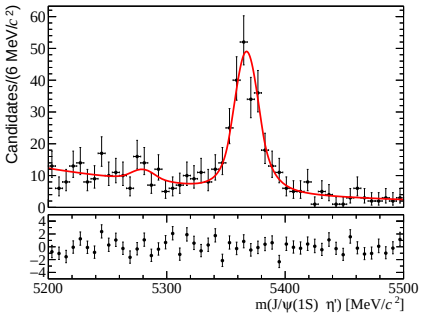

(f) $2.0\ \text{ps} < t < 2.5\ \text{ps}$

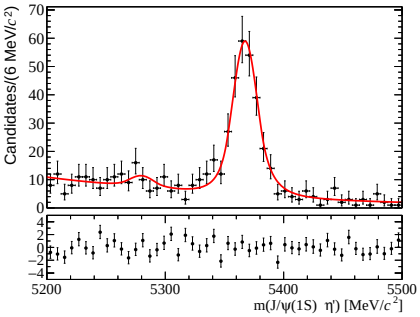

(g) $2.5\ \text{ps} < t < 3.5\ \text{ps}$

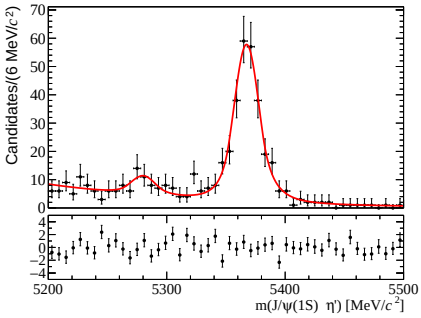

(h) $3.5\ \text{ps} < t < 10.0\ \text{ps}$

Figure G.5 *Fit to the eight time bins described in table 7.1 for the 2018 η' data set. The fit to the model described in the text is shown in red. The pull distributions are shown below the plot.*

Parameter	Value
α	$(9.79 \pm 0.30) \times 10^{-1}$
$\Delta m_{B_s^0 - B^0}$	(8.72 ± 0.16) MeV/c^2
Comb-bkg yield$_1$	$(1.32 \pm 0.04) \times 10^3$
Comb-bkg yield$_2$	$(1.16 \pm 0.04) \times 10^3$
Comb-bkg yield$_3$	$(6.14 \pm 0.35) \times 10^2$
Comb-bkg yield$_4$	$(3.44 \pm 0.25) \times 10^2$
Comb-bkg yield$_5$	$(3.11 \pm 0.24) \times 10^2$
Comb-bkg yield$_6$	$(1.59 \pm 0.17) \times 10^2$
Comb-bkg yield$_7$	$(1.45 \pm 0.17) \times 10^2$
Comb-bkg yield$_8$	$(9.93 \pm 1.42) \times 10^1$
$\mu_{B_s^0}$	$(5.36690 \pm 0.00004) \times 10^3$ MeV/c^2
$\sigma_{B_s^0}$	(10.74 ± 0.043) MeV/c^2
B_s^0 yield$_1$	$(1.71 \pm 0.21) \times 10^2$
B_s^0 yield$_2$	$(1.67 \pm 0.19) \times 10^2$
B_s^0 yield$_3$	$(2.17 \pm 0.19) \times 10^2$
B_s^0 yield$_4$	$(1.53 \pm 0.16) \times 10^2$
B_s^0 yield$_5$	$(2.08 \pm 0.18) \times 10^2$
B_s^0 yield$_6$	$(1.63 \pm 0.48) \times 10^2$
B_s^0 yield$_7$	$(1.74 \pm 0.52) \times 10^2$
B_s^0 yield$_8$	$(1.83 \pm 0.48) \times 10^2$
B^0 fraction yield$_1$	$(5.6 \pm 10.4) \times 10^{-2}$
B^0 fraction yield$_2$	$(2.24 \pm 0.90) \times 10^{-1}$
B^0 fraction yield$_3$	$(1.15 \pm 0.65) \times 10^{-1}$
B^0 fraction yield$_4$	$(1.50 \pm 0.76) \times 10^{-1}$
B^0 fraction yield$_5$	$(1.14 \pm 0.53) \times 10^{-1}$
B^0 fraction yield$_6$	$(5.30 \pm 4.60) \times 10^{-2}$
B^0 fraction yield$_7$	$(5.65 \pm 4.40) \times 10^{-2}$
B^0 fraction yield$_8$	$(1.10 \pm 0.44) \times 10^{-1}$
Exp coeff$_1$	$(-3.68 \pm 0.35) \times 10^{-3}$
Exp coeff$_2$	$(-3.34 \pm 0.49) \times 10^{-3}$
Exp coeff$_3$	$(-5.18 \pm 0.54) \times 10^{-3}$
Exp coeff$_4$	$(-4.48 \pm 0.70) \times 10^{-3}$
Exp coeff$_5$	$(-4.91 \pm 0.75) \times 10^{-3}$
Exp coeff$_6$	$(-6.74 \pm 0.11) \times 10^{-3}$
Exp coeff$_7$	$(-6.32 \pm 11.4) \times 10^{-3}$
Exp coeff$_8$	$(-8.00 \pm 16.7) \times 10^{-3}$

Table G.2 *Simultaneous fit result for the 2011-2012 $B_s^0 \to J/\psi\eta'$ channel.*

Parameter	Value
α	$(9.73 \pm 0.30) \times 10^{-1}$
$\Delta m_{B_s^0 - B^0}$	(8.72 ± 0.16) MeV/c^2
Comb-bkg yield$_1$	$(2.45 \pm 0.06) \times 10^3$
Comb-bkg yield$_2$	$(1.16 \pm 0.04) \times 10^3$
Comb-bkg yield$_3$	$(9.63 \pm 0.40) \times 10^2$
Comb-bkg yield$_4$	$(5.99 \pm 0.32) \times 10^2$
Comb-bkg yield$_5$	$(4.98 \pm 0.30) \times 10^2$
Comb-bkg yield$_6$	$(2.50 \pm 0.22) \times 10^2$
Comb-bkg yield$_7$	$(2.07 \pm 0.20) \times 10^2$
Comb-bkg yield$_8$	$(1.36 \pm 0.18) \times 10^2$
$\mu_{B_s^0}$	$(5.36700 \pm 0.00004) \times 10^3$ MeV/c^2
$\sigma_{B_s^0}$	(11.47 ± 0.043) MeV/c^2
B_s^0 yield$_1$	$(2.65 \pm 0.29) \times 10^2$
B_s^0 yield$_2$	$(2.30 \pm 0.23) \times 10^2$
B_s^0 yield$_3$	$(2.89 \pm 0.23) \times 10^2$
B_s^0 yield$_4$	$(2.25 \pm 0.20) \times 10^2$
B_s^0 yield$_5$	$(3.20 \pm 0.21) \times 10^2$
B_s^0 yield$_6$	$(1.95 \pm 0.17) \times 10^2$
B_s^0 yield$_7$	$(2.68 \pm 0.18) \times 10^2$
B_s^0 yield$_8$	$(2.47 \pm 0.17) \times 10^2$
B^0 fraction yield$_1$	$(2.0 \pm 10.8) \times 10^{-2}$
B^0 fraction yield$_2$	$(1.62 \pm 0.82) \times 10^{-1}$
B^0 fraction yield$_3$	$(1.09 \pm 0.60) \times 10^{-1}$
B^0 fraction yield$_4$	$(3.39 \pm 5.97) \times 10^{-2}$
B^0 fraction yield$_5$	$(1.03 \pm 0.43) \times 10^{-1}$
B^0 fraction yield$_6$	$(1.60 \pm 0.56) \times 10^{-1}$
B^0 fraction yield$_7$	$(9.03 \pm 3.85) \times 10^{-2}$
B^0 fraction yield$_8$	$(1.42 \pm 0.40) \times 10^{-1}$
Exp coeff$_1$	$(-2.84 \pm 0.25) \times 10^{-4}$
Exp coeff$_2$	$(-2.62 \pm 0.36) \times 10^{-4}$
Exp coeff$_3$	$(-3.99 \pm 0.41) \times 10^{-4}$
Exp coeff$_4$	$(-3.99 \pm 0.52) \times 10^{-4}$
Exp coeff$_5$	$(-5.40 \pm 0.60) \times 10^{-4}$
Exp coeff$_6$	$(-3.53 \pm 0.82) \times 10^{-4}$
Exp coeff$_7$	$(-8.09 \pm 0.11) \times 10^{-4}$
Exp coeff$_8$	$(-7.74 \pm 0.13) \times 10^{-4}$

Table G.3 *Simultaneous fit result for the 2015-2016 $B_s^0 \to J/\psi\eta'$ channel.*

Parameter	Value
α	$(9.71 \pm 0.30) \times 10^{-1}$
$\Delta m_{B_s^0 - B^0}$	(8.72 ± 0.16) MeV/c^2
Comb-bkg yield$_1$	$(1.95 \pm 0.06) \times 10^3$
Comb-bkg yield$_2$	$(1.01 \pm 0.04) \times 10^3$
Comb-bkg yield$_3$	$(7.97 \pm 0.36) \times 10^2$
Comb-bkg yield$_4$	$(4.48 \pm 0.27) \times 10^2$
Comb-bkg yield$_5$	$(3.71 \pm 0.26) \times 10^2$
Comb-bkg yield$_6$	$(2.10 \pm 0.19) \times 10^2$
Comb-bkg yield$_7$	$(2.19 \pm 0.20) \times 10^2$
Comb-bkg yield$_8$	$(1.59 \pm 0.17) \times 10^2$
$\mu_{B_s^0}$	$(5.36720 \pm 0.00004) \times 10^3$ MeV/c^2
$\sigma_{B_s^0}$	(10.26 ± 0.04) MeV/c^2
B_s^0 yield$_1$	$(2.54 \pm 0.26) \times 10^2$
B_s^0 yield$_2$	$(1.63 \pm 0.20) \times 10^2$
B_s^0 yield$_3$	$(2.69 \pm 0.21) \times 10^2$
B_s^0 yield$_4$	$(2.08 \pm 0.18) \times 10^2$
B_s^0 yield$_5$	$(2.56 \pm 0.19) \times 10^2$
B_s^0 yield$_6$	$(1.78 \pm 0.15) \times 10^2$
B_s^0 yield$_7$	$(2.13 \pm 0.17) \times 10^2$
B_s^0 yield$_8$	$(1.95 \pm 0.16) \times 10^2$
B^0 fraction yield$_1$	$(8.51 \pm 8.45) \times 10^{-2}$
B^0 fraction yield$_2$	$(1.18 \pm 0.99) \times 10^{-1}$
B^0 fraction yield$_3$	$(1.48 \pm 0.59) \times 10^{-1}$
B^0 fraction yield$_4$	$(1.88 \pm 0.60) \times 10^{-1}$
B^0 fraction yield$_5$	$(1.33 \pm 0.48) \times 10^{-1}$
B^0 fraction yield$_6$	$(1.39 \pm 0.53) \times 10^{-1}$
B^0 fraction yield$_7$	$(1.21 \pm 0.46) \times 10^{-1}$
B^0 fraction yield$_8$	$(5.27 \pm 4.02) \times 10^{-2}$
Exp coeff$_1$	$(-2.91 \pm 0.28) \times 10^{-3}$
Exp coeff$_2$	$(-3.60 \pm 0.39) \times 10^{-3}$
Exp coeff$_3$	$(-4.82 \pm 0.46) \times 10^{-3}$
Exp coeff$_4$	$(-3.87 \pm 0.60) \times 10^{-3}$
Exp coeff$_5$	$(-6.67 \pm 0.73) \times 10^{-3}$
Exp coeff$_6$	$(-6.17 \pm 0.95) \times 10^{-3}$
Exp coeff$_7$	$(-7.68 \pm 1.01) \times 10^{-3}$
Exp coeff$_8$	$(-7.15 \pm 1.18) \times 10^{-3}$

Table G.4 *Simultaneous fit result for the 2017 $B_s^0 \to J/\psi\eta'$ channel.*

Parameter	Value
α	$(9.73 \pm 0.30) \times 10^{-1}$
$\Delta m_{B_s^0 - B^0}$	(8.72 ± 0.16) MeV/c^2
Comb-bkg yield$_1$	$(2.28 \pm 0.06) \times 10^3$
Comb-bkg yield$_2$	$(1.20 \pm 0.04) \times 10^3$
Comb-bkg yield$_3$	$(9.39 \pm 0.40) \times 10^2$
Comb-bkg yield$_4$	$(5.68 \pm 0.31) \times 10^2$
Comb-bkg yield$_5$	$(5.27 \pm 0.30) \times 10^2$
Comb-bkg yield$_6$	$(3.01 \pm 0.23) \times 10^2$
Comb-bkg yield$_7$	$(2.57 \pm 0.22) \times 10^2$
Comb-bkg yield$_8$	$(1.53 \pm 0.18) \times 10^2$
$\mu_{B_s^0}$	$(5.36740 \pm 0.00003) \times 10^3$ MeV/c^2
$\sigma_{B_s^0}$	(10.59 ± 0.04) MeV/c^2
B_s^0 yield$_1$	$(2.90 \pm 0.28) \times 10^2$
B_s^0 yield$_2$	$(2.18 \pm 0.22) \times 10^2$
B_s^0 yield$_3$	$(3.16 \pm 0.24) \times 10^2$
B_s^0 yield$_4$	$(2.60 \pm 0.20) \times 10^2$
B_s^0 yield$_5$	$(3.30 \pm 0.22) \times 10^2$
B_s^0 yield$_6$	$(2.16 \pm 0.18) \times 10^2$
B_s^0 yield$_7$	$(2.69 \pm 0.19) \times 10^2$
B_s^0 yield$_8$	$(2.73 \pm 0.18) \times 10^2$
B^0 fraction yield$_1$	$(2.81 \pm 7.84) \times 10^{-2}$
B^0 fraction yield$_2$	$(0.00 \pm 3.14) \times 10^{-2}$
B^0 fraction yield$_3$	$(9.06 \pm 5.34) \times 10^{-2}$
B^0 fraction yield$_4$	$(6.87 \pm 5.02) \times 10^{-2}$
B^0 fraction yield$_5$	$(5.04 \pm 3.87) \times 10^{-2}$
B^0 fraction yield$_6$	$(7.95 \pm 4.61) \times 10^{-2}$
B^0 fraction yield$_7$	$(7.18 \pm 3.77) \times 10^{-2}$
B^0 fraction yield$_8$	$(1.14 \pm 0.36) \times 10^{-1}$
Exp coeff$_1$	$(-3.64 \pm 0.26) \times 10^{-3}$
Exp coeff$_2$	$(-3.67 \pm 0.36) \times 10^{-3}$
Exp coeff$_3$	$(-3.95 \pm 0.42) \times 10^{-3}$
Exp coeff$_4$	$(-4.78 \pm 0.55) \times 10^{-3}$
Exp coeff$_5$	$(-5.76 \pm 0.59) \times 10^{-3}$
Exp coeff$_6$	$(-5.33 \pm 0.77) \times 10^{-3}$
Exp coeff$_7$	$(-5.60 \pm 0.85) \times 10^{-3}$
Exp coeff$_8$	$(-8.12 \pm 1.29) \times 10^{-3}$

Table G.5 *Simultaneous fit result for the 2018 $B_s^0 \to J/\psi\eta'$ channel.*

G.2 $B_s^0 \to J/\psi f_0$

In tables G.6, G.7, G.8 and G.9 the simultaneous fit results are listed while in figs. G.6, G.7, G.8 and G.9 the mass fit in each time bin for each year are shown.

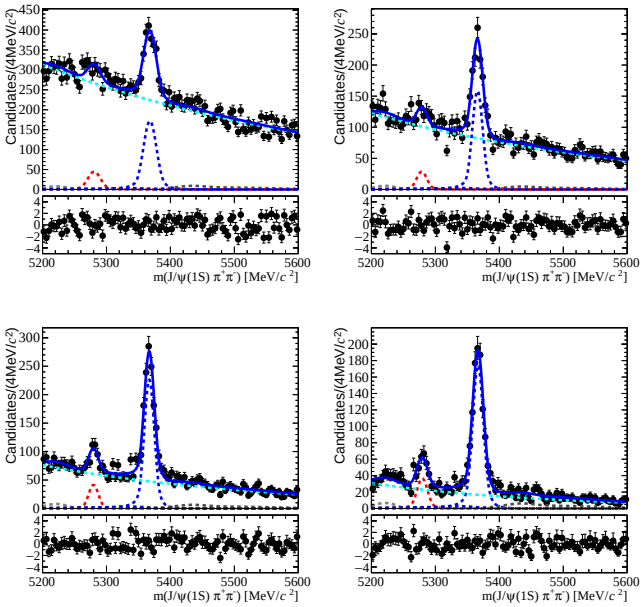

(a)

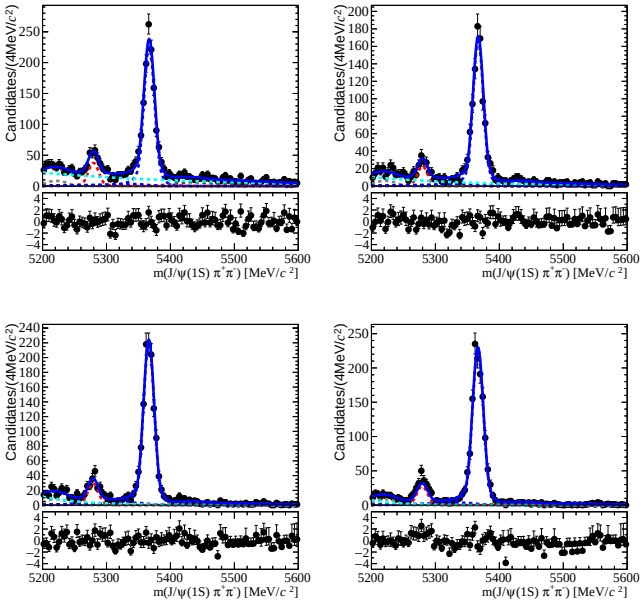

(b)

Figure G.6 *Fit to the eight time bins described in table 7.1 for the 2011-2012 f_0 data set. The fit to the model described in the text is shown in red. The pull distributions are shown below the plot.*

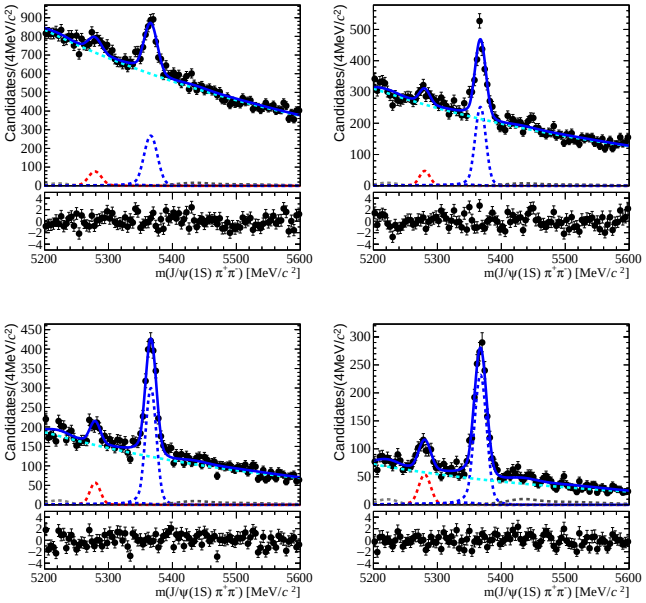

(a)

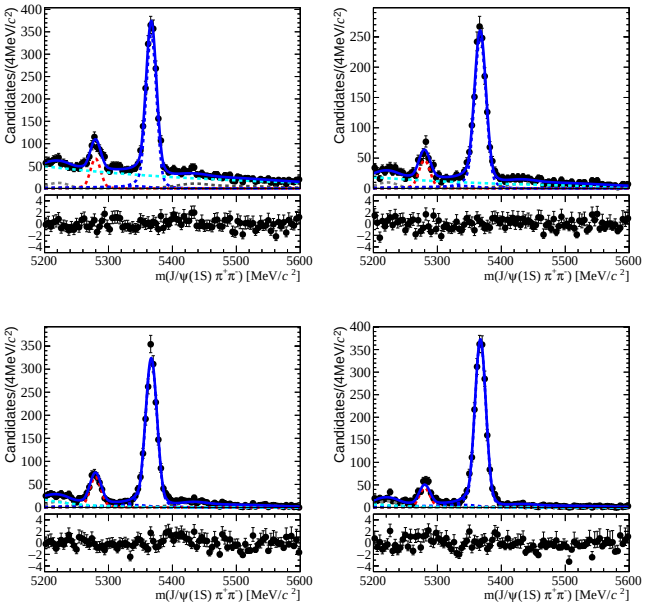

(b)

Figure G.7 *Fit to the eight time bins described in table 7.1 for the 2015-2016 f_0 data set. The fit to the model described in the text is shown in red. The pull distributions are shown below the plot.*

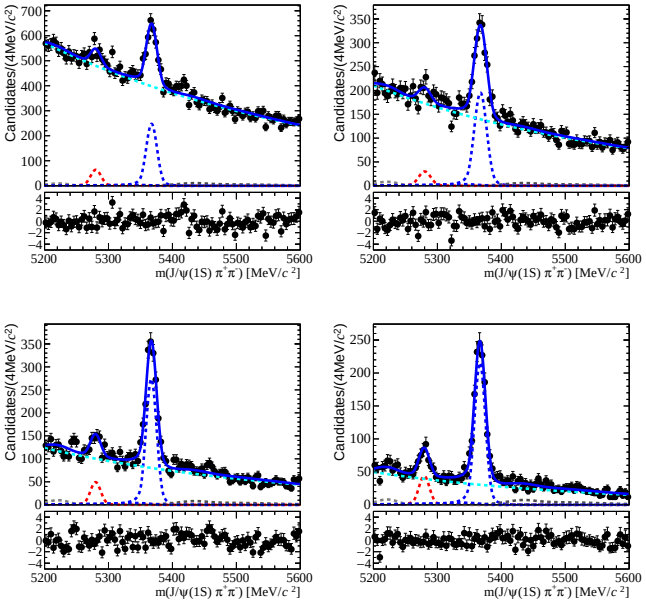

(a)

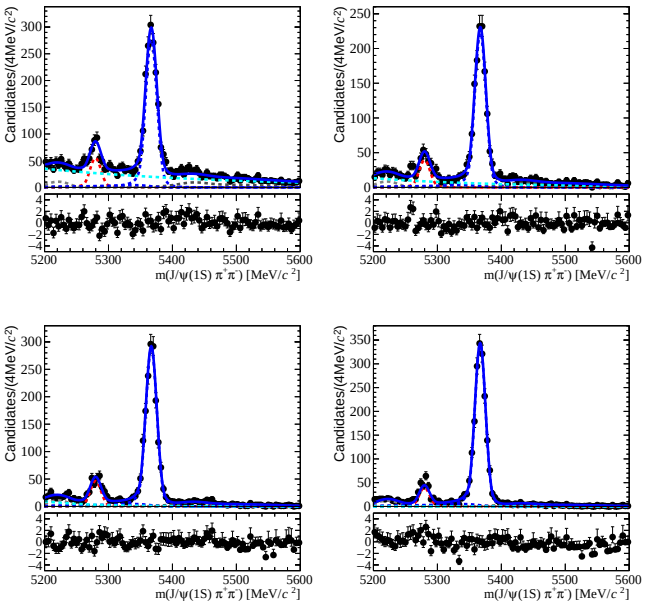

(b)

Figure G.8 *Fit to the eight time bins described in table 7.1 for the 2017 f_0 data set. The fit to the model described in the text is shown in red. The pull distributions are shown below the plot.*

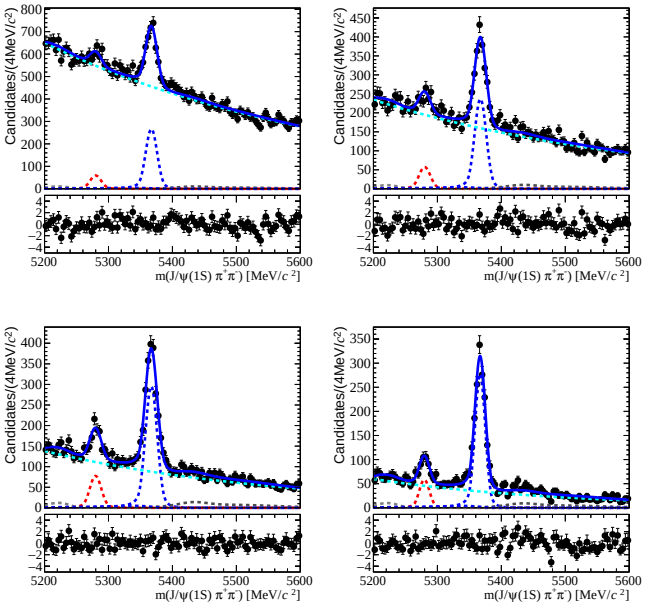

(a)

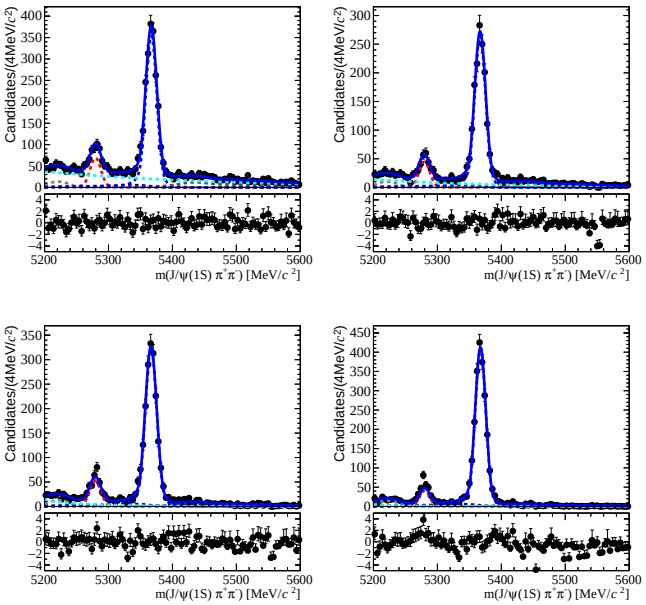

(b)

Figure G.9 *Fit to the eight time bins described in table 7.1 for the 2018 f_0 data set. The fit to the model described in the text is shown in red. The pull distributions are shown below the plot.*

Parameter	Value
α	$(9.70 \pm 0.30) \times 10^{-1}$
$\Delta m_{B_s^0 - B^0}$	(87.15 ± 0.15) MeV/c^2
Comb-bkg yield$_0$	$(2.36 \pm 0.03) \times 10^4$
Comb-bkg yield$_1$	$(8.5978e+03 \pm 0.19) \times 10^3$
Comb-bkg yield$_2$	$(4.87 \pm 0.15) \times 10^3$
Comb-bkg yield$_3$	$(1.73 \pm 0.10) \times 10^3$
Comb-bkg yield$_4$	$(1.09 \pm 0.09) \times 10^3$
Comb-bkg yield$_5$	$(3.87 \pm 0.36) \times 10^2$
Comb-bkg yield$_6$	$(2.06 \pm 0.42) \times 10^2$
Comb-bkg yield$_7$	59.3 ± 18.8
B^+ yield$_0$	$(3.89 \pm 2.26) \times 10^2$
B^+ yield$_1$	$(1.53 \pm 1.43) \times 10^2$
B^+ yield$_2$	$(3.03 \pm 1.08) \times 10^2$
B^+ yield$_3$	$(2.44 \pm 0.71) \times 10^2$
B^+ yield$_4$	$(2.85 \pm 0.65) \times 10^2$
B^+ yield$_5$	$(1.98 \pm 0.37) \times 10^2$
B^+ yield$_6$	$(1.57 \pm 0.20) \times 10^2$
B^+ yield$_7$	$(1.10 \pm 0.12) \times 10^2$
$\mu_{B_s^0}$	$(5.3666 \pm 0.0001) \times 10^3$ MeV/c^2
$\sigma_{B_s^0}$	(8.55 ± 0.12) MeV/c^2
B_s^0 yield$_0$	$(1.07 \pm 0.06) \times 10^3$
B_s^0 yield$_1$	$(9.08 \pm 0.47) \times 10^2$
B_s^0 yield$_2$	$(1.28 \pm 0.05) \times 10^3$
B_s^0 yield$_3$	$(1.03 \pm 0.04) \times 10^3$
B_s^0 yield$_4$	$(1.32 \pm 0.04) \times 10^3$
B_s^0 yield$_5$	$(9.64 \pm 0.36) \times 10^2$
B_s^0 yield$_6$	$(1.30 \pm 0.03) \times 10^3$
B_s^0 yield$_7$	$(1.37 \pm 0.04) \times 10^3$
B^0 fraction yield$_0$	$(2.31 \pm 0.54) \times 10^{-1}$
B^0 fraction yield$_1$	$(1.80 \pm 0.41) \times 10^{-1}$
B^0 fraction yield$_2$	$(1.74 \pm 0.25) \times 10^{-1}$
B^0 fraction yield$_3$	$(1.91 \pm 0.23) \times 10^{-1}$
B^0 fraction yield$_4$	$(1.56 \pm 0.17) \times 10^{-1}$
B^0 fraction yield$_5$	$(1.26 \pm 0.16) \times 10^{-1}$
B^0 fraction yield$_6$	$(1.43 \pm 0.14) \times 10^{-1}$
B^0 fraction yield$_7$	$(1.70 \pm 0.14) \times 10^{-1}$
Exp coeff$_0$	$(-2.03 \pm 0.08) \times 10^{-3}$ $(\text{MeV}/c^2)^{-1}$
Exp coeff$_1$	$(-2.36 \pm 0.14) \times 10^{-3}$ $(\text{MeV}/c^2)^{-1}$
Exp coeff$_2$	$(-2.93 \pm 0.20) \times 10^{-3}$ $(\text{MeV}/c^2)^{-1}$
Exp coeff$_3$	$(-3.86 \pm 0.40) \times 10^{-3}$ $(\text{MeV}/c^2)^{-1}$
Exp coeff$_4$	$(-4.67 \pm 0.65) \times 10^{-3}$ $(\text{MeV}/c^2)^{-1}$
Exp coeff$_5$	$(-6.52 \pm 0.78) \times 10^{-3}$ $(\text{MeV}/c^2)^{-1}$
Exp coeff$_6$	$(-1.41 \pm 0.39) \times 10^{-2}$ $(\text{MeV}/c^2)^{-1}$
Exp coeff$_7$	$(-3.39 \pm 1.34) \times 10^{-2}$ $(\text{MeV}/c^2)^{-1}$

Table G.6 *Simultaneous fit result for the 2012 $B_s^0 \to J/\psi f_0$ channel.*

Parameter	Value
α	$(9.74 \pm 0.25) \times 10^{-1}$
$\Delta m_{B_s^0 - B^0}$	(87.25 ± 0.15) MeV/c^2
Comb-bkg yield$_0$	$(5.80 \pm 0.05) \times 10^4$
Comb-bkg yield$_1$	$(2.02 \pm 0.03) \times 10^4$
Comb-bkg yield$_2$	$(1.14 \pm 0.02) \times 10^4$
Comb-bkg yield$_3$	$(4.21 \pm 0.14) \times 10^3$
Comb-bkg yield$_4$	$(2.51 \pm 0.12) \times 10^3$
Comb-bkg yield$_5$	$(7.86 \pm 0.90) \times 10^2$
Comb-bkg yield$_6$	$(2.80 \pm 0.52) \times 10^2$
Comb-bkg yield$_7$	$(2.16 \pm 0.55) \times 10^2$
B^+ yield$_0$	$(3.15 \pm 3.61) \times 10^2$
B^+ yield$_1$	$(4.76 \pm 2.11) \times 10^2$
B^+ yield$_2$	$(6.07 \pm 1.66) \times 10^2$
B^+ yield$_3$	$(5.27 \pm 1.06) \times 10^2$
B^+ yield$_4$	$(5.04 \pm 0.88) \times 10^2$
B^+ yield$_5$	$(3.56 \pm 0.65) \times 10^2$
B^+ yield$_6$	$(4.00 \pm 0.27) \times 10^2$
B^+ yield$_7$	$(1.19 \pm 0.36) \times 10^2$
$\mu_{B_s^0}$	$(5.3670 \pm 0.0001) \times 10^3$ MeV/c^2
$\sigma_{B_s^0}$	(8.83 ± 0.10) MeV/c^2
B_s^0 yield$_0$	$(1.69 \pm 0.09) \times 10^3$
B_s^0 yield$_1$	$(1.43 \pm 0.06) \times 10^3$
B_s^0 yield$_2$	$(1.75 \pm 0.06) \times 10^3$
B_s^0 yield$_3$	$(1.45 \pm 0.04) \times 10^3$
B_s^0 yield$_4$	$(1.93 \pm 0.05) \times 10^3$
B_s^0 yield$_5$	$(1.51 \pm 0.04) \times 10^3$
B_s^0 yield$_6$	$(1.91 \pm 0.04) \times 10^3$
B_S^0 yield$_7$	$(2.09 \pm 0.04) \times 10^3$
B^0 fraction yield$_0$	$(2.26 \pm 0.53) \times 10^{-1}$
B^0 fraction yield$_1$	$(2.01 \pm 0.39) \times 10^{-1}$
B^0 fraction yield$_2$	$(1.66 \pm 0.25) \times 10^{-1}$
B^0 fraction yield$_3$	$(1.94 \pm 0.22) \times 10^{-1}$
B^0 fraction yield$_4$	$(1.91 \pm 0.16) \times 10^{-1}$
B^0 fraction yield$_5$	$(1.66 \pm 0.15) \times 10^{-1}$
B^0 fraction yield$_6$	$(1.78 \pm 0.13) \times 10^{-1}$
B^0 fraction yield$_7$	$(1.35 \pm 0.10) \times 10^{-1}$
Exp coeff$_0$	$(-2.00 \pm 0.05) \times 10^{-3}$ $(\text{MeV}/c^2)^{-1}$
Exp coeff$_1$	$(-2.26 \pm 0.09) \times 10^{-3}$ $(\text{MeV}/c^2)^{-1}$
Exp coeff$_2$	$(-2.66 \pm 0.13) \times 10^{-3}$ $(\text{MeV}/c^2)^{-1}$
Exp coeff$_3$	$(-3.16 \pm 0.23) \times 10^{-3}$ $(\text{MeV}/c^2)^{-1}$
Exp coeff$_4$	$(-3.74 \pm 0.34) \times 10^{-3}$ $(\text{MeV}/c^2)^{-1}$
Exp coeff$_5$	$(-5.70 \pm 0.10) \times 10^{-3}$ $(\text{MeV}/c^2)^{-1}$
Exp coeff$_6$	$(-1.54 \pm 0.40) \times 10^{-2}$ $(\text{MeV}/c^2)^{-1}$
Exp coeff$_7$	$(-3.61 \pm 0.16) \times 10^{-3}$ $(\text{MeV}/c^2)^{-1}$

Table G.7 *Simultaneous fit result for the 2016 $B_s^0 \to J/\psi f_0$ channel.*

Parameter	Value
α	$(9.83 \pm 0.25) \times 10^{-1}$
$\Delta m_{B_s^0 - B^0}$	(87.20 ± 0.01) MeV/c^2
Comb-bkg yield$_0$	$(3.88 \pm 0.03) \times 10^4$
Comb-bkg yield$_1$	$(1.36 \pm 0.02) \times 10^4$
Comb-bkg yield$_2$	$(7.44 \pm 0.18) \times 10^3$
Comb-bkg yield$_3$	$(2.81 \pm 0.12) \times 10^3$
Comb-bkg yield$_4$	$(1.80 \pm 0.10) \times 10^3$
Comb-bkg yield$_5$	$(6.07 \pm 0.70) \times 10^2$
Comb-bkg yield$_6$	$(1.91 \pm 0.46) \times 10^2$
Comb-bkg yield$_7$	$(2.10 \pm 1.25) \times 10^1$
B^+ yield$_0$	$(9.79 \pm 24.0) \times 10^1$
B^+ yield$_1$	$(2.07 \pm 1.47) \times 10^2$
B^+ yield$_2$	$(5.97 \pm 1.34) \times 10^2$
B^+ yield$_3$	$(4.11 \pm 0.90) \times 10^2$
B^+ yield$_4$	$(4.85 \pm 0.77) \times 10^2$
B^+ yield$_5$	$(2.13 \pm 0.50) \times 10^2$
B^+ yield$_6$	$(2.51 \pm 0.25) \times 10^2$
B^+ yield$_7$	$(1.58 \pm 0.14) \times 10^2$
$\mu_{B_s^0}$	$(5.36695 \pm 0.0001) \times 10^3$ MeV/c^2
$\sigma_{B_s^0}$	(8.63 ± 0.10) MeV/c^2
B_s^0 yield$_0$	$(1.43 \pm 0.02) \times 10^3$
B_s^0 yield$_1$	$(1.21 \pm 0.01) \times 10^3$
B_s^0 yield$_2$	$(1.55 \pm 0.01) \times 10^3$
B_s^0 yield$_3$	$(1.25 \pm 0.01) \times 10^3$
B_s^0 yield$_4$	$(1.62 \pm 0.01) \times 10^3$
B_s^0 yield$_5$	$(1.30 \pm 0.01) \times 10^3$
B_s^0 yield$_6$	$(1.68 \pm 0.01) \times 10^3$
B_S^0 yield$_7$	$(1.83 \pm 0.01) \times 10^3$
B^0 fraction yield$_0$	$(2.63 \pm 0.52) \times 10^{-1}$
B^0 fraction yield$_1$	$(1.38 \pm 0.37) \times 10^{-1}$
B^0 fraction yield$_2$	$(1.64 \pm 0.24) \times 10^{-1}$
B^0 fraction yield$_3$	$(1.94 \pm 0.22) \times 10^{-1}$
B^0 fraction yield$_4$	$(1.73 \pm 0.16) \times 10^{-1}$
B^0 fraction yield$_5$	$(1.64 \pm 0.16) \times 10^{-1}$
B^0 fraction yield$_6$	$(1.63 \pm 0.13) \times 10^{-1}$
B^0 fraction yield$_7$	$(1.47 \pm 0.10) \times 10^{-1}$
Exp coeff$_0$	$(-2.11 \pm 0.06) \times 10^{-3}$ $(\text{MeV}/c^2)^{-1}$
Exp coeff$_1$	$(-2.48 \pm 0.11) \times 10^{-3}$ $(\text{MeV}/c^2)^{-1}$
Exp coeff$_2$	$(-2.89 \pm 0.16) \times 10^{-3}$ $(\text{MeV}/c^2)^{-1}$
Exp coeff$_3$	$(-3.37 \pm 0.30) \times 10^{-3}$ $(\text{MeV}/c^2)^{-1}$
Exp coeff$_4$	$(-4.09 \pm 0.43) \times 10^{-3}$ $(\text{MeV}/c^2)^{-1}$
Exp coeff$_5$	$(-4.71 \pm 0.90) \times 10^{-3}$ $(\text{MeV}/c^2)^{-1}$
Exp coeff$_6$	$(-1.13 \pm 0.34) \times 10^{-2}$ $(\text{MeV}/c^2)^{-1}$
Exp coeff$_7$	$(-1.13 \pm 1.03) \times 10^{-1}$ $(\text{MeV}/c^2)^{-1}$

Table G.8 *Simultaneous fit result for the 2017 $B_s^0 \to J/\psi f_0$ channel*

Parameter	Value
α	$(9.67 \pm 0.14) \times 10^{-1}$
$\Delta m_{B_s^0 - B^0}$	(87.15 ± 0.15) MeV/c^2
Comb-bkg yield$_0$	$(4.38 \pm 0.04) \times 10^4$
Comb-bkg yield$_1$	$(1.51 \pm 0.02) \times 10^4$
Comb-bkg yield$_2$	$(8.72 \pm 0.18) \times 10^3$
Comb-bkg yield$_3$	$(3.08 \pm 0.12) \times 10^3$
Comb-bkg yield$_4$	$(1.88 \pm 0.11) \times 10^3$
Comb-bkg yield$_5$	$(4.89 \pm 0.74) \times 10^2$
Comb-bkg yield$_6$	$(2.73 \pm 0.59) \times 10^2$
Comb-bkg yield$_7$	$(1.67 \pm 1.06) \times 10^1$
B^+ yield$_0$	$(2.27 \pm 2.75) \times 10^2$
B^+ yield$_1$	$(5.33 \pm 1.73) \times 10^2$
B^+ yield$_2$	$(2.60 \pm 1.33) \times 10^2$
B^+ yield$_3$	$(4.57 \pm 0.89) \times 10^2$
B^+ yield$_4$	$(4.44 \pm 0.82) \times 10^2$
B^+ yield$_5$	$(3.21 \pm 0.51) \times 10^2$
B^+ yield$_6$	$(2.51 \pm 0.34) \times 10^2$
B^+ yield$_7$	$(1.21 \pm 0.13) \times 10^2$
$\mu_{B_s^0}$	$(5.36696 \pm 0.0001) \times 10^3$ MeV/c^2
$\sigma_{B_s^0}$	(8.71 ± 0.09) MeV/c^2
B_s^0 yield$_0$	$(1.56 \pm 0.02) \times 10^3$
B_s^0 yield$_1$	$(1.41 \pm 0.01) \times 10^3$
B_s^0 yield$_2$	$(1.77 \pm 0.01) \times 10^3$
B_s^0 yield$_3$	$(1.54 \pm 0.01) \times 10^3$
B_s^0 yield$_4$	$(2.06 \pm 0.01) \times 10^3$
B_s^0 yield$_5$	$(1.53 \pm 0.01) \times 10^3$
B_s^0 yield$_6$	$(1.93 \pm 0.01) \times 10^3$
B_S^0 yield$_7$	$(2.17 \pm 0.01) \times 10^3$
B^0 fraction yield$_0$	$(1.84 \pm 0.48) \times 10^{-1}$
B^0 fraction yield$_1$	$(2.03 \pm 0.33) \times 10^{-1}$
B^0 fraction yield$_2$	$(2.40 \pm 0.24) \times 10^{-1}$
B^0 fraction yield$_3$	$(1.97 \pm 0.20) \times 10^{-1}$
B^0 fraction yield$_4$	$(1.85 \pm 0.14) \times 10^{-1}$
B^0 fraction yield$_5$	$(1.62 \pm 0.14) \times 10^{-1}$
B^0 fraction yield$_6$	$(1.58 \pm 0.12) \times 10^{-1}$
B^0 fraction yield$_7$	$(1.37 \pm 0.89) \times 10^{-1}$
Exp coeff$_0$	$(-2.13 \pm 0.05) \times 10^{-3}$ $(\text{MeV}/c^2)^{-1}$
Exp coeff$_1$	$(-2.37 \pm 0.10) \times 10^{-3}$ $(\text{MeV}/c^2)^{-1}$
Exp coeff$_2$	$(-2.59 \pm 0.13) \times 10^{-3}$ $(\text{MeV}/c^2)^{-1}$
Exp coeff$_3$	$(-3.83 \pm 0.28) \times 10^{-3}$ $(\text{MeV}/c^2)^{-1}$
Exp coeff$_4$	$(-4.00 \pm 0.43) \times 10^{-3}$ $(\text{MeV}/c^2)^{-1}$
Exp coeff$_5$	$(-7.12 \pm 1.55) \times 10^{-3}$ $(\text{MeV}/c^2)^{-1}$
Exp coeff$_6$	$(-1.02 \pm 0.29) \times 10^{-2}$ $(\text{MeV}/c^2)^{-1}$
Exp coeff$_7$	$(-1.23 \pm 0.01) \times 10^{-1}$ $(\text{MeV}/c^2)^{-1}$

Table G.9 *Simultaneous fit result for the 2018 $B_s^0 \to J/\psi f_0$ channel.*

Appendix H

DLS cuts

At trigger and stripping level, the J/ψ is required to be detached by applying a DLS cut. Since data and Monte Carlo are not perfectly aligned, additional studies are required in order to have a better agreement between data and simulation. This study was performed with the $B^+ \to J/\psi K^+$ decay using similar selection cuts. The p_T cut on the K^+ is slightly tighter than the one applied on the η' (2.1 GeV vs 2.0 GeV) but this is not expected to have an impact on the final result. This study is needed since there is a misalignment between data and Monte Carlo DLS cuts. In addition, the data and Monte Carlo agreement of the primary and secondary vertex resolution is not perfect due to the simplifications in the simulations and the effects of VELO misalignment.

To find the optimal DLS value, a scan with multiple DLS cuts was performed and a χ^2 test between data and Monte Carlo was plotted for each year. The DLS value minimizing the χ^2 test was used in the analysis. The full list of DLS cuts is shown in table H.1.

Year	J/ψ DLS cut [σ]
2012	3.0
2016	3.45
2017	3.1
2018	3.2

Table H.1 *Effective J/ψ DLS cuts for each year.*

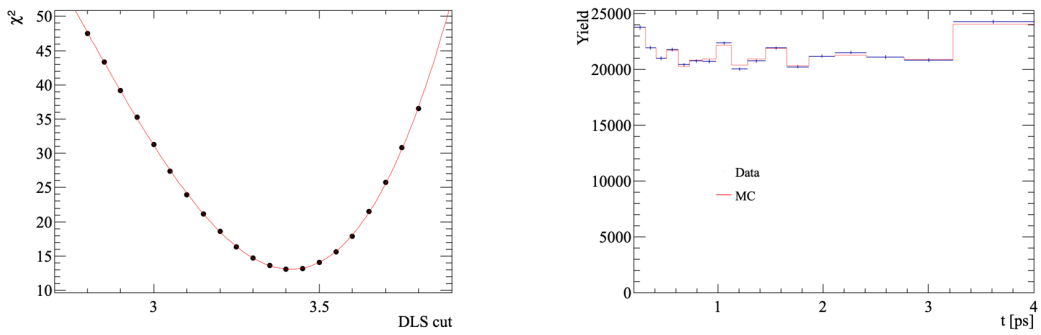

(a) **(b)**

Figure H.1 *Data and Monte Carlo comparison for the optimal 2016 DLS cut. Figure H.1a shows the DLS scan, fig. H.1b shows data and Monte Carlo comparison for the optimal DLS cut.*

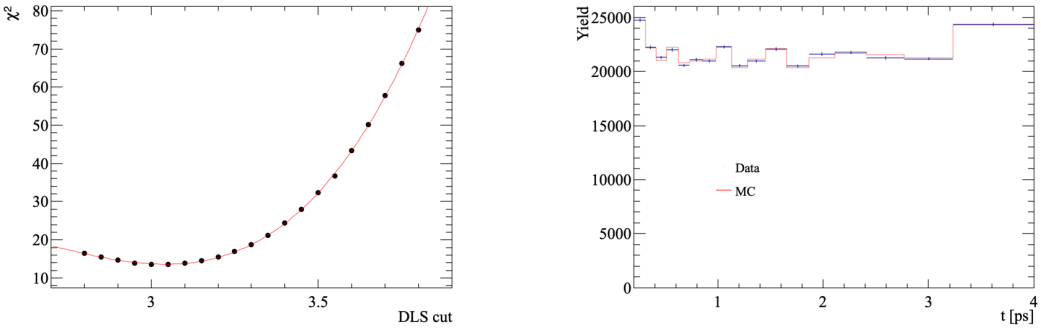

(a) **(b)**

Figure H.2 *Data and Monte Carlo comparison for the optimal 2017 DLS cut. Figure H.2a shows the DLS scan, fig. H.2b shows data and Monte Carlo comparison for the optimal DLS cut.*

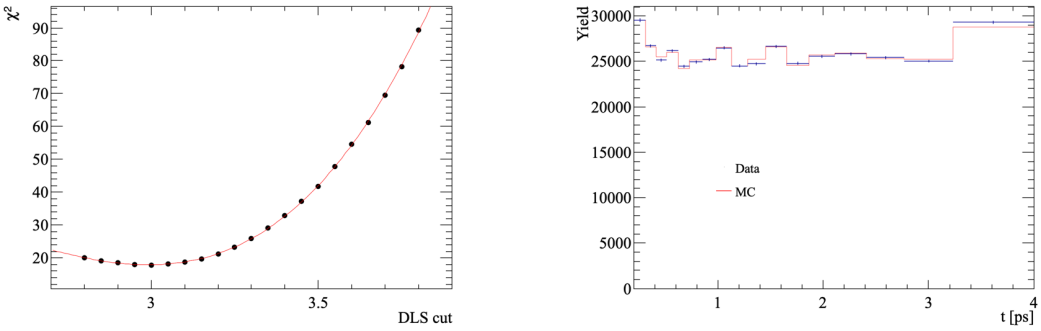

(a) **(b)**

Figure H.3 *Data and Monte Carlo comparison for the optimal 2018 DLS cut. Figure H.3a shows the DLS scan, fig. H.3b shows data and Monte Carlo comparison for the optimal DLS cut.*

Appendix I

Time resolution in bins of decay time

The time resolution is estimated in the simulation from the distribution of the difference between the reconstructed decay time and the real Monte Carlo decay time. This is well described by a triple Gaussian model. The distribution and the fit are shown in fig. I.1. Even if the unbinned time resolution was much smaller than the bin sizes, the time resolution was also computed in each bin as an additional check. In fig. I.2 the fit for each time bin. As shown in table I.2, the time resolution in each bin is much smaller than the bin width. This assures the chosen binning scheme works fine with the decays used in this analysis.

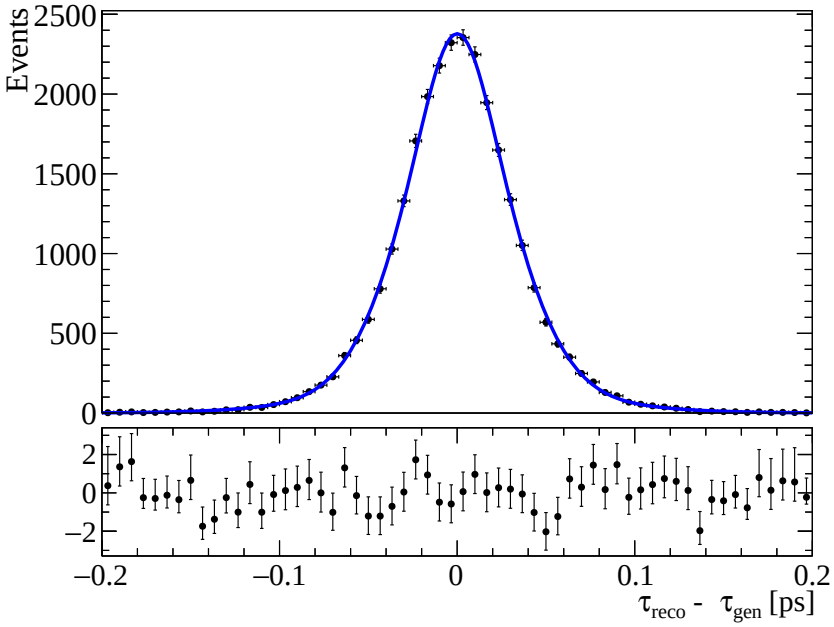

Figure I.1 *Time resolution computed on 2016 η' Monte Carlo sample.*

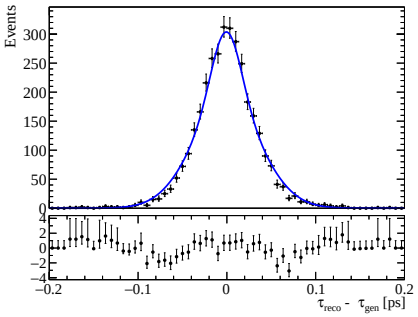

(a) *Bin 1*

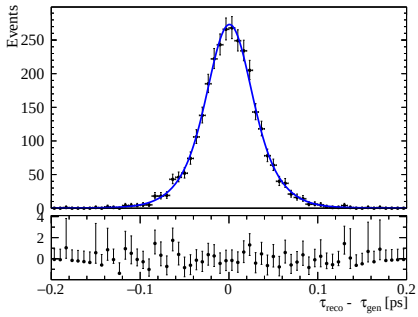

(b) *Bin 2*

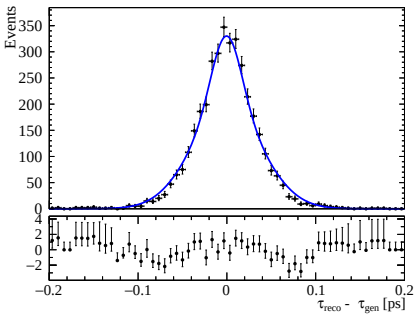

(c) *Bin 3*

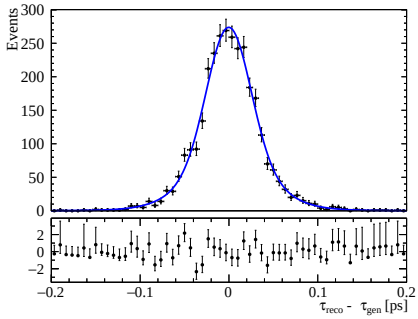

(d) *Bin 4*

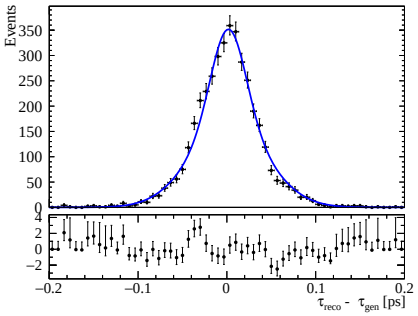

(e) *Bin 5*

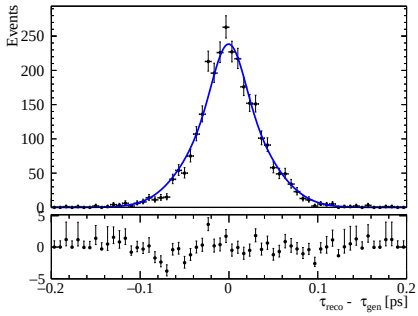

(f) *Bin 6*

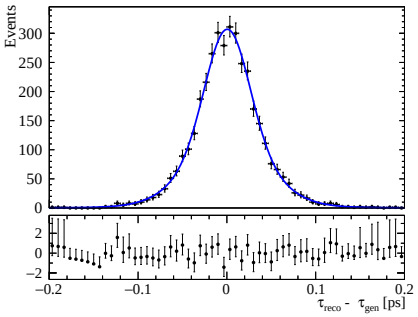

(g) *Bin 7*

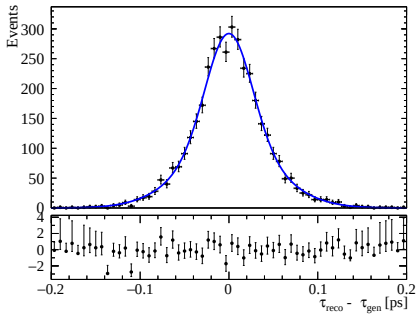

(h) *Bin 8*

Figure I.2 *Time resolution fit in bin of reconstructed time for the 2016 η'.*

Bin	μ [ps] $\times 10^{-4}$	σ_1 [ps] $\times 10^{-2}$	σ_2 [ps] $\times 10^{-2}$	σ_3 [ps] $\times 10^{-2}$	$\texttt{frac}_1 \times 10^{-1}$	$\texttt{frac}_2 \times 10^{-1}$
1	-5.88 ± 6.40	1.66 ± 1.04	3.86 ± 0.097	1.05 ± 6.85	2.39 ± 3.35	7.61 ± 5.34
2	5.96 ± 5.82	2.14 ± 0.26	6.62 ± 1.74	3.73 ± 0.52	4.24 ± 1.67	5.49 ± 7.24
3	-3.72 ± 5.49	1.67 ± 0.24	3.98 ± 0.13	1.11 ± 5.11	2.44 ± 0.95	7.56 ± 0.63
4	-2.11 ± 5.89	2.44 ± 0.24	4.52 ± 0.85	9.73 ± 7.59	6.20 ± 1.66	3.55 ± 1.41
5	17.6 ± 1.10	1.95 ± 0.02	4.28 ± 0.02	3.07 ± 5.80	3.55 ± 0.06	6.44 ± 1.80
6	-3.61 ± 6.90	1.75 ± 0.91	4.12 ± 0.07	1.01 ± 8.88	2.27 ± 3.16	7.72 ± 0.25
7	4.74 ± 5.78	2.45 ± 0.22	4.52 ± 0.36	10.0 ± 6.60	5.10 ± 1.14	4.65 ± 1.10
8	-0.99 ± 6.31	2.59 ± 0.89	5.26 ± 0.26	1.07 ± 5.57	4.97 ± 0.91	5.03 ± 1.21
Unbinned	0.28 ± 2.05	1.71 ± 0.20	3.21 ± 0.17	6.44 ± 0.34	1.34 ± 6.26	7.25 ± 0.41

Table I.1 *Time resolution fit results from 2016 η' Monte Carlo.*

Bin	Time resolution [fs]
1	34
2	36
3	36
4	36
5	36
6	37
7	39
8	41
Unbinned	37

Table I.2 *Time resolution calculated from 2016 η' Monte Carlo.*

Appendix J

Time acceptance

The time acceptance plots described in section 7.3 and not shown in the main text are listed below. They are split by decay channel and by type of acceptance.

J.1 $B_s^0 \to J/\psi\eta'$

J.1.1 DLS

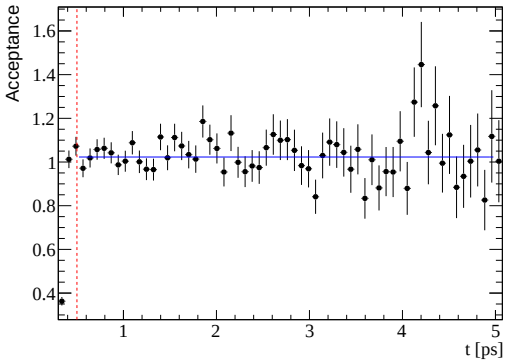

(a) *2012*

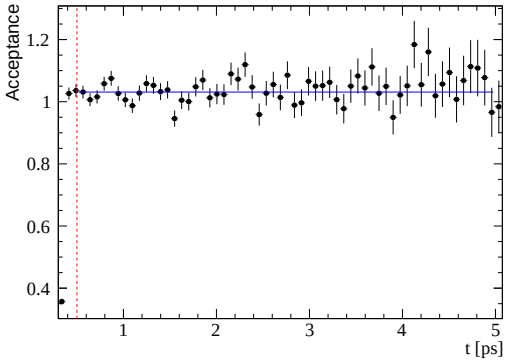

(b) *2017*

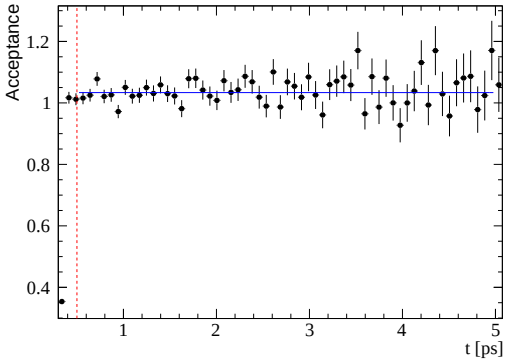

(c) *2018*

Figure J.1 *2012, 2017 and 2018 DLS acceptance for the η' channel. The red dashed line highlights the reconstructed decay time cut applied.*

J.1.2 VELO

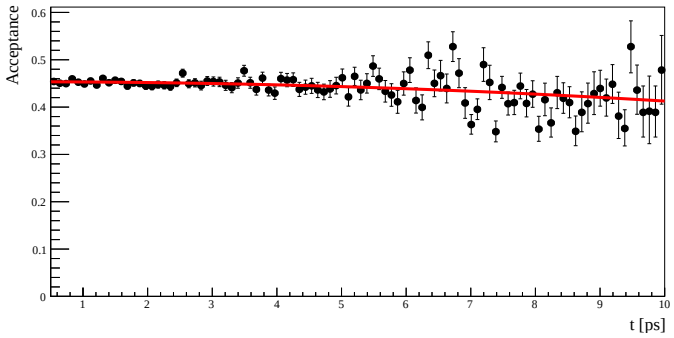

(a) *2012*

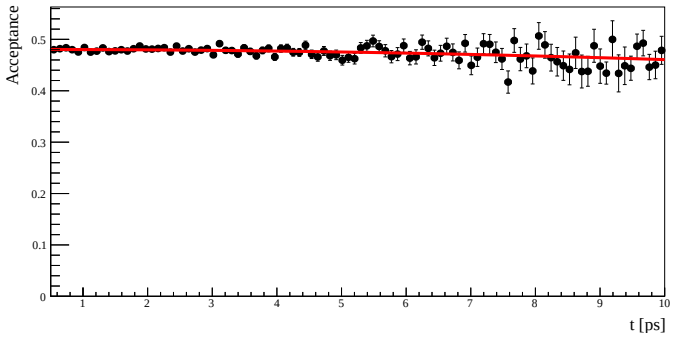

(b) *2017*

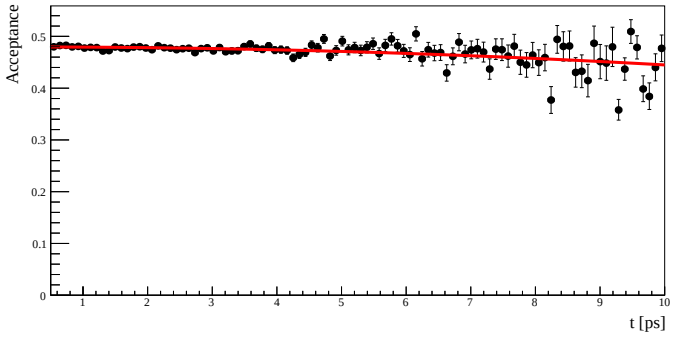

(c) *2018*

Figure J.2 *2012, 2017 and 2018 VELO acceptance for the η' channel.*

J.1.3 MVA

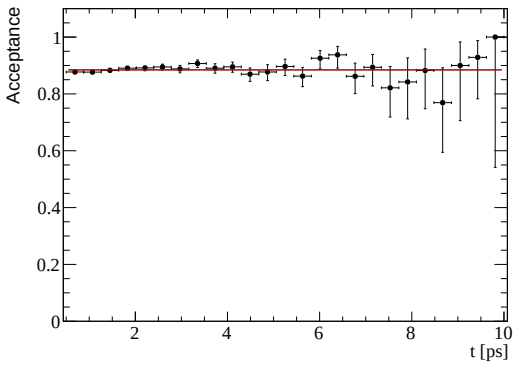

(a) *2012*

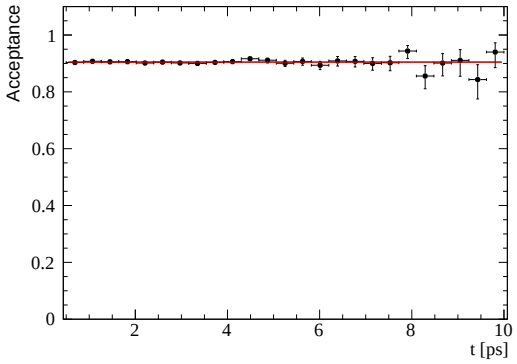

(b) *2017*

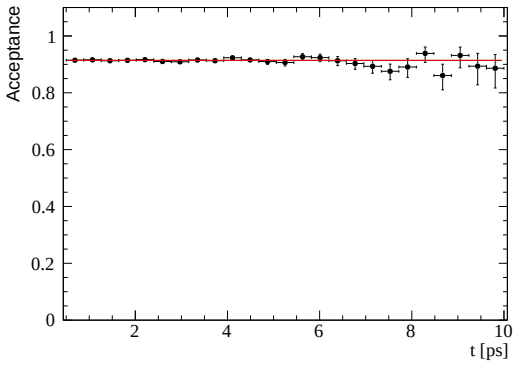

(c) *2018*

Figure J.3 *2012, 2017 and 2018 MVA acceptance for the η' channel.*

J.2 $B_s^0 \to J/\psi f_0$

J.2.1 DLS

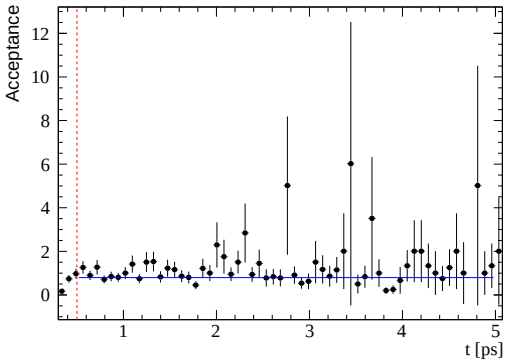

(a) *2012*

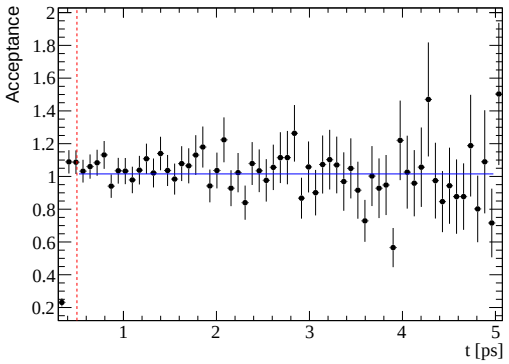

(b) *2017*

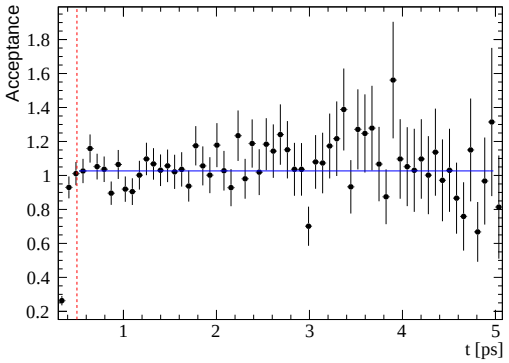

(c) *2018*

Figure J.4 *2012, 2017 and 2018 DLS acceptance for the f_0 channel. The red dashed line highlights the reconstructed decay time cut applied.*

J.2.2 VELO

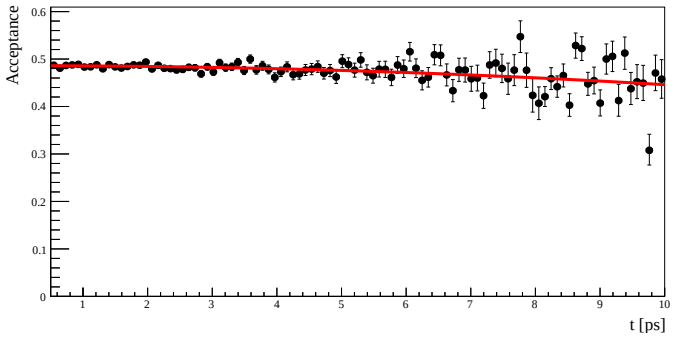

(a) *2012*

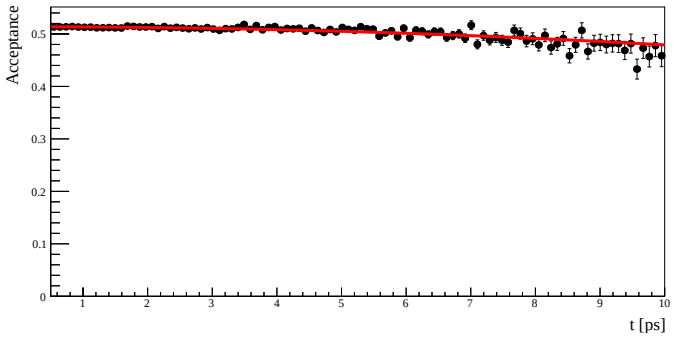

(b) *2017*

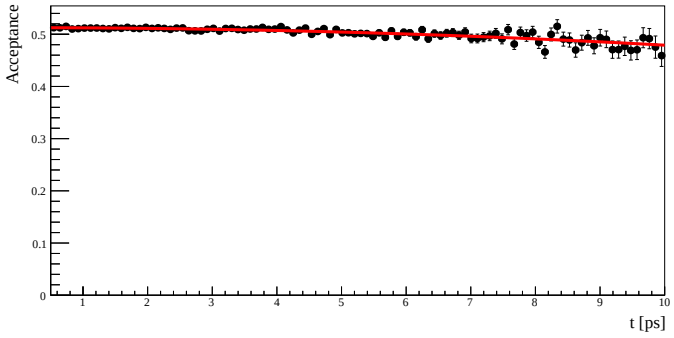

(c) *2018*

Figure J.5 *2012, 2017 and 2018 VELO acceptance for the f_0 channel.*

J.2.3 MVA

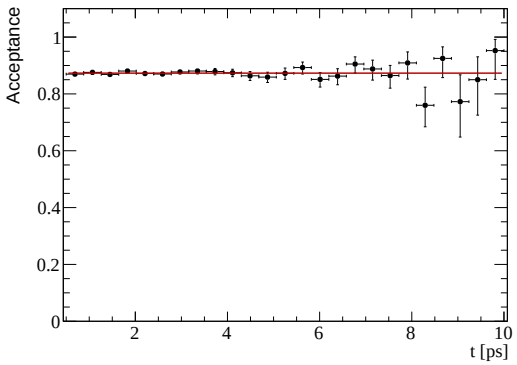

(a) *2012*

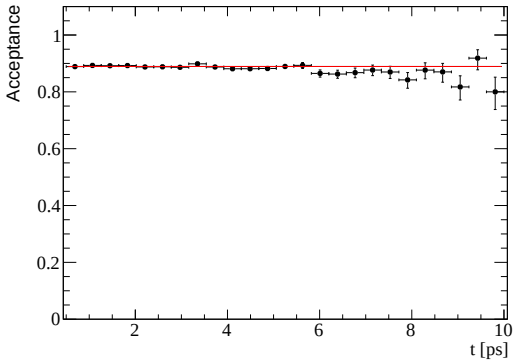

(b) *2017*

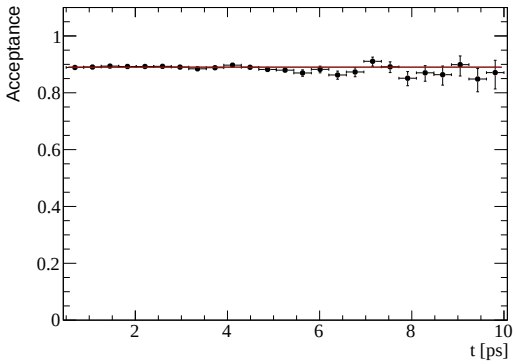

(c) *2018*

Figure J.6 *2012, 2017 and 2018 MVA acceptance for the f_0 channel.*

J.2.4 Global acceptance fit

To better understand the systematic uncertainty the global acceptance fit would introduce into the $\Delta\Gamma_s$ measurement, the fit function was changed to $\mathcal{A}_{\text{fit}} = (1 - bt^{1.5})\, e^{-t/\tau_{\text{MC}}}$ and $\mathcal{A}_{\text{fit}} = (1 - bt^{0.5})\, e^{-t/\tau_{\text{MC}}}$. The fits for both functions and channels are shown in figs. J.7, J.8, J.9 and J.10.

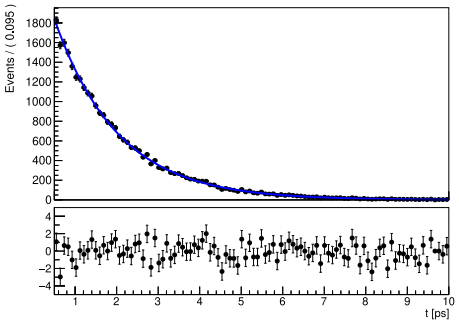

(a) *2011-2012*

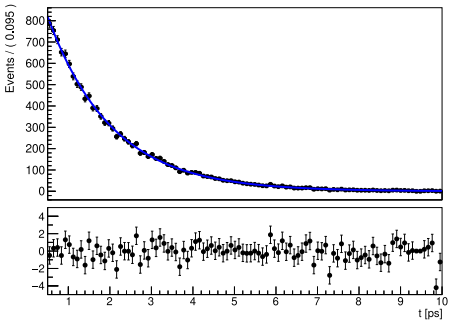

(b) *2015-2016*

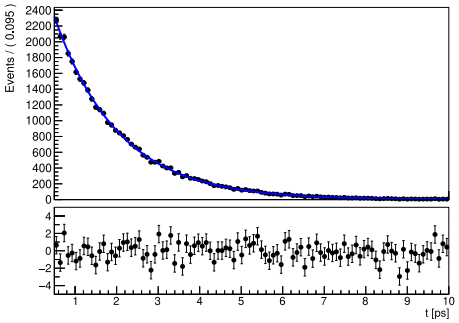

(c) *2017*

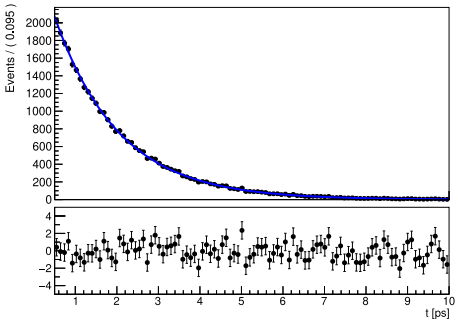

(d) *2018*

Figure J.7 *Time acceptance fits for the* $B_s^0 \to J/\psi\eta'$ *channel with* $\mathcal{A}_{\text{fit}} = \left(1 - bt^{1.5}\right) e^{-t/\tau_{\text{MC}}}$.

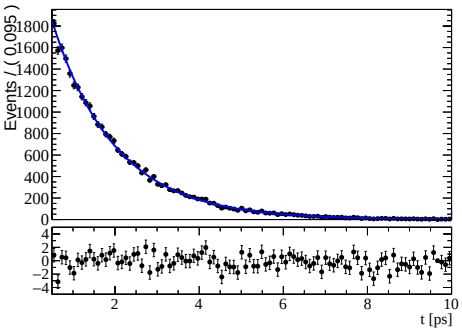

(a) *2011-2012*

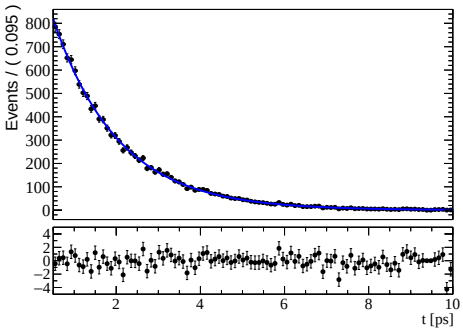

(b) *2015-2016*

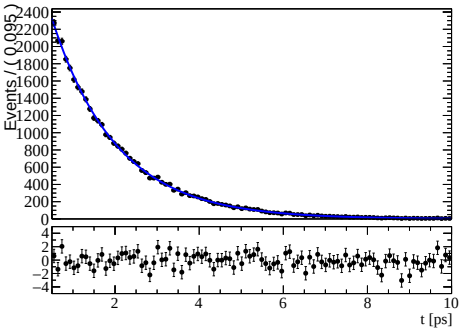

(c) *2017*

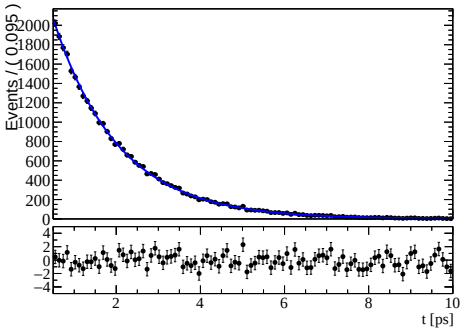

(d) *2018*

Figure J.8 *Time acceptance fits for the* $B_s^0 \to J/\psi\eta'$ *channel with* $\mathcal{A}_{\text{fit}} = \left(1 - bt^{0.5}\right) e^{-t/\tau_{\text{MC}}}$

.

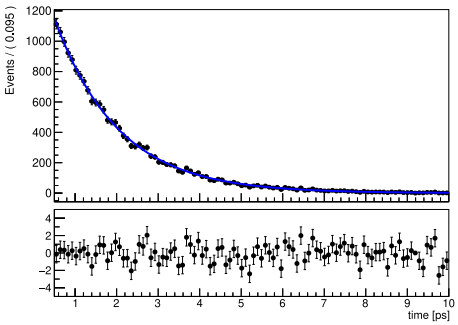

(a) *2011-2012*

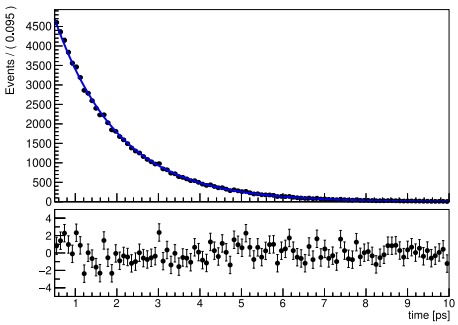

(b) *2015-2016*

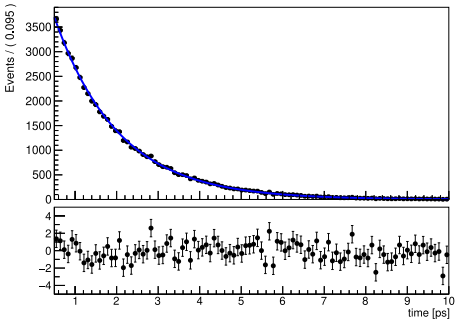

(c) *2017*

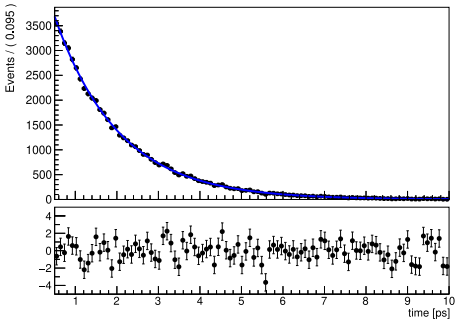

(d) *2018*

Figure J.9 *Time acceptance fits for the* $B_s^0 \to J/\psi f_0$ *channel with* $\mathcal{A}_{\text{fit}} = \left(1 - bt^{1.5}\right) e^{-t/\tau_{\text{MC}}}$

.

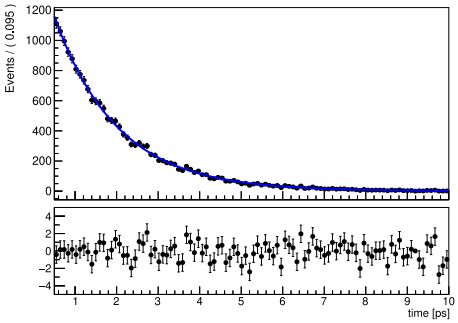

(a) *2011-2012*

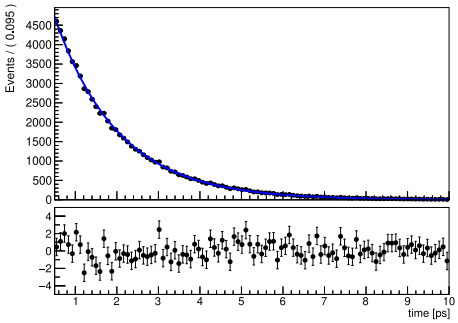

(b) *2015-2016*

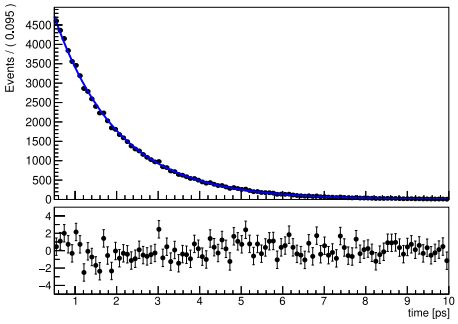

(c) *2017*

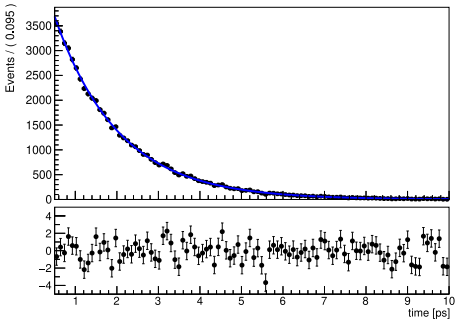

(d) *2018*

Figure J.10 *Time acceptance fits for the* $B_s^0 \to J/\psi f_0$ *channel with* $\mathcal{A}_{\text{fit}} = \left(1 - bt^{0.5}\right) e^{-t/\tau_{\text{MC}}}$.

Bibliography

[1] S. Petrucci et al. Scalable monitoring data processing for the LHCb software trigger. *EPJ Web Conf.*, 245:01039, 2020. doi: 10.1051/epjconf/202024501039. URL https://doi.org/10.1051/epjconf/202024501039.

[2] J. D. Barrow et al. Baryosynthesis and the origin of galaxies. *Nature*.

[3] A. D. Sakharov. Violation of CP in variance, C asymmetry, and baryon asymmetry of the universe. *Phys. Usp.*, 34(5):392–393, 1991. doi: 10.1070/PU1991v034n05ABEH002497. URL https://ufn.ru/en/articles/1991/5/h/.

[4] S. Weinberg. The Making of the Standard Model. *Eur. Phys. J. C*, 34:5–13. 21 p. ; streaming video, 2003. URL https://cds.cern.ch/record/799984.

[5] E. D. Bloom et al. High-energy inelastic $e-p$ scattering at 6° and 10°. *Phys. Rev. Lett.*, 23:930–934, Oct 1969. doi: 10.1103/PhysRevLett.23.930. URL https://link.aps.org/doi/10.1103/PhysRevLett.23.930.

[6] P. W. Higgs. Broken symmetries and the masses of gauge bosons. *Phys. Rev. Lett.*, 13:508–509, Oct 1964. doi: 10.1103/PhysRevLett.13.508. URL https://link.aps.org/doi/10.1103/PhysRevLett.13.508.

[7] Standard model of elementary particles, 2021. URL https://upload.wikimedia.org/wikipedia/commons/0/00/Standard_Model_of_Elementary_Particles.svg.

[8] S. Weinberg. A Model of Leptons. *Phys. Rev. Lett.*, 19:1264–1266, Nov 1967. doi: 10.1103/PhysRevLett.19.1264. URL https://link.aps.org/doi/10.1103/PhysRevLett.19.1264.

[9] A. Salam and J. C. Ward. Weak and electromagnetic interactions. *Il Nuovo Cimento (1955-1965)*, 11, 1959. doi: 10.1007/BF02726525. URL https://doi.org/10.1007/BF02726525.

[10] Gargamelle, 2021. URL https://home.cern/science/experiments/gargamelle.

[11] UA1, 2021. URL https://home.cern/science/experiments/ua1.

[12] UA2, 2021. URL https://home.cern/science/experiments/ua2.

[13] J. H. Christenson et al. Evidence for the 2π Decay of the K_2^0 Meson. *Phys. Rev. Lett.*, 13:138–140, Jul 1964. URL https://link.aps.org/doi/10.1103/PhysRevLett.13.138.

[14] A. Ceccucci et al. CKM Quark-Mixing Matrix. *PDG*. URL https://pdg.lbl.gov/2019/reviews/rpp2019-rev-ckm-matrix.pdf.

[15] M. Kobayashi and T. Maskawa. CP-Violation in the Renormalizable Theory of Weak Interaction. *Progress of Theoretical Physics*, 49(2):652–657, 02 1973. ISSN 0033-068X. doi: 10.1143/PTP.49.652. URL https://doi.org/10.1143/PTP.49.652.

[16] L. Wolfenstein. Parametrization of the Kobayashi-Maskawa Matrix. *Phys. Rev. Lett.*, 51:1945, 1983. doi: 10.1103/PhysRevLett.51.1945.

[17] CKM quark-mixing matrix, 2008. URL https://pdg.lbl.gov/2008/reviews/kmmixrpp.pdf.

[18] T. Gershon and V. V. Gligorov. CP violation in the B system. *Reports on Progress in Physics*, 80(4):046201, Feb 2017. ISSN 1361-6633. doi: 10.1088/1361-6633/aa5514. URL http://dx.doi.org/10.1088/1361-6633/aa5514.

[19] J. Charles et al. CKMfitter Group, 2022. URL http://ckmfitter.in2p3.fr.

[20] HFLAV collaboration. Pdg 2021 averages. URL https://hflav-eos.web.cern.ch/hflav-eos/osc/PDG_2021/.

[21] S. Amato et al. LHCb technical proposal: A Large Hadron Collider Beauty Experiment for Precision Measurements of CP Violation and Rare Decays. 2 1998.

[22] M. Gell-Mann et al. Behavior of neutral particles under charge conjugation. *Phys. Rev.*, 97:1387–1389, 1955. doi: 10.1103/PhysRev.97.1387.

[23] K. Lande et al. Observation of long-lived neutral v particles. *Phys. Rev.*, 103:1901–1904, Sep 1956. doi: 10.1103/PhysRev.103.1901. URL https://link.aps.org/doi/10.1103/PhysRev.103.1901.

[24] H. Albrecht et al. Observation of $B^0 - \overline{B}^0$ mixing. *Physics Letters B*, 192(1):245–252, 1987. ISSN 0370-2693. doi: https://doi.org/10.1016/0370-2693(87)91177-4. URL https://www.sciencedirect.com/science/article/pii/0370269387911774.

[25] A. Abulencia et al. Observation of $B_s^0 - \overline{B}_s^0$ oscillations. *Physical Review Letters*, 97(24), Dec 2006. ISSN 1079-7114. doi: 10.1103/physrevlett.97.242003. URL http://dx.doi.org/10.1103/PhysRevLett.97.242003.

[26] R. Aaij et al. Measurement of the $B_s^0 - \overline{B}_s^0$ oscillation frequency Δm_s in $B_s^0 \to D_s^-(3)\pi$ decays. *Physics Letters B*, 709(3):177–184, Mar 2012. ISSN 0370-2693. doi: 10.1016/j.physletb.2012.02.031. URL http://dx.doi.org/10.1016/j.physletb.2012.02.031.

[27] Y. Amhis et al. Averages of b-hadron, c-hadron, and τ-lepton properties as of 2018. *The European Physical Journal C*, 81(3), mar 2021. URL https://doi.org/10.1140%2Fepjc%2Fs10052-020-8156-7.

[28] A. Lenz and G. Tetlalmatzi-Xolocotzi. Model-independent bounds on new physics effects in non-leptonic tree-level decays of B-mesons. *JHEP*, 07:177, 2020. doi: 10.1007/JHEP07(2020)177.

[29] R. Aaij et al. Precise determination of the $B_s^0 - \overline{B}_s^0$ oscillation frequency, 2021.

[30] R. Fleischer and R. Knegjens. Effective Lifetimes of B_s Decays and their Constraints on the B_s^0-$\bar{B}_s^0$ Mixing Parameters. *Eur.Phys.J.*, C71:1789, 2011. doi: 10.1140/epjc/s10052-011-1789-9.

[31] C. T. H. Davies et al. Lattice QCD matrix elements for the $B_s^0 - \bar{B}_s^0$ width difference beyond leading order. *Phys. Rev. Lett.*, 124(8):082001, 2020. doi: 10.1103/PhysRevLett.124.082001.

[32] H. M. Asatrian et al. Penguin contribution to the width difference and CP asymmetry in B_q-$\bar{B}_q$ mixing at order $\alpha_s^2 N_f$. *Phys. Rev. D*, 102(3):033007, 2020. doi: 10.1103/PhysRevD.102.033007.

[33] M. Gerlach et al. The width difference in $B - \overline{B}$ mixing at order α_s and beyond. 2022. URL https://arxiv.org/abs/2202.12305.

[34] R. Fleischer et al. Exploring CP Violation and η-η' Mixing with the $B_{s,d}^0 \to J/\psi\eta^{(\prime)}$ Systems. *Eur.Phys.J.*, C71:1798, 2011. doi: 10.1140/epjc/s10052-011-1798-8.

[35] M. Aaboud et al. Measurement of the relative width difference of the $B^0 - \overline{B}^0$ system with the ATLAS detector. *Journal of High Energy Physics*, 2016(6), Jun 2016. ISSN 1029-8479. doi: 10.1007/jhep06(2016)081. URL http://dx.doi.org/10.1007/JHEP06(2016)081.

[36] G.D. Lafferty and T.R. Wyatt. Where to stick your data points: The treatment of measurements within wide bins. *Nuclear Instruments and Methods in Physics Research Section A: Accelerators, Spectrometers, Detectors and Associated Equipment*, 355(2):541–547, 1995. ISSN 0168-9002. doi: https://doi.org/10.1016/0168-9002(94)01112-5. URL https://www.sciencedirect.com/science/article/pii/0168900294011125.

[37] R. Fleischer et al. Anatomy of $B_{s,d}^0 \to J/\psi f_0(980)$. *The European Physical Journal C*, 71(12), Dec 2011. ISSN 1434-6052. doi: 10.1140/epjc/s10052-011-1832-x. URL http://dx.doi.org/10.1140/epjc/s10052-011-1832-x.

[38] CERN - About, . URL https://home.cern/about.

[39] A. A. Alves et al. The LHCb Detector at the LHC. *JINST*, 3(LHCb-DP-2008-001. CERN-LHCb-DP-2008-001):S08005, 2008. URL https://cds.cern.ch/record/1129809. Also published by CERN Geneva in 2010.

[40] O. S. Brüning et al. *LHC Design Report*. CERN Yellow Reports: Monographs. CERN, Geneva, 2004. doi: 10.5170/CERN-2004-003-V-1. URL https://cds.cern.ch/record/782076.

[41] *LEP design report*. CERN, Geneva, 1984. URL https://cds.cern.ch/record/102083. Copies shelved as reports in LEP, PS and SPS libraries.

[42] K. Aamodt et al. The ALICE experiment at the CERN LHC. A Large Ion Collider Experiment. *JINST*, 3:S08002. 259 p, 2008. doi: 10.1088/1748-0221/3/08/S08002. URL https://cds.cern.ch/record/1129812. Also published by CERN Geneva in 2010.

[43] A. Airapetian et al. *ATLAS detector and physics performance: Technical Design Report, 1*. Technical Design Report ATLAS. CERN, Geneva, 1999. URL https://cds.cern.ch/record/391176.

[44] G. L. Bayatian et al. *CMS Physics: Technical Design Report Volume 1: Detector Performance and Software*. Technical Design Report CMS. CERN, Geneva, 2006. URL https://cds.cern.ch/record/922757.

[45] E. Mobs. The CERN accelerator complex. Complexe des accélérateurs du CERN. Jul 2016. URL https://cds.cern.ch/record/2197559. General Photo.

[46] R. Aaij et al. Design and performance of the LHCb trigger and full real-time reconstruction in Run 2 of the LHC. Performance of the LHCb trigger and full real-time reconstruction in Run 2 of the LHC. *JINST*, 14 (arXiv:1812.10790. 04):P04013. 43 p, Dec 2018. URL https://cds.cern.ch/record/2652801.

[47] LHCb Collaboration. LHCb-Facts. URL https://twiki.cern.ch/twiki/bin/view/Main/LHCb-Facts.

[48] LHCb Collaboration. Integrated recorded luminosity at the lhcb experiment, 2018. URL http://lhcb-public.web.cern.ch/.

[49] C. Elsässer. $\bar{b}b$ production angle plots. URL https://lhcb.web.cern.ch/lhcb/speakersbureau/html/bb_ProductionAngles.html.

[50] P. R. Barbosa-Marinho et al. *LHCb VELO (VErtex LOcator): Technical Design Report*. Technical Design Report LHCb. CERN, Geneva, 2001. URL https://cds.cern.ch/record/504321.

[51] R. Aaij et al. LHCb Detector Performance. *Int. J. Mod. Phys. A*, 30(LHCB-DP-2014-002. CERN-PH-EP-2014-290. LHCB-DP-2014-002. CERN-LHCB-DP-2014-002):1530022. 73 p, Dec 2014. doi: 10.1142/S0217751X15300227. URL https://cds.cern.ch/record/1978280.

[52] R. Arink et al. Performance of the LHCb Outer Tracker. *JINST*, 9(LHCB-DP-2013-003. LHCB-DP-2013-003. CERN-LHCB-DP-2013-003):P01002. 30 p, Nov 2013. doi: 10.1088/1748-0221/9/01/P01002. URL http://cds.cern.ch/record/1629476.

[53] M. Adinolfi et al. Performance of the lhcb rich detector at the lhc. *The European Physical Journal C*, 73(5), May 2013. ISSN 1434-6052. doi: 10.1140/epjc/s10052-013-2431-9. URL http://dx.doi.org/10.1140/epjc/s10052-013-2431-9.

[54] P. A. Cherenkov. Visible luminescence of pure liquids under the influence of γ-radiation. *Dokl. Akad. Nauk SSSR*, 2(8):451–454, 1934. doi: 10.3367/UFNr.0093.196710n.0385.

[55] S. Amato et al. *LHCb calorimeters: Technical Design Report*. Technical Design Report LHCb. CERN, Geneva, 2000. URL https://cds.cern.ch/record/494264.

[56] *LHCb muon system: second addendum to the Technical Design Report*. Technical Design Report LHCb. CERN, Geneva, 2005. URL http://cds.cern.ch/record/831955. Submitted on 9 Apr 2005.

[57] F. Legger et al. TELL1: development of a common readout board for LHCb. TELL1. a common readout board for LHCb. Technical Report LHCb-2004-100. CERN-LHCb-2004-100. 1-2, CERN, Geneva, Nov 2004. URL https://cds.cern.ch/record/806933.

[58] M. Borkov et al. The LHCb Level Muon Trigger. URL https://lhcb-muon.web.cern.ch/detector/PNPI_prod/documentation/lhcb-98-002.pdf.

[59] R. Aaij et al. Design and performance of the LHCb trigger and full real-time reconstruction in run 2 of the LHC. *Journal of Instrumentation*, 14(04): P04013–P04013, apr 2019. doi: 10.1088/1748-0221/14/04/p04013. URL https://doi.org/10.1088/1748-0221/14/04/p04013.

[60] LHCb trigger system. URL https://lhcb-public.web.cern.ch/en/Data%20Collection/Triggers2-en.html.

[61] R. Aaij and J. Albrecht. Muon triggers in the High Level Trigger of LHCb. Technical Report LHCb-PUB-2011-017. CERN-LHCb-PUB-2011-017, CERN, Geneva, Sep 2011. URL https://cds.cern.ch/record/1384386.

[62] LHCb collaboration. The BRUNEL Project, . URL http://lhcbdoc.web.cern.ch/lhcbdoc/brunel/.

[63] LHCb collaboration. The DAVINCI Project, . URL https://lhcbdoc.web.cern.ch/lhcbdoc/davinci/.

[64] LHCb collaboration. Starterkit lessons, . URL https://lhcb.github.io/starterkit-lessons/index.html.

[65] R. Aaij et al. Measurement of the $B_s^0 \to J/\psi\eta$ lifetime. *Physics Letters B*, 762:484–492, 2016. ISSN 0370-2693. doi: https://doi.org/10.1016/j.physletb.2016.10.006. URL https://www.sciencedirect.com/science/article/pii/S0370269316305779.

[66] M. Benayoun and O. Callot. The forward tracking, an optical model method. Technical report, CERN, Geneva, Feb 2002. URL http://cds.cern.ch/record/684710. revised version number 1 submitted on 2002-02-22 17:19:02.

[67] R. Hierk et al. Performance of the LHCb 00 track fitting software. Technical Report LHCb-2000-086, CERN, Geneva, Aug 2000. URL http://cds.cern.ch/record/684697.

[68] J. B. Zonneveld. Measurement of the CP violating phase ϕ_s using $B_s^0 \to J/\psi K^+K^-$ decays at the LHCb Experiment, 2020. URL http://cds.cern.ch/record/2734077. Presented 28 May 2020.

[69] F. Ferrari. Novel strategies at LHCb for particle identification, 2017.

[70] C. Abellán Beteta et al. Calibration and performance of the LHCb calorimeters in Run 1 and 2 at the LHC. Aug 2020. URL https://arxiv.org/abs/2008.11556.

[71] J. Albrecht et al. Upgrade trigger reconstruction strategy: 2017 milestone. Technical report, CERN, Geneva, Mar 2018. URL https://cds.cern.ch/record/2310579.

[72] O Deschamps et al. Photon and neutral pion reconstruction. Technical report, CERN, Geneva, Sep 2003. URL https://cds.cern.ch/record/691634.

[73] S. Miglioranzi et al. The LHCb Simulation Application, Gauss: Design, Evolution and Experience. Technical Report LHCb-PROC-2011-006. CERN-LHCb-PROC-2011-006, CERN, Geneva, Jan 2011. URL https://cds.cern.ch/record/1322402.

[74] T. Sjöstrand et al. High-energy-physics event generation with pythia6.1. *Computer Physics Communications*, 135(2):238–259, Apr 2001. ISSN 0010-4655. doi: 10.1016/s0010-4655(00)00236-8. URL http://dx.doi.org/10.1016/S0010-4655(00)00236-8.

[75] Geant4. URL https://geant4.web.cern.ch/node/1.

[76] E. Barberio et al. PHOTOS: a universal Monte Carlo for QED radiative corrections. *Comput. Phys. Commun.*, 79:291–308. 23 p, Oct 1993. doi: 10.1016/0010-4655(94)90074-4. URL https://cds.cern.ch/record/254343.

[77] R. Antunes-Nobrega et al. *LHCb computing: Technical Design Report*. Technical design report. LHCb. CERN, Geneva, 2005. URL https://cds.cern.ch/record/835156. Submitted on 11 May 2005.

[78] E. Rodrigues. Dealing with clones in the tracking. Technical Report LHCb-2006-057. CERN-LHCb-2006-057, CERN, Geneva, Nov 2006. URL http://cds.cern.ch/record/1000723.

[79] J. Shiers. The Worldwide LHC Computing Grid (worldwide LCG). *Comput. Phys. Commun.*, 177(1-2):219–223, 2007. doi: 10.1016/j.cpc.2007.02.021. URL https://cds.cern.ch/record/1063847.

[80] CERN. WLCG Tier centres. URL https://wlcg-public.web.cern.ch/tier-centres.

[81] C. Gaspar and M. Dönszelmann. DIM - A distributed information management system for the DELPHI experiment at CERN. Jan 1994. URL https://cds.cern.ch/record/2629101.

[82] O. Callot et al. Online data monitoring in the LHCb experiment. *Journal of Physics: Conference Series*, 119(2):022015, jul 2008. doi: 10.1088/1742-6596/119/2/022015. URL https://doi.org/10.1088/1742-6596/119/2/022015.

[83] Boost::serialize, . URL https://www.boost.org/doc/libs/1_76_0/libs/serialization/doc/index.html.

[84] ZeroMQ. URL https://zeromq.org/.

[85] Apache Kafka. URL https://kafka.apache.org/.

[86] H. U. Mohamed. Deploying a "push" model Prometheus. Jul 2018. URL https://cds.cern.ch/record/2631797.

[87] Kubernetes. URL https://kubernetes.io/.

[88] Confluent Kafka. URL https://github.com/confluentinc/confluent-kafka-python.

[89] Standard set of performance numbers, . URL https://lhcb.web.cern.ch/speakersbureau/html/PerformanceNumbers.html.

[90] LoKi's Array Particle Functions, . URL https://twiki.cern.ch/twiki/bin/view/LHCb/LoKiArrayFunctions#LoKiACUTDOCACHI2.

[91] D. Volyanskyy and J. van Tilburg. Selection of the $B_s^0 \to J/\psi(\mu^+\mu^-)\ \eta'(\rho^0\gamma)$ decay at LHCb and its sensitivity to the B_s^0 mixing phase ϕ_s. Technical report, CERN, Geneva, Apr 2007. URL https://cds.cern.ch/record/1026902.

[92] P.A. Zyla et al. Review of Particle Physics. *PTEP*, 2020(8):083C01, 2020. doi: 10.1093/ptep/ptaa104.

[93] A. Hoecker et al. TMVA - Toolkit for Multivariate Data Analysis. 2007. URL https://arxiv.org/abs/physics/0703039v5.

[94] G. Cowan et al. RapidSim: An application for the fast simulation of heavy-quark hadron decays. *Computer Physics Communications*, 214:239–246, May 2017. ISSN 0010-4655. doi: 10.1016/j.cpc.2017.01.029. URL http://dx.doi.org/10.1016/j.cpc.2017.01.029.

[95] R. Aaij et al. Analysis of the resonant components in $\overline{B}^0 \to J/\psi\pi^+\pi^-$. *Phys. Rev.*, D87:052001, 2013. doi: 10.1103/PhysRevD.87.052001.

[96] M. Needham. Private communication.